

DISSERTATION

EXTREME ULTRAVIOLET LASER ABLATION MASS SPECTROMETER FOR
MOLECULAR IMAGING AT THE NANOSCALE

Submitted by

Ilya Kuznetsov

Department of Electrical and Computer Engineering

In partial fulfillment of the requirements

For the Degree of Doctor of Philosophy

Colorado State University

Fort Collins, Colorado

Spring 2018

Doctoral Committee:

Advisor: Carmen Menoni

Jorge Rocca

Dean Crick

Elliot Bernstein

Diego Krapf

Copyright by Ilya Kuznetsov 2018

All Rights Reserved

ABSTRACT

EXTREME ULTRAVIOLET LASER ABLATION MASS SPECTROMETER FOR MOLECULAR IMAGING AT THE NANOSCALE

The demand for high-precision analytical instrumentation in modern science and technology is exploding. The quality of questions to be answered sets the requirements for a given piece of technology. The type of analytical instrumentation that enables users to unambiguously identify, quantify, and map the chemical structure of a solid is imaging mass spectrometry (IMS). Most common commercially available instruments include desorption electrospray ionization (DESI), matrix-assisted laser desorption and ionization (MALDI), and secondary ion mass spectrometry (SIMS) as well as their derivatives. Each of these methods possesses a set of capabilities that define its use for one or another research task. None of them, however, enables scientists to map a solid's molecular composition in three dimensions at the nanoscale.

We have developed an extreme ultraviolet laser ablation time-of-flight mass spectrometer (EUV TOF) that relies on sample probing by a 46.9 nm wavelength laser. In this work, the unique interaction of EUV light with matter was experimentally assessed and compared to SIMS TOF. It was found that the spatial resolution can be as small as 80 nm in molecular and atomic analysis in organic and inorganic materials respectively. Depth resolution is as high as 20 nm as measured on an organic bilayer. Sensitivity of the EUV TOF reaches ~ 0.02 amol, which is estimated to be $20\times$ better than that of SIMS TOF in the sample of the amino acid

alanine. Sensitivity in other units—sample utilization efficiency (SUE)—was found to be similar to SIMS TOF when assessed by means of detecting trace actinides in a glass matrix. It was shown that it can be further improved by means of post-ablation ionization (PI) with a secondary UV laser source. Using vacuum ultraviolet (VUV) laser light can increase the mass range of molecular detection. For instance, an intact cholesterol molecule was first detected by EUV TOF operating in VUV PI mode. This approach opens a range of opportunities to use the technique for biological studies.

EUV TOF is capable to image chemical composition. This capability is demonstrated by imaging the 3D nanoscale spatial distribution of low mass fragments in a single mycobacterium. With additional instrumental modifications, it will be possible to achieve sub-cellular imaging of the molecular structure of a single microorganism without the need for using externally applied ionization-promoting matrix. Such capabilities may help to steer the development of new drugs in pharmacology and identify the signature isotope pattern of the miniscule bits of material examined by nuclear scientists.

ACKNOWLEDGEMENTS

First of all I must acknowledge the work and positive influence on my personal development of all my teachers and mentors prior to the start of my PhD program at CSU.

I would like to express my gratitude to my advisors Carmen Menoni and Jorge Rocca for giving me the opportunity of working in their research group. I would also like to acknowledge professors Dean Crick, Elliot Bernstein and Diego Krapf for serving on my committee.

I am indebted to Jorge Filevich and the early league of EUV ERC comrades for their knowledge transfer and time spent together in the lab: Lukasz Urbanski, Fernando Brizuela, Sergio Carbajo, Isela Howlett, Jonathan Tollerud, Jonathan Grava, Federico Furch, Mike Grisham, Mike Purvis, Dale Martz and many more.

For the EUV photodetectors work I am in particular thankful to Mark Woolston, Jonas Boch, Gonzalo Orejas, Ricky Krahn. Mark Woolston was available at any moment for the help with electronics and he designed reliable and precise high voltage power supplies, HV pulsers and voltage dividers for the spectrometer. LabView software development was initiated by Jorge Filevich and continued by Tyler Green and Olanrewahu Oludipe. Thanks to Nengyun Zhang for modeling on SIMION software. Thanks to Cornelius Oster and to Jaroslav Nejdil for optimization of the alignment procedure. Thanks to Yin Shi for helpful discussion on VUV post-ionization. Thanks to Yong Wang, Alex Rockwood and Shoujun Wang for helping with YAG laser. Thanks to Liang Ying, Clayton Bargsten, Wei Li and other team mates for immense support.

For fruitful collaboration I thank Andrew Duffin, Gregory Tallents, Andrew Rossal, Valentin Aslanyan, Libor Juha, Tomas Burian, Amit Munshi and Venugopal Pujari.

Without my family and friends this work would be impossible.

TABLE OF CONTENTS

Abstract.....	ii
Acknowledgements.....	iv
I Introduction.....	1
I.a Composition imaging role in research	1
I.b EUV laser ablation TOF mass spectrometer.....	5
I.c Comparison of EUV TOF to other systems.....	10
I.d Scope of the dissertation	14
II Instrumentation	17
II.a System overview	17
II.b System description.....	25
II.b.i EUV laser and optics for ablation and ionization	25
II.b.i.1 Laser parameters	25
II.b.i.2 EUV laser setup	28
II.b.i.3 EUV optics.....	30
II.b.ii Mass spectrometry	34
II.b.ii.1 Ion extraction and discrimination	34
II.b.ii.2 Signal acquisition and detector performance.....	37
II.b.ii.3 Positive and negative ion detection modes	39

II.b.iii Post-ablation ionization	45
II.b.iii.1 YAG laser for harmonics generation	45
II.b.iii.2 Post-ablation ionization performance	48
II.b.iii.3 Results on inorganics	53
II.c EUV TOF comparison to SIMS TOF	59
II.c.i Static SIMS mode for molecular analysis.....	59
II.c.ii Mass and spatial resolutions	62
II.c.iii Sensitivity	66
II.d Operation.....	72
II.d.i Vacuum.....	73
II.d.ii Timing.....	74
II.d.iii Beam energy control.....	75
II.d.iv Sample handling.....	78
II.e Data analysis	81
II.e.i Mass calibration	81
II.e.ii Mass spectrometry imaging	85
II.e.ii.1 Imaging of heterogeneous samples	85
II.e.ii.2 Depth profiling of multilayers	87
III Nature Communications paper on EUV TOF.....	92
III.a Paper title page.....	92

III.b	Introduction.....	92
III.c	Results.....	95
III.c.i	Concept and implementation of 3D chemical imaging by EUV laser ablation....	95
III.c.ii	Demonstration of 3D molecular imaging at the nanoscale.....	97
III.d	Discussion.....	103
III.e	Methods.....	105
III.e.i	Samples and ablation conditions for each experiment.....	105
III.e.ii	Data Analysis.....	106
IV	Biological applications of the system.....	108
IV.a	Current state of cell membrane lipids research.....	108
IV.b	Phospholipid detection on EUV TOF.....	113
IV.c	Detection of cholesterol by post-ablation ionization.....	120
V	Conclusions and outlook.....	127
VI	References.....	131
VII	Appendix.....	136
VII.a	Various procedures for system operation.....	136
VII.a.i	SOP.....	136
VII.a.ii	TOF setting optimization.....	137
VII.a.iii	Zone plate fine-focusing.....	137
VII.a.iv	Data acquisition.....	138

VII.a.v PI laser tuning and use	139
VII.b EUV laser operation principles	140
VII.c EUV optical properties for various media	144
VII.d Ion optics.....	145
VII.e Optics alignment	146
VII.e.i EUV laser alignment procedure with HeNe	153
VII.e.ii Zone plate alignment and sample loading	154
VII.e.iii Nd:YAG harmonics alignment near ZP and sample	156
VII.f EUV photodetectors.....	157
VII.g MCP sensitivity.....	165
VII.h PI efficiency calculation	167
VII.i Vacuum	168
VII.i.i Pumping down the sample and TOF chambers	171
VII.i.ii Pumping down the tripling cell.....	171
VII.i.iii Pumping down the switchyard and laser chambers	172
VII.i.iv Establishing required gas flows and pressures.....	172
VII.i.v Complete shutting down and venting of the system	173
VII.i.vi Partial venting and re-pumping for quick sample replacement	173
VII.j Timing.....	175
VII.k Baseline adjustment	175

VII.l Fragmentation	176
VII.m Nature Communications paper supplementary material.....	182
VII.m.i Comparison of EUV TOF and other mass spectrometry methods	182

I INTRODUCTION

In this chapter basic principles of imaging mass spectrometry techniques and their typical results will be described. The main advantages of the Extreme Ultraviolet Laser Ablation Mass Spectrometry (EUV TOF) approach will be covered and compared to commercial systems performance. The scope of the dissertation is discussed last.

I.a Composition imaging role in research

Composition or chemical imaging is an essential analytical technique in many fields: material science, microbiology, forensics, medicine¹⁻⁴. Composition imaging is a visual representation of the complex solid chemistry of the sample by scanning it with a probe beam. An array of signals detected and characterized from loci of the sample represents key parameters of the chemical image: type of compounds present in the sample, their concentration and volumetric distribution. The goal of every imaging technique is in providing these parameters with:

- a) highest range of compound variety detection (qualitative analysis);
- b) sufficient mass resolution that allows distinguishing peaks of similar masses;
- c) precise concentration grading (quantitative analysis);
- d) highest resolution of the volumetric compositional variation.

The principle of operation of a number of imaging mass spectrometry (IMS) techniques is represented in Figure I.1. A focused probe beam that can be composed of photons or ions evaporates and ionizes the sample. Charged species get accelerated in the electric field applied

between the sample and the grounded grid of the mass analyzer entrance pupil. In the time-of-flight (TOF) tube they get segregated according their mass-to-charge ratio (m/z). This happens due to the difference in the flight times of species with different mass and same charge based on the energy conservation law. Identical potential energy acquired in the electric field converses to same kinetic energy for all species, thus lighter elements gain higher velocity. Upon arrival at the detector lighter elements are identified by mass peaks in the beginning of the spectrum. The time axis is later converted to the mass axis by the process of mass calibration. After each probing pulse and detection event sequence, the sample is displaced within a plane perpendicular to the TOF axis (x or y direction) and the process repeats until the desired area is analyzed laterally. In addition, probing in the same ($x;y$) coordinate provides with z or depth compositional profile of the sample. An array of data with three coordinates, with time and amplitude of multiple peaks in the mass spectra has dimensionality of five. The visual representation of such data sets is usually done by integrating only one or few peaks that represent the same compound in every single shot spectrum of the ($x;y;z$) array. The intensity value in the voxel can then be plotted in a set of 2D slices or 3D form. The series of such images attributed to the compounds of interest is a chemical fingerprint of the analyzed section.

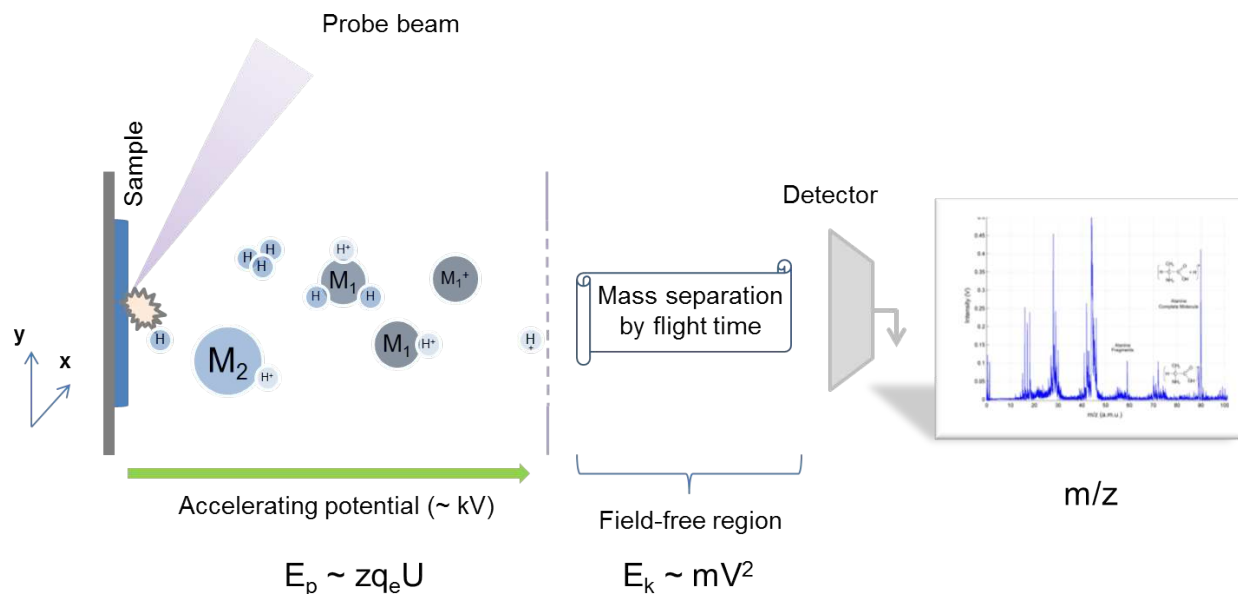


Figure I.1: Principle of operation of the imaging mass spectrometry (IMS). A focused photon or ion probe beam evaporates and ionizes the sample creating a plasma plume consisting partially of the charged species. These atoms and molecules get accelerated in the static electric field between the sample and the entrance pupil of the mass analyzer. The acquired potential energy gets converted into kinetic energy resulting in difference of velocities of the different mass species based on their mass-to-charge ratio m/z . Lighter particles cover the field-free region of the time-of-flight tube faster forming a peak at the beginning of the spectrum. Heavier species arrive later. Time to mass conversion is done by mass calibration by peaks of known elements or molecules. After each probe pulse and detection event the sequence is repeated in the same locus of the sample creating a depth profile of it or in the new coordinate by x or y displacement rendering a lateral composition image. 5D acquired array ($x;y;z;m/z$;amplitude) is analyzed by integration of selected peaks followed by their 2D or 3D representation.

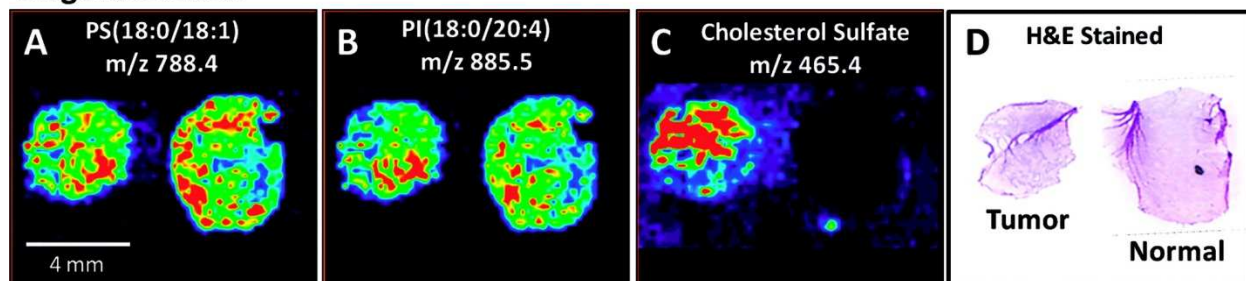
Achieving the highest performance in all the attributes of the chemical imaging is virtually impossible. Every technique is usually tailored to a set of specific applications that have common performance requirements. For example, researchers in medicine are accustomed to use histological staining of tissue sections with subsequent use of fluorescent microscopy. This allows learning about structural integrity of the tissue section and some target compounds distribution. With the development of mass spectrometry methods, the same tissue sections became analyzed by focused laser or ion beams with the goal of improving chemical specificity and imaging resolution. The chemistry involved in biological samples is extremely complex: it is

a mixture of low and high mass compounds (proteins, peptides, lipids) at often low concentrations. Differentiation between them is of higher priority than the spatial resolution that should be better or similar to other techniques. That is why low-resolution methods among mass spectrometry imaging systems like desorption electrospray ionization (DESI) and matrix-assisted laser desorption and ionization (MALDI) are extremely successful in this field.

DESI employs a stream of negatively charged solvent droplets carried by a buffer gas that impacts the sample at an angle causing its desorption and charge transfer. Resulting secondary analyte ions are extracted to the mass spectrometer. The analysis is carried out at atmospheric pressure meaning that minimal or none sample preparation is required except for slicing. Soft ionization by low-energy electron attachment allows keeping complex heavy molecules intact, although spatial resolution is on the order of tens of micrometers. Figure I.2 demonstrates DESI capabilities in diagnosis of acute illnesses like prostate cancer⁴. Every image represents a 2.7 mm thick tumorous and normal tissue blocks. The top row shows that two phospholipids are distributed evenly over both segments, while cholesterol sulfate is present only in the tumorous section. The histologically stained image shows only some structural differences. Thus, cholesterol sulfate serves as cancerous identifier. It was verified on a set of images in the bottom row that monitor this molecule at different cross sections of each of the specimens.

The most valuable attribute of modern IMS techniques is the identification of complex chemicals without tagging or other laborious sample preparation procedure. Visualization of compounds volumetric distribution allows associating their role to specific phenomena. This sets imaging mass spectrometry techniques apart from other analytical methods.

Original Section



Serial Sections

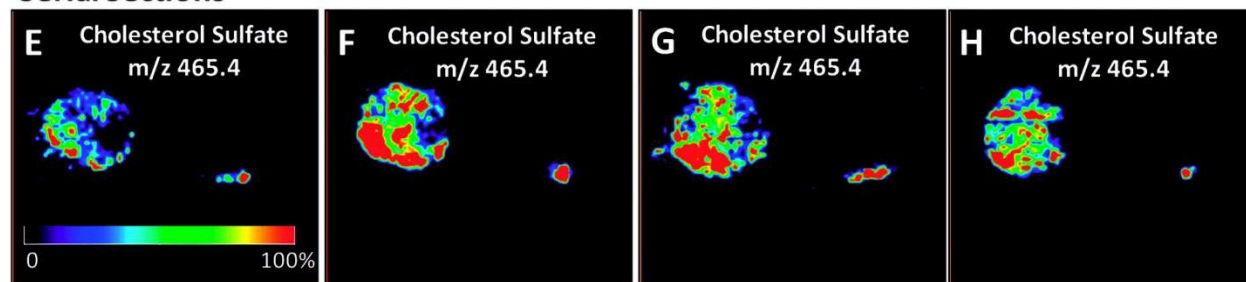


Figure I.2: DESI images⁴ of cancer (left) and normal (right) prostate tissue section of 2.7 nm thickness. A and B show an even distribution of two selected phospholipids, while C indicates cholesterol presence only in the tumor. Images E-H monitor cholesterol sulfate in several consecutive sections showing a similar distribution pattern that confirms the finding.

I.b EUV laser ablation TOF mass spectrometer

We have developed an imaging mass spectrometer that utilizes 46.9 nm extreme ultraviolet (EUV) laser for sample ablation and ionization. EUV radiation, as shown on Figure I.3, is in between vacuum ultraviolet (VUV) and soft X-ray (SXR) electromagnetic ranges. EUV spans in $\sim 5\div 40$ nm wavelengths interval with corresponding energy per photon of $\sim 250\div 30$ eV⁵.

The use of such band offers several advantages for IMS:

- 46.9 nm wavelength can be focused to <100 nm spots for high lateral resolution imaging⁶;
- EUV light is absorbed within few tens of nanometers of the carbonaceous sample. It renders high degree of ablation localization for 3D imaging when combined with (a);

- c) 26.4 eV photons are capable for single photon ionization (SPI) of every atom and molecule with high ionization cross section;
- d) The plasma created by EUV laser ablation is transparent for EUV light resulting in less heating and lower probability of molecular fragmentation.

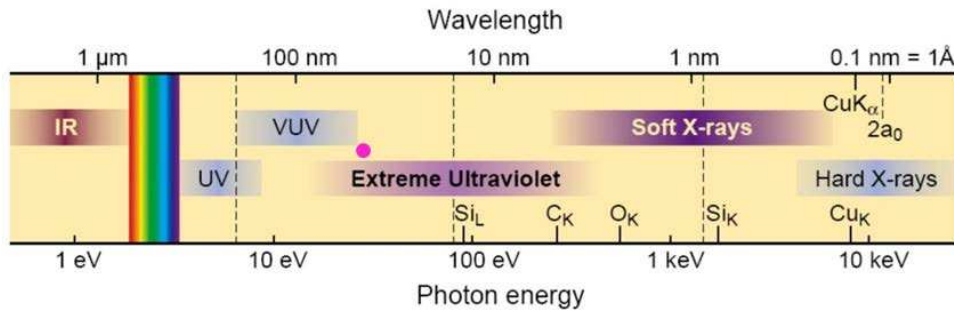


Figure I.3: Electromagnetic spectrum showing the 46.9 nm radiation (pink dot) within the EUV spectral range (adopted from⁵ Attwood 2000).

The described advantages allow using EUV light for probing of biological samples with high spatial and depth resolutions. Detection of molecular signal can be done with subsequent 3D distribution visualization. As shown on Figure I.4, EUV TOF IMS operates in the following way: a collimated EUV laser beam gets tightly focused by the zone plate lens on the heterogeneous solid sample. A plasma plume that contains a partially ionized vapor mixture emerges from the corresponding ablation crater. Ions in the plume get accelerated towards the TOF mass discriminator. The precision of TOF detection is improved by using a reflectron configuration that doubles the flight path and compensates for ion energy dispersion acquired during acceleration. The diameter, depth and consequently volume of the ablation crater are controlled by laser fluence, reaching dimensions of the order of 100 and 7 nm correspondingly. Lateral displacement of the sample tightly packs ablation craters in the analysis area resulting in

high resolution composition maps. Overlapping craters in the same lateral coordinates adds depth layers to the nanoscale images.

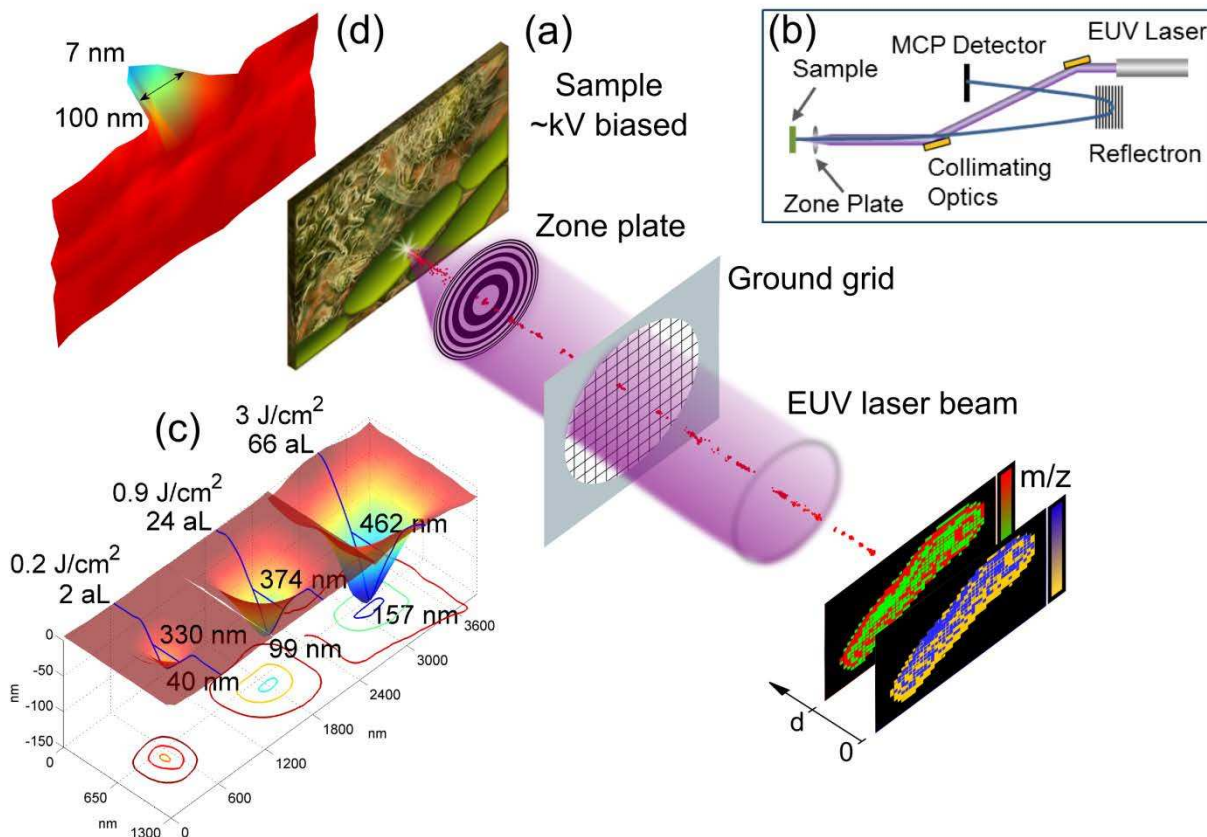


Figure I.4: EUV TOF IMS principle of operation. (a) A zone plate lens focuses the collimated EUV laser beam onto sample creating an ablation plasma plume out of the material in the crater. Ionized atoms and molecules accelerate in the static electric field applied between the sample and ground grid towards the mass analyzer. (b) TOF tube operates in reflectron mode allowing doubling the flight path of ions and compensating their energy dispersion. In this way better separated and more Gaussian-like peaks in mass spectra are obtained. (c) Variation of EUV laser fluence allows controlling the ablation crater dimensions and thus imaging resolution. (d) The smallest ablation crater observed in polymethyl methacrylate (PMMA) has 100 nm FWHM diameter and 7 nm depth.

The key advantage of EUV light utilized in this system is the ablation mechanism. When an intense laser pulse interacts with the solid, it creates a plasma plume that expands into vacuum creating an exponentially decaying electron density profile as shown on Figure I.5. At the critical

electron density the plasma frequency equals that of the incoming light causing its reflection by the inverse bremsstrahlung mechanism. This is the case for the commonly used ultraviolet light in instruments like MALDI. Ablation initiated by the light continues thermally through the interaction with the heated plasma. For EUV light critical electron density of $5 \times 10^{23} \text{ cm}^{-3}$ is higher than the solid density. This makes the plasma essentially transparent and allows for direct photoabsorption and ionization at the sample. The combined effect is a colder plasma⁷, increased efficiency of ionization by the single photoionization (SPI) process and lesser fragmentation.

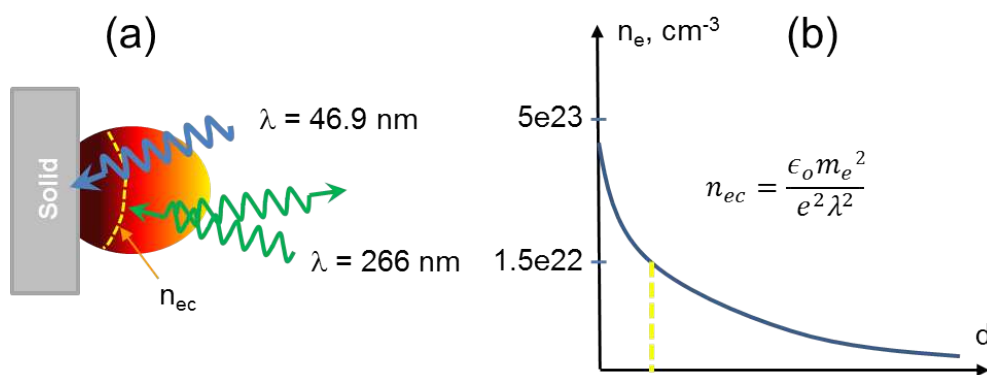


Figure I.5: Ablation mechanism for UV and EUV light. (a) An intense pulse of laser light initiates ablation that creates a plasma plume expansion into vacuum. The critical electron density n_{ec} shown as a yellow dashed line is an imaginary surface at which UV light gets reflected. Upon that, heated plasma continues the ablation thermally while EUV light interacts directly with the surface due to the shorter wavelength. (b) Exponentially decaying electron density profile as a function of distance from the surface. For EUV light the critical density is higher than solid density thus allowing direct photoabsorption and promoting efficient ionization. Decoupling of the plasma creation and its expansion keeps the plasma much colder.

The softer EUV laser ablation and ionization approach compared to the UV process results in observation of molecules and their clusters in the mass spectra obtained in EUV TOF. Figure I.6 shows positive and negative ion spectra of ionic crystal LiF^8 . LiF crystal is often used for imaging and dosimetry in the SXR range⁹, as well as a material for refractive optics in the VUV range. In positive ion extraction mode clusters of $\text{Li}_n\text{F}_{n-1}$ are observed together with their oxides and hydrates. Elemental peaks of H, Li, C, O and F indicate that some fragmentation does

take place. In the negative ion extraction mode clusters of $\text{Li}_n\text{F}_{n+1}$ are formed. Ample clustering was also observed on gold—up to Au_9 —that was used for mass resolution assessment of the EUV TOF (section II.e.i). Spectra of C_{60} reveal stable giant fullerene formation up to 2.8 kDa¹⁰.

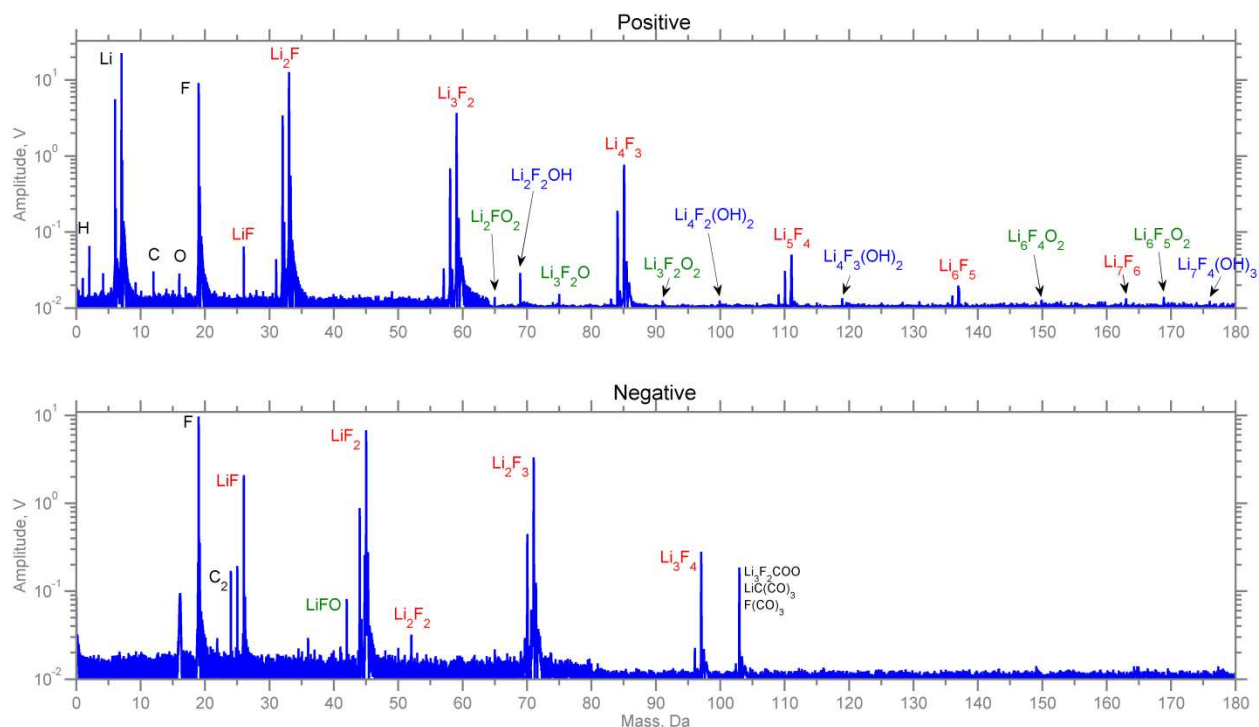


Figure I.6: Positive and negative ion extraction mode spectra of LiF ionic crystal. Formation of $\text{Li}_n\text{F}_{n-1}$ and $\text{Li}_n\text{F}_{n+1}$ clusters is observed respectively together with their oxides and hydroxides.

The EUV TOF system was conceived as an analytical tool that would allow molecular imaging at the nanoscale – a capability often unattainable by other techniques. With single photon soft ionization and high localization of the ablation it was possible to show that the aminoacid alanine molecular peak can be detected from a 50 zL crater with single a laser shot. Figure I.7 shows a 120 nm in diameter and 3.5 nm in depth crater obtained at similar conditions on PMMA. Molecular and protonated molecular ions of intact alanine can be routinely detected from therein¹¹. Protonation is often the dominant mechanism of ionization of carbohydrates in positive ion extraction mode. Detection of parent molecular ion at these conditions represents

~0.02 amol sensitivity. In other words, it is an amount of probed substance resulting in single ion count on the detector. SIMS TOF sensitivity was measured to be 20× worse indicating great promise of the EUV TOF approach (section *Ic.iii*).

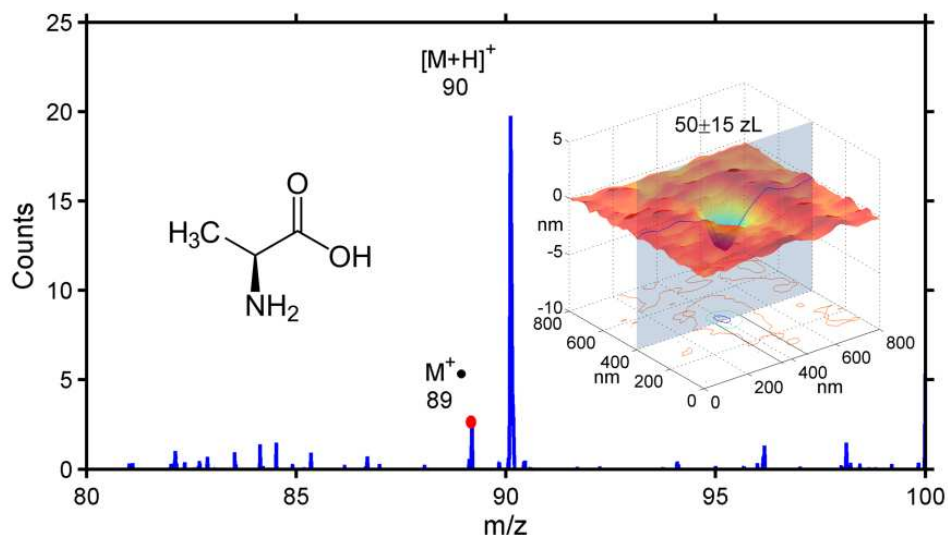


Figure I.7: Single shot spectrum of the aminoacid alanine (89.09 g/mol) showing parent and protonated molecular peaks at 89 and 90 Da. Corresponding atomic force microscope (AFM) scan of the PMMA crater is shown in the inset. This crater was obtained in similar conditions. Miniscule volume of 50 zL was enough for intact alanine detection. FWHM diameter of the crater is 120 nm and depth is 3.5 nm.

I.c Comparison of EUV TOF to other systems

There are three main imaging mass spectrometry methods that can be considered as competitors to EUV TOF: desorption electrospray ionization (DESI), matrix-assisted laser desorption and ionization (MALDI), secondary ion mass spectrometry (SIMS), and their derivatives. As can be seen from Table I.1, the newly developed EUV laser ablation system achieves similar performance to the relatively mature SIMS technique rendering it as a main competitor. In certain cases EUV TOF outperforms: sensitivity for molecular imaging is 20× better. With similar spatial and depth resolutions only EUV TOF can achieve 3D nanoscale

resolution for molecular imaging. However, impressive results of SIMS TOF and its principle of work must be introduced as well.

Table I.1: Comparison of competing IMS methods.

Method	Ionization	Lateral resolution, μm	Depth resolution, μm	Detection range, Da
DESI	Electrospray	>10	$>1\text{e}3$	$\sim 1\text{e}5$
MALDI	UV laser	$1\div 10$	~ 0.1	$>1\text{e}3$
SIMS TOF	Ion beam	≤ 1	~ 0.01	$<1\text{e}3$
EUV TOF	EUV laser	≤ 1	~ 0.01	$<1\text{e}3$

Secondary ions in SIMS are generated upon sputtering of the sample with a focused primary ion beam as shown on Figure I.8. Ions of typically >10 keV energy are focused down to $0.05\div 30$ μm spot. Upon collision with the surface they initiate a cascade of interactions. Both primary ions or atoms and molecules of the sample upon several recoils distribute the energy within few tens of nanometers area around the initial impinging spot. During recoils both primary and secondary species eventually receive momentum that liberates them from the solid phase. Secondary species often get fragmented upon energetic interaction but some leave the surface intact. Usually all sputtered particles have elevated internal energy though. And only a small portion of them acquire positive or negative charge that allows them to be manipulated by the electric field and get detected. Typical useful yield of such process is of the order of $1\text{e-}4$, i.e. one detected molecular ion after sputtering with $1\text{e}4$ primary ions. This parameter significantly varies from sample to sample and between different experimental conditions. For instance, the use of polyatomic primary ions can increase the yield up to three times. It is caused by more efficient surface localization of the collisional cascade at the surface. A softer removal process is

also aided by collective sputtering of many low-energy constituent atoms of the primary projectile¹². The drawbacks of the technique are:

- a) accumulation of chemical damage under prolonged bombardment that reduces useful yield of molecular signal;
- b) damaged/alterd volume extends deeper into the sample than the signal-contributing surface layers;
- c) the presence of complex chemistry may significantly reduce due to “matrix effect” useful yield and represent false concentration map of the compound;
- d) low useful yield limits imaging resolution by the need of probing bigger volumes.

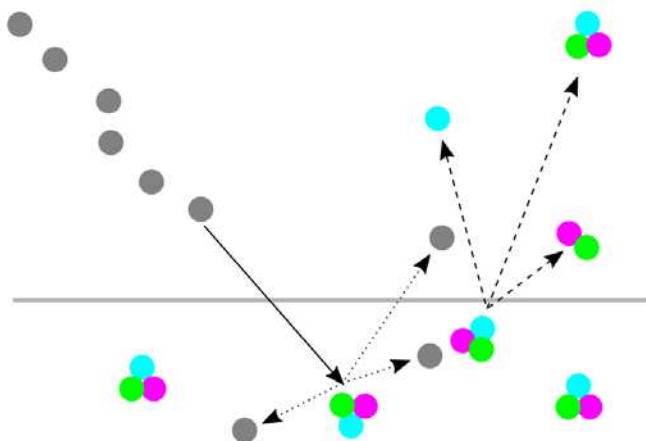


Figure I.8: Schematic representation of sputtering. Grey circles illustrate primary ions that deliver energy to the sample. Primary ions: a) get implemented into the sample altering its chemistry, b) break down analyte molecules, c) recoil from analyte molecules and deliver momentum that lifts other molecules off the surface, and d) reflect back into vacuum. Triple colored circles represent analyte molecules which can: a) be displaced by the primary ions, b) fragment under impact, c) get sputtered into vacuum intact or fragmented. Only a small portion of sputtered species bear charge yielding only ~0.01% detection rate.

With the use of polyatomic projectiles detection of molecular compounds becomes feasible in the so-called static dose limit. In the static limit conditions the primary ion dose density is limited to typically $1e13$ ions/cm². Cluster primary ions reduce chemical damage and increase yield while operation in static limit causes every projectile to hit a fresh undamaged spot

on the surface. Although obtaining high signal to noise ratio requires signal accumulation during prolonged scanning. The spectrum of the aminoacid alanine (Figure I.9) was acquired at typical experimental conditions of the SIMS TOF utilizing 30 keV Bi_3^+ beam focused to 5 μm spot. An area of $500 \times 500 \mu\text{m}^2$ was scanned 20 times with cleanup removal of the damaged layer by Ar_{1500}^+ clusters in between. The resultant spectrum clearly shows the protonated alanine molecule at 90 Da together with its signature fragments and protonated clusters. As it will be described in the section *II.c.iii*, even 1×10^5 counts of protonated molecular peak results in $20 \times$ lower sensitivity than that of EUV TOF. With consideration that the damaged volume is $5 \times$ greater, the sensitivity difference can reach two orders of magnitude.

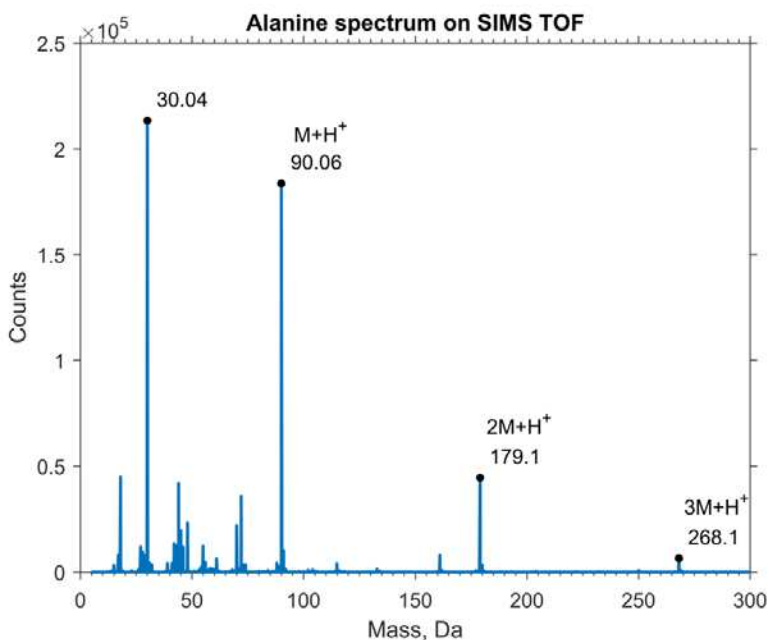


Figure I.9: Alanine mass spectrum acquired at standard conditions with SIMS TOF at 0.5 pA of 30 keV Bi_3^+ beam focused to 5 μm spot. Signal was accumulated from an area of $500 \times 500 \mu\text{m}^2$ scanned 20 times with cleanup removal of damaged layer by Ar_{1500}^+ clusters in between scans.

Nevertheless SIMS TOF could demonstrate fantastic result for imaging the distribution of two common antibiotics in *E.coli* at a subcellular level with 300 nm spatial and 400 depth

resolutions. C_{60}^+ cluster ion beam with the dose of 3×10^{14} ions/cm² imaged ampicillin (AMP) and tetracycline (TET) in the *E.coli* aggregates². Integration and summation of the parent and few molecular ion fragment peaks helped to assign pixels to each antibiotic. The background signal from the silicon substrate illustrates the localization of bacteria and proves that antibiotic-related signal comes from within bacterial aggregates as shown on Figure I.10.

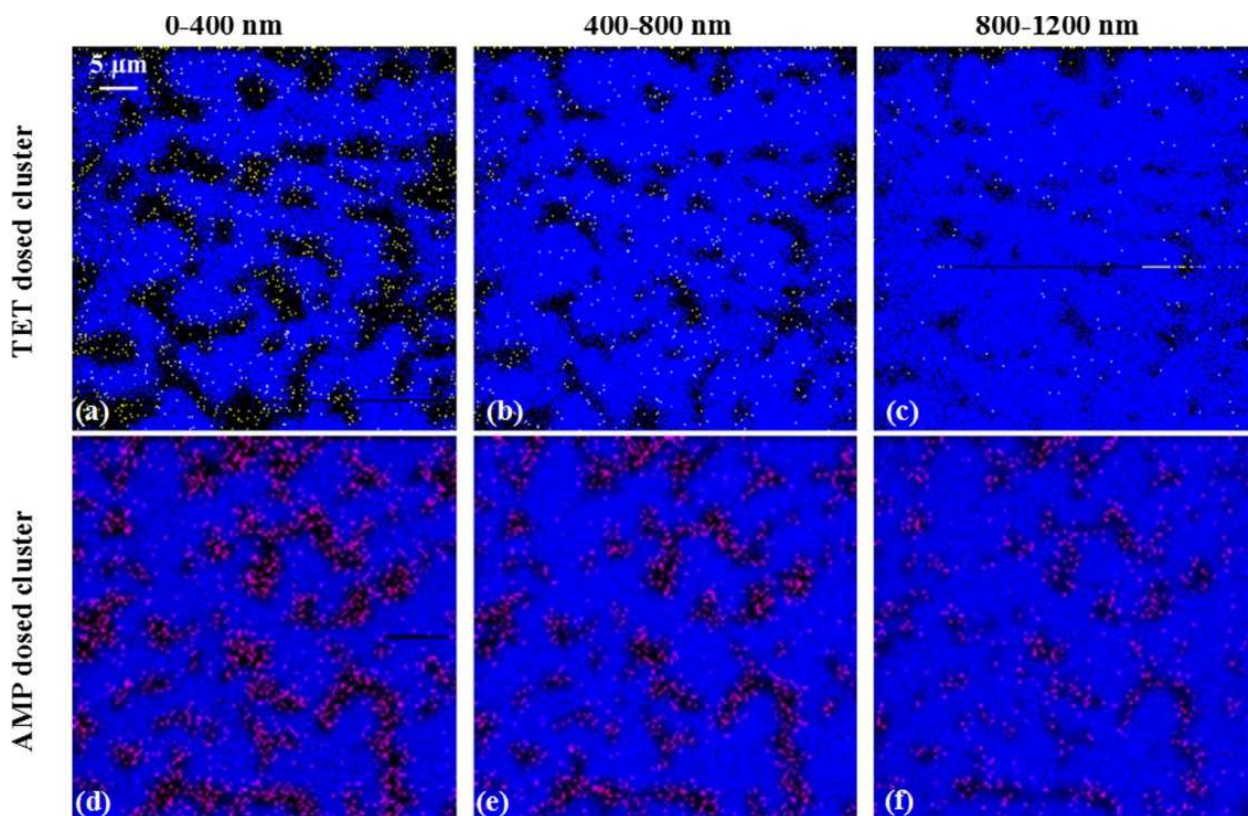


Figure I.10: 2D image slices² of the *E.coli* aggregates showing distribution of tetracycline (TET, yellow dots) and ampicillin (AMP, red dots). Bacteria were treated with 20 μg/mL of each antibiotic. Blue background represents Si substrate signal clearly showing that antibiotics were localized mainly within the bacterial aggregates.

I.d Scope of the dissertation

This introduction is followed with Chapter II where the EUV TOF instrument design and operation are described. Its first section is devoted to the EUV laser developed at CSU back in

2005¹³. Emphasis is given to which parameters make the EUV TOF system better than competing IMS techniques. The uniqueness of the light source defines the uniqueness of the optics that in our case consist of grazing incidence toroidal mirrors and Fresnel zone plate lens¹⁴. The next section talks about the mass spectrometry side of the system, particularly on the mechanism of analyte ions extraction, aiming, and detection by the microchannel plate (MCP). With positive and negative ion extraction modes developed, typical results and advantages of each on organic and inorganic samples will be discussed. The third section of the chapter talks about the addition of post-ionization setup on the basis of Nd:YAG laser generating UV and VUV harmonics. Post-ionization (PI) allows extraction of information from the more abundant and less thermally excited neutral portion of the EUV-created plasma plume. Inorganic materials analysis showed an increase of sensitivity for elemental detection in UV post-ionization mode. VUV PI showed similar results on detection of As₂ from GaAs as found with a SIMS TOF system with synchrotron post-ionization. The fourth section spreads more on the comparison with existing SIMS TOF techniques in terms of mass and imaging resolution as well as sensitivity. The following section on operation overviews the vacuum system that is needed for EUV light propagation and energetic ion detection. The timing scheme describes synchronous operation of the laser pulses, detector driving voltage, and signal triggering and acquisition in all modes of operation. Controlling of the laser beam energy and sample handling during data acquisition is covered as well. The closing section talks about data analysis in terms of mass calibration and image processing for 2D and 1D cases.

3D nanoscale imaging and its aspects are covered in detail in Chapter III that was fully acquired from the formatted reprint of the Nature Communication paper¹¹. A lateral imaging resolution on organic compounds of 75 nm and depth resolution of 20 nm were achieved. A 3D

map of an isolated *M.smegmatis* bacterium will be presented along with performance comparison to SIMS and MALDI systems.

The extent of biological relevance of the EUV TOF system is covered in the Chapter IV. The niche example discussed refers to cell membrane lipids and the current state of mass spectrometry-related understanding of it. Several lipids were analyzed in EUV TOF in all available operation modes: positive and negative ion extraction as well as VUV post-ablation ionization. The most promising data were obtained on the detection of intact cholesterol molecules in the VUV PI mode.

In the Conclusions, Chapter V, the current progress and directions for future work are discussed. Excessive technical details like schematics and operation procedures are compiled in Appendix.

II INSTRUMENTATION

In this chapter¹ details on the implementation and operation of the extreme ultraviolet time of flight (EUV TOF) mass spectrometer will be discussed. A system overview is first presented, followed by a description of the EUV laser source and its optics for ablation and ionization of the sample. Positive and negative analyte ion extraction, ion transport and detection are covered in the mass spectrometry section together with results on organic and inorganic compounds. Topics related to the addition of post-ablation ionization using a Nd:YAG laser and the experimental outcome are discussed in section *b.iii*. Next a comparison of EUV TOF performance to the competing and commercially available SIMS TOF analytical method is presented. Operational aspects regarding vacuum equipment, timing scheme, laser beam energy control and sample handling are briefly described in section *c*. The chapter is concluded with data analysis where mass calibration of the spectrometer, image acquisition and processing are described.

II.a System overview

The Extreme Ultra Violet (EUV) laser ablation time-of-flight (TOF) imaging mass spectrometer was developed at Colorado State University for nanoscale molecular imaging of biologically relevant samples¹¹. The uniqueness of the system is defined by the light source – an EUV laser developed at CSU by Rocca and collaborators¹³. This laser emits pulses at a wavelength of 46.9 nm that can be focused to spots 80 nm in diameter for high lateral resolution

1. A version of this chapter will be published in *Review of Scientific Instruments*: Kuznetsov I. et al. (2018)

imaging. Shallow penetration depth of EUV radiation in solids provides with few tens of nanometers or even better depth resolution¹¹. 26.4 eV energy per photon promotes highly efficient and relatively soft ionization of any atom or molecule by single photon ionization (SPI)¹⁵. The short 1.5 ns pulse duration allows seamless coupling of the ion source to TOF mass spectrometer that together with ample amount of $>1e12$ photons per pulse achieves single-shot detection capability. Figure II.1 shows a 3D assembly model of the EUV TOF system made in SolidWorks® computer-aided design program together with the scheme describing the operation principle of the instrument. The highly monochromatic and 5 mrad divergence EUV laser beam is guided to the sample chamber using two toroidal mirrors acting as collimators to illuminate the zone plate lens. This lens designed with a central opening focuses the EUV laser to ablate the sample. The sample is biased to create with a ground grid a potential difference that is necessary to extract ions. The ions are accelerated through the central opening of the zone plate towards the ground grid and enter the TOF. In the TOF the ions follow an elliptical trajectory defined by their deflection in the reflectron to hit a microchannel plate (MCP). As explained in more detail in section *b.ii*, the use of the reflectron contributes to narrow the ion energy distribution. Figure II.1 also includes the post ablation ionization (PI) set up which is described in detail in section *b.iii*.

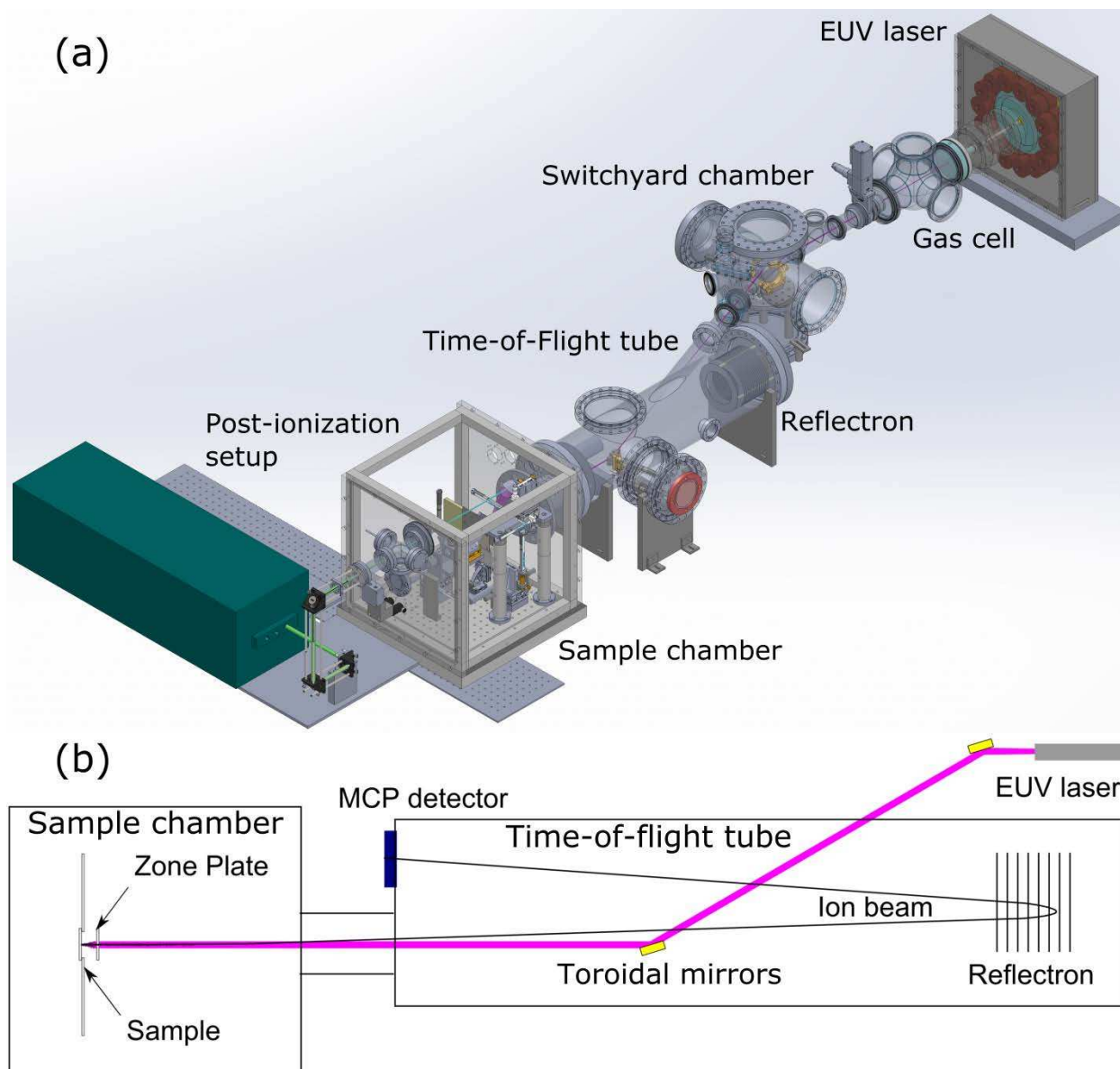


Figure II.1: EUV TOF 3D assembly (a) and principle of operation (b). (a) EUV laser head shows a circular array of capacitors for charge storage and spark gap behind them that facilitates delivering the main discharge pulse in the capillary where 46.9 nm lasing happens. The gas cell next to the capillary serves for attenuation of the laser energy for controlling the fluence at the sample. The switchyard chamber hosts the first toroidal mirror on a translation stage that directs the beam into the TOF tube where a second toroidal mirror is positioned. The combined function of these toroidals is to collimate the laser beam before it reaches the sample chamber where a zone plate lens focuses it onto the sample. Post-ionization setup behind the sample chamber brings 3rd or 9th harmonic of the Nd:YAG laser into the sample chamber for secondary ionization of the neutrals in the EUVL-created plasma plume. (b) Diagram showing the path of the EUV laser beam (magenta) into the sample chamber and of the ions from the plasma plume that are accelerated through the central opening of the zone plate, injected into the TOF tube, and reflected off by the reflectron to hit the active area of a MCP detector.

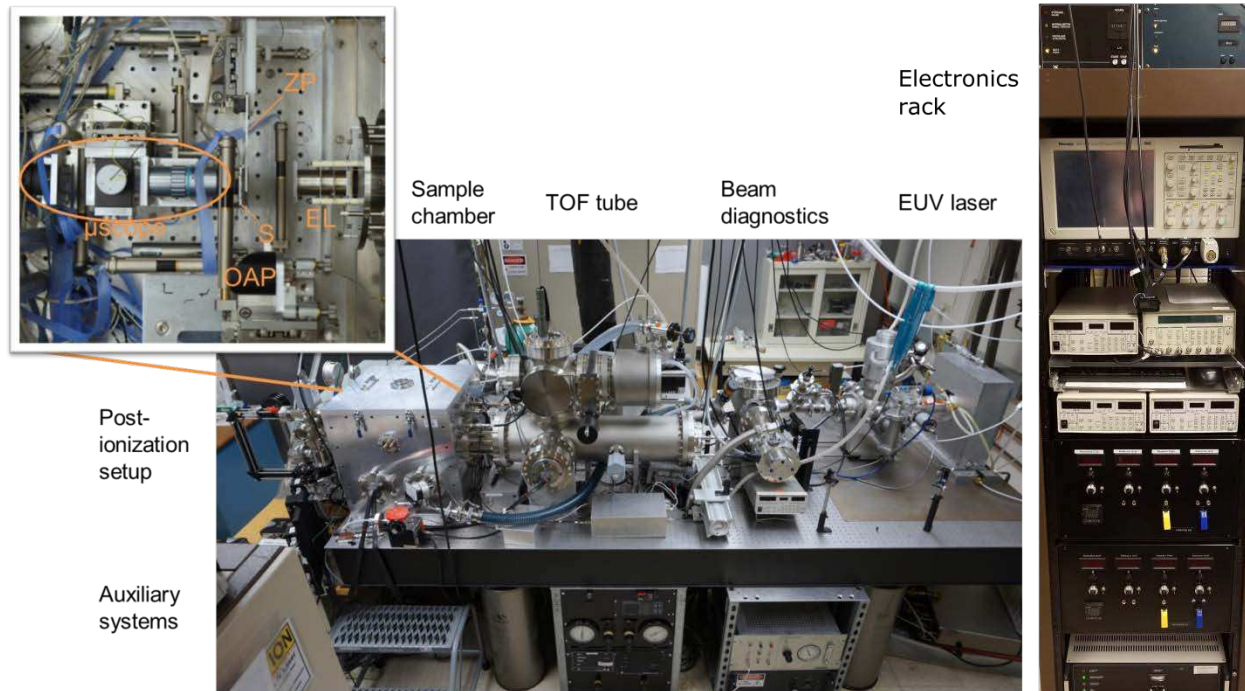


Figure II.2: EUV TOF photograph showing positioning of EUV laser and other parts of the system. Sample chamber interior and electronics rack are presented in the insets.

The current version of the EUV TOF system fits onto a 5×10' optical table. The photograph in Figure II.2 identifies the EUV and Nd:YAG lasers, vacuum chambers and conduits, and vast number of supporting elements not shown on the 3D model (Figure II.1). The key components list is summarized in Table II.1.

Lasing at 46.9 nm occurs inside a 3.2 mm diameter alumina capillary of 21 cm length filled with 300 mTorr argon and installed in the EUV laser head. Since this is a single pass gain medium, the resulting beam is relatively highly divergent – about 5 mrad¹⁶. Considering the geometry of the capillary, it is safe to assume that beam originates in the point source in the capillary center. If such beam is allowed to propagate uncorrected up to the sample for ~3 m, it would become 15 mm in diameter. The zone plate lens would have to be of the like size in order to increase acceptance. That is why it was decided to collimate the 46.9 nm beam by the set of

two identical near-grazing incidence toroidal mirrors. After two reflections and through the Switchyard and TOF chambers collimated laser beam gets to the sample chamber. There it hits 0.5 mm zone plate that focuses it onto the sample. More details on the use of EUV and other optics will be presented in the following sections.

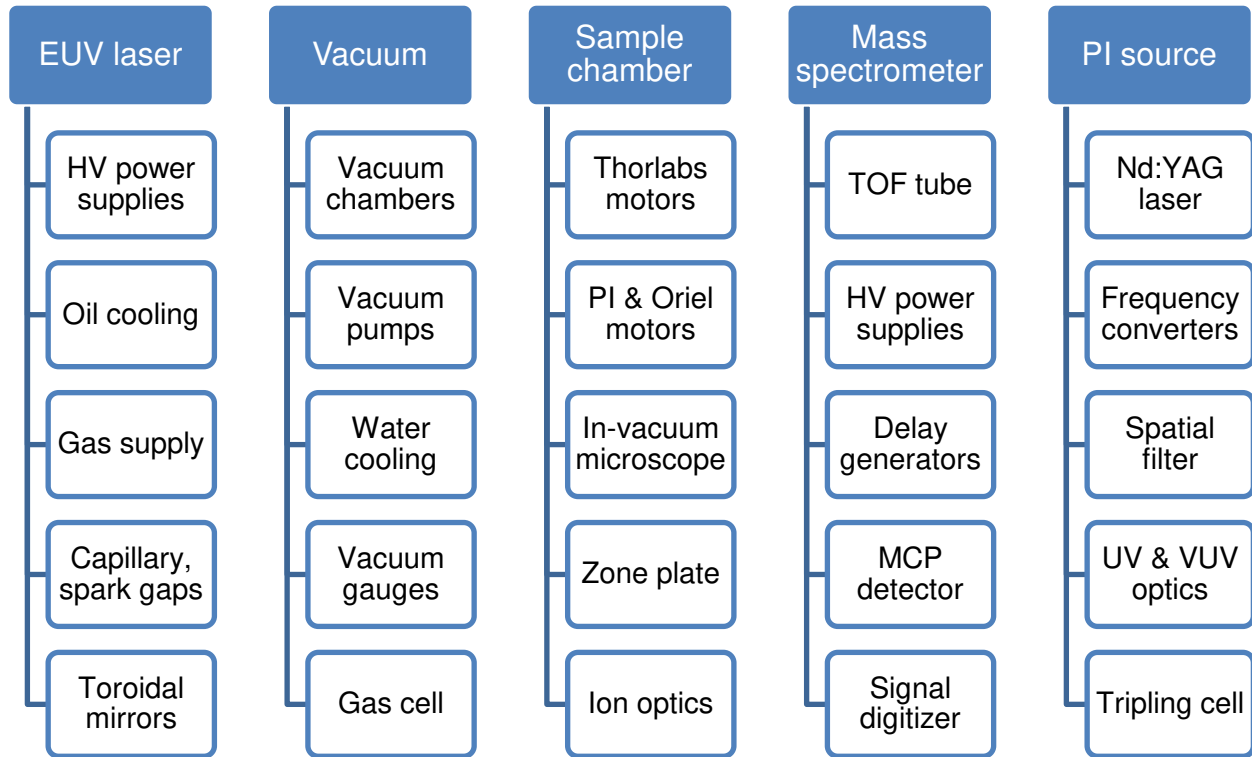
Ionized portion of the ablation plume gets accelerated by the repelling potential of the sample plate following the same trajectory of the collimated laser beam but towards the TOF tube. After passing through the zone plate central opening and ion optics these ions enter the field-free region of the TOF tube until they reach the reflectron where they are turned backwards. Reflectron doubles the flight path resulting in better separation of ion bunches by mass and compensates for the energy dispersion acquired during acceleration phase. Bounced back, the ions reach the microchannel plate (MCP) detector.

In order to provide a) EUV beam delivery from the laser head to the sample and b) ion beam delivery from the sample to the MCP detector, an elaborate vacuum system had to be constructed. Since 46.9 nm radiation bears 26.4 eV energy per photon, it is capable to ionize every atom and molecule by the process of single photon ionization (SPI). Hence it is essential that vacuum is good enough to eliminate laser beam attenuation via highly efficient SPI of residual gas molecules. Calculation of air transmissivity through 3 m length shows that at vacuum of $1\text{e-}4$ Torr the transmissivity is 98% (Figure VII.17), while at $1\text{e-}3$ it is 78%. So the system has to operate below $1\text{e-}4$ Torr, i.e. at high vacuum conditions. As for ions, what matters is their mean free path. In the assumption that ion velocity is much greater than the residual gas molecules at 300 K, the mean free path at $5\text{e-}8$ Torr is ~ 500 m which is much greater than the TOF ~ 1 m length.

Recently a post-ionization system utilizing 3rd (355 nm) and 9th (118 nm) harmonics of Nd:YAG laser was added to the EUV TOF instrument with a goal of signal yield enhancement of atoms and molecules by probing neutral components of the EUVL-created ablation plume. Figure II.1 shows that second laser and its optics are stationed on the opposite side than the EUV laser. Green YAG beam on the figure is shown to be bouncing off of several adjustable mirrors until it reaches a small 5-axis tee chamber where 3rd to 9th frequency up conversion happens in the Xe:Ar medium via non-resonant frequency tripling process¹⁷. Since the produced vacuum ultraviolet (VUV) light of 118 nm wavelength can freely propagate only in vacuum due to the same reasons as EUV light, the tripling cell is attached directly to the Sample chamber separated only by a VUV-transparent MgF₂ lens. Inside the chamber VUV beam is then redirected and refocused by the parabolic reflector onto the emerging ablation plume near the sample. Details of this setup will be described in section *b.iii*.

In addition to these critical parts of the EUV TOF instrument just described, there is a variety of equipment that supports the operation of the system. These components are grouped into the flowchart shown in Table II.1. The EUV laser, capillary and spark gap switches are brought into a separate group due to their importance in lasing and service requirements. Toroidal mirrors compensate the divergence of the beam and are also attributed to the EUV laser.

Table II.1: EUV TOF sub-systems and their key components.



As was shown above, vacuum is crucial for the proper functioning of the EUV TOF instrument. An attenuation/gas cell operating on argon is listed among other obvious vacuum components because of its immediate effect on vacuum, although it is meant for adjusting the EUV laser power.

The sample chamber has three types of motors/actuators: low precision Thorlabs® motors for coarse positioning of zone plate and microscope, Oriel® motors for their fine movement in the direction of laser beam propagation, and PI® motors for nm-scale precise transverse translation of the sample for high resolution imaging. An in-vacuum microscope allows coordinating ablation location with the sample features and measuring sample-to-zone plate distance. The ion optics sit behind the zone plate and focus and steer ion beam so that it hits the active area of the detector downstream.

According to Table II.1, the first essential component of the mass spectrometer is TOF tube. Power supplies provide with high voltage for acceleration and navigation of ions to the detector. Delay generators manage necessary timings to successfully overlay ions arrival with the active time of MCP detector, and signal digitizer records amplified ion signal and stores it in the connected PC.

The post-ionization source consists of Nd:YAG (neodymium-doped yttrium aluminum garnet) laser. Lasing at fundamental 1064 nm harmonic is initiated by optical flashtubes pumping of the crystal gain medium. Pulsing is achieved by operating in a Q-switch mode - when an optical switch opens only when a maximum population inversion between Nd lasing levels of ${}^4F_{3/2}$ and ${}^4I_{11/2}$ is achieved. YAG laser is equipped with built-in frequency doubling crystal for conversion from 1064 to 532 nm and a frequency mixer for mixing them in order to get filtered by laser-line mirrors 355 nm at the output. Past that the beam is filtered with a small pumped spatial filter consisting of two lenses that focus the beam onto a stainless steel aperture inside a low vacuum vessel and re-collimate it after it has passed through. Afterwards the beam is delivered by a set of mirrors to a tripling cell, where it is focused in the Xe:Ar (1:10) gas medium at 250 Torr for the frequency up-conversion to 118 nm VUV light. The resulting 9th harmonic is focused onto EUVL-created ablation plume for post-ionization.

The alignment, tuning, using and servicing of the system is a complex procedure. In Appendix VII.e most of these critical steps are covered in addition to extensive video tutorials recorded in the past year in order to facilitate experience transition to subsequent users.

II.b System description

The parameters of EUV laser and details on its embedment into the system are given in this section. The EUV optics for laser beam collimation and focusing and strategies for beam energy attenuation and control are discussed.

II.b.i EUV laser and optics for ablation and ionization

II.b.i.1 Laser parameters

The EUV TOF mass spectrometer uses a compact capillary discharge laser¹³. Lasing happens in the argon gain medium at 300 mTorr created inside the alumina capillary of 21 cm length during a pulsed plasma discharge at 90 kV and 22 kA. Rogowski coil surrounding the capillary is the main diagnostics of the capillary discharge¹³ also allowing for triggering the external events since the jitter between current pulse and light emitted does not exceed ~1 ns. The repetition rate of the laser is kept at 1 Hz for standard data acquisition and imaging. The alumina capillary forms a channel for the pinched plasma column formation where Neon-like ions of Ar^{8+} produce a population inversion between the $3p\ ^1S_0$ and $3s\ ^1P_1$ levels leading to 46.9 nm amplification¹⁶. A DC pre-ionization followed by a pre-pulse are used to create a conducting medium for efficient delivery of the main pulse. Due to harsh plasma conditions in this arrangement and the relatively low reflectivity of multilayer mirrors at normal incidence at the EUV wavelength of interest, it is difficult to advantageously use mirrors to achieve multi-pass amplification through the medium as in conventional lasers. Therefore the laser is designed based on a single-pass amplifier. Although the high aspect ratio of the inner capillary space aids in limiting of divergence to 5 mrad, other optics, i.e. grazing incidence mirrors, Schwarzschild

objective or zone plates are used to collimate or focus the EUV laser beam¹⁸. Due to the fact that plasma column exhibits refractive index gradient in the cross section, amplified rays tend to deflect sideways forming a doughnut-shaped beam profile as shown in Figure II.3. Upon collimation of the beam its diameter is kept at 3 mm that allows full illumination of the 0.5 mm zone plate by the most intense portion of the beam.

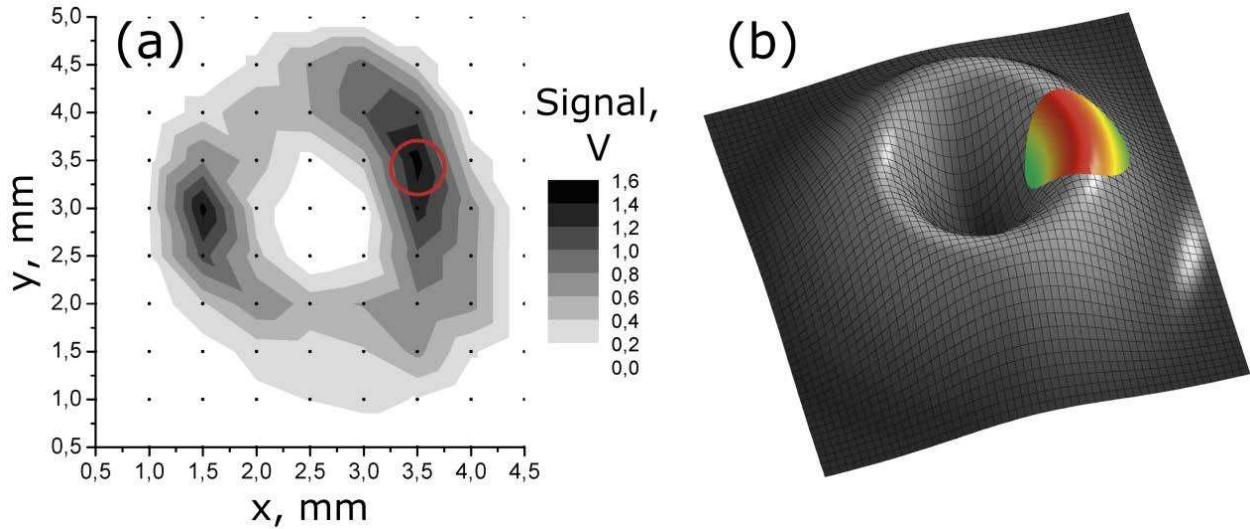


Figure II.3: Profile of the collimated laser beam at the zone plate (adopted from Burian 2015¹⁹). (a) Intensity profile of the laser beam measured at the zone plate position inside the sample chamber. The profile has a shape of doughnut with approximately 3 mm outer and 1 mm inner diameters. The intensity distribution is always uneven due to capillary geometry and mirrors reflectivity variations. The red circle indicates the position of the beam selected for experiment. (b) 3D rendering of the ideal beam profile with colored region showing its scale versus the zone plate.

The repetition rate of the laser is kept at 1 Hz for standard data acquisition and imaging. At this frequency, it takes a little over 6 min to collect 20×20 pixels image. With 0.5 μm size pixel the imaged area is 10×10 μm². Detailed laser specifications are listed in Table II.2.

Table II.2. EUV laser specifications.

Parameter	Value
Wavelength	46.9 nm
Pulse energy	13 μ J
Pulse length	1.5 ns
Repetition rate	12 Hz max, operational 1÷3 Hz
Divergence	5 mrad
Operating voltage	\leq 90 kV
Operating current	$>$ 20 kA
Alumina capillary dimensions	21 cm length, 3.2 mm ID, 6.4 mm OD
Argon pressure	\sim 300 mTorr
Capillary lifetime	10÷50 kshots

The capillary lifetime strongly depends on several factors: quality of the capillary, HV pulsing performance and required energy for the experiment. After lasing the plasma temperature quickly raises to $T_i > 1$ keV (\sim 1 MK) causing subsequent column breakage and deposition of the energy onto the capillary walls and thus their ablation and degradation. Even though the capillary is cooled by circulating oil at 19°C, it still leads to gradual changes of the inside channel geometry and topography that results in a lesser power output over time. This is the reason for the pulse energy decay as a function of shot number as shown on Figure II.4. In case when the experiment requires the use of highest laser energy, for example in work related to trace elements detection, it is quite common to replace the capillary after 10÷20 thousand shots. In case of analyzing organic compounds or imaging at high spatial and/or high depth resolution, the capillary may last up to 50 thousand shots and beyond.

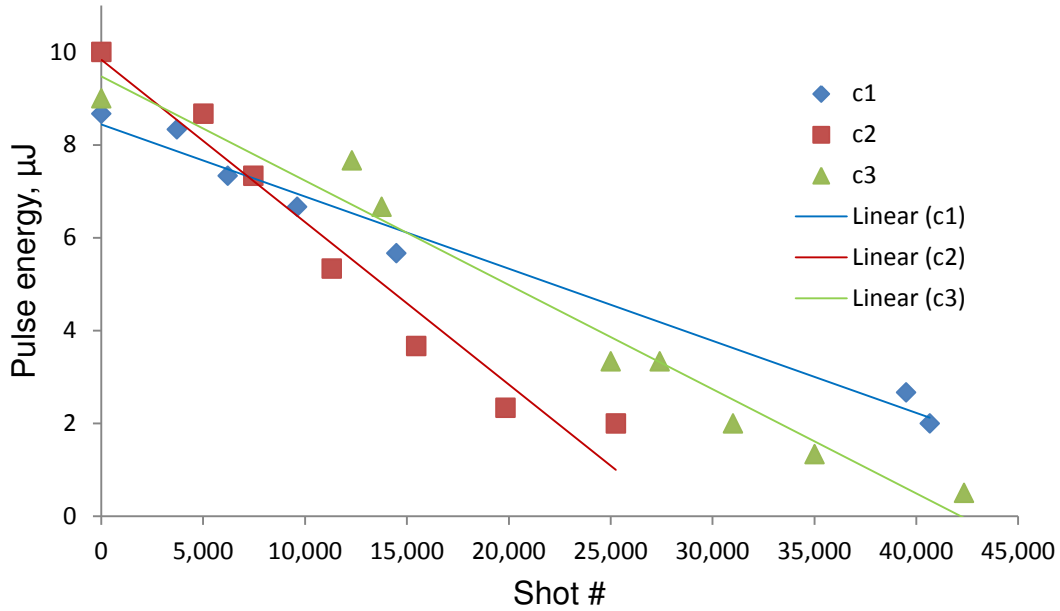


Figure II.4: Pulse energy as a function of shot number for three used capillaries for experiments as recorded in year 2017.

II.b.i.2 EUV laser setup

The EUV laser is placed at the back end of the 5×10' optical table that is almost entirely occupied by the EUV TOF system. The laser head itself is the most compact part of the laser assembly, and it stores only the main spark gap switch and a circular array of high voltage capacitors. These capacitors accumulate charge that is then quickly delivered to the capillary via closing the spark gap switch. The end of the capillary is inserted in the hot electrode which is the core of the main spark gap (Figure II.5). The other end of capillary stems out and is capped by the ground electrode with a hole in the center for argon delivery, pumping and light extraction. Transformer circulating oil surrounds the capillary all over in a gap between itself and the aluminum body of the laser.

Vacuum in the system is achieved through differential pumping of sections divided by the set of four apertures significantly opaque for gas and fully transparent for EUV light. The first aperture *a1* is located few millimeters beyond the ground electrode encapsulating together with aperture *a2* the argon attenuation cell shown as light blue cylinder on Figure II.5. The length of the gas column in the cell is about 10 cm and it is capable of providing full laser attenuation through argon photoionization. The attenuation factor is controlled by varying the argon pressure without exceeding the pressure in the capillary.

The laser chamber is designed to provide high vacuum necessary for the successful laser beam propagation. It is also instrumental as a hub for a number of tools: a high vacuum gauge, Laser chamber venting, safety valve and the inline photodetector (PD). The tube attached to the chamber connects it to the switchyard chamber holding a first toroidal mirror for beam divergence compensation and steering toward application. In between there is a retractable aluminum photodetector for measuring absolute laser power since the inline PD can provide only relative indication of beam intensity. More details are provided in Appendix VII.f.

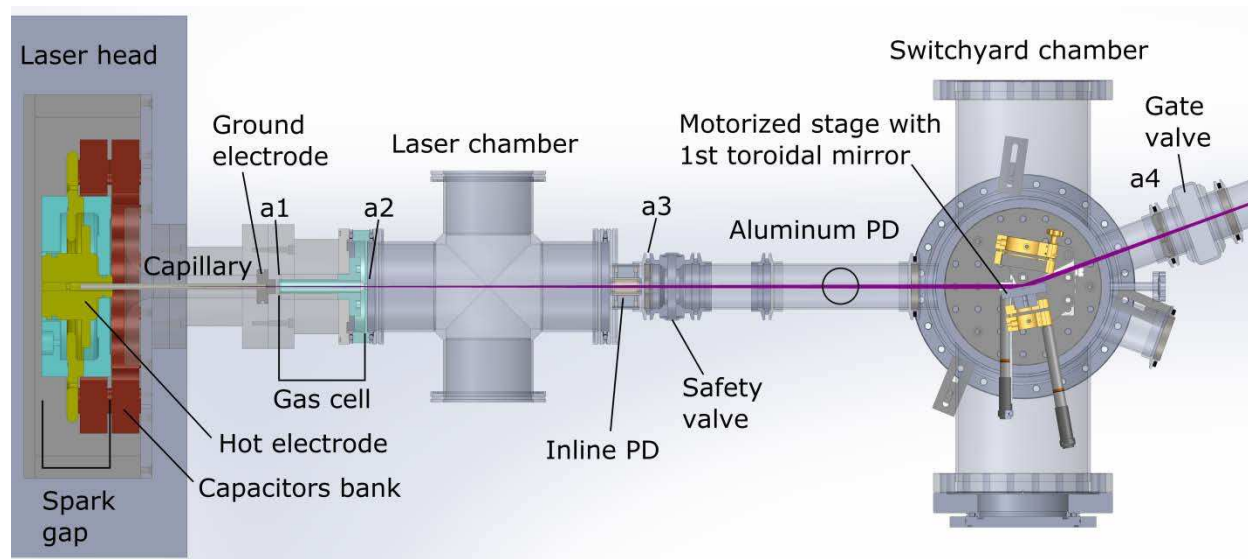


Figure II.5: Top view of the EUV laser section of the mass spectrometer.

II.b.i.3 EUV optics

The EUV optics utilized in the current setup consist of two elements: toroidal mirrors for laser beam collimation and a Fresnel zone plate (ZP) for its focusing onto the sample. The use of conventional refractive optics is hampered by the small absorption length of any material in the EUV range^{5,20}.

The toroidal mirrors perform two key functions: beam collimation and steering. Given the almost 3 m extension of the whole system, without collimation and 5 mrad beam divergence it would result in a 15 mm doughnut-shaped spot at the sample, rendering miniscule collection efficiency for the 0.5 mm diameter ZP lens. More common spherical or parabolic reflectors would cause inevitable deviation of the circular cross section of the beam (astigmatism), but toroidal mirrors allow avoiding this kind of aberration. Collimation is achieved by unequal meridional (vertical) and sagittal (horizontal) radii of the mirror as shown in Figure II.6. Selection of proper radii values is defined by the focal length and the angle of incidence:

$$R_m = \frac{2f}{\sin\theta} = 4334.8 \text{ mm} \quad (\text{II.1})$$

$$R_s = 2f \sin\theta = 130.7 \text{ mm} \quad (\text{II.2})$$

Where R_m and R_s – meridional and sagittal radii, $f = 376.4 \text{ mm}$ – focal length and $\theta = 10^\circ$ - angle of incidence. In order to avoid astigmatism the meridional and sagittal focal lengths f should be equal at selected incidence angle. For increasing the beam steering efficiency toroidal mirrors were coated with 100 nm of gold resulting in combined 50% transmissivity at 10° as shown on Figure VII.5. The dimensions of mirrors made out of fused silica slab are $2'' \times 1'' \times 0.5''$. With long axis parallel to the optical axis of the system and the center (focal point) of the capillary located at a distance of $s = 36''$ from the center of the first mirror, a full diverged EUV laser beam is captured. The focal point of a combination of lenses measured from the first lens is calculated as:

$$s = \frac{f_1 f_2 - d f_2}{f_1 + f_2 - d} \quad (\text{II.3})$$

Where $d = 40''$ - distance between two mirrors, and $f_1 = f_2 = f$ – focal length of each.

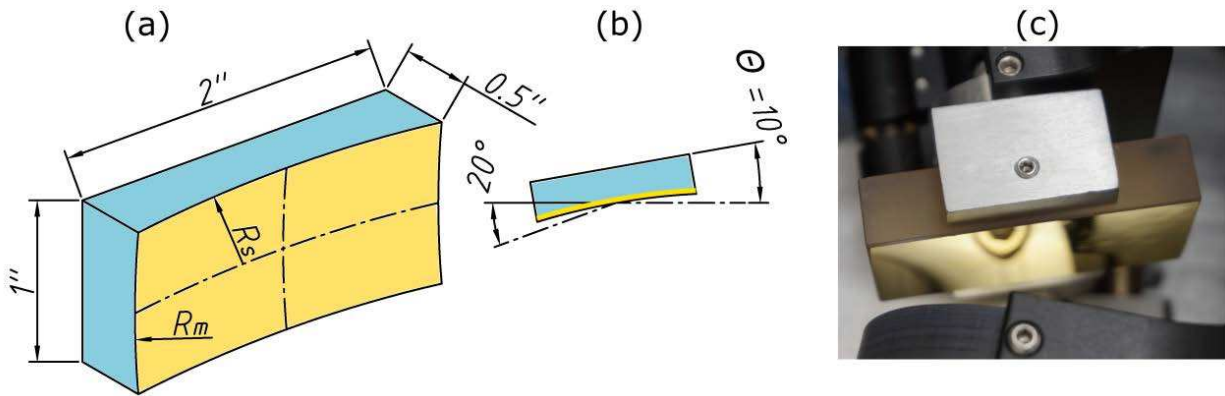


Figure II.6: Toroidal mirror for EUV laser beam collimation and steering. A pair of identical toroidal mirrors is used. (a) 3D model of the mirror showing main dimensions and gold reflective surface coating. (b) Top view of the mirror with the axis of the beam reflected upon 10° incidence. (c) Photograph of the first toroidal mirror installed in the switchyard chamber with EUV laser on the right.

The ZP lens focuses the collimated 3 mm diameter EUV laser beam onto the sample. Collimation restricts beam divergence and promotes high zone plate focusing performance. The ZP was engineered and manufactured by W. Chao and collaborators at LBNL²¹. The ZP is designed and fabricated onto a 100 nm thick silicon nitride membrane by electron beam lithography in a free standing geometry, whereby the region between the zones are etched away. A thin layer of Au coats both sides of the ZP. The ZP consists of an array of alternating fully opaque and fully transparent (fully etched membrane) concentric rings. So-called zone width – a pitch of this pattern – starts from a few micrometers near the central 50 μm opening and gradually decreases down to 200 nm on the edge of 0.5 mm outer diameter. The outer zone width defines the focal length, numerical aperture and the focal spot diameter of the ZP at the laser illumination. The free-standing ZP efficiency is 0.1 when operating in first order⁵. 100 nm outer zone width ZPs were utilized in the setup as well, but 200 nm one is the most convenient because its NA of it can be matched to the 100 nm one when switching to 3rd order ablation at $f_3 = f_1/3 = 0.7$ mm as shown in Figure II.7. The imminent disadvantage of doing so is 10 \times loss of the

efficiency. The smallest consistently ablated crater in the 3rd order on PMMA resist reached dimensions as low as 120 nm FWHM diameter and 3.5 nm depth¹¹. In previously reported experiments, a diameter of 80 nm was demonstrated⁶.

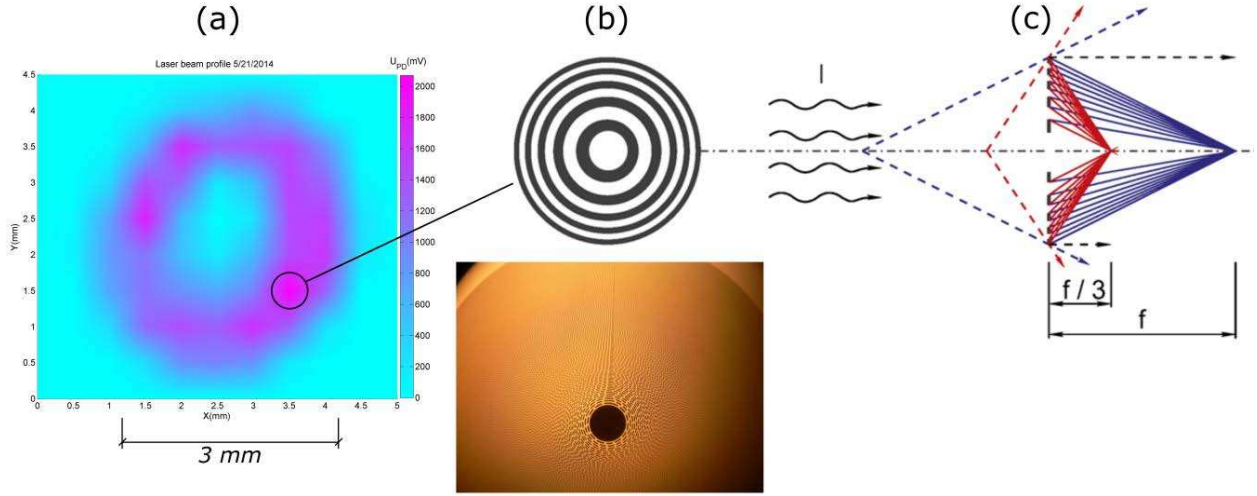


Figure II.7: Fresnel zone plate lens for laser focusing for sample ablation and ionization. (a) Intensity profile of the collimated laser beam at the zone plate. The circle of 0.5 mm diameter shows the zone plate to scale on the beam background. (b) Structure and photograph of concentric rings of variable width of the zone plate. The central opening of 50 μm is necessary for ion extraction upon ionization. (c) Illustration of the first (blue lines) and third (red lines) order focus of the zone plate (adopted from Burian 2015¹⁹).

The overall throughput of the optics between the EUV laser and the sample is calculated as follows:

$$T = R_{tor}^2 \frac{d_{zp}^2}{d_{BOD}^2 - d_{BID}^2} T_{zp} = 1.5e - 3 \quad (\text{II.4})$$

Where $R_{tor} = 0.7$ – reflectivity of the toroidal mirror, $d_{zp} = 0.5$ mm – ZP outer diameter, $d_{BOD} = 3$ mm and $d_{BID} = 1$ mm – outer and inner diameter of the doughnut-shaped laser beam upon collimation, $T_{zp} = 0.1$ – zone plate efficiency. In the 3rd order focus $T_{zp} = 0.01$ and the overall throughput is $1.5e-4$ instead. 70% reflectivity of the toroidals is subject to degradation over time due to hydrocarbon deposition from primarily oil fumes from the capillary. This layer

is then decomposed by EUV photons resulting in non-volatile carbon layer that is very opaque for 46.9 nm radiation. Figure VII.5 shows that reflectivity through 5 nm C layer drops by 60%.

II.b.ii Mass spectrometry

Details on ion extraction, transportation, discrimination and detection are given in this section. A detector gain measurement experiment allowing for exact conversion of oscilloscope signal to ion counts is presented. Advantages of positive and negative ion extraction modes are discussed on the examples of organic and inorganic compounds together with specific experimental conditions related to each mode.

II.b.ii.1 Ion extraction and discrimination

Ions are formed upon EUV laser ablation and ionization of the sample. Ion extraction occurs in the static electric field applied between the sample and the ground grid. In fact, the accelerating field is split between sample and zone plate with usually higher gradient, and between zone plate and ground grid. Then the ion bunch travels through ion optics for focusing and steering as shown on Figure II.8. In the case that the ion beam is more divergent due to bigger zone plate opening and/or has lower energy, then focusing by Einsel lens is required to maintain its spreading until the detector is reached. The reflectron configuration of the TOF tube requires the ion beam to propagate at a certain angle to the axis of the tube in order to hit the active detector area. This is achieved by a pair of deflection plates positioned right after the Einsel lens.

Discrimination of ions happens in the long field-free region of ~0.9 m where they separate according to their mass-to-charge ratio. The TOF is always operated in the reflectron mode except for rare investigative cases. The linear mode can be used by simply allowing ions to reach the far end of the TOF tube where a smaller microchannel plate (MCP) is located. However, if increasing the flight path for better ions separation and sharpening of the mass peaks is required, then the reflectron is operated in a way that allows fast ions to be reflected deeper inside. Careful optimization of retarding and reflecting potentials of the reflectron (Figure II.8) allows for slow and fast ions time-focusing, i.e. reaching the main MCP detector simultaneously.

The MCP detector is essentially an electron multiplier of the ion current. Ions hit the walls of the silicon microchannels with consequent high gain conversion to electrons. Two silicon plates that have these channels have them inclined in a chevron configuration to maximize electron yield through multiplication. The anode behind the plates collects $1e6\div 1e7\times$ amplified current and directs it to the oscilloscope. Upon arrival to the detector, ions are first accelerated by an extra 2 kV potential until they hit the first chevron-shaped tube array where the electrons are emitted (Figure II.8). These electrons are further multiplied through successive acceleration in the field (≤ 1 kV per plate), interaction with the channel wall and secondary electron emission.

The mass spectrometer can operate in positive and negative ion extraction modes. Switching between them is performed by change of high voltage power supplies polarity with some minor changes of acceleration field configuration and significant rewiring of MCP operation as is described in Appendix VII.d.

In the post-ablation ionization mode ions originate from the plasma plume in between the sample and zone plate but closer to the sample where the density of the plume is still high

enough for efficient ionization by secondary laser source. The gas phase ion source locates in between zone plate and additionally installed extraction grid. A detailed potential diagram of each mode is also described in Appendix VII.d.

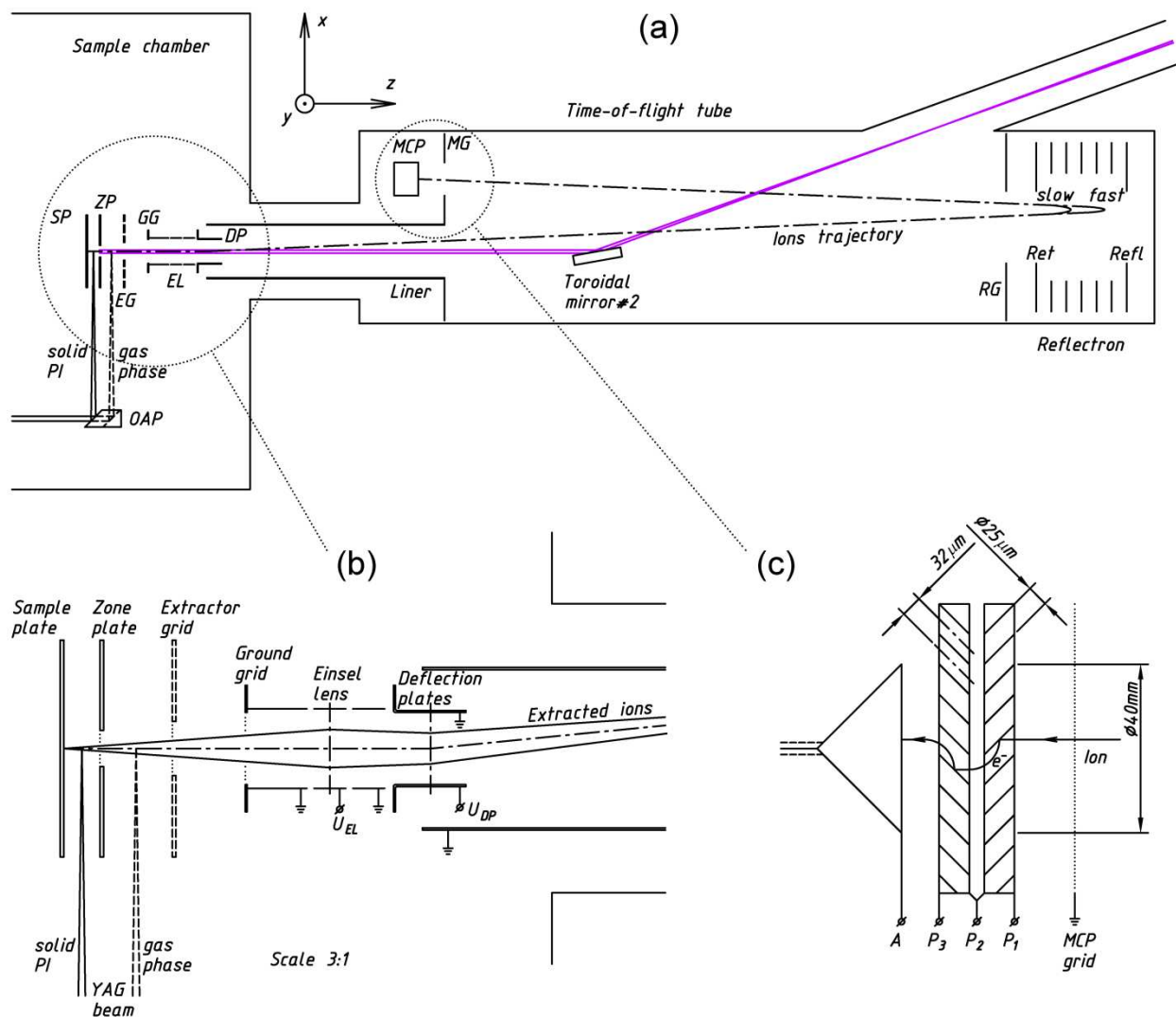


Figure II.8: Ion extraction, transport and detection. (a) Sample chamber and TOF tube hosting all electrodes necessary for ion beam manipulation. After ablation ions get accelerated in the field between sample and ground grid and segregate in the field-free region of the TOF tube according to their mass-to-charge ratio. In the reflectron mode more energetic ions reflect deeper inside the reflectron compared to slower ions. The difference in travelled path is adjusted by retarding and reflecting grid potentials of the reflectron such that all ions of the same mass arrive together to the detector forming a sharp Gaussian-like pulse on the mass spectrum. (b) Magnified view of the ion source and optics. Ions gain the most acceleration in the field between the sample and zone plate, where the zone plate central opening restricts the beam diameter. In cases when further narrowing of the beam is required, the Einsel lens does the focusing by regulating the voltage applied to its central tubular section. For proper steering of the beam

towards the reflectron and MCP a corrective voltage is applied to one of the deflection plates housed right after the Einsel lens. A grounded liner beyond the ion optics isolates the beam from possible external fields. (c) Magnified view of the MCP detector with 40 mm diameter active area. Incoming ions generate electrons upon hitting of the microchannels in the first plate. These electrons are further amplified in the second plate and detected by the anode down the line. Typical gain is $1e6\div 1e7$ electrons/ion.

II.b.ii.2 Signal acquisition and detector performance

The main microchannel plate for reflectron configuration is Galileo MCP-40B, supplied together with ion optics by Jordan TOF Products, Inc. Specified ion-to-electron gain of $1e6\div 1e7$ is loosely defined possibly because of applications variety. For exact conversion of measured peak voltage to ion counts at our conditions an ion counting experiment was conducted with more details in Appendix VII.g. Figure II.9 shows an averaged histogram of the analyzed mass spectra arrays of the diluted calibration sample. The histogram has two apparent Gaussian distributions of voltages that correspond to zero and single ion detection events. The voltage difference between the Gaussian centroids is 18.5 mV. This signal is generated upon detection of a single ion that corresponds to an exact $2.31e6$ electrons/ion gain of the MCP. This experiment was done for ions in 200 \div 300 Da range at energies of 6 and 18 kV that allows for making a safe assumption that the measured gain is accurate for ions with mass up to 1 kDa.

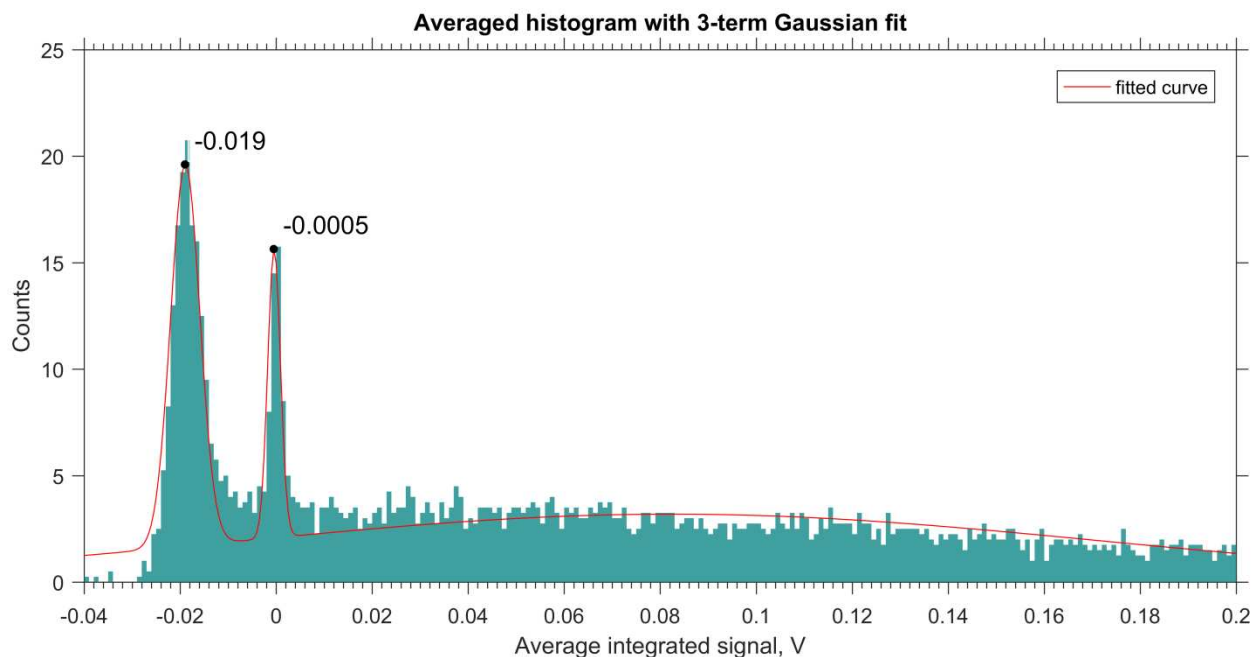


Figure II.9: Averaged histogram in the single ion counting experiment. First and second distributions correspond to zero (left) and single (right) ion detection events. The voltage difference between them equals to 18.5 mV per ion. The red line is a three-term Gaussian fit that encompasses both distribution and the baseline unevenness.

To avoid saturation of the dual MCP detector by scattered EUV photons of the incoming laser pulse, and to keep it unsaturated from incoming intense ion bunches usually associated with low-mass peaks, it is pulse-charged to the operating potentials with a variable delay. Idle operation of the detector in the positive mode corresponds to zero voltages on all plates. In the negative mode, due to electronics-imposed limitations, voltages across plates are instead limited to 0.6 kV as shown in Figure VII.6.b. With this bias the dual MCP detector is insensitive to incoming particles. In either mode, the transition between the idle and fully operational states takes up to 5 μs , which at 6 keV acceleration corresponds to not recording masses within 20 to 100 Da from the mass corresponding to the time of switching (5 and 40 μs), depending on the mass of the analyte (7 and 415 Da). Timing is controlled by the delay generator and discussed in section *d*.

Mass spectra are processed, displayed and stored in the inside-PC digitizer GaGe® EON CS121G1 (1 channel, 12-bit, 1 GS/s) card. With 50 Ω impedance input, the input amplitude is limited to ± 5 V. In order to avoid digitizer saturation as well as promoting full digitizer vertical resolution utilization, a set of impedance-matched fast attenuators and amplifiers is used. Depending on the experiment, up to 100 \times attenuation can be required. For amplification of the signal or for filtering the low-frequency contribution that affects the baseline, a GHz-rated 20 \times Ortec® VT-120 preamplifier is used. After signal collection the overall multiplication factor is considered during data analysis. In addition to adjustment of the signal amplitude these elements also serve as a protection device for the digitizer in negative ion detection mode when the MCP anode is biased with +4.2 kV potential (Appendix VII.d).

II.b.ii.3 Positive and negative ion detection modes

Alteration of the EUV TOF mass spectrometer polarity is instrumental for analytical applications where detection of intact molecular signals or, on the contrary, elemental decomposition of the sample chemistry is preferred. In both cases, the zone plate-focused laser beam evaporates and partially ionizes the material leaving usually a Gaussian-shaped crater as shown on Figure II.10. Ions get accelerated towards the biased ZP where they are, in addition, collimated by its central aperture. The rest of the acceleration is performed in the space between the ZP and ground grid after which the field-free region lets the ion packets of same m/z segregate in space. After arriving at the detector at specific flight times the mass spectrometric signal is formed.

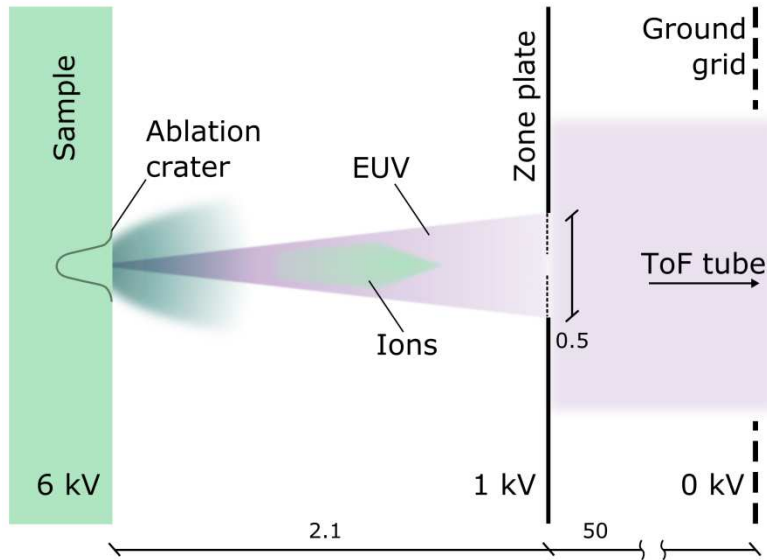


Figure II.10: Schematics of positive ion extraction mode. Negative ion mode is the same except that the ZP voltage is set to $-5.5\div-5.7$ kV. The focused EUV laser beam ablates and ionizes the sample. Accelerated ions get through the ZP central opening toward TOF tube.

It was empirically verified that the most suitable acceleration conditions in the positive mode occur when using a 5 kV voltage difference between the sample and the ZP. The sample is usually biased to 6 kV, however it can be as high as 18 kV limited by the power supply output. Higher voltages are desired for detection of low concentration high mass species. Ions with higher energy arrive at detector earlier and form narrower peaks that help better distinguishing them from the noise floor of the baseline as shown on Figure II.11.

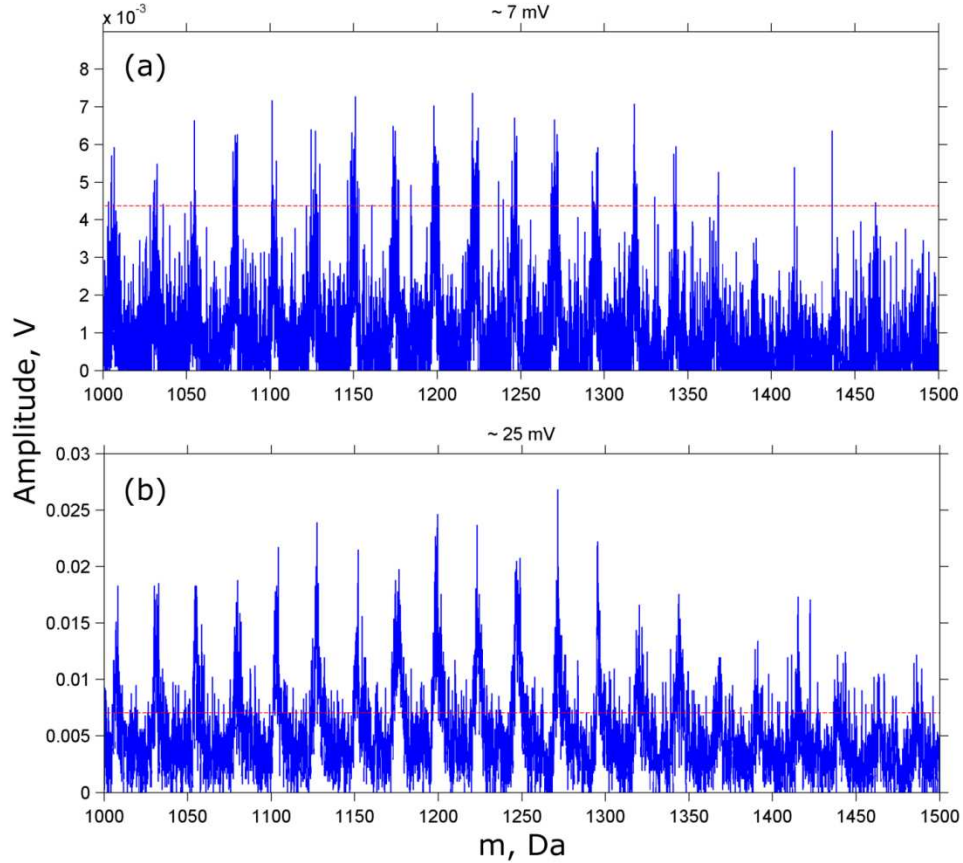


Figure II.11: Comparison of averaged C_{60} mass spectra at 6 kV (a) and 18 kV (b) acceleration. The red dashed lines represent 5σ noise level. At higher acceleration potential ions are recorded with $3\times$ larger amplitudes due to the peaks compression at earlier arrival times. C_{60} has a mass of 720 Da while the observed species represent giant fullerenes.

In negative mode extraction, the voltage difference between sample and ZP has to be limited to ≤ 0.5 kV in order to prevent ZP failure under optical-induced discharge. For extracting negative ions the sample plate is biased to -6 kV, while the ZP should have -6 \div 0 kV potential. Under these conditions the sample, unlike in positive ion extraction mode, becomes a cathode. When an intense laser pulse is focused onto such cathode, it promotes an optically-induced breakdown of the biased gap. Photoelectrons liberation from the sample is supported by accelerating potential favorable for the negatively-charged species. If the voltage difference between sample and ZP is higher than 0.5 kV, it promotes destruction of the sample surface in a

star-shaped pattern with ablation crater in the center. The ZP gets damaged by the incoming flux of material and charge as shown on the Figure II.12.a. Sustainable avoidance of such phenomenon can be accomplished by two-step process: limiting laser beam energy to $\leq 1 \mu\text{J}$ and limiting the sample-ZP potential difference. In this situation the main acceleration of negative ions happens in the gap between ZP and ground grid. It is less efficient especially when combined with lesser laser fluence; hence negative mode has in general lower sensitivity than the positive one.

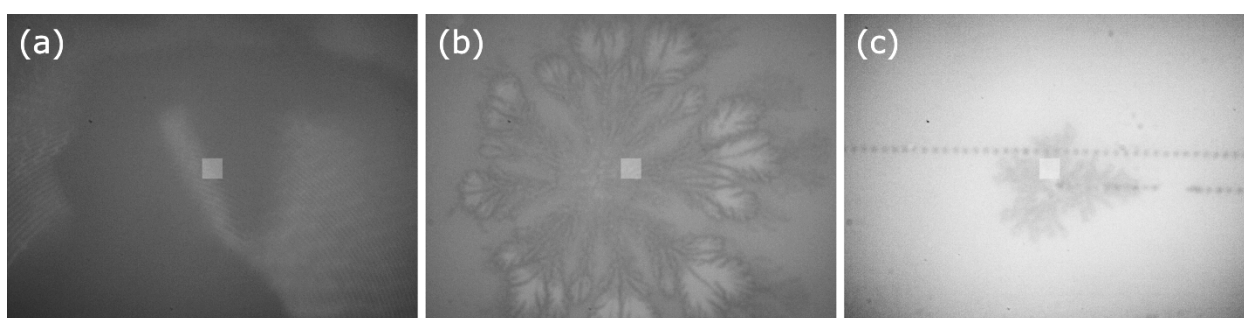


Figure II.12: In-chamber microscope pictures of the effect that is caused by incorrect conditions selected for negative ion extraction mode. (a) Destroyed ZP after <100 shots with 5 kV difference between sample and ZP. (b) Star-shaped pattern stemming out of the ablation crater. (c) Sample destruction is a lot smaller with reduced laser fluence and only 1 kV potential difference. The ablation crater corresponding to the last shot that caused sample destruction is visible in the lower right corner of the white square that is in the middle of the picture.

Ions collected in positive and negative modes are formed via different ionization channels. The dominant mechanisms in positive mode are: single photon ionization (SPI) by direct interaction of 26.4 eV photons with a neutral particle, and protonation by attachment of H^+ to the neutral. In negative mode free electron attachment to the neutral particle or attachment of negatively charged atom like O^- are dominant. Depending on the compound properties, its intact molecule can be successfully detected in one of the modes.

Soda-lime glass, an ITO film and dry-spotted trimethoprim and Nile red compounds (Figure II.13) were used to demonstrate the different ionization mechanisms observed in positive

and negative ion extraction modes. Soda-lime glass is the most widespread type of glass used in windowpanes and glass ware. ITO is a transparent, colorless conductive film of ternary indium, tin and oxygen mixture. Our standard sample slides usually have 30÷60 nm of ITO coating on 25×25×1 mm soda-lime glass. Trimethoprim antibiotic is widely used to treat human diseases; it is on the Essential Medicines list of the World Health Organization. Nile red is an organic dye, widely used as lipophilic stain in fluorescence experiments.

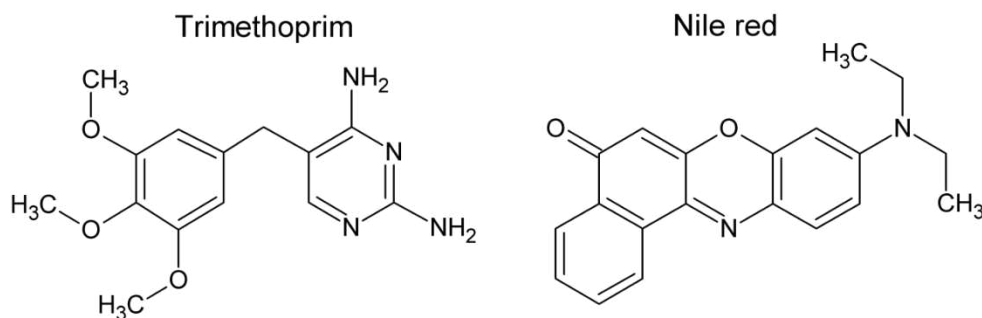


Figure II.13: Molecular structures of trimethoprim antibiotic ($C_{14}H_{18}N_4O_3$, 290.32 Da) and Nile red organic dye ($C_{20}H_{18}N_2O_2$, 318.37 Da).

Figure II.14 shows averaged mass spectra of aforementioned compounds obtained in positive and negative mode extraction. Inorganic and organic spectra have similar mass and intensity scales. Indium is present on the glass spectra because the glass substrate is reached by laser ablation through the ITO layer.

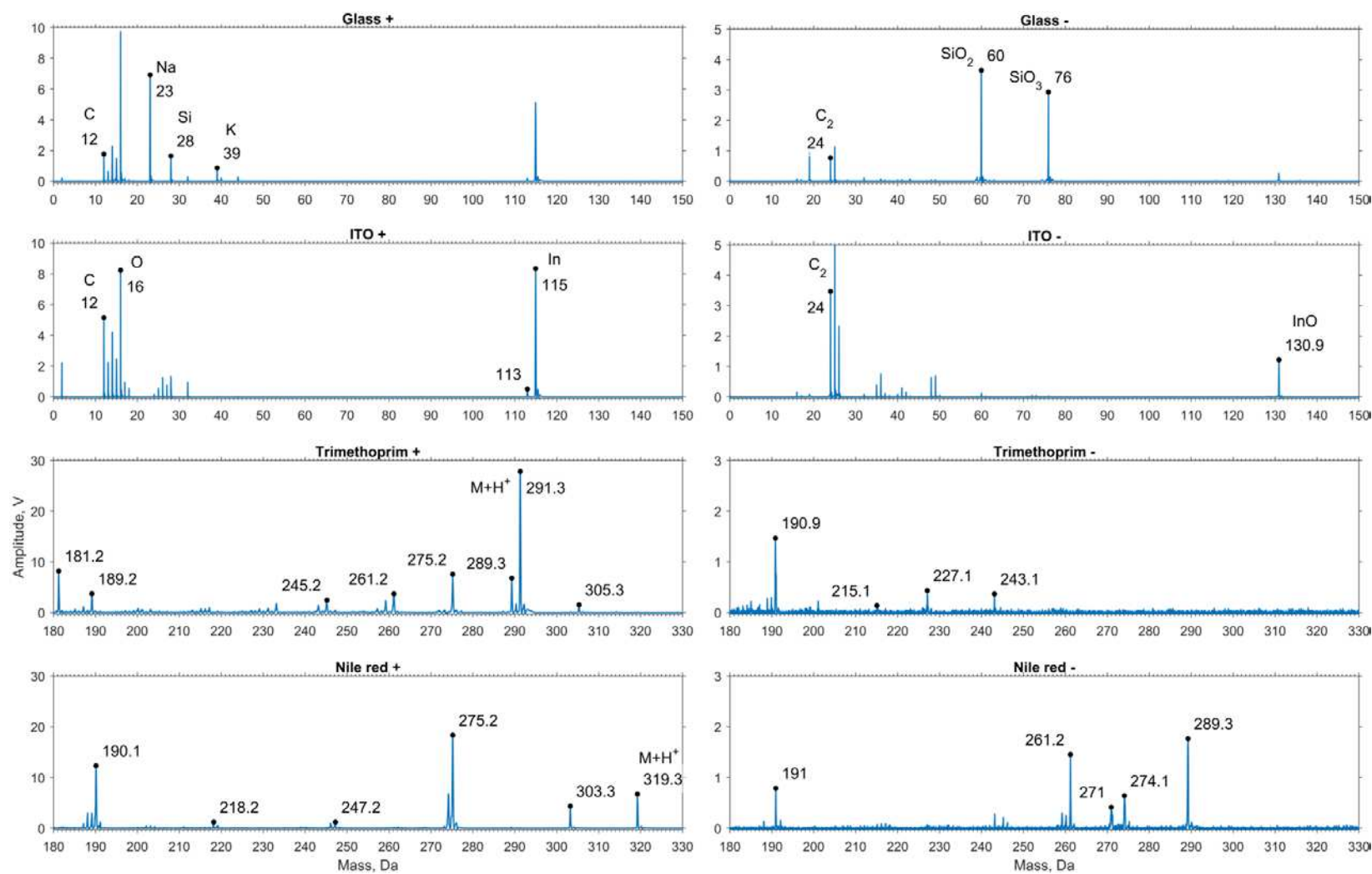


Figure II.14: Positive and negative mode spectra of glass, ITO, trimethoprim and Nile red (top to bottom). Left column is positive spectra, right column – negative. Glass in positive mode shows mostly C, Na, Si and K elemental peaks, as well as the residual In peak at 115 Da. The negative mode spectrum of glass is dominated by the full SiO_2 molecule, followed by SiO_3 . The ITO spectra show two In isotopes in positive mode and InO molecule in the negative one. Trimethoprim and Nile demonstrate their protonated molecular ions only in positive mode.

II.b.iii Post-ablation ionization

Improvement of EUV TOF sensitivity and increase of the capability towards selective detection of atomic or molecular signal is achieved via the implementation of a second laser with UV or VUV switchable output that probes into the highly abundant neutral portion of the initial ablation plume by the mechanism of post-ablation ionization. Details on the respective harmonics generation and ionization mechanism are given. Results on the example of inorganic compounds of uranium filter glass and GaAs crystal are presented.

II.b.iii.1 YAG laser for harmonics generation

A Nd:YAG laser is used in the system as an ultraviolet (UV, 355 nm) and vacuum ultraviolet (VUV, 118 nm) light source for post-ablation ionization. Continuum Powerlite 7010 laser was upgraded with a mixing crystal for obtaining 3rd harmonic from 1064 and 532 nm two-wave mixing. 355 nm light was then spatially filtered using a pair of 10 cm quartz lenses. Filtering was done through the on-site machined stainless steel Ø150 µm aperture placed in the joint focus of the lenses in the low-vacuum cell with quartz windows. The spatially filtered and re-collimated beam is then guided with a set of mirrors to the 25 cm quartz lens that focuses it in the pre-pumped high vacuum cell with 250 Torr of Xe:Ar (1:10) to achieve non-resonant frequency tripling of the 355 nm to 118 nm – 9th harmonic as shown on Figure II.15. This is relatively inefficient process with typical¹⁷ conversion rate of ~1e-4, resulting in about a micro joule of VUV pulse of <10 ns duration as Table II.3 shows. At this point both UV and VUV beams propagate collinearly until they reach a MgF₂ lens. If the quartz lens focuses the beam at the VUV focal point of the MgF₂ lens, then VUV light gets collimated while UV one disperses.

The off-axis parabolic (OAP) mirror refocuses the VUV light into the sample region where it interacts with plasma plume.

For experiments requiring UV laser post-ionization the tripling cell is evacuated and the 25 cm quartz lens is moved back in order to overlay its focus with the focal length of the MgF₂ lens for UV light. Since refractive index for this wavelength is higher (Table II.3), the focal length is longer than for VUV light. This results in re-collimation of the 355 nm beam and its subsequent focusing into the sample region with the aid of the OAP. Due to low damage threshold of the OAP mirror the output of 355 nm light should be limited to 20 mJ. More details on optical design are given in the Appendix VII.e.

Table II.3: Nd:YAG laser and optics parameters. 20 mJ at 355 nm energy at 10 Hz measured prior to the tripling cell is limited by OAP mirror damage threshold.

Wavelength, nm	1064	532	355	118
Pulse energy, mJ	850	400	200 (20*)	~1 μJ
Pulse length, ns	6÷8	5÷7		
Maximum repetition rate, Hz	10			
Divergence, mrad	0.45			?
Quartz refraction index			1.4761	-
MgF ₂ refraction index			1.3870	1.6779
MgF ₂ transmission			0.93	0.29

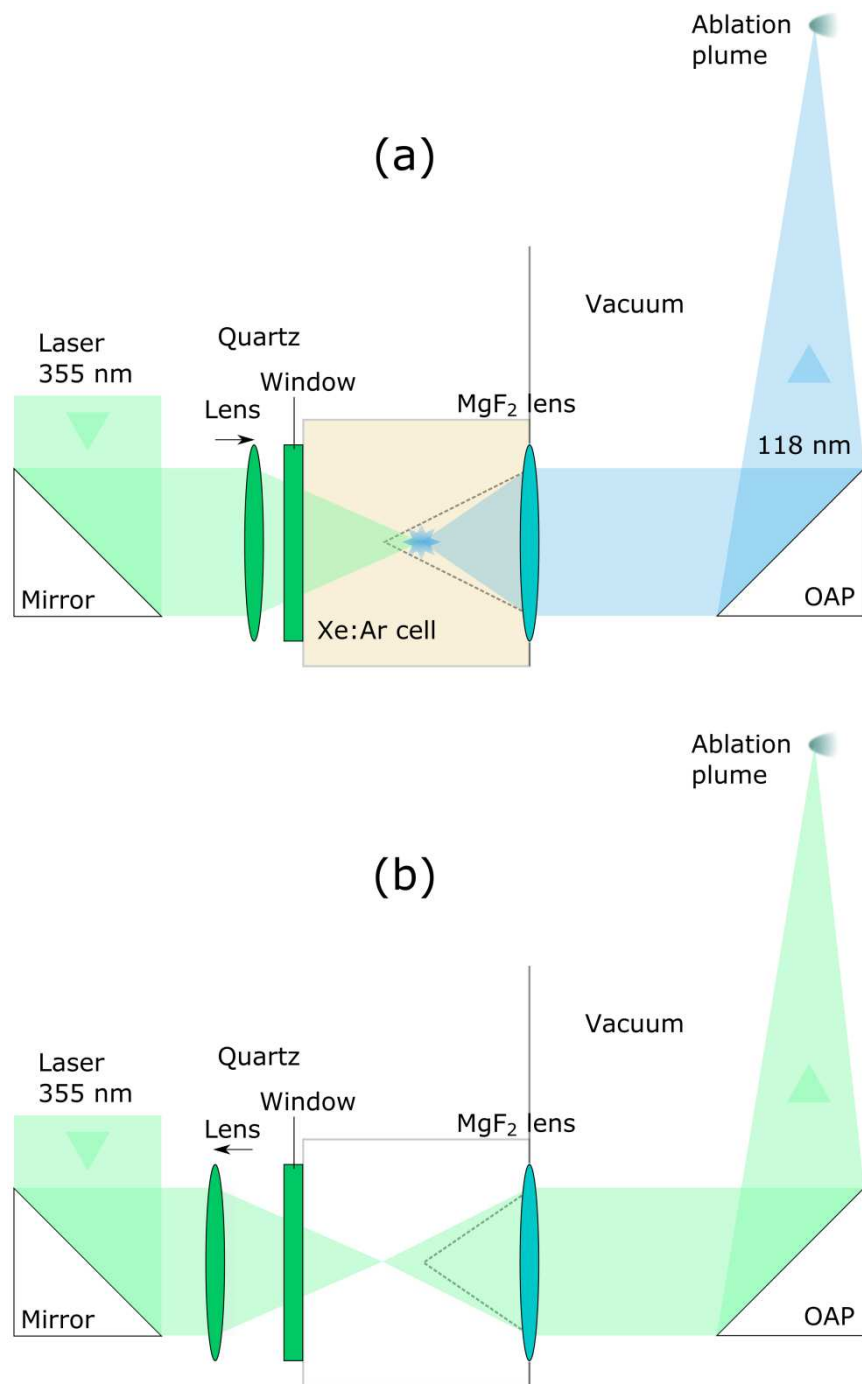


Figure II.15: Schematic of VUV (a) and UV (b) light generation with 1064 nm Nd:YAG laser for post-ablation ionization in the EUV TOF. (a) Collimated and spatially filtered 3rd harmonic gets focused by quartz lens into the tripling cell with 250 Torr of Xe:Ar (1:10) mixture. In there an upconversion to 9th harmonic happens followed by recollimation by MgF₂ lens. This lens also acts as a high vacuum window into the sample chamber where an off-axis parabolic reflector refocuses the light onto ablation plume. (b) In UV post-ionization mode quartz lens is retracted back to match longer focal length of the MgF₂ lens for UV light. Tripling cell is evacuated of the gas mixture to avoid harmonic upconversion.

II.b.iii.2 Post-ablation ionization performance

The ablation plume created by the EUV laser consists of >99% neutrals, with low initial kinetic energy of <0.1 eV⁷. The amount of information that can be extracted from here is vast compared to detection of primarily ionized species. In addition, neutrals are expected to have less thermal excitation and hence contain more unfragmented species that are of main interest in the bio-related applications. Since many critical compounds like cholesterol were not detected in the regular EUV-only positive and negative ion detection modes, a post-ablation ionization (PI) deemed the last resort for proving of the extended molecular detection capability of the EUV TOF. PI mode was first approached by trying a continuous-wave VUV source with broad 170÷2100 nm output range from Energetiq®. With no detected signal from a test sample this negative result served as lowest limit in terms of estimated (Appendix VII.h) number of PI ions as assessed for alternative sources as table below shows.

Table II.4: Calculated performance of various VUV light sources for post-ionization. F – photon flux onto ablation plume, t – duration of the light pulse, N_{PI} – estimated number of post-ionized species detected.

Light source	EQ-99X	Synchrotr. at 11.9 eV	EQ-77	E-lux 126	EP 172	10.5 eV YAG laser
Comm./ param.	CW lamp, experiment failed	From Takahashi 2009 ²²	3× brighter than EQ-99X	The only lamp in low VUV range	Geometry losses are 90%	118 nm 9 th harmonic
F , ph/cm ²	4e17	1.8e18	1.2e18	2.8e18	1.6e18	7.4e21
t , s	1.3e-6				8e-8	1e-8
N_{PI}	9.4e3	4.2e4	2.8e4	6.6e4	2.3e3	1.3e6

These results show that unfortunately EQ-99X lamp could not produce detectable signal, although most of the implemented modifications into the system were utilized in currently functional PI setup. A brighter lamp EQ-77 would increase PI performance only three times.

Lamp-like source E-lux 126 from Excitech® GmbH would provide twice higher photon flux than EQ-77 at similar price range. And only 118 nm laser has two orders of magnitude higher chance to demonstrate decent signal from the VUV ionization of neutrals, which was experimentally verified later on. In future, when the cost of setup has to be carefully considered, more affordable and compact lamp sources than YAG laser could be used. At that time knowledge gathered on true PI performance could be used to make sure that enough PI-generated signal is produced. Pulsed extraction, ion collector, and more efficient detection system may be implemented to make sure that continuous-wave light sources perform well.

Even with YAG laser as a PI source obtaining initial results in VUV mode was challenging. In order to reduce complexity of VUV light output optimization, a gas phase experiment was devised and conducted. In this setup (Figure II.16) a wide gas column formed in the semi-isolated compartment in the high vacuum Sample chamber interacted with focused YAG laser beam. Minimal or no focal point adjustment was required, and in the case of EUV counter-experiment for ionization comparison the beam was only collimated. Maximum signal yield was found at optimal Xe:Ar (1:10) gas pressure of 200÷300 Torr. TOF voltages were adjusted to accommodate to median 6 kV acceleration to the ions as shown in Appendix VII.d.

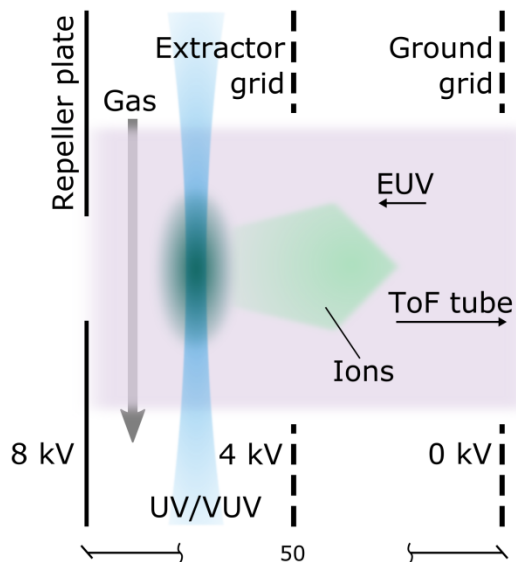


Figure II.16: Gas phase ionization scheme. Accelerating potential is applied between repeller and extractor electrodes that encompass a differentially pumped cell where a steady gas supply is maintained. 5% NO₂ in He and He:propene (1:1) gases were tried. Incoming EUV, UV or VUV pulses create ions that are extracted toward TOF.

The molecule to study optimal parameters and photoionization mechanism was chosen to be propene, an unsaturated gaseous organic compound at 300 K. It is one of the most significant by-products of oil refinement and is used for production of plastics etc. Propene (C₃H₆, 42.08 Da, 9.73 eV IE) was mixed with He (4 Da, 24.59 eV IE) in a 1:1 ratio to reduce flammability and add a known low mass peak for proper mass calibration. Figure II.17 shows mass spectra obtained with ionization of propene by each of three wavelength selected.

With an ionization energy of 9.73 eV propene requires three photons (multiphoton ionization or MPI) of 3.5 eV energy to be absorbed for ionization. Due to plasma heating it results in extensive fragmentation and loss of the parent ion signal – the heaviest mass of 39 Da is associated with C₃H₃ but not C₃H₆. In contrast, 10.5 eV wavelength provides soft single-photon ionization (SPI) that reveals the full propene molecule and very few non-dominant fragments with the lowest mass of 27 Da (C₂H₃). EUV light also provides with SPI process, but

more than half of the photon energy stays in the molecule or releases with the liberated electron causing fragmentation. This process results in a spectrum that still shows the parent propene ion peak but the dominant features are fragments. This conclusion is also supported by ion yield calculation in the Table II.5. Difference of single photon ionization process when using EUV or VUV light is exemplary. It illustrates that with EUV-only ionization detection of sensitive to excessive energy molecules is impossible or hampered by extensive fragmentation.

Table II.5: Yields of propylene molecular ion signal in gas phase ionization mode. Since both VUV and EUV ionization is single-photon process, VUV yield is higher due to lesser fragmentation.

Method	Sample	Mass, Da	Secondary ion counts	Photons	Primary photons number	Secondary ion yield	Comments
VUV	C ₃ H ₆ :He 1:1 gas @ 1e-6 torr	42	9857	10.5 eV	6e11	1.6e-8	100-shot averaged spectra
EUV			1729	26.4 eV	2.7e11	6.4e-9	

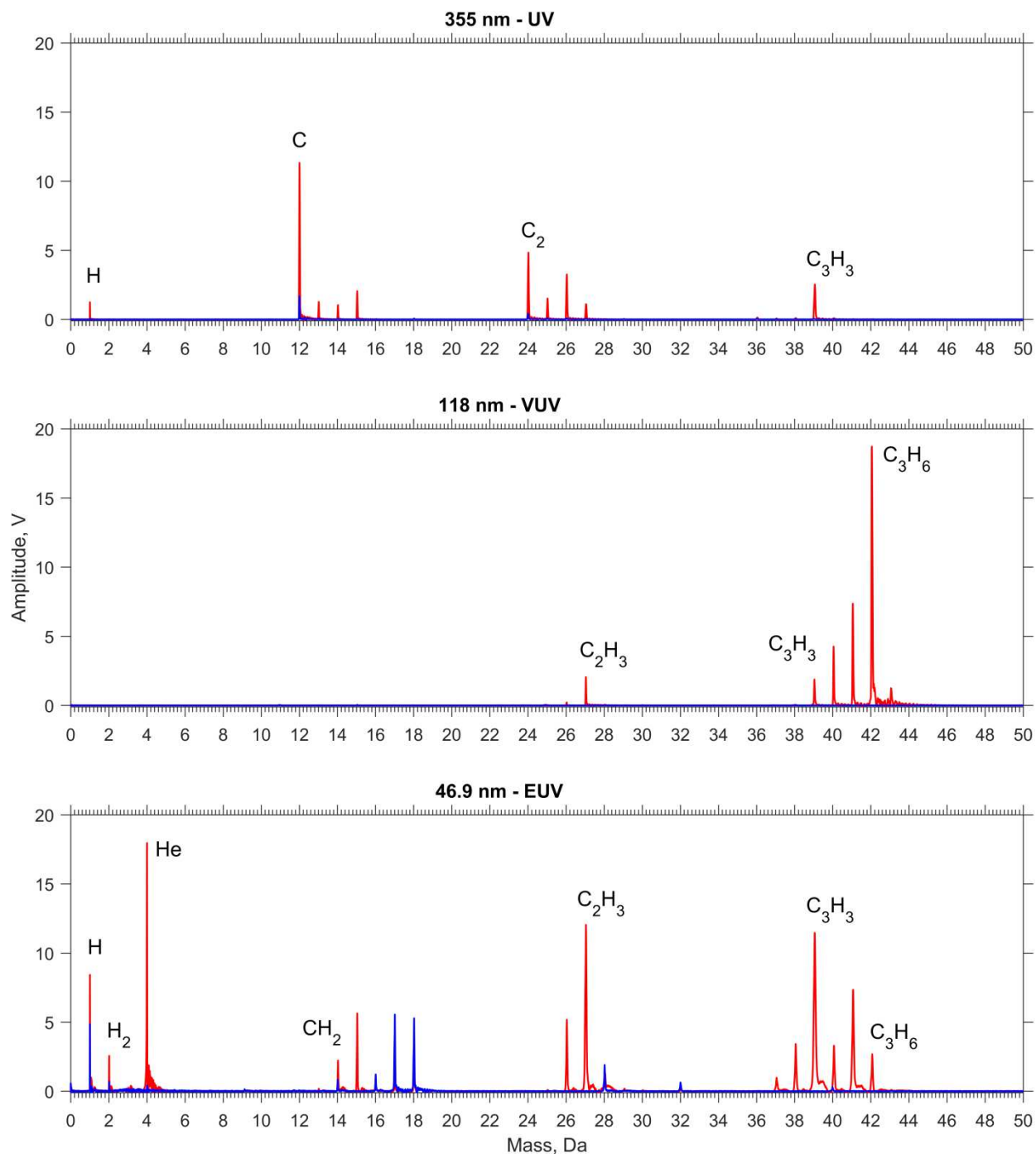


Figure II.17: Gas phase ionization of propene (C_3H_6 , 42.08 Da, 9.73 eV IE) with various laser wavelengths used. Propylene molecular ion signal is the highest and least accompanied with fragments at 118 nm. Peak at 43 Da is propylene isotopologue that is 3.3% of the amplitude of the parent molecule at natural isotope abundance. Blue spectral lines represent background signal – when gas is pumped out of the ionization cell.

II.b.iii.3 Results on inorganics

After tuning of the VUV output performance in gas phase we could switch to experiments with solid samples. When working with solid sample in PI mode, the focal point of the secondary laser beam—UV or VUV—has to be precisely overlapped with the emerging ablation plume from the sample that was created by the focused EUV light as Figure II.18 shows. Moreover, timing of two laser pulses must also be taken into account. The minimum delay of the YAG pulse from the EUV one is ~ 260 ns. For example, it takes $1.3 \mu\text{s}$ for Aluminum to cover 1 mm distance (Appendix VII.h) at thermal velocity of $\sim 7.7 \times 10^{-4}$ cm/s. As a result, with approximately a quarter microsecond PI pulse delay, it can ionize neutrals as close as quarter millimeter away from the sample which was experimentally proven to be practical.

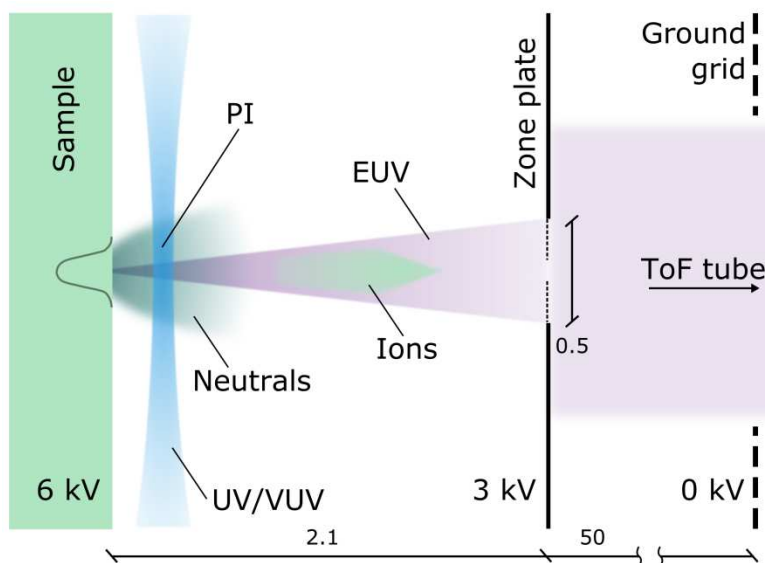


Figure II.18: Post-ablation ionization mode of EUV TOF for solid samples. The UV or VUV beam from the YAG laser intersects with neutrals that are the majority of the EUV ablation plume. PI ions are accelerated toward TOF tube optimized for their detection. EUV-created ions also get to the detector, and due to ~ 260 ns delay of YAG pulse they do it faster. But since reflectron in TOF is optimized for PI ion packs compression, EUV peaks appear with lower mass resolution as Figure II.20 shows.

As it was shown on the example of propene, VUV light is preferential for SPI ionization of organic molecules, although it is not the case for atomic or small molecular species. If the ionization energy of an atom or small molecule does not require absorption of more than two UV photons for ionization, then this MPI process is highly probable. Two most prominent advantages of using intense UV laser for the analysis of solid samples with PI are: a) increasing the signal yield by probing into more abundant neutral species in the initial plasma plume, and b) increasing atomic signal fraction by extra heating and fragmentation in the plasma.

To demonstrate these effects we chose a sample with diluted uranium in it. The sample is a yellow optical filter glass (Figure II.19) obtained by addition of colorant into the glass matrix in the form of depleted uranium oxide which typically produces lemon yellow to green colors depending on concentration. The measured content of the uranium in the tested sample is 9.26 ± 0.82 % by weight. The procedure was performed at PNNL via dissolution, addition of a standard spike, and then thermal ionization mass spectrometry (TIMS) measurement.

The sample was initially ablated with full power of ~ 10 μJ EUV laser and then post-ionized with 20 mJ of UV laser. UV beam energy is measured by PowerMax5100 laser power meter from Molectron®, to which the beam was redirected by 45° tilted laser-line mirror placed in front of the tripling cell. The spectrum on Figure II.20 shows single and double ionized uranium and single ionized U oxides. Some background contaminant signal in the form of Ce and CeO was also detected. In the UV PI mode (bottom spectrum), the intensity of U-related single ionized components increased ~ 3 times revealing UO_2 peak. The analysis of total U-associated counts showed an increase of sensitivity by 2.5 times when using UV PI mode. It can be further improved by implementing more damage resistant optics than OAP mirror. Table II.6

compares U and its oxides secondary ion counts and yield showing that despite higher sensitivity in terms of detected species the MPI is much less efficient compared to SPI.



Figure II.19: Back view (opposite to EUV laser) of U filter glass sample mounted in the sample holder. Glass was coated with ~30 nm of Al to provide surface conductivity. Al layer was then electrically connected to ITO-coated glass slide with conductive copper tape on both sides.

Table II.6: UV PI secondary ion count of U peaks is 2.5 times higher compared to EUV-only ablation and ionization. However, secondary ion yield is much smaller due to low efficiency of the MPI process.

Method	Sample	Peaks	Secondary ion counts	Photons	Primary photons number	Secondary ion yield	Comments
UV PI	Uranium filter glass with 30 nm aluminum	U+UO+UO ₂	12619	3.5 eV	3.6e16	1.1e-14	16-shot averaged spectrum
EUV		U+UO	5063	26.4 eV	3e9	1.7e-6	

Vacuum ultraviolet post-ablation ionization (VUV PI) technique is exceptionally well suited for the analysis of molecules, especially organic. But the advantages of soft VUV single-photon ionization are also clearly seen on inorganic molecules on the examples of GaAs crystal (Figure II.21) and CdTe film (Figure II.36) described in mass calibration paragraph *e.i.*

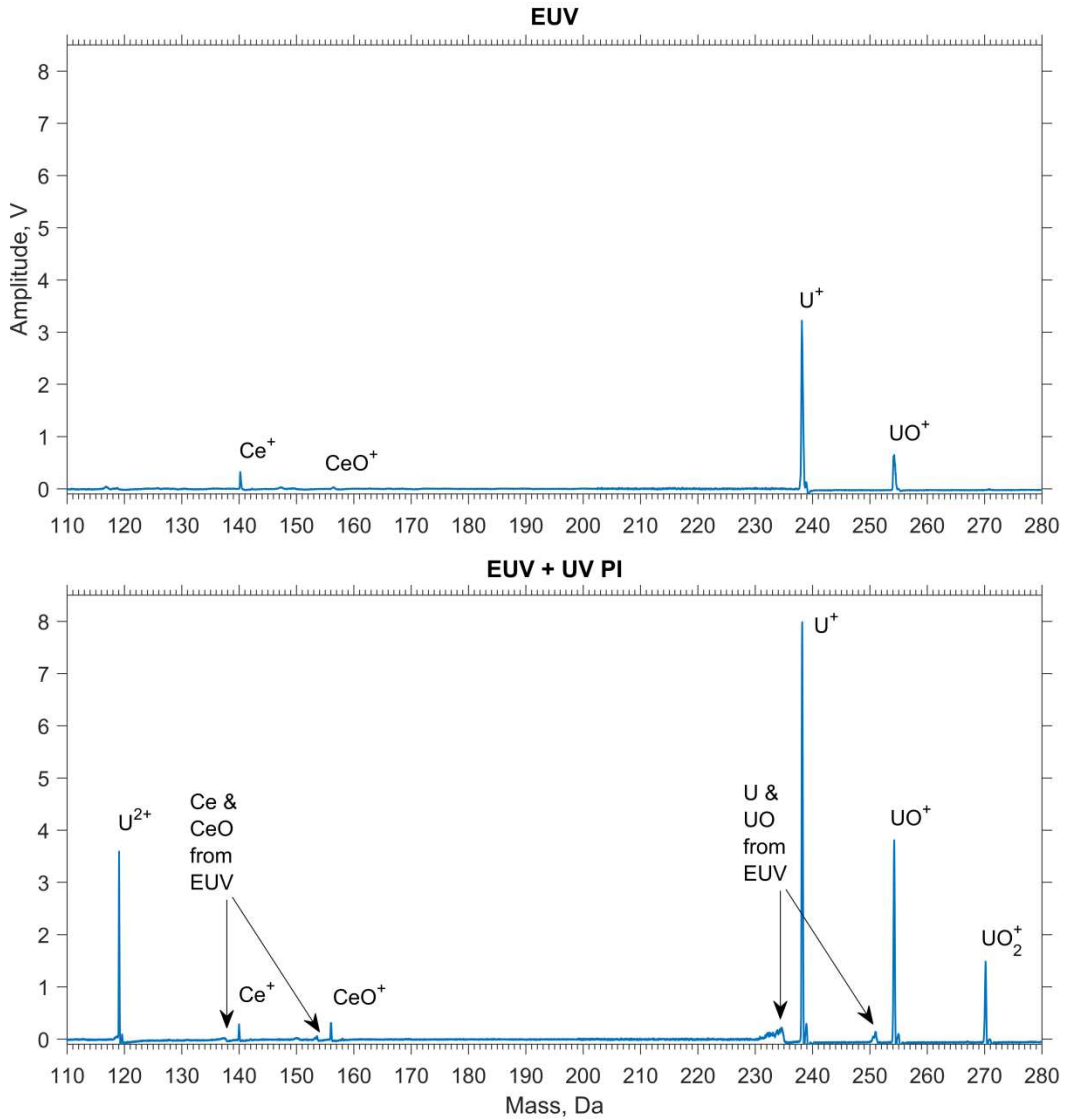


Figure II.20: Comparison of U filter glass mass spectra obtained by direct EUV laser ionization (top) and UV laser post-ionization (bottom). UV PI reveals U double-ionized and UO₂ peaks. Depleted uranium in the glass contains mostly 238.03 Da isotope of ²³⁸U.

Post-ablation, post-sputtering or post-ionization is an emerging technique²³ and thus starts to be utilized in material studies with tunable PI sources like synchrotron^{22,24,25}. In a fundamental work by Takahashi et al.²² the photoionization energy (PIE) threshold of As, As₂, and Au clusters of n=1÷4 were studied. They used SIMS equipped with Bi_{1÷3} primary ion source to sputter the sample, and synchrotron with VUV range in 7.5÷25 eV to photoionize neutrals in

the sputtered plume of material. By varying the VUV wavelength they were able to observe the onset of the PIE curve and thus determine the PIE threshold. Results matched theoretical studies.

Since the EUV TOF system is equipped with a 10.5 eV VUV source, we could only compare our results in terms of useful signal yield to the same synchrotron energy of SIMS TOF PI. As Table II.7 and Figure II.21 show, As_2^+ signal appeared both in EUV and VUV PI modes of EUV TOF, unlike in SIMS-only and SIMS+PI modes of the aforementioned study. Interestingly, VUV PI secondary ion yields of As_2^+ in PI mode of both systems appear to be very close, $\sim 1e-9$. This is an encouraging discovery showing that much less resource-demanding systems like EUV TOF can sometimes provide similar results compared to more sophisticated synchrotron-based systems. It is also notable that SIMS without PI barely contributes to the detection of As_2 ions²², whilst EUV laser ablation does it seamlessly even without PI as shown on Figure II.21.f. But as was mentioned earlier, both systems in PI mode suffer lower yield – a common drawback for the option to detect more pronounced molecular signal.

Table II.7: Yields of As_2^+ signal of EUV TOF VUV PI and SIMS TOF PI. In the PI mode both instruments demonstrate similar yield indicating high potential of significantly more compact EUV TOF.

Method	Sample	Peak	Secondary ion counts	Photon/ion type	Primary photon/ion number	Secondary ion yield	Comments
VUV PI	GaAs crystal	As_2	412	10.5 eV	6e11	6.9e-10	10-shot averaged spectrum
SIMS PI			5e4		3.5e13	1.4e-9	Takahashi 2009 ²²
EUV			121	26.4 eV	8.1e8	1.5e-7	10-shot averaged spectrum
SIMS			5.6e3	5 μm Bi_3^+	2e8	2.8e-5	Takahashi 2009 ²²

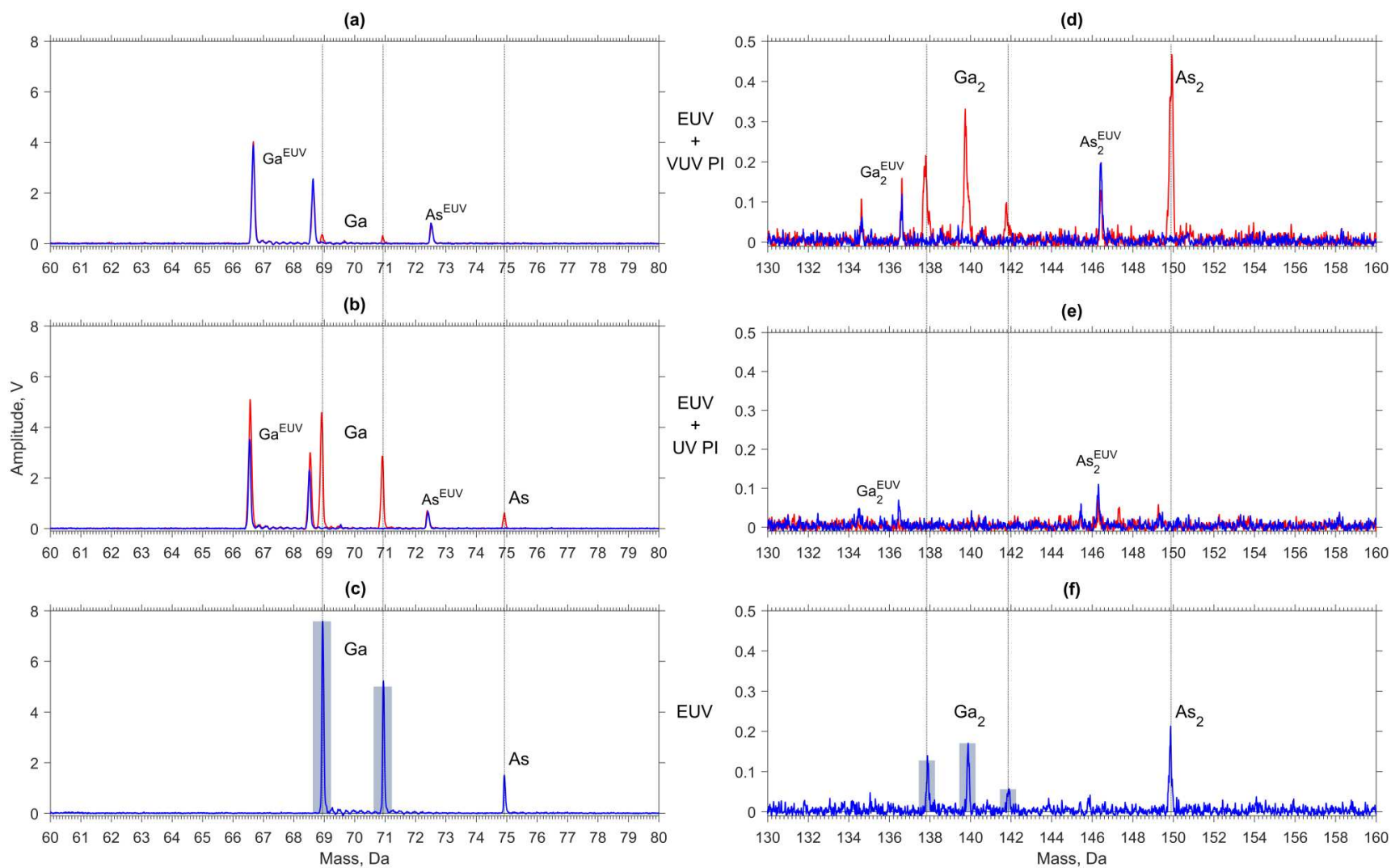


Figure II.21: GaAs crystal mass spectra in VUV PI (a,d), UV PI (b,e) and EUV-only (c,f) modes. In contrast to UV PI, only VUV PI reveals molecular signal of Ga_2 and As_2 (d,e), while UV PI nicely shows their elemental counterparts (b). On EUV spectra (c,f) semi-transparent bars indicate natural isotope abundance of Ga_1 and Ga_2 .

II.c EUV TOF comparison to SIMS TOF

Secondary ion mass spectrometry (SIMS) is considered to be one of the most accurate commercially available tools for study of organic and inorganic systems. SIMS allows imaging at nanoscale spatial or depth resolutions without external labelling of large class of compounds typically of the mass of <1 kDa. This brings SIMS TOF in direct competition with the EUV TOF approach. However, there are few aspects of SIMS that cause limitations compared to laser ablation techniques with single photon ionization capability like EUV TOF. In the current section these limitations will be discussed together with comparison of key performance parameters of both systems: spatial resolution, mass resolution and sensitivity.

II.c.i Static SIMS mode for molecular analysis

SIMS uses a focused primary ion beam for sputtering and ionization of the solid sample. Primary ions of typically tens of keV energy induce a collision cascade in the upper layers of the sample resulting in emission of surface atoms and molecules that partially bear a charge, i.e. secondary ions. The key parameter for this process is sputter yield Y – the ratio of removed atomic and molecular ions to the primary particles influx. In mass spectrometry only ionized portion of the sputtered species gets analyzed, hence in SIMS the useful yield is defined as:

$$Y = \frac{N_s}{N_p} \quad (\text{II.5})$$

Where N_s – number of detected secondary ions and N_p – number of primary ions in the sputter beam. Yield significantly varies between $1e-1 \div 1e-6$ and beyond as a function of primary ions type, energy, focal spot diameter, dose, as well as sample composition and the desired signal for monitoring. SIMS provides impressive sensitivity in the analysis of atomic elements.

However, the complex and destructive sputtering mechanism causes inevitable chemical damage and molecular fragmentation. In organic compounds, some molecules break down to smaller constituents, some get fully removed, ionized and detected. It is known that using cluster ions of heavy elements like gold (Au_3^+) or bismuth (Bi_3^+) in the primary beam reduces fragmentation. Smaller elements like carbon and argon achieve the same goal by forming bigger clusters – C_{60}^+ , Ar_{1500}^+ . In clusters, the energy of each projectile is equally divided between the atomic constituents causing a shallower penetration into the sample compared to single primary ions of the same species. The collective impact of many low-energy projectiles leads to surface localization of the sputtering and evens out the energy distribution to the analyte molecules resulting in a higher molecular signal yield and depth resolution. Polyatomic projectiles increase secondary molecular ion yield up to three orders of magnitude from typical $1\text{e-}4$ value^{12,26}. Although the primary ion dose density (PIDD) of any type and energy of ions is still a major factor in controlling fragmentation. PIDD is defined as follows:

$$PIDD = \frac{I_p t}{Ae} \quad (\text{II.6})$$

Where I_p – primary ion current, t – time, A – impact area, e – elemental charge. In order for SIMS to be able to detect ample molecular signal, it has to operate in the so-called static limit condition, i.e. when $PIDD \leq 1\text{e}13$ ions/ cm^2 . This is a general guidance that is again extremely sample- and experimental conditions-dependent. The explanation of static limit can be simplified to a model in Figure II.22.

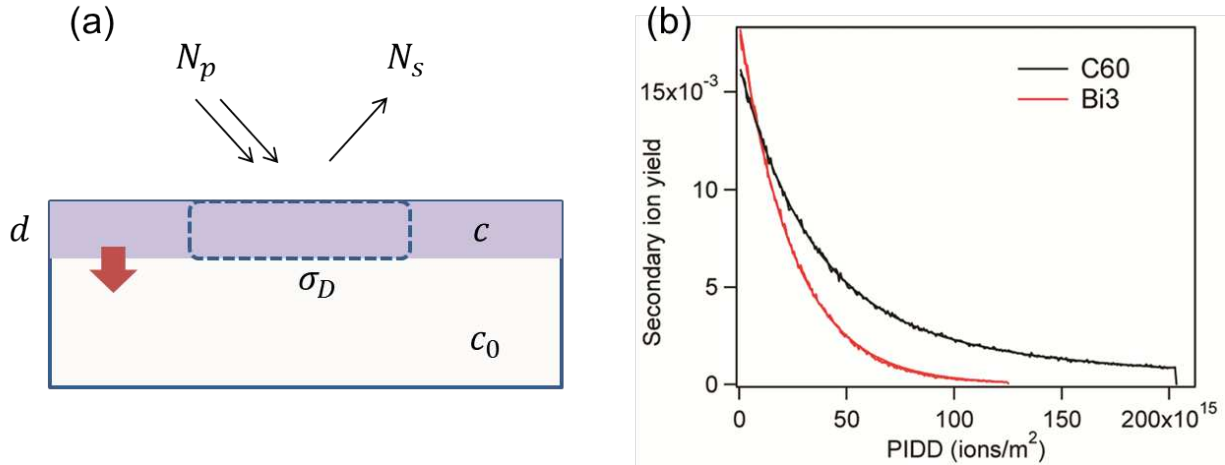


Figure II.22: Static ion dose limit for molecular detection in organic samples with SIMS. (a) Model of the damaged layer propagation during sputtering of a sample with primary ions N_p . c_0 and c – natural and modified concentration of intact molecular species in the bulk sample and in the surface layer of thickness d . σ_D is a disappearance cross section that links c and resulting secondary ion signal N_s . With continuous erosion the damaged layer increases in thickness resulting in smaller signal yield as depicted on (b) – exponential decay of m/z 184 ion of POPC bilayer (headgroup structure) as a function of accumulated $PIDD$ during the analysis with Bi_3^+ or C_{60}^+ primary ion beams²⁷. Heavier polyatomic projectiles induce less chemical damage. The static limit for SIMS TOF analysis refers to operation at $PIDD$ at which secondary ion yield is kept at maximum due to interaction of primary ions only with unaltered surface.

When primary ions N_p interact with a sample that has c_0 concentration of intact molecules, they induce fragmentation in the surface layer of depth d that now has reduced concentration of unfragmented molecules c . As primary ion dose increases, depth of the altered layer does the same accompanied with the surface layer erosion that is the source of secondary ions N_s . The dynamics of the whole process is extremely complex, although it can be simplified and experimentally verified to be represented by an exponential decay of the useful yield under prolonged bombardment²⁸:

$$Y = Y_0 e^{-\sigma_D * PIDD} \quad (II.7)$$

Where Y_0 – useful yield at the beginning of erosion and σ_D – disappearance cross section. The static limit is essentially a primary ion dose that allows keeping yield at Y_0 value by letting each subsequent ion interact with only fresh spot on the surface of the sample. This is often the

case²⁹ for the *PIDD* of $\sim 1e13$ ions/cm². The static limit is not a universal parameter and it heavily depends on primary ion type, energy, type of secondary ions under investigation etc. After the first monolayer is sputtered, the static limit equals to $1/\sigma_D$. In the case where *PIDD* is much greater than that, the erosion is performed under dynamic sputtering condition which is often used in elemental analysis.

The main limitation of staying within the static limit restricts SIMS attainable lateral resolution, empirically defined as the size of an area, from where 4 secondary ion counts are collected^{27,29}. In our system, as will be shown later, we need to collect at least 40 counts per shot to be able to perform single-pixel imaging due to lower signal-to-noise ratio defined by poor detector performance. For SIMS the useful lateral resolution can be calculated as:

$$\Delta L = \sqrt{\frac{N_S \sigma_D}{Y}} \quad (\text{II.8})$$

Where $N_S = 4$ – empirically defined lower limit of ion counts from a single pixel. Increase of *PIDD* often limits the attainable resolution as binning of a few pixels may be required to add up secondary molecular ion counts. Typical values of lateral resolution can be deduced from the probe beam diameter listed in several yield comparison tables in the Biological applications of the system section.

II.c.ii Mass and spatial resolutions

SIMS TOF utilizes a pulsed primary ion beam for analysis in order to keep the primary ion dose below the static limit and to form a pulsed secondary ion beam for convenient differentiation in the time-of-flight mass analyzer. The key characteristic of the TOF mass spectrometer is mass resolution:

$$R = \frac{t}{\Delta t} = \frac{m}{\Delta m} \quad (\text{II.9})$$

Where t and m – time or mass of the signal peak and Δt and Δm – their corresponding full width at half maximum (FWHM). Mass resolution of the EUV TOF was calculated using Au clusters peaks. The spectra shown in Figure II.23 were obtained by averaging of few tens of shots on ~50 nm Au film. Each peak was then analyzed and corresponding result was plotted. Resolution of 1100 results in acceptable ~0.1 Da detection precision for masses up to 1 kDa.

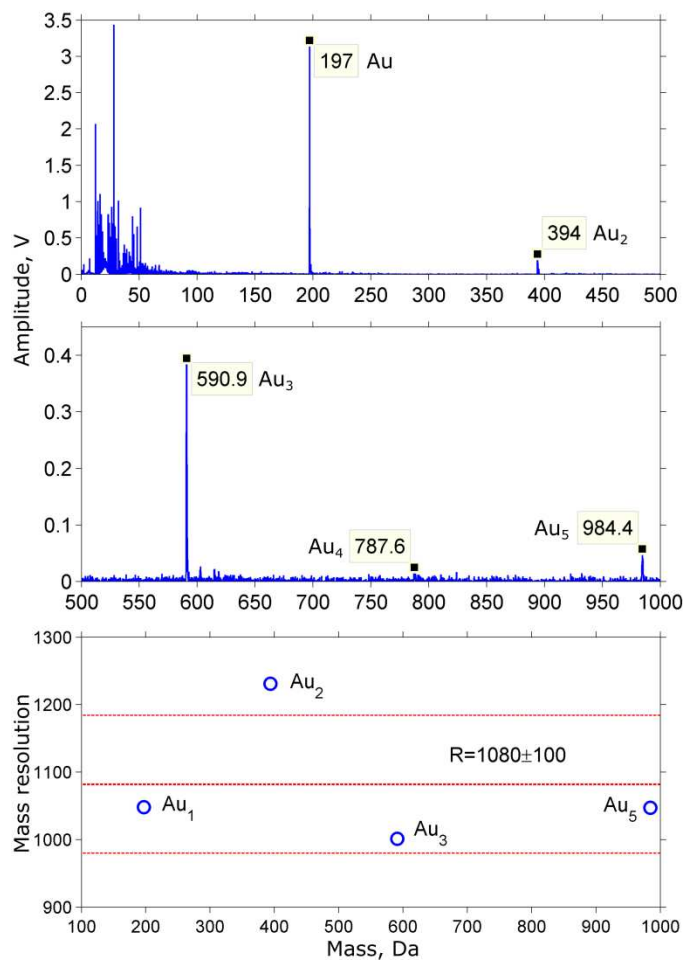


Figure II.23: Mass resolution assessment of the EUV TOF MS on the example of Au clusters at 6 keV.

The mass resolution of SIMS TOF depends on the primary ion beam configuration as shown on Figure II.24. Ion bunches with the same number of primary ions can be focused tighter

to achieve higher spatial resolution needed for 2D imaging. Also they can be defocused resulting in worse spatial resolution but higher depth resolution for 1D imaging: in such configuration ions interact mostly with upper layers of the surface. In the time domain high spatial resolution is obtained with $\Delta t_1^{2D} > \Delta t_1^{1D}$ compared to high depth resolution mode. The resultant time stretch of the secondary ions is assumed to be equal to the primary ones, $\Delta t_2 = \Delta t_1$, hence for longer primary ion pulses mass resolution is worse because it is inversely proportional to the width of the detected signal peaks.

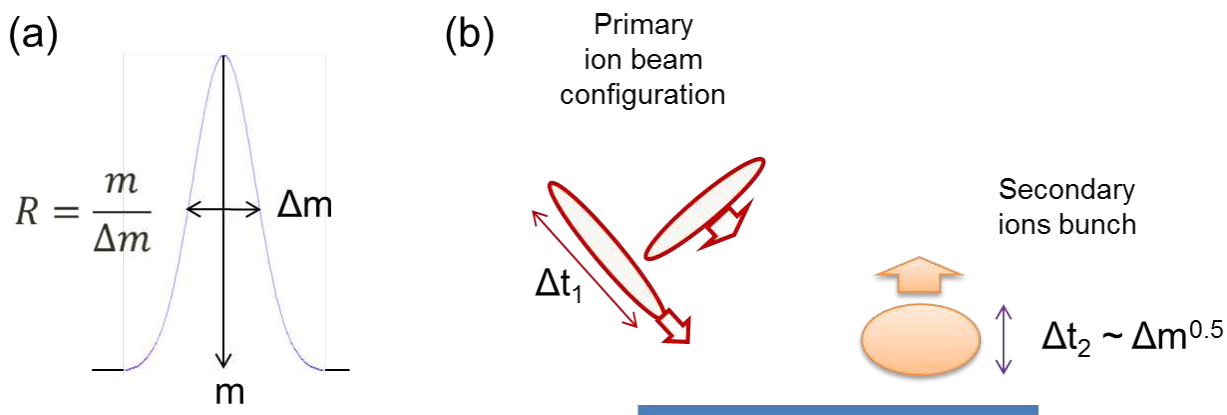


Figure II.24: Dependence of mass resolution on spatial resolution in SIMS TOF. (a) Mass resolution is defined as the ratio of mass of the signal peak in mass spectrum to its FWHM. (b) Secondary ions that form the mass spectrum inherit the temporal profile of the primary ion bunches that can be focused (longer pulse) for higher spatial resolution imaging and defocused (shorter pulse) for higher depth profiling resolution. Inverse dependence of the mass resolution on the pulse duration means that in the former case it is worse than in the latter.

In conjunction with the static limit it is worth to note that the primary ion beam configured for high spatial resolution leads to local *PIDD* increase resulting in possibly lower useful molecular signal yield. Instrumentation-wise it is also harder to focus polyatomic ion beams to small spots due to the nature of their formation from gaseous source. Although recently C_{60}^+ beam was focused to 300 nm spot^2 by placing $20 \text{ }\mu\text{m}$ aperture near the ion source that allowed to image antibiotic distribution at subcellular level of *E.coli*. However, lower ion yield

from reduced number of primary ions in the bunch required accumulation of signal for several milliseconds on a 400 nm deep voxel.

The drawback of the pulsed beam approach is that it is virtually impossible to provide simultaneous high spatial and depth resolution in SIMS TOF. A possible solution is using a CW primary ion beam and pulse secondary ions in a separate arrangement in between source and TOF tube³⁰. This approach also saves a lot of acquisition time by rising the duty cycle by ~4 orders of magnitude, but it needs further development and commercialization.

Typical mass resolution of SIMS TOF utilizing Bi_3^+ 30 keV primary ion beam focused to 5 μm is 1.1e4 as shown on Figure II.25. At a mass resolution of 1.1e3 – similar to EUV TOF – the beam diameter is expected to be 1.6 μm . This is significantly larger than the ~100 nm focal spot diameter of the 46.9 nm EUV laser that yields ample molecular alanine signal¹¹. In case of EUV TOF the mass resolution depends only on laser pulse duration and extraction efficiency, so the only limiting factor to high resolution 3D imaging is the sensitivity of the detection system³ and/or ionization efficiency.

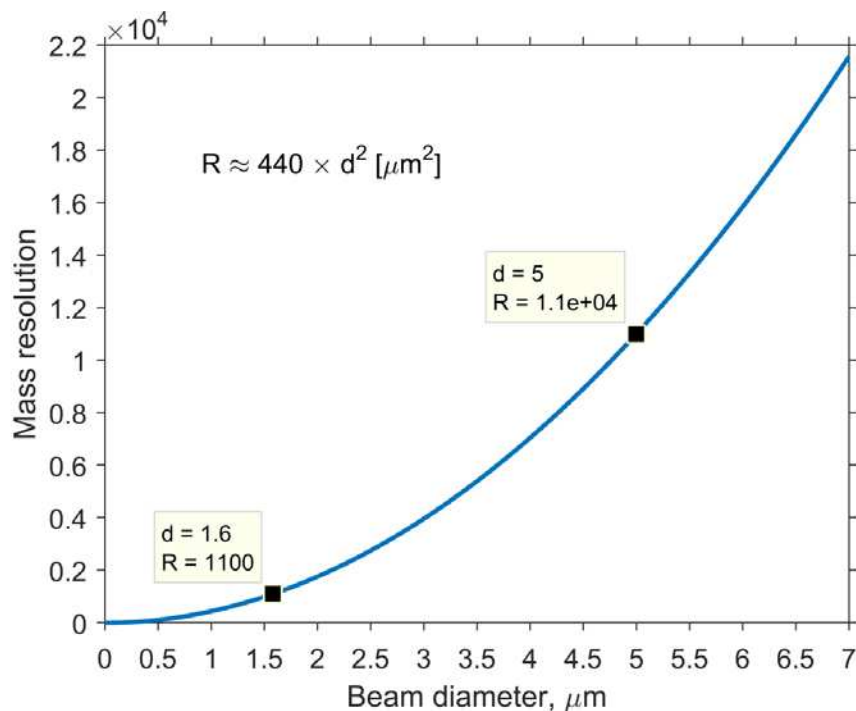


Figure II.25: Mass resolution of a typical SIMS TOF as a function of probe beam diameter. At similar mass resolution to the EUV TOF, the ion beam needs to be focused to 1.6 μm . At the standard 5 μm beam diameter, the resolution is as high as 1.1e4.

II.c.iii Sensitivity

Sensitivity is an important parameter for imaging mass spectrometers as it affects the attainable imaging resolution for composition mapping. Low sensitivity means that more material has to be probed resulting in bigger pixels/voxels composing an image. The sensitivity of EUV TOF and SIMS TOF was assessed using organic and inorganic samples. For the analysis of organic samples, a ~ 100 nm pure aminoacid alanine layer was deposited by thermal evaporation onto ITO slide¹¹. For inorganic samples a NIST 610 calibration standard of ~ 500 $\mu\text{g/g}$ of U and Th in the glass matrix was used³.

The approach for calculating sensitivity in research areas differs. We have developed an approach that defines sensitivity S as the amount of ablated substance in moles resulting in single secondary ion count:

$$S = \frac{\nu}{N_s} \quad (\text{II.10})$$

Where ν – amount of substance removed (ablated or sputtered) from the probed volume of the sample (crater or erosion track), N_s – integrated number of secondary ion counts from the mass spectrum peak. ν is calculated by first measuring the topography of the ablated sample crater by atomic force microscope (AFM) and then converting the crater volume to the amount of substance using the density and molar mass which for alanine are 1.424 g/cm³ and 89.09 g/mol (Da) respectively. Both the amount of substance and ion counts were averaged across ~20 craters/shots. A typical crater involved in the calculation of sensitivity is shown in Figure II.26.a. SIMS at standard operating conditions is set to raster a 150×150 μm² area using 30 keV Bi₃⁺ probe beam focused to Ø5 μm. The depth of the active erosion was obtained from the TRIM® modeling of a 10 keV Bi⁺ beam sputtering of the pure carbon layer. As Figure II.26.b shows, even though collision cascading and ion implantation happens at a depth down to 10 nm, most of the displaced target atoms represented by the orange palette are localized within first 2 nm of the sample. Most likely from here the sputtered secondary ions originate prevalently. In contrast, ablation crater shows lack of damage of material beyond, because it has a smooth Gaussian shape without extra topographical features introduced.

Based on these assumptions and the integrated molecular alanine peaks from corresponding spectra shown in Figure II.27, the sensitivity of EUV TOF is 0.023 amol and ~20× bigger compared 0.41 amol of that of SIMS TOF. It is twice smaller than was published before¹¹ because after publication the exact MCP sensitivity was measured: 18.5 mV per count

rather than conservative value of 8 mV from a specified 8÷80 mV range. With further look at Table II.8, it is interesting to note that pure ion yield, as calculated versus number of primary particles – EUV photons or Bi_3^+ ions, is exactly three orders of magnitude better for SIMS. This only tells about the difference of ablation and sputtering mechanisms resulting in removal of analyte molecules and their ionization. This is the easiest parameter to calculate though because it does not require laborious AFM measurement of the resultant sample topography. In the previous section such comparison by secondary ion yield was already done routinely, so one should bear in mind that ~2 orders of magnitude difference in yield in favor of SIMS actually indicates similar sensitivity of both systems. For example, Table II.7 states that signal yield for As_2^+ is $1.5\text{e-}7$ for EUV TOF and $2.8\text{e-}5$ for SIMS TOF. This is two orders of magnitude difference in favor of SIMS, but same sensitivity based on the alanine experiment.

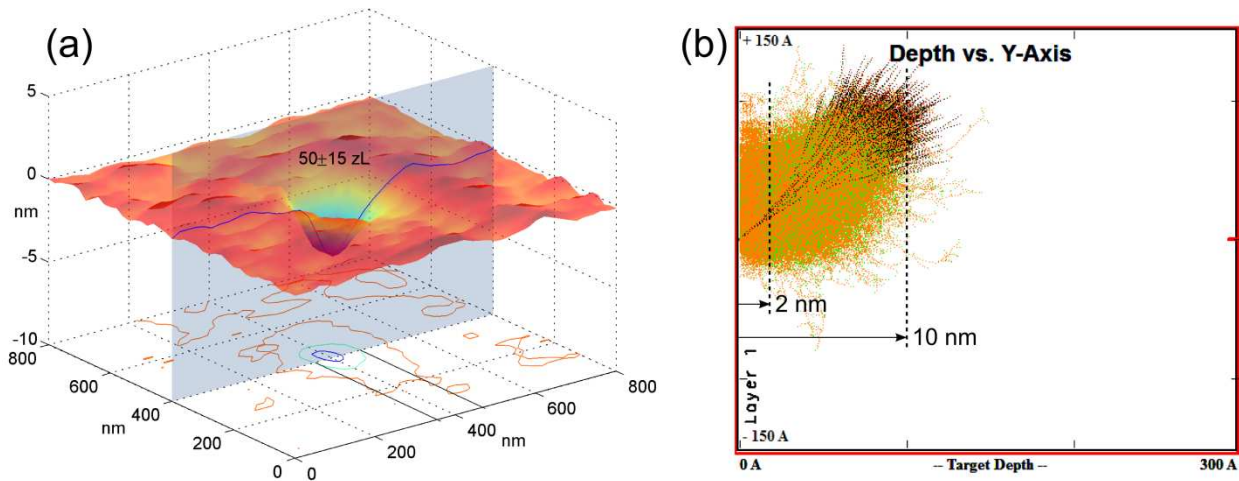


Figure II.26: (a) AFM image of the 50 zL crater in PMMA resist obtained at same conditions as on alanine with single laser shot. FWHM diameter is 120 nm, depth is 3.5 nm. Crater profile indicated by blue line fits well the Gaussian function. (b) TRIM model of $1\text{e}3$ ions of 10 keV Bi^+ sputtering of solid carbon target at 45° . Orange lines represent displaced target atom trajectories mostly within top 2 nm of the surface. Green dots are the end of displaced atoms trajectories, black lines – primary ion trajectories. Cascading happens within 10 nm of the surface that attributes to chemical damage of the sample.

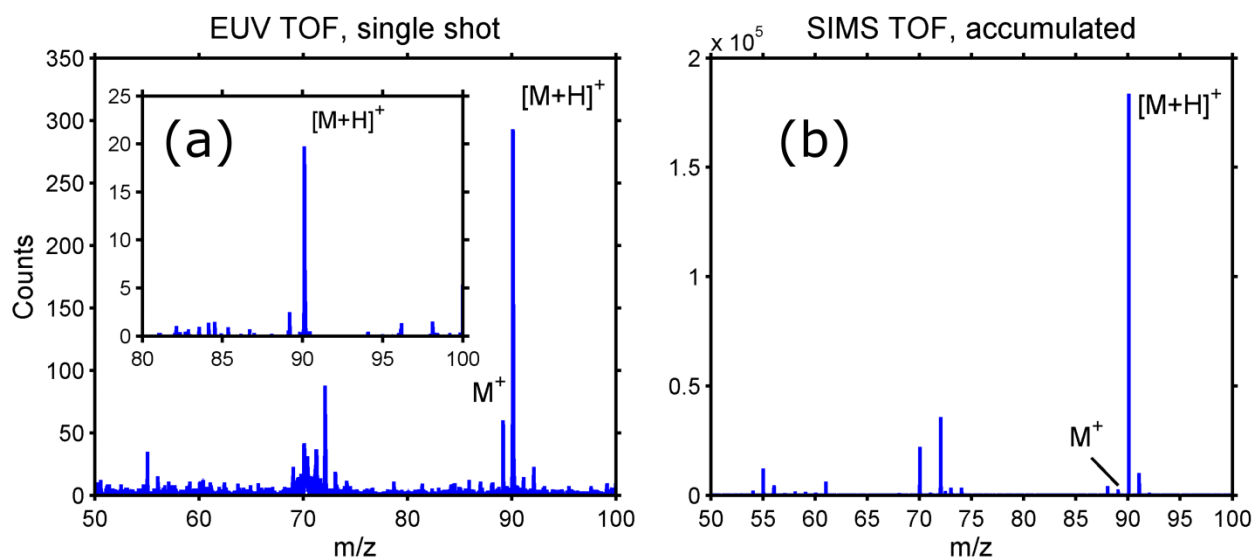


Figure II.27: Mass spectra of ~100 nm alanine layer obtained in three systems: (a) EUV TOF and (b) SIMS TOF. The spectrum in (a) was collected from 12.8 aL crater while the inset represents spectrum from the 50 zL one.

Table II.8: Parameters for sensitivity calculation.

Parameter	EUV	SIMS
Primary particles, N_p	3.9e6	2.05e8
Secondary ion counts, N_s	35	1.76e6
Yield, $Y=N_s/N_p$	9e-6	8.6e-3
Crater area at FWHM, μm^2	0.011	2.25e4
Crater depth, μm	3.5e-3	2e-3
Crater volume, $V, \mu\text{m}^3$ (aL)	4e-5 (0.04)	45 (4.5e4)
Amount of substance in crater, v, amol	0.8	7.19e5
Removed molecules from crater, N_r	4.82e5	4.33e11
Sensitivity, $S, \text{amol}/N_s$	0.023	0.41
Normalized to volume yield, $Y/V, \text{L}^{-1}$	2.25e14	1.9e11
Sample utilization efficiency (SUE), N_s/N_r	7.3e-5	4.1e-6

The sensitivity experiment on the alanine sample was repeated at several EUV laser beam energies. Figure II.28 shows that sensitivity deviates from a linear behavior as the laser fluence diminishes resulting in about twice higher sensitivity than would be expected at the given pulse

energy. Such occurrence is a possible consequence from lower fragmentation at low laser fluences and more efficient ion extraction from the ablation plume due to reduced recombination.

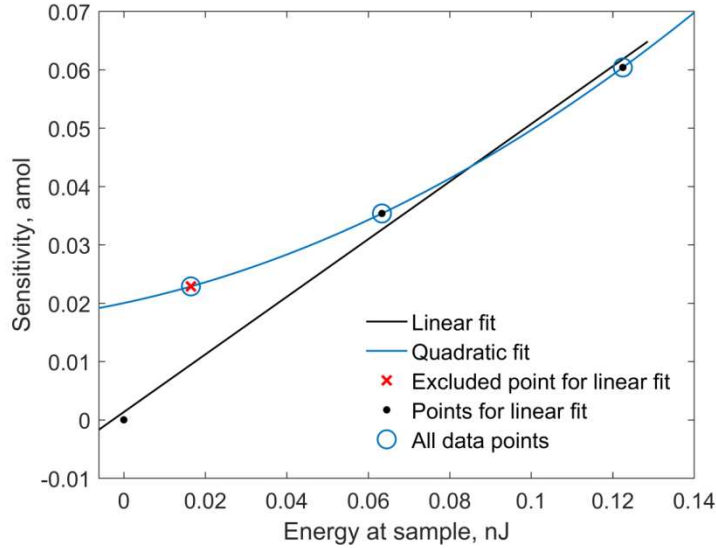


Figure II.28: Sensitivity dependence on EUV laser energy. Three experimental points fit quadratic function. It deviates from linear function obtained by excluding a data point at 0.02 nJ energy at which crater of 50 zL volume forms in PMMA. Other points were obtained from 0.62 and 2 aL volumes.

In analytical atomic spectroscopy different approach is used to assess sensitivity. It is called sample utilization efficiency (SUE) defined as:

$$SUE = \frac{N_s}{N_r} \quad (\text{II.11})$$

Where N_s – secondary ion counts and N_r – number of total removed atoms or molecules from the sample. Here the number of atoms/molecules is used instead of the amount of removed substance molecules as in equation II.10. As shown in Table II.8 and in Figure II.28 and Figure II.29, the variation of the SUE is inverse to the sensitivity S obtained for alanine.

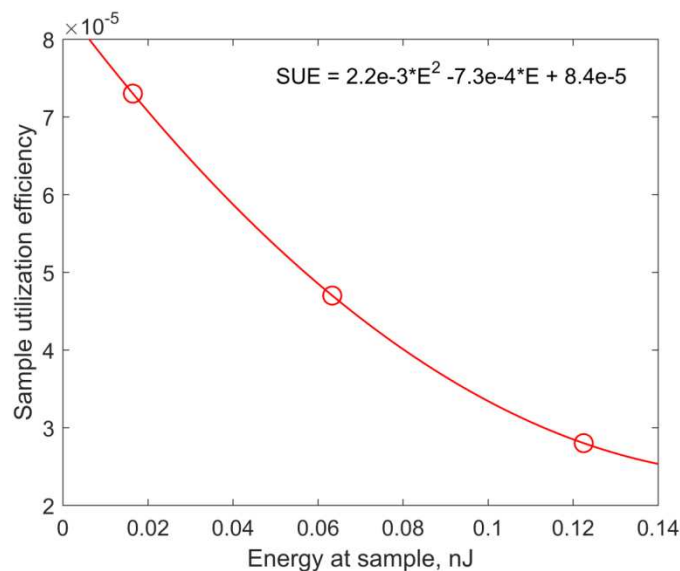


Figure II.29: Sample utilization efficiency (SUE) of alanine calculated using same data obtained with EUV TOF and used for calculation of sensitivity S .

SUE was used to evaluate the sensitivity of EUV TOF to trace element detection in comparison to SIMS TOF. Figure II.30 shows average spectra of NIST 610 glass (~500 ppm of U and Th) in which the U, Th, and their oxide ion peaks are identified³. SUE of trace elements showed excellent linearity as a function of laser energy rendering suitable performance of EUV TOF in the field of atomic trace spectrometry especially in the area of nuclear forensics. It also has advantage over SIMS in showing less molecular interferences in the spectrum, i.e. cleaner baseline that well segregates useful signal from unknown fragmentation. Similar SUE of 0.014% was measured on EUV and SIMS TOF. This is 10× worse performance of EUV TOF as compared to alanine data at higher than 0.02 nJ beam energies. But sensitivity in general varies from sample to sample even at similar experimental conditions – this is well-studied phenomena in SIMS TOF. What is important is that overall EUV TOF performs similarly or better to the technique that has been under development for over 30 years.

Both sensitivity and SUE were calculated using averaged data sets without correction to noise level of the detection system. It means that these parameters should be treated with caution with respect to imaging capabilities of the system. Actual detector performance in terms of signal-to-noise ratio will affect attainable resolution in single shot operation for imaging. More on this matter will be shown in the section *IV.c*.

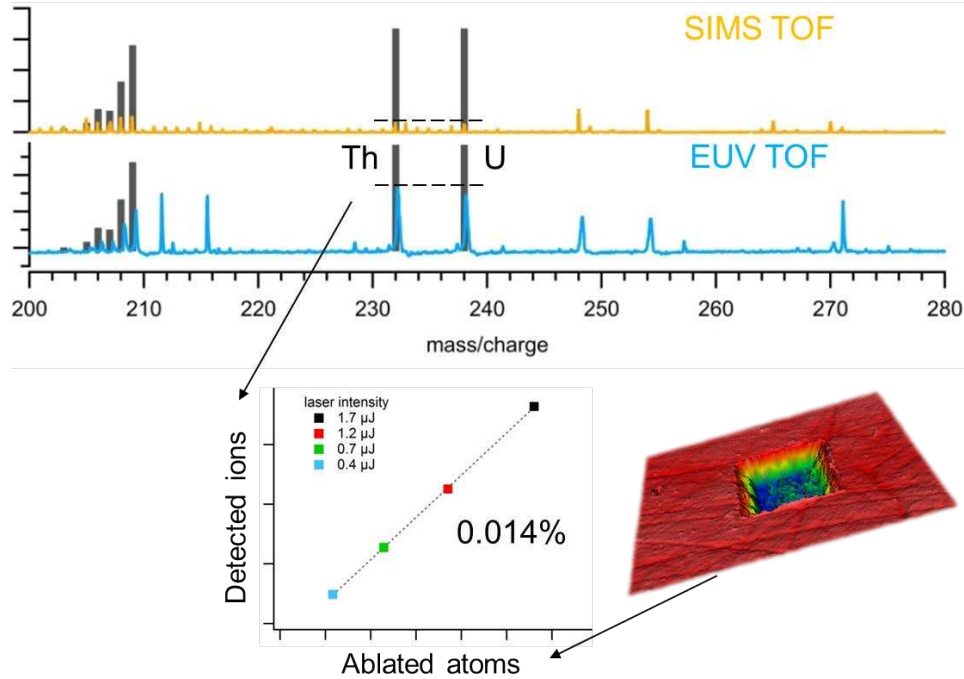


Figure II.30: Averaged mass spectra of NIST 610 calibration standard revealing U and Th ion peaks at ~500 ppm concentration in the glass matrix. 0.014% ratio of detected ions to ablated atoms as measured on $10 \times 10 \mu\text{m}^2$ craters does not depend on EUV laser energy. Same SUE was obtained on SIMS. In EUV supercrater was made by overlapping individual craters: 20×20 array was printed with $0.5 \mu\text{m}$ steps in between and with 3 shots per pixel. Resultant square pocket was measured with white light interferometer as shown. In SIMS supercraters were made separately from the analyzed area by increasing probe beam current $10 \times$ with otherwise same conditions. With the assumption that the crater depth is proportional to the current, profilometry acquired depth was scaled back 10 times.

II.d Operation

Key aspects related to the operation of the EUV TOF IMS are given in this section. Main classes of components of the vacuum system and their interplay are discussed. The timing

scheme that orchestrates the symphony of pulsed events like laser light generation, ions detection and triggering of auxiliary equipment is explained. Strategies for beam energy control and sample handling depending on the sample type are presented.

II.d.i Vacuum

Operation of the EUV TOF IMS is impossible without establishing proper vacuum conditions and necessary gas supplies. High vacuum is required for efficient EUV laser propagation, ion transmission, surfaces cleanliness and MCP detector operation. The most convenient way to achieve high vacuum is by using turbomolecular pumps in conjunction with oil-free scroll pumps. Without strict vibrations or excessive gas load requirements this combination allows rather quick startup and shutdown – within about half an hour. High vacuum of less than $1e-7$ Torr is achieved during overnight pumping after sample and TOF chambers exposure to atmosphere for sample loading.

Vacuum measurements are done with a set of gauges: membrane baratron, thermocouple, ionization/combination, and diaphragm. They are placed in locations where differential pumping provided by four apertures defines the corresponding vacuum reading need. Differential pumping allows for gradual improvement of vacuum through each compartment isolated by the apertures from 0.3 Torr in the capillary to $<1e-7$ Torr in the TOF tube.

Gas supply to capillary, attenuation and tripling cells is facilitated by a set of needle and shut-off valves for convenient flow control. A set of gate valves isolate chambers allowing for separate pumping of them and even bypassing through parallel vacuum conduits. Special safety measures were employed on the laser side of the vacuum system. An automatic shut-off valve and oil collection reservoir prior to immediately connected pump were introduced since the

capillary is under high pressure, and current and temperature loads may suddenly disintegrate it and release surrounding cooling oil.

Mixing of gases at high pressure for gas phase experiment, i.e. He and propene mixture, can be facilitated in the reservoir attached to corresponding tanks on the post-ionization setup side of the instrument. With proper directions via designed tubing He can also be diverted into the main chambers for venting along with usually used ultra-high purity nitrogen for this purpose. Prepared mixtures can be released primarily into the sample chamber and also into the tripling cell if Xe:Ar pre-mixed tank expires.

A tabulated procedure must be exercised each time during pumping, venting or other adjustments in the vacuum system. High-speed and precisely manufactured turbo pumps are subject to failure when abruptly exposed to high pressures especially of that of heavy gases like xenon. They may also critically fail by detaching from the mounting flange and destroying equipment around with a lot of kinetic energy stored in them at full 3×10^4 rpm speed. Detailed instructions are grouped in Appendix VII.i for every standard laboratory situation, although one should refer to a common sense, understanding of vacuum equipment working principles and safety guidelines each time when working with vacuum sub-system of the EUV TOF.

II.d.ii Timing

All system processes are synchronized via three delay generators DG1÷3 as shown on Figure II.31. Firing execution is done via operator's action ($T = 0$) or programmatically in the LabView environment that is used for large data arrays collection and for imaging. DG1 splits the pulse into the Nd:YAG and EUV lasers, while the exact laser timings is facilitated by DG2 in case of EUV and by DG3 in case of the YAG laser. A current pulse in the EUV capillary laser

measured by Rogowski coil surrounding the capillary has <1 ns jitter to the emerging light pulse. Hence it is often used for triggering external events like MCP pulsing and oscilloscope/digitizer spectra collection initiation. When the EUV laser intensity is high enough, an inline detector may replace the Rogowski coil because its main signal becomes well distinguished among the pronounced plasma background (Appendix VII.j). For the gas phase mass spectrometry only one light source is used at a time. Bypassing of EUV laser is thus required for sole YAG laser operation and triggering of associated events as shown by dashed lines on the diagram of Figure II.31.

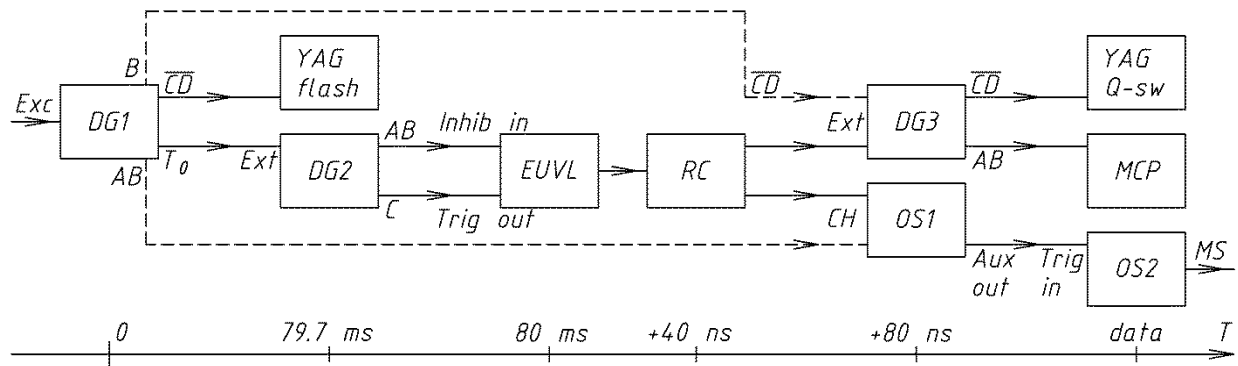


Figure II.31: Timing diagram of synchronization pattern of all related events that generate and collect the mass spectra. Description of each block acronym and its precise setting for every operational mode is listed in the Appendix VII.j. The time scale shown below the diagram describes the flow of events as followed by the lower set of components.

II.d.iii Beam energy control

The laser fluence delivered to the sample for ablation has to be tailored to specific experimental need and measured. Fluence variation can be done by two means: defocusing of the zone plate³¹ or by attenuation of the beam itself. Defocusing works best when spatial resolution is not an issue. While for imaging at high resolution focusing of the light should remain as tight as possible regardless of optimal fluence. For that reason an argon attenuation cell was

introduced into the laser compartment right next to the exit aperture of the capillary as shown on Figure II.32.

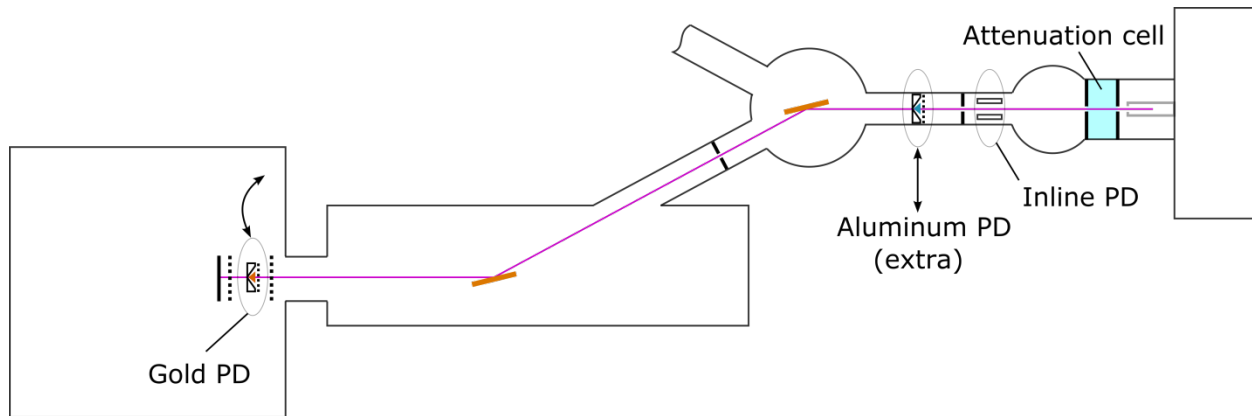


Figure II.32: Beam energy control scheme of the EUV TOF. At the exit aperture of the capillary an argon attenuation cell provides variable transmission factor for the EUV beam. The inline photodetector (PD) after the cell measures relative beam intensity based on signal collected from EUV photoionization of the residual argon gas. The inline detector is fully transparent for the beam. A retractable aluminum detector provides a better calibrated measurement of the beam energy. However, the reflectivity of the toroidal mirrors after the aluminum PD tends to degrade over time by an unformalizable rate due to surface contamination. The gold PD is mounted on a flip stage after the mirrors and right before the zone plate allowing for taking into account this factor. Gold is also a better material than Al for stable photoelectric conversion of the number of incident EUV photons for absolute power calibration.

The attenuation cell, also called argon cell or gas cell, is a ~10 cm long semi-isolated compartment with two apertures facing the capillary open end and high vacuum part of the system as Figure II.33.a shows. Transmission of the cell exhibits exponential dependence as the function of argon pressure. It asymptotically reaches zero at about 300 mTorr which is also optimal capillary pressure. A clear advantage of using the cell is the ability to extensively modulate attenuation as compared to free standing foil filters with fixed transmission. The plot in Figure II.33.b shows that a 200 nm thick Al foil provides with only 10% transmission. A 100 nm thick filter (not shown) exhibits about 50% transmission, but it is already too thin and fragile for routine operation. The attenuation cell is capable of smooth adjustment of its transmission starting off from ~50% of a given laser pulse energy.

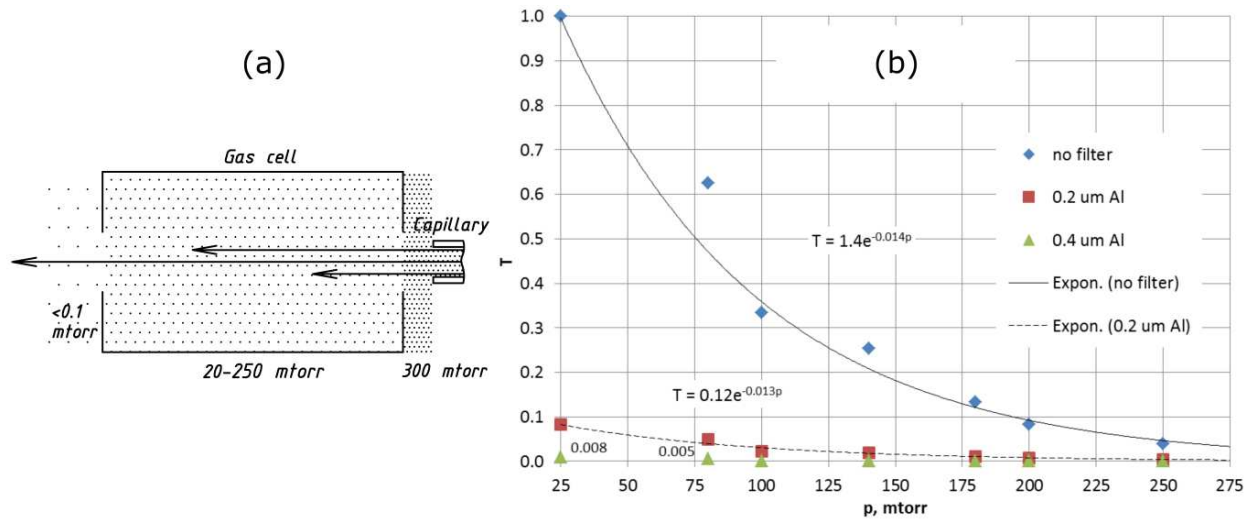


Figure II.33: Attenuation cell schematic and performance. (a) Schematic of the attenuation cell working principle. Variable argon pressure that is maintained by steady supply via an independent line (Appendix VII.i) and pumping through the apertures absorbs excess EUV photons by means of photoionization. (b) Exponential dependence of cell transmission as a function of Ar pressure. A 0.2 μm Al freestanding foil filter can be combined with the cell if precise low-transmission adjustment is required.

The 46.9 nm pulsed radiation provided by the EUV laser cannot be measured by commercial photodetectors (PD) because they are neither responsive at the laser wavelength nor fast enough to resolve the 1.5 ns duration pulse. Thus differentiation of the longer lifetime spontaneous emission background from the EUV pulse is unattainable. In response to this challenge a set of custom detectors was developed. Since the introduction of the EUV laser an aluminum-cathode detector employing the photoelectric effect was used with prior calibration of electron yield at the synchrotron¹⁶. This type of very simple and reliable PD is still utilized in the system, but there are concerns about its measurement reliability. First, aluminum oxidizes in air, so even though the electron/photon yield was measured on the oxidized surface, it may not be considered as an ultimate solution in the long term. Second, its design does not allow for *in situ* measurement of the laser pulse energy during experiment. And since the laser pulse energy variation is quite significant¹³, it causes uncertainty of the exact delivered energy per shot. This

may be critical for high spatial resolution single shot composition imaging measurements that the system is designed for. Lastly, mirrors degradation over time caused by hydrocarbon deposition results in a discrepancy between the power measured before the mirrors and the expected power to be delivered to the sample.

It would be possible to overcome these issues with the implementation of a pair of detectors: front-line transparent inline detector for relative intensity measurement on-the-go, and opaque gold absolute power measurement photodetector placed right before the zone plate and a sample as shown in Figure II.32. The principle of operation of the inline detector involves photoionization of residual argon gas coming off the capillary and attenuation cell. For absolute power measurement a PD with gold-coated photocathode is the most reliable, because gold is not a reactive material. The laser beam energy measured by the gold PD in the shown location is $\sim 11 \mu\text{J}$ at full power which correlates well with the published specifications. Details on PDs design and implementation strategy are given in the Appendix VII.f.

II.d.iv Sample handling

The sample chamber interior is designed to provide easy and precise positioning of the sample with respect to probing laser beams, a process that is monitored by the in-vacuum custom-build microscope. This is a problematic task for several reasons:

- a) ZP focal length is extremely short – 2.13 mm in 1st order and only 0.7 mm in the 3rd one with depth of focus of a few microns;
- b) sample and ZP are both biased with voltage difference up to 5 kV – if they touch, the ZP gets destroyed by passing current;

- c) the high magnification microscope objectives usually has short focal length and not designed for vacuum operation – we had to find a long working distance objective and assemble the microscope by ourselves only from vacuum-rated components;
- d) high resolution imaging requires stable, repeatable and precise, down to few tens of nanometers, positioning of all linked components for imaging;
- e) post-ionization beam has to be focused in between closely positioned sample and zone plate without interference with them that can also lead to ZP destruction.

Due to all these limitation the design of the sample and zone plate holder had to be finessed within fractions of millimeter, a rigid alignment and operational protocol listed in the Appendix VII.a & VII.e was carried out, and protection systems were implemented to avoid sample and ZP accidental touching – a set of manually adjusted stoppers that do not let stages to move past desired limits even after actuators failure.

The standard substrate for the EUV TOF spectrometer is a microscope glass slide with $25 \times 25 \times 1 \text{ mm}^3$ dimensions. The top is coated with $30 \div 60 \text{ nm}$ of ITO that consists of 95% of indium oxide and 5% of tin oxide providing conductivity for supplying the acceleration bias to the sample located on it. Transparency of the ITO coating allows for the microscope to look through the glass and see where ablation happens. Although in cases when an opaque thick sample is placed on the ITO slide, the microscope can focus only on its back side. But knowing the sample thickness it may still be helpful for adjusting ZP-to-sample distance. Normally it is done by translating microscope stage forward until it sees the lens and reading the travelled distance from the sample. For post-ablation ionization the use of a thicker slide placed on top of the standard ITO one helps separating parallel to the sample PI beam for avoidance of its interaction with the sample.

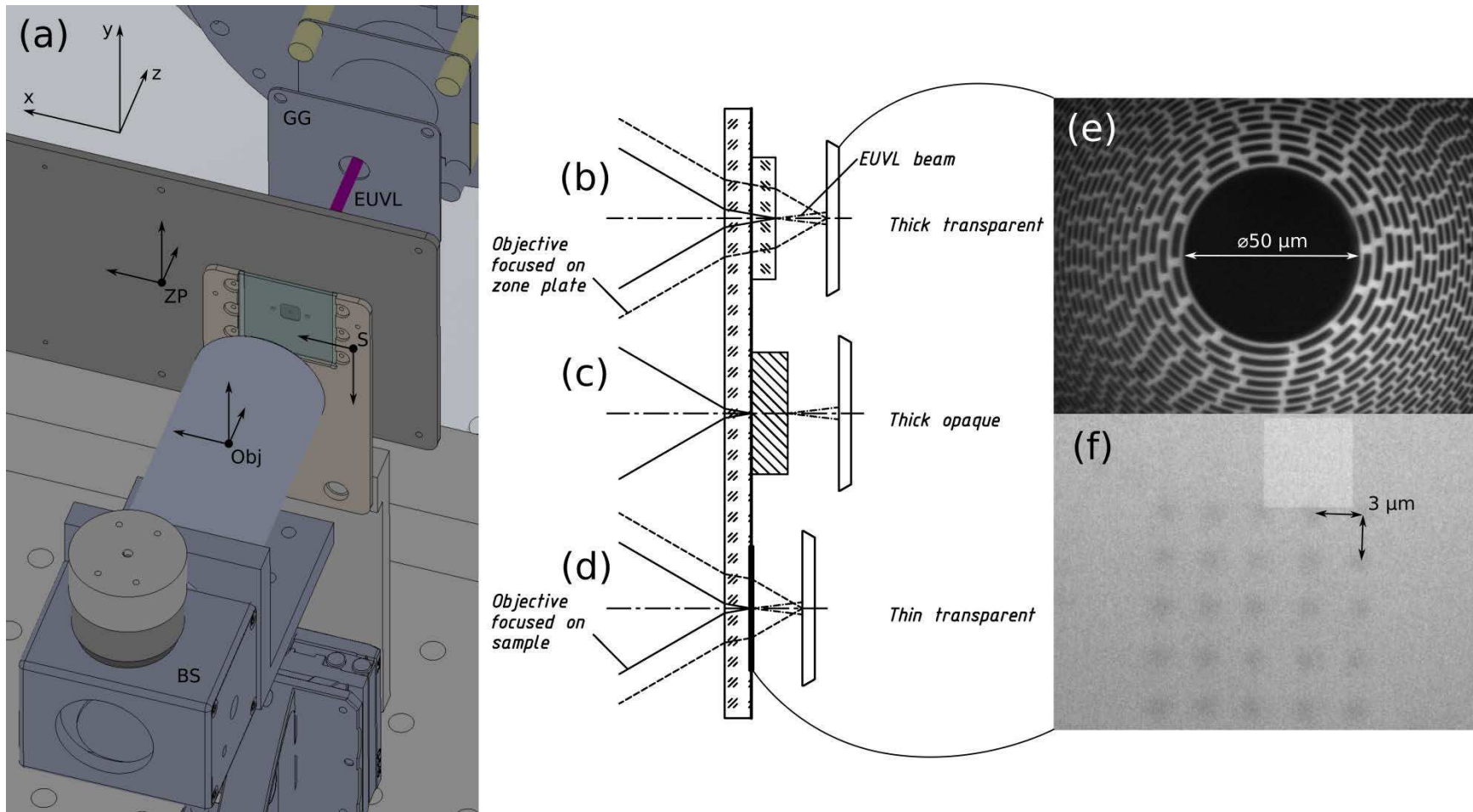


Figure II.34: (a) The view of sample chamber interior of the 3D assembly in SolidWorks. Incoming EUVL beam gets focused by the zone plate *ZP* that is mounted on a stainless steel plate holder with 3 degrees of freedom. The ITO glass slide is mounted on a smaller sample plate *S* with only 2 degrees of freedom but provided with precise piezo actuators. The microscope objective *Obj* behind the sample can move in three directions. Illumination of the sample is performed through a beam splitter *BS* by in-house built LED source. (b,c,d) Schematics of focusing the microscope on front or back of the sample and on *ZP* depending on sample transparency. (e) *ZP* as seen through the ITO slide using the microscope when measuring distance. (f) Zoomed as-seen picture of the ablation craters made on 50 nm Te film with single shot per spot calibration.

II.e Data analysis

The EUV TOF IMS produces a vast amount of data that has to be meticulously processed in order to accurately mass calibrate the spectra and assign each single shot spectrum to the locus of the sample where it was collected. This section describes the details of calibration of each ionization mode that system can work in. Two types of imaging: 2D mapping and 1D depth profiling are presented on the examples of uranium dots of various isotope ratios located on the glass slide, and CdTe multilayer stack identical to the one utilized for photovoltaic purposes.

II.e.i Mass calibration

The EUV TOF mass spectrometer works on a time-of-flight principle: preferentially singly charged ions of different masses get the same potential energy from the static electric acceleration field and thus same kinetic energy. Mass difference results in variance in velocity and consecutively in the time that is required for each type of ion to travel down the TOF and hit the MCP detector. From the energy conservation law a time-to-mass conversion formula is:

$$E_p = E_k \Rightarrow zeU = \frac{mv^2}{2} \Rightarrow m = (at + b)^2 \quad (\text{II.12})$$

Where E – potential and kinetic energies, z – ionization state of the ion, e – elemental charge, U – acceleration voltage, m – ion mass, v – ion velocity, t – time to cross the distance, $a = 0.5087$ and $b = 0.0296$ – calculated coefficients from the Figure II.35. Equation II.12 shows that two data points—two mass peaks—are needed for calculating the coefficients. Since TOF technology allows simultaneous identification of all ions created during a laser ablation event, it is best to calibrate the mass by very low and very high mass peaks that essentially encompass all other peaks in between. Very often though there is no known peak in the high mass range. In this

case relying on a peak in the 100÷300 Da interval proved to be precise enough when combined with hydrogen, carbon or other known low-mass peak. Two plots in Figure II.35 show carbon and $^{260}\text{Te}_2$ peaks as naturally detected versus time scale. The vertical line placed at ~1 V amplitude level indicates the beginning of the arrival time for the corresponding ion – these two time points are then fed into the equation II.12 and above mentioned coefficients are obtained.

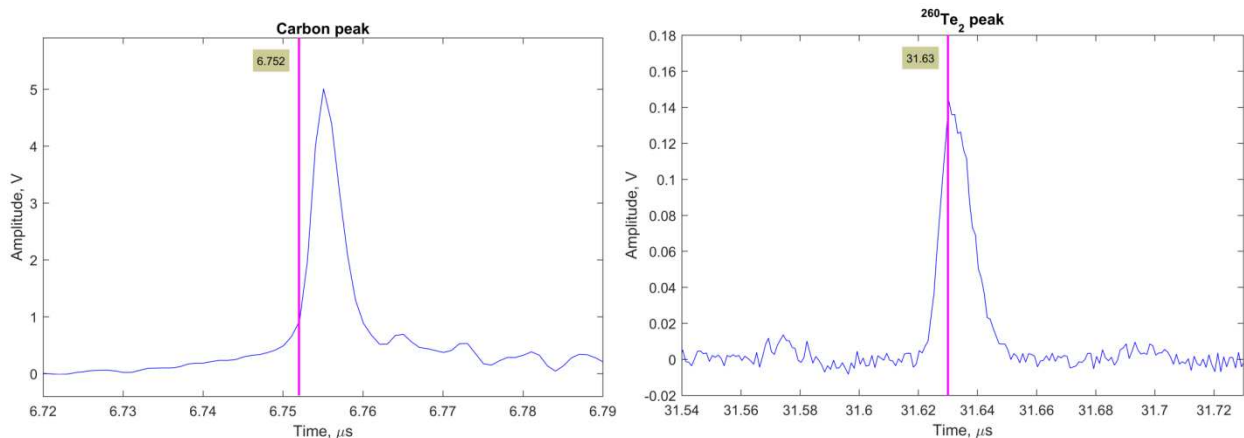


Figure II.35: Peaks of carbon and diatomic tellurium with masses of 12 and 259.8125 Da correspondingly selected for mass calibration.

Figure II.36 shows a CdTe film that can be used for spectra calibration in every mode of operation: EUV ionization only, UV post-ionization and VUV PI. A thin film photovoltaic-grade CdTe was obtained from the Next Generation PV Center (NGPV) at CSU. The film was deposited by co-sublimation from two sublimation sources³². Ionization energies of Cd and Te are very similar – 8.99 and 9.01 eV correspondingly. But photoionization cross section at 10.5 eV (VUV PI mode) differs significantly: ~0.3 versus ~66 Mb³³. This fact results in a situation when 3.5 eV multiphoton ionization ionizes both elements, although with low probability due to necessity to absorb three photons, while single-photon 10.5 eV ionization yields only Te ions. Due to the much softer ionization process, VUV PI also generates Te_2 ions dominating the spectrum as compared to Te ions by integrated intensity of two intense isotopes: ~2400

secondary ion counts on $^{254}\text{Te}_2$ versus ~600 counts on ^{128}Te as shown on Table II.9. The signal background on VUV PI spectra (Figure II.36) originating from defocused UV ionization is negligible and is observed as a minor contribution only on Te^+ peaks. It indicates that Te_2^+ ions originate purely due to ionization by focused VUV light. Focused UV light also produces the monomer signal only and absolutely no dimer one. After experimental verification of this expected behavior, a thin ~50 nm Te film was adopted for the routine use in fine-tuning the parameters of EUV TOF system in VUV PI mode by maximising Te_2^+ signal yield.

These are instrumental findings for calibration and tuning, but the real advantage of soft VUV PI mode comes when organic compounds have to be studied (section IV.c).

Table II.9: Yields of CdTe signal in three EUV TOF operational modes.

Method	Peak	Secondary ion counts	Photon type	Primary photon number	Secondary ion yield	Comments
UV PI	^{112}Cd	413	3.5 eV	3.6e16	1.1e-14	10-shot averaged spectrum
EUV		3237	26.4 eV	1.2e9	2.7e-6	
VUV PI	^{128}Te	1324	10.5 eV	6e11	2.2e-9	Defocused UV subtracted
UV PI		1204	3.5 eV	3.6e16	3.3e-14	10-shot averaged spectrum
EUV		1405	26.4 eV	1.2e9	1.2e-6	
VUV PI	$^{254}\text{Te}_2$	2415	10.5 eV	6e11	4e-9	Defocused UV subtracted
EUV		596	26.4 eV	1.2e9	5e-7	10-shot averaged spectrum

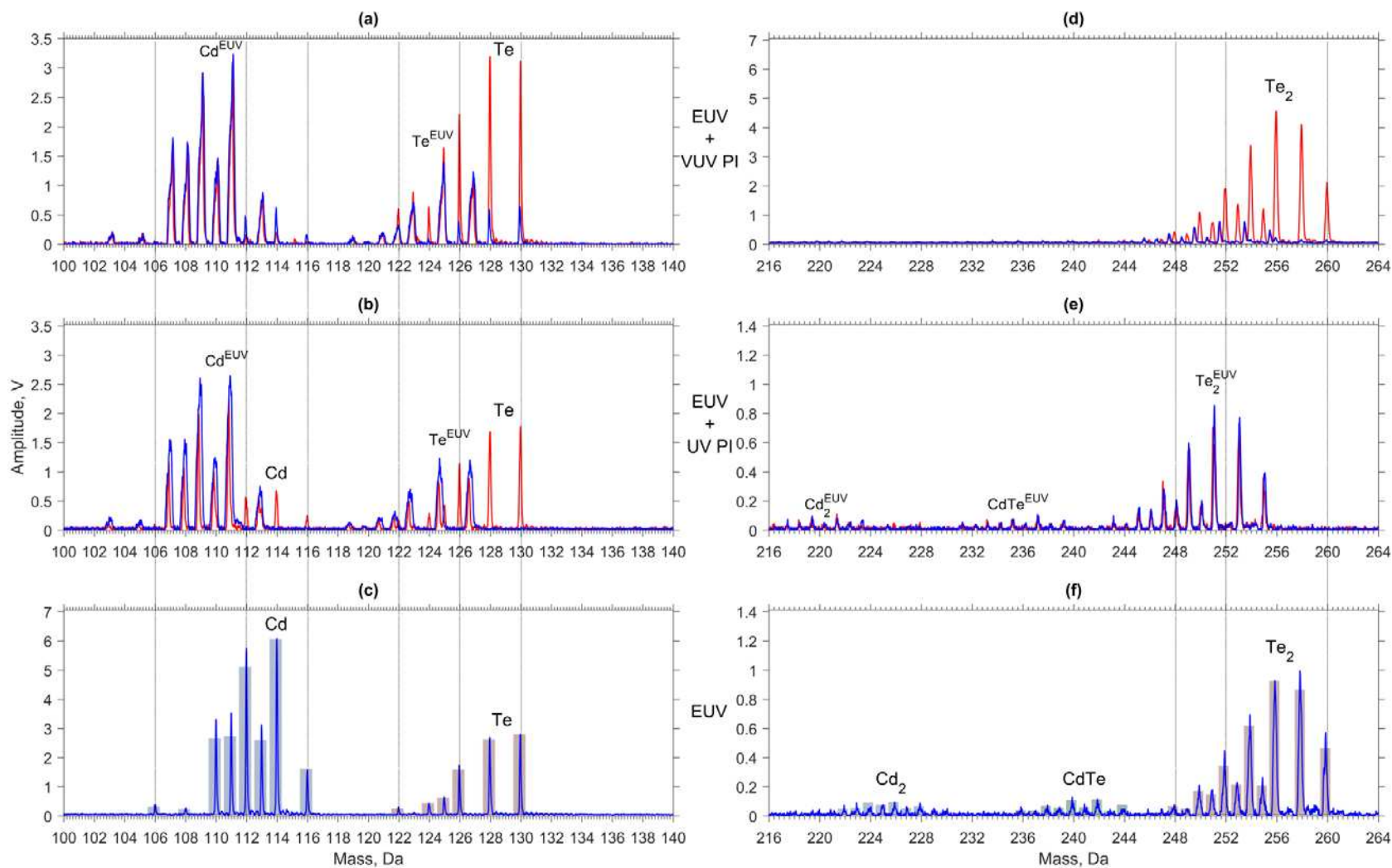


Figure II.36: CdTe mass spectra in different regimes: VUV PI (a,d), UV PI (b,e) and EUV only (c,f). Red spectral lines indicate PI mode utilizing focused VUV or UV radiation, blue lines – background signal of the PI mode with the absence of VUV or UV focused light. VUV PI mode demonstrates higher Te yield (a) and massive presence of Te₂ (d) isotopes compared to UV PI, but UV PI mode reveals some Cd isotopes at 112, 114 and 116 Da (b). EUV mass spectra show overlaid half-transparent bars indicating natural isotope abundance of Cd₁, Te₁, Cd₂, CdTe, and Te₂.

II.e.ii Mass spectrometry imaging

II.e.ii.1 Imaging of heterogeneous samples

The EUV TOF system was designed and built with the main purpose of high resolution 3D imaging of molecular distributions in heterogeneous, primarily biological systems. It had demonstrated 80 nm spatial resolution from an organic sample knife edge test, 20 nm depth resolution for specially deposited organic bilayer, sub-micrometer (350 nm wide and 80 nm deep voxels) image of single *M.smegmatis*, and sensitivity on the example of Alanine 20× greater than that of SIMS TOF¹¹. It was recently shown that together with VUV post-ionization the intact cholesterol molecule can be detected. Altogether, these are promising results for continuation of EUV TOF development toward higher sensitivity and higher resolution molecular imaging.

In addition, the system demonstrated the same spatial resolution on inorganic sample and similar SUE to SIMS TOF for isotope trace analysis³. Improvements in sensitivity by upgrading of the detection system would place EUV TOF to surpass the performance of SIMS TOF in main specifications. Even at the current state, EUV TOF is already useful for both organic and inorganic mass spectrometry imaging, molecular and elemental – from hydrogen to uranium.

Figure II.37 illustrates the principle of MSI: the probe beam is focused to a spot with variable diameter (depending on laser fluence and ZP focusing) on a sample, creating a full mass spectrum upon single laser pulse ablation. Then the sample is moved by a defined step size in *x* or *y* directions, and another signal gets collected from a nearby crater. Such translation, ablation and data collection is repeated in an array pattern shown by blue circles. In addition to *x*- and *y*-rastering, the laser can fire multiple times at one spot and gather depth information on composition by essentially drilling through the sample. In this case, one creates 5D spectrometric

array (x, y, z for coordinates, t and amplitude for spectra) that often occupies GB-scale memory on a computer hard drive. Processing of such data sets results in 4D images: 3 coordinates and integrated counts in a voxel.

Figure II.37.b-c demonstrates 2D image composition maps of two micron-scale metal dots that have uneven isotope ratio of ^{235}U and ^{238}U . The dot on the left, CRM U200 standard, has 1:4 ratio of the isotopes, while CRM 129A has natural abundance with low 0.7% ^{235}U content. The image was collected with 5 μJ tightly focused laser pulses. An array consists of $25 \times 25 \times 3$ pixels spaced by 400 nm laterally. All layers in depth were then averaged to reduce signal fluctuation from voxels on top of each other, a process that converts them to a single pixel. The picture on the left is a map of fissile ^{235}U isotope showing up to 300 counts only on the left particle. Due to current limitations of TOF sensitivity, detection of compounds with <1% concentration is hardly possible. The map on the right is a distribution of non-fissile ^{238}U isotope highly abundant in both particles. The maximum counts are now up to 900. Superimposed and half transparent is a SEM image of the imaged area showing great correlation with the composition map. Such functionality is extremely important for nuclear forensics applications.

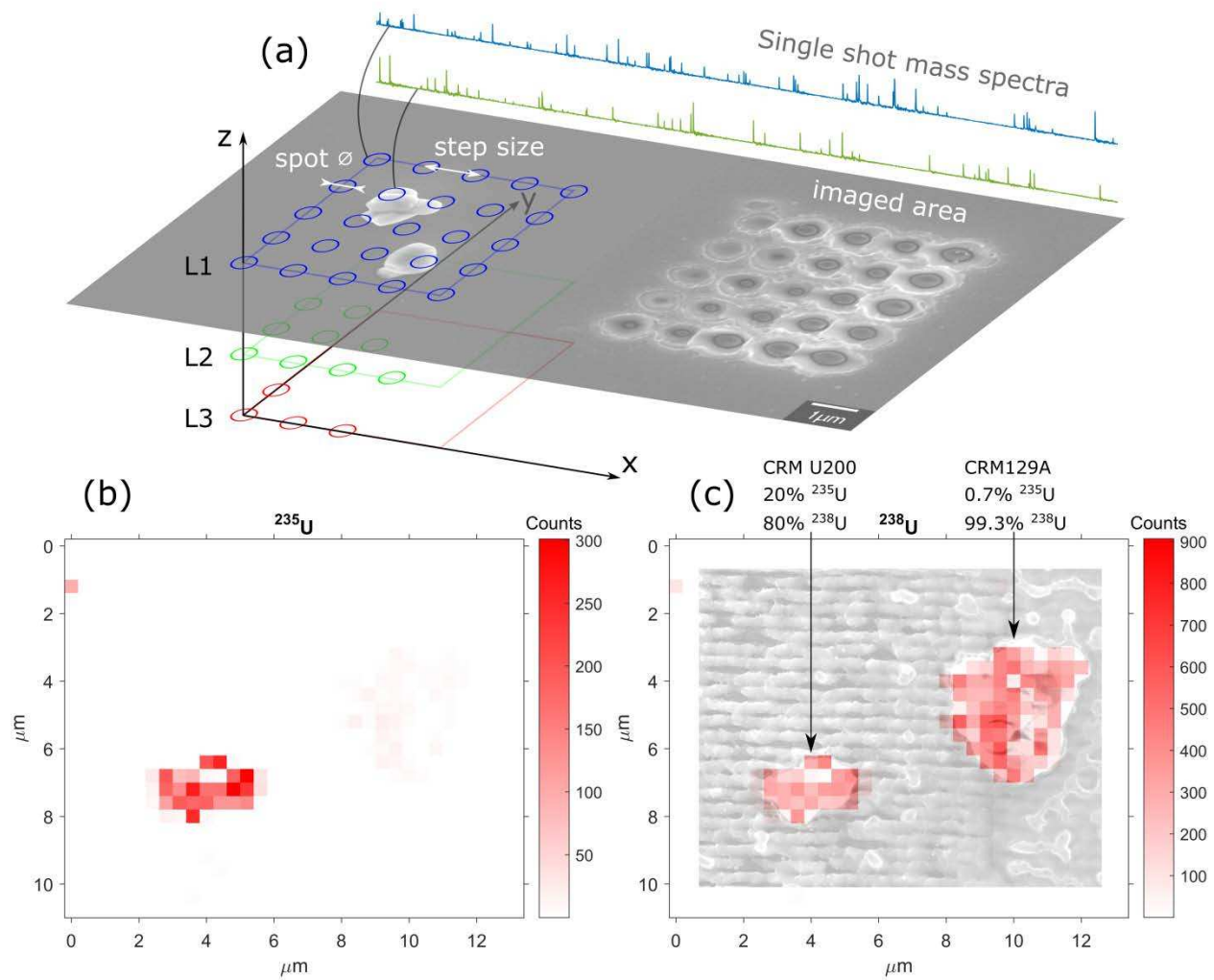


Figure II.37: Principle of mass spectrometry imaging on the example of two dots composed of unequal ^{235}U and ^{238}U isotope content

II.e.ii.2 Depth profiling of multilayers

The ability to ionize any atom or molecule with 26.4 eV photons results in a rich atomic presence in the single shot spectra, starting from hydrogen². This element used to be of a traditional interest to metal alloys community, and with recent developments of novel

2. A version of this section will be published in *Journal of Electronic Materials*: Munshi A., Kuznetsov I. et al. (2018)

photovoltaic components quickly became a central topic there as well¹. The New Generation Photovoltaics (NGPV) laboratory at CSU introduced a method for the dramatic increase of CdTe-based PV-elements efficiency³⁴ from 12.54 to 14.8% by passivating them in a hydrogen plasma. CdTe films have microstructural defects, such as stacking faults, upon deposition that are traditionally passivated by CdCl₂. In this set of samples both CdCl₂ and H passivation were applied as previous studies showed that H passivation itself does not lead to substantial gain in efficiency; however, it is capable of passivating defects that are omitted by CdCl₂ process. NGPV team got interested in figuring out if this efficiency resulted from the surface modification of the photovoltaic stack or if hydrogen got deeply embedded into layered structure. The goal of the experiment was then to depth profile hydrogen treated and non-treated samples at same probing conditions and compare hydrogen presence and its depth distribution inside those films.

All common high resolution and high sensitivity metrology methods experience low interaction cross section when applied to direct detection and mapping of the H distribution in solids leading to the adoption of indirect analyses. For example, tracking changes of the Fe electron levels allows XANES to determine Fe-H phase presence by X-ray induced fluorescence, and it allows TEM-EELS image the Fe-H distribution by looking at electrons energy loss³⁵. Currently the most common, although the least accessible, direct method is neutron radiography or tomography (NR or NT). Recent advances in NT allow reaching 25 μm resolution in 3D with ~1e18 cm⁻² detection limit, although tomographic data acquisition takes up to 14 h or more if other experimental procedures are taken into account¹. In-situ nuclear reaction analysis (NRA) does not require a neutron source, rather it uses a Van der Graaff accelerator for obtaining ~6.4 MeV ¹⁵N²⁺ or ¹⁹F³⁺ for using in a probe beam. NRA can perform non-destructive metrology of H distribution near the surface with ~5 nm depth resolution. Modern nano-SIMS performance

has the ability to reach nanoscale resolution and $7 \times 10^{18} \text{ cm}^{-3}$ sensitivity by using $>10 \text{ keV Cs}^+$ ions, however further increase of sensitivity down to $1 \times 10^{16} \text{ cm}^{-3}$ can be provided only with non-imaging techniques such as thermal desorption spectroscopy (TDS)³⁶. EUV TOF is a viable alternative to SIMS for direct H distribution mapping at potentially nanoscale 3D resolution.

Both control and hydrogen passivated samples were mounted on the holder and analyzed right after another during a single experimental run (Figure II.38). Imaging was performed with $4 \times 4 \times 10$ (x-y-z) shots with $\sim 3 \text{ }\mu\text{J}$ EUV laser pulses tightly focused to $\sim 1 \text{ }\mu\text{m}$ diameter spots and separated by $3 \text{ }\mu\text{m}$ to avoid overlapping. 10 shots per spot allowed reaching the deepest regions of the sample prior to the glass substrate layer of SnO_2 on both thick and thin samples. The analysis is shown on Figure II.39.

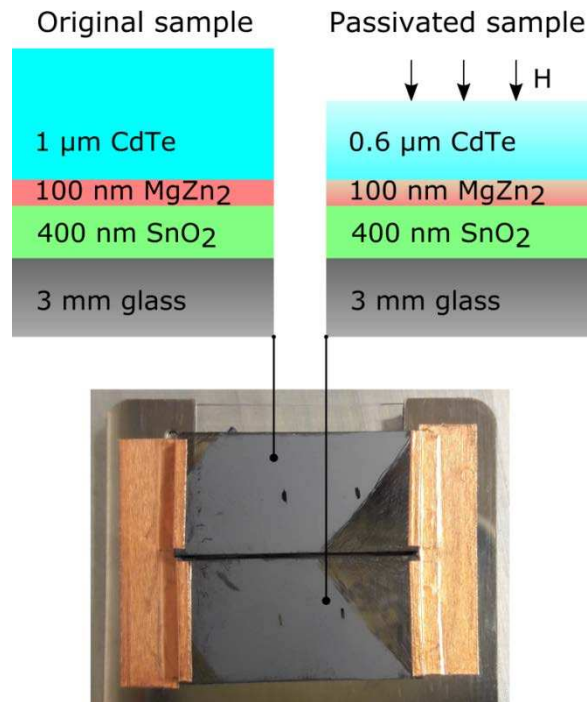


Figure II.38: Structure of hydrogen enriched (right) and standard CdTe photovoltaic stack. Thinning of CdTe layer is caused by material etching due to exposure to H plasma source.

Data of each sample were layer-averaged and displayed in a form of mass spectra showing roughly how the transition between layers occurs. In a specially written Matlab® script, all chemistry corresponding to each layer was integrated and summed, i.e. for CdTe film the isotopes of both elements were integrated and summed together with their diatomic isotopes. The same was done for H+H₂ peaks. Since the laser has a certain degree of variation in the energy per pulse, CdTe was chosen as an internal normalization standard for calibration of the H content by simple dividing the integrated intensity of the H-related peaks to the CdTe-related ones. The final result plotted on the bottom right part of Figure II.39 shows that bulk H enrichment of CdTe is fairly consistent and is about 1.5× of the H content in the control sample. The jump in content to 2.3× visible on the first shot is most likely attributed to preferential ion implantation on the surface of CdTe film during passivation together with the always present elevated C_xH_y contamination of any surface analyzed in EUV TOF. For better results the analysis should be performed in an ultra-high vacuum environment without exposure of the sample to atmosphere after treatment and prior to the experiment. With these conditions met the EUV TOF system might also be of interest to the emerging higher efficiency battery technologies and other energy-related materials characterization.

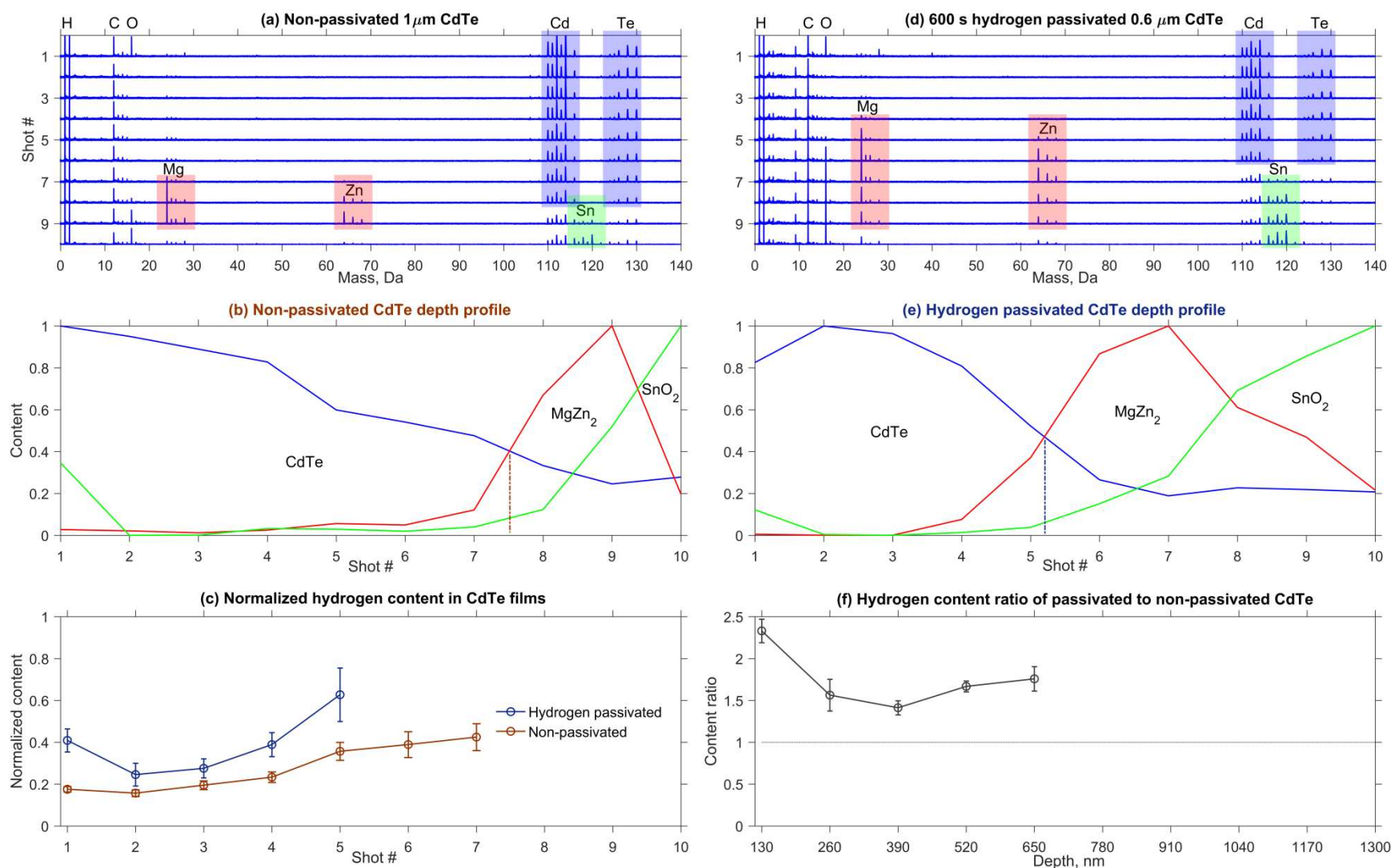


Figure II.39: Non-passivated (left) and hydrogen passivated (right) stacks analysis showing layer-by-layer averaged mass spectra (a,d). (b,e) Layered structure of each sample as a function of shot number plotted after integration of signal from corresponding compound. (c) Normalized hydrogen content in both samples. (f) Ratio of H content showing $\sim 2.3\times$ surface and $\sim 1.5\times$ bulk enrichment factor in the passivated CdTe layer.

III NATURE COMMUNICATIONS PAPER ON EUV TOF

III.a Paper title page

Three dimensional nanoscale molecular imaging by extreme ultraviolet laser ablation mass spectrometry³

Analytical probes capable of mapping molecular composition at the nanoscale are of critical importance to materials research, biology and medicine. Mass spectral imaging makes it possible to visualize the spatial organization of multiple molecular components at a sample's surface. However, it is challenging for mass spectrometry imaging to map molecular composition in three dimensions (3D) with submicron resolution. Here we describe a mass spectral imaging method that exploits the high 3D localization of absorbed extreme ultraviolet laser light and its fundamentally distinct interaction with matter to determine molecular composition from a volume as small as 50 zL in a single laser shot. Molecular imaging with a lateral resolution of 75 nm and a depth resolution of 20 nm is demonstrated. These results open opportunities to visualize chemical composition and chemical changes in 3D at the nanoscale.

III.b Introduction

Mass spectral imaging (MSI) is an essential tool for surface analysis. MSI has achieved high sensitivity and spatial resolution in the identification and profiling of element-specific

3. This paper was received on 25 April 2014, accepted on 17 March 2015 and published online on 23 April 2015 on Nature Communications website www.nature.com/naturecommunications. I. Kuznetsov et al., volume 6, article number 6944, DOI: 10.1038/ncomms7944.

signatures from dopants and impurities in semiconductors, metals and dielectrics. The elemental specificity of MSI has also motivated studies in biology, medicine and environmental sciences in which fundamental molecular processes have been identified from characteristic signatures from metallic or isotopic tags³⁷⁻³⁹. Adapting MSI to molecular imaging has required the implementation of ionization strategies which control molecular fragmentation⁴⁰. In biochemistry and medicine molecular MSI is used, for example, in studies of metabolic exchange in micro-organisms⁴¹ and localization of drugs and metabolites in tissue⁴².

MSI typically uses a laser or an ion beam to ablate or sputter the sample's surface and desorb and ionize atoms and molecules. Spatially resolved mass detection of the ejected material allows one to construct two dimensional (2D) maps of the spatial organization of multiple molecular components at the sample's surface. The leading molecular MSI methods are laser desorption ionization (LDI) and secondary ion mass spectrometry (SIMS)⁴⁰. LDI MSI has been demonstrated using laser wavelengths ranging from the near infrared to the ultraviolet (UV) and pulse durations from nanoseconds to femtoseconds. The ablation, desorption and ionization mechanisms depend significantly on the laser pulse duration, fluence and the absorption characteristics of the material at the laser wavelength. For applications to organics LDI MSI is most commonly implemented using nanosecond UV pulses. The relatively low absorption of UV light by organic samples requires the use of a highly absorbing matrix to promote absorption, desorption and ionization^{43,44}. In UV LDI MSI, the diffraction limit of the UV illumination coupled with the properties of the matrix affect the lateral spatial resolution which is typically ~10 μm and at best ~1 μm . In addition it is difficult to obtain high depth resolution⁴⁵. Matrix assisted UV LDI time of flight mass (TOF) MSI is used in biomedical imaging for its ability to detect large molecules ($m/z > 1000$) as lipids and proteins in tissue^{46,47 45,46,48}.

SIMS uses energetic ion bombardment to erode the sample's surface. In this process secondary ions are created from the top few monolayers through collision cascade events that extend tens of nanometers into the bulk depending on the material, the energy and type of the primary ions. For molecular imaging of organic solids secondary ion time-of-flight mass spectrometry (SIMS TOF) uses primary ions with energies of $\sim 10\div 30$ keV and the dose at the sample is limited to $< 10^{12}$ cm⁻² to minimize damage. SIMS TOF MSI is capable to image the 2D distribution of intact analyte molecules within a mass range of $m/z \sim 1000$ with typically 1 μm lateral resolution and independently depth profile molecular content with ~ 10 nm depth resolution^{49,50}. A higher lateral resolution of 60 nm has been demonstrated with SIMS TOF using 80 keV primary ions although at the expense of molecular fragmentation and thus reduced mass range ($m/z 184$)²⁷.

There are significant challenges for MSI to reach nanoscale 3D spatial resolution in the chemical imaging of organic samples. In matrix assisted UV LDI TOF, the matrix/analyte interaction combined with fundamental wavelength limitations precludes the increase of lateral spatial resolution below ~ 1 μm and at the same time makes it difficult to implement depth profiling. In SIMS TOF analyte ion yield and molecular fragmentation limit the ability to achieve nanoscale lateral and depth resolution simultaneously.

In this article we describe a new laser ablation and ionization MSI method that exploits the superior focusability of extreme ultraviolet (EUV) laser light, its shallow absorption depth and its distinct interactions with materials to map chemical composition of organic samples in 3D at the nanoscale. In this first demonstration of EUV laser ablation TOF MSI (EUV TOF) the method is shown to detect singly ionized intact analyte ions with a superior sensitivity of 0.01 amol within the mass range of up to $m/z 400$. Molecular composition across a sharp

boundary is assessed with lateral resolution of 75 nm, and a depth resolution of 20 nm. We exploited the high localization of the focused EUV light for 3D molecular imaging of a single *Mycobacterium smegmatis*.

III.c Results

III.c.i Concept and implementation of 3D chemical imaging by EUV laser ablation

The concept of EUV TOF MSI is illustrated in Figure III.c.1a. Bright laser pulses from a compact 46.9 nm wavelength (λ) laser¹³ are focused into nanometer size spots to ablate craters a few nanometers deep on selected regions of the sample. The ions in the laser-created plasma are extracted and identified by their mass-to-charge ratio (m/z) using a TOF mass spectrometer. 3D composition images are constructed from the analysis of spatially resolved mass spectra obtained as the sample is displaced with respect to the focused laser beam.

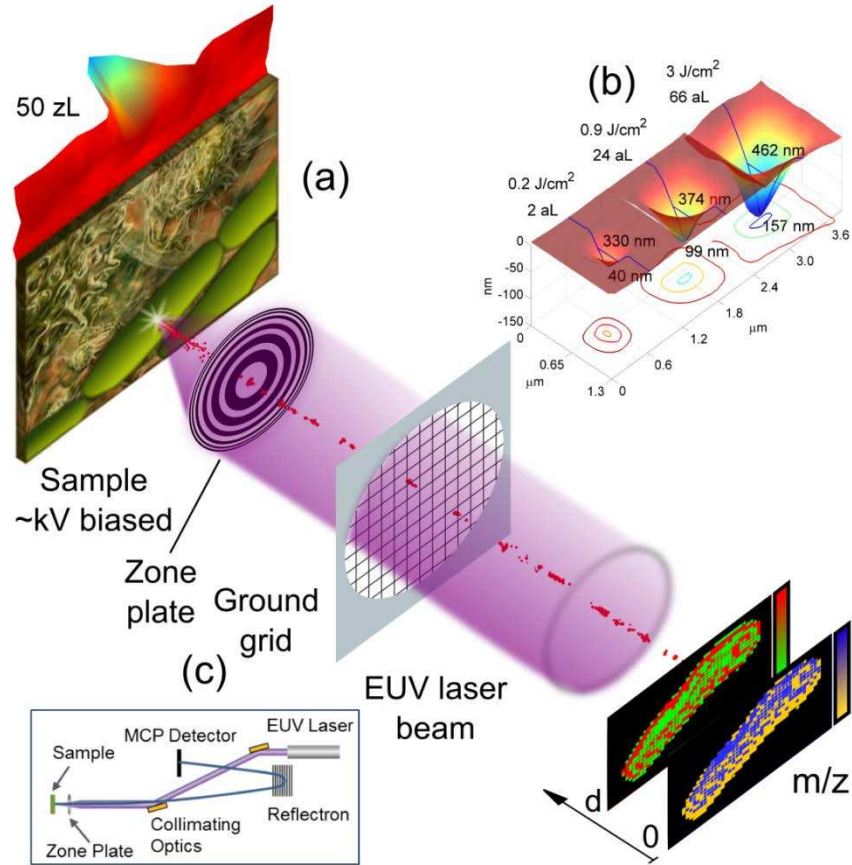


Figure III.c.1: Extreme Ultraviolet Laser Ablation Mass Spectrometry Imaging Concept. (a) Schematics showing the focused EUV laser beam ablating a sample to produce an ion stream that is analyzed by a TOF mass spectrometer. (b) Atomic force microscope (AFM) images of craters ablated in polymethyl methacrylate (PMMA) by a single EUV laser shot at different irradiation fluences. The smallest ablation crater has a volume of 50 zL. The craters show smooth profiles with no signs of thermal damage. (c) Schematic of the instrument set up including the collimating EUV laser optics, focusing zone plate and TOF spectrometer.

The EUV MSI instrument is schematically shown in Figure III.c.1c. The EUV laser generates pulses of $\sim 10 \mu\text{J}$ energy, 1.5 ns duration at a wavelength of $\lambda = 46.9 \text{ nm}^{13}$. The laser output is collimated using a pair of grazing incidence toroidal mirrors to fully illuminate a zone plate (ZP) lens that focuses the laser beam onto the sample. The free standing ZP consists of concentric zones with outermost zone width of 200 nm and a central zone opening of 50 μm diameter that allows for ion extraction⁵¹. Positive ions from the EUV laser-produced nano-

plasma are accelerated across a typically 6 kV potential difference and are injected into a TOF tube operated in reflectron mode. The mass resolution of the TOF detector was determined to be $m/\Delta m = 1100$. For operation in imaging mode, the sample was mounted on x-y-z nanopositioners.

Atomic force microscope (AFM) images of craters ablated in polymethyl methacrylate (PMMA) with single EUV laser shots at different irradiation fluences are displayed in Figure III.c.1b. The profiles were obtained by placing the sample at the first order focus of the ZP and attenuating the laser beam intensity by photoionization of Argon in a variable pressure gas cell. The laser fluence necessary to ablate each of the craters is indicated in Figure III.c.1b. The ablated volume was varied from 66 aL to 2 aL when decreasing the laser fluence by 15 \times . Smaller craters can be created operating in the third order of the ZP (see Methods). The smallest crater ablated from which distinct analyte signatures were obtained has a volume of ~50 zL (Figure III.c.1a and Figure III.h.2a). The AFM images of the ablated craters also show their profile is very smooth with no signs of thermal damage. This results from the prevalence of chain scission in the polymer by the EUV photons⁵².

III.c.ii Demonstration of 3D molecular imaging at the nanoscale

A set of experiments was designed to benchmark the ability of EUV TOF MSI to detect intact molecular ions from relevant organic molecules, to determine its lateral and depth spatial resolution when imaging heterogeneous samples, and to image molecular composition in 3D.

The mass detection range and sensitivity were assessed from mass spectrometry experiments that used thin layer samples of the amino-acid alanine ($\text{CH}_3\text{CH}(\text{NH}_2)\text{COOH}$, molecular mass: 89.09 Da, monoisotopic mass: 89.05 Da), and the organic dye Nile red

($C_{20}H_{18}N_2O_2$, molecular mass: 318.369 Da, monoisotopic mass: 318.14 Da). Single-shot mass spectra were obtained ablating the analyte placed at either the first or the third order focus of the ZP lens. The mass spectrum of alanine in Figure III.c.2a contains intense peaks that are identified as the protonated molecular ion $[M+H]^+$ with m/z 90 and the radical M^+ with m/z 89. These signatures are well resolved even when ablating a 50 zL crater (Figure III.h.2a). By taking the ratio of the ablated analyte mass in moles to the total counts within the area of $[M+H]^+$, the sensitivity of EUV TOF is calculated to be 0.01 amol. The level of fragmentation was also calculated from the alanine spectrum as the ratio of the integrated counts in $[M+H]^+$ to the total number of counts in the spectrum within $50 \leq m/z \leq 89$ and found to be 1.1. The single shot mass spectrum of Nile red is shown in Figure III.c.2b. This spectrum contains intense peaks at m/z 319 and 318 which correspond to $[M+H]^+$ and M^+ and salient molecular fragments at m/z 303, 275 and 261. A comparison of the sensitivity and level of fragmentation of EUV TOF with SIMS TOF is shown in Figure III.h.1 and summarized in Table III.1. Details of this analysis, presented in the Supplementary section, show EUV TOF to be highly more sensitive.

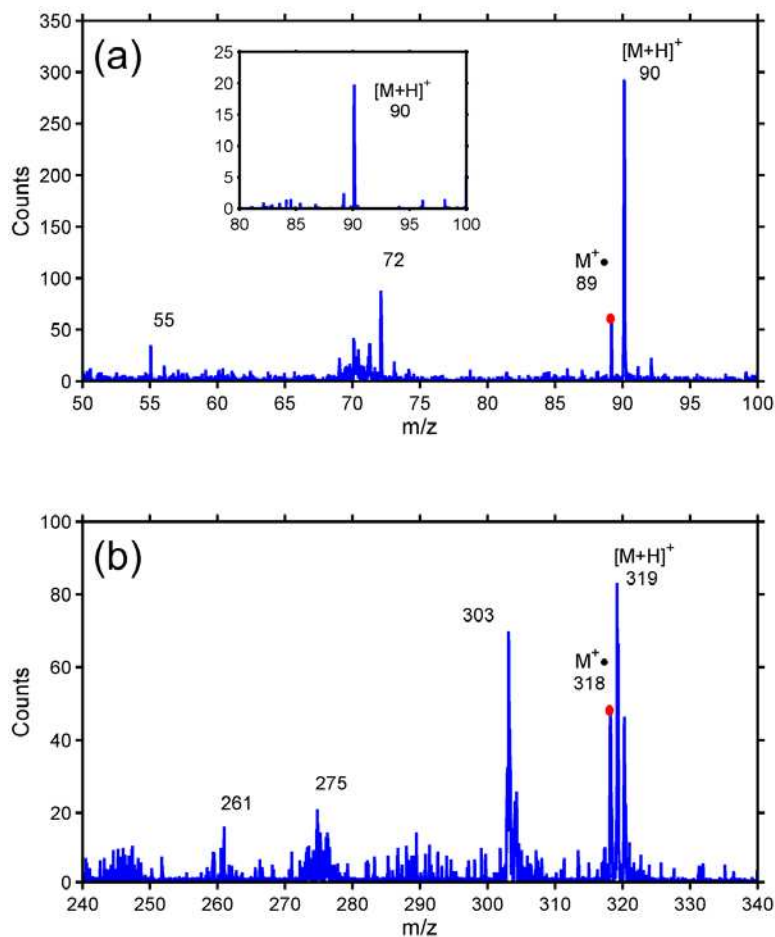


Figure III.c.2: Single-shot mass spectra of organic analytes. (a) Mass spectrum of alanine obtained from an ablated analyte volume of 12.8 aL in which the protonated molecule peak $[M+H]^+$ and the radical $M^{\cdot+}$ are identified. The inset shows the amplitude of $[M+H]^+$ is significantly above the noise floor when the ablated analyte volume is 50 zL. The alanine peak at m/z 72 corresponds to the loss of water $[M+H-H_2O]^+$ and the peak at m/z 55 to $[M+H-CH_3-NH_2]^+$. (b) Mass spectrum of Nile red obtained from the same ablated analyte volume showing $[M+H]^+$ and $M^{\cdot+}$ with m/z of 319 and 318 respectively.

Alanine and Nile red were selected to assess the depth resolution of EUV TOF MSI as their molecular signatures are in distinct m/z ranges. A sample consisting of a 105 nm thick layer of Nile red and a 73 nm thick layer of alanine deposited by evaporation onto an ITO-covered glass slide was used. A laser fluence of 0.13 J/cm^2 was selected to ablate the organic layers but not the ITO-coated glass substrate. The depth profile of the organic bilayer structure was obtained by recording the mass spectrum from 13 consecutive laser shots fired on the same spot.

For statistical purposes, the process was repeated on other sites arranged in a 4x4 array of points separated by 2.5 μm . Laser shot number was correlated to depth through independent AFM measurements of the ablated analyte profiles. Beyond the 10th ablation event the depth of the craters remained unchanged, indicating that the ITO layer was reached. The normalized abundance or composition profile (see Methods) of each of the analytes versus depth is plotted in Figure III.c.3. A depth resolution of 20 nm was determined from a fit of these profiles with a sigmoid function. This is the distance corresponding to the 20÷80% change in the amplitude of the analyte signal across the interface.

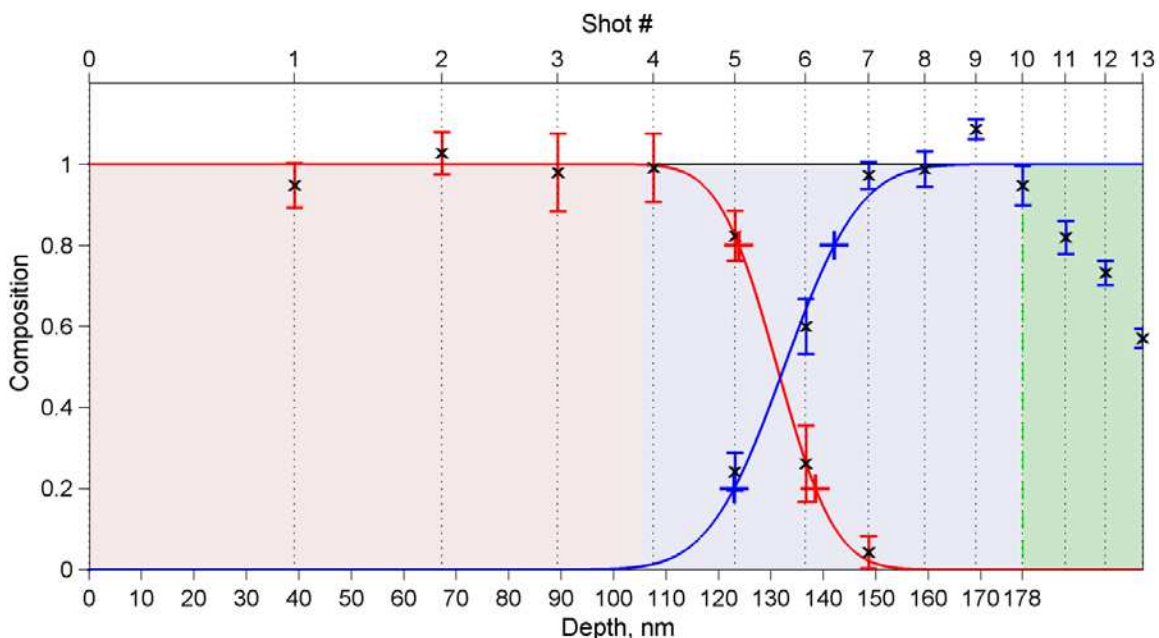


Figure III.c.3: Variation of molecular composition versus depth. The average amplitude of the Nile red—in red—and alanine—in blue—peaks in the spectra of Figure III.c.2 is plotted versus ablation event number and ablation depth. After the 10th shot, the depth of the ablation craters remains practically unchanged indicating the ITO layer was reached. The depth scale was determined from atomic force measurements of the ablated craters. The error bars represent the variance in the amplitude for each analyte at each depth obtained from the 16 consecutive ablation events as described in Methods. The plus signs in the intensity profiles indicate the 20 and 80% levels from which the depth resolution is obtained.

Nanoscale 2D MSI was demonstrated using a sample consisting of a ~120 nm layer of resist containing a trench that exposed the ITO-coated glass substrate. In these experiments a

laser fluence of 0.43 J/cm^2 was selected to ablate craters in the resist with a mean full width at half maximum (FWHM) diameter of 400 nm and a depth of 40 nm in a single shot. A broad area image of the trench with pixel size of 250 nm is shown in Figure III.c.4a. Each pixel in the image plots the resist content which was determined by averaging the amplitude of four characteristic resist fragments in the m/z range of 74÷121. A region extending $4.5 \mu\text{m}$ across and $0.8 \mu\text{m}$ along the trench was imaged with higher resolution. In this experiment, consecutive mass spectra were obtained as the sample was displaced in 75 nm steps with respect to the focused laser spot. The 2D ion image of this region is shown in Figure III.c.4b. The grey scale indicates the resist content in each pixel calculated as in the broad area image of Figure III.c.4a. To assess the lateral resolution the amplitude of each 10 pixel high column in the 2D ion image of Figure III.c.4b was averaged to create the average profile of Figure III.c.4c. Analysis of this profile shows the 20÷80% change in amplitude occurs within one pixel, i.e. 75 nm (Figure III.c.4d). AFM profiles of the resist edge before ablation (blue trace) and after consecutive ablation (green traces) are shown in Figure III.c.4e. The sharp edge of the ablation profile with subpixel 20÷80% rise enables the demonstrated high spatial resolution in the imaging of organic materials.

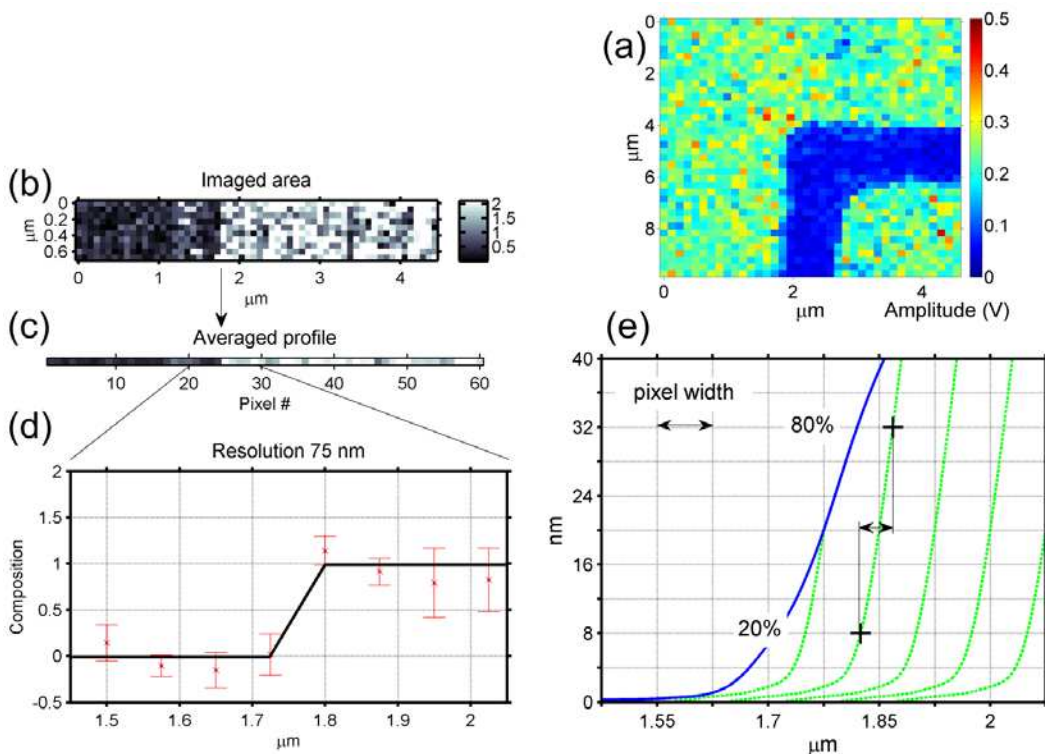


Figure III.c.4: Demonstration of 2D nanoscale molecular imaging. (a) 2D ion image depicting the distribution of resist over a $10 \times 10 \mu\text{m}^2$ region of the sample in which a trench was defined by photolithography. The pixel size in the image is 250 nm. The color scale represents the resist content. (b) High resolution 2D ion image of the trench region showing in a grey scale the resist content. The pixel size is 75 nm. (c) Vertically averaged intensity profile over the region of the sample extending $4.5 \mu\text{m}$. (d) The intensity lineout of this profile shows the 20÷80% change occurs within one pixel. (e) Resist edge profiles obtained from AFM images before ablation (blue trace) and after consecutive ablation events (green trace). The + signs indicate the 20÷80% rise in the ablation profiles is sub-pixel.

To demonstrate 3D molecular imaging we used a sample consisting of *Mycobacterium smegmatis* bacteria deposited on an ITO-coated glass substrate. The laser fluence 0.5 J/cm^2 was selected to ablate only the micro-organisms and not the ITO-coated substrate. Mass spectra were obtained from a voxel size 300 nm in diameter and 80 nm in depth. Figure III.c.5 plots the distribution of two dominant ions in the spectra with m/z 70.1 and 81.1. The traces are iso-lines corresponding to different peak intensities. The evolution of a bacterium's profile is clearly seen in Figure III.c.5a. The mass resolution of the TOF is not sufficient to univocally identify these ions.

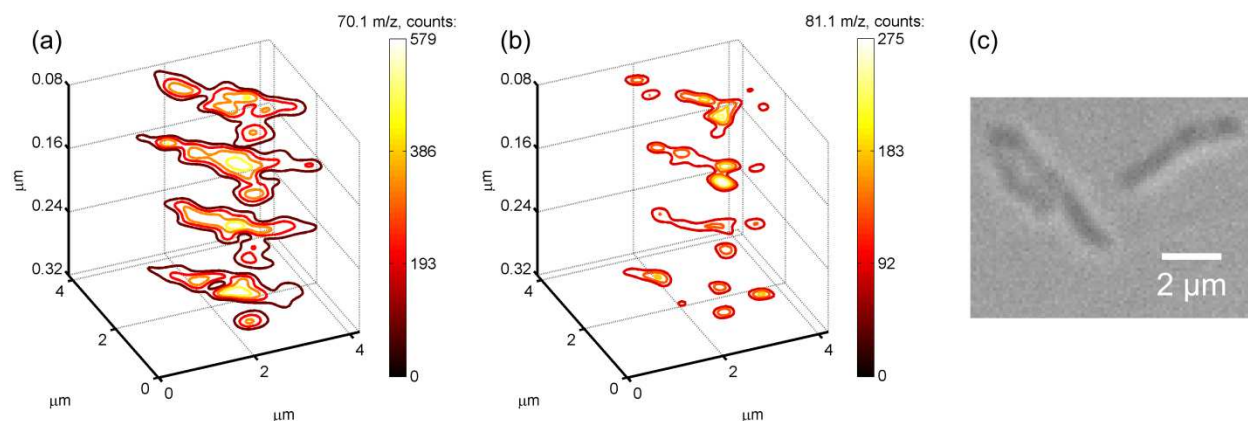


Figure III.c.5: Demonstration of 3D molecular imaging. 3D ion image of a *Mycobacterium smegmatis*. The iso-lines show the distribution of two significant fragments, m/z 70.1 (a) and 81.1 (b) detected by single-shot EUV TOF. The image is constructed from spline-interpolated $0.3 \times 0.3 \times 0.08 \mu\text{m}^3$ voxels. A confocal microscope image of the sample is shown (c).

III.d Discussion

The high lateral, 75 nm, and depth, 20 nm, resolution and high sensitivity of EUV TOF demonstrated in this work are the result of the unique properties of EUV light and of its interaction with organic solids. The use of $\lambda = 46.9 \text{ nm}$ laser light for MSI is optimal because: i) it can be focused into spots of $\sim 100 \text{ nm}$, significantly smaller than those obtained with UV light resulting in superior lateral resolution⁶; ii) its absorption depth is extremely shallow, i.e. $\sim 20 \text{ nm}$ ⁵³, thus, making it possible to ablate craters a few nanometers deep by controlling the laser fluence at the sample (Figure III.c.1a and Figure III.h.2a); and iii) the EUV photons can directly photoionize organic molecules. Moreover, the inherent high absorption of organic materials at $\lambda = 46.9 \text{ nm}$ eliminates the need for a matrix for ablation and ionization as used in UV LDI MSI.

The EUV laser-created plasmas are also fundamentally different from those created by nanosecond UV LDI, thereby impacting the characteristics of the ablation. In visible/UV laser

ablation, when the laser fluence is sufficient to ablate the material, the subsequent interaction is dominated by absorption of the laser radiation by inverse bremsstrahlung in the region of the plasma where the electron density approaches the critical density ($n_{ec} \sim 10^{22} \text{ cm}^{-3}$ for $\lambda = 333 \text{ nm}$). Therefore, once the plasma is created, the UV laser pulse can no longer reach the sample. However, in spite of this, the sample continues to ablate because heat is conducted from the critical electron density plasma region into the sample. In this heat-driven process ionization of atoms and molecules in the material is dominated by collision with free electrons heated by inverse bremsstrahlung, a process that leads to increased molecular fragmentation. In contrast for EUV light the critical density is larger than solid density (for $\lambda = 46.9 \text{ nm}$ $n_{ec} = 5 \times 10^{23} \text{ cm}^{-3}$). Therefore the heating of free-electrons by bremsstrahlung absorption is significantly reduced and the plasma is transparent to the incident EUV laser light. Instead the EUV laser light is predominantly absorbed by photoionization directly on the sample. The absence of significant thermal ablation processes is evident in the AFM profiles of Figure III.c.1b which are very smooth and show no damage beyond the ablated region. The mechanisms of ionization are also distinct from those in UV laser created plasmas. The EUV photons can ionize any molecule, making photoionization the dominant ionization mechanism over electron impact ionization⁵⁴. At the low fluences necessary to achieve nanoscale spatial resolution, most ions are singly charged, as observed for alanine and Nile red in Figure III.c.2.

The high 3D localization of the laser/matter interactions of EUV TOF and its superior sensitivity that produces mass spectra from zL volumes open new opportunities to visualize molecular composition at the nanoscale. Optimization of the interaction of the EUV laser light and organic materials in combination with post-ablation ionization²³ will contribute to extend the mass range. This, coupled with the superior 3D nanoscale resolution will maximize the potential

of EUV TOF MSI for life science applications by enabling, for example, nanoscale compositional imaging of intracellular structure⁵⁵, and the study of chemical interactions between a single micro-organism and its host⁴¹.

III.e Methods

III.e.i Samples and ablation conditions for each experiment

The samples used for the experiments were single or bilayers of organic compounds deposited by thermal evaporation onto a glass substrate coated with a 15÷30 nm thick conductive ITO layer. Thin films of polymethyl methacrylate (PMMA) with thickness varying between 60 and 350 nm spun over the ITO-covered glass substrates were used to assess the shape and volume of the ablation crater for each of the laser fluence conditions. The sequence of AFM crater profiles shown in Figure III.c.1b was obtained by placing the sample at the 1st order focus of the ZP and by attenuating the laser beam intensity by photoionization of Argon in a variable pressure gas cell. Instead the craters in Figure III.c.1 and Figure III.h.2a were obtained by ablating the sample when placed at the 3rd order focus of the ZP. The use of the 3rd order focus reduces the size of the ablation spot as a result of the ZP higher numerical aperture, and attenuates the laser fluence by 9× due to the reduction in the ZP efficiency¹⁹. The laser fluence necessary to ablate each of the craters was estimated from the FWHM diameter of the AFM profiles of Figure III.c.1b and from the laser pulse energy measured using a calibrated photodiode.

The sample used for the 2D composition imaging experiments was fabricated by patterning a trench in a ~120 nm thick resist film (Shipley 1818) using photolithography and

standard processing. The removal of the resist in the trench exposed the ITO coated glass substrate. The ion images of Figure III.c.4 were obtained using single shot laser ablation events with an elliptical laser spot with a FWHM minor axis of 300 nm, and a FWHM major axis of 500 nm. The fluence at the sample was estimated to be $\sim 0.43 \text{ J/cm}^2$. At this fluence, the depth of the ablation crater in the resist was 40 nm.

The sample used for the 3D imaging experiments was prepared by spinning a solution in which the *M. smegmatis* was diluted onto the ITO-covered glass substrate. A microscope image of the region of the sample interrogated is shown in Figure III.c.5c. Mass spectra were acquired from four consecutive single shot ablation events on the same sample spot at a laser fluence of 0.5 J/cm^2 . Then the sample was displaced with respect to the laser focal spot by 300 nm and the process was repeated. Each ablation event defined a voxel $0.3 \times 0.3 \times 0.08 \text{ }\mu\text{m}^3$. The ion images of Figure III.c.5 plot iso-lines showing the distribution of two of most salient fragments with m/z 70.1 and 81.1.

III.e.ii Data Analysis

The analysis of the mass spectra was carried out using a code developed with the scientific software MATLAB® that allows for mass calibration, spectra analysis with background subtraction, peak identification and image processing. All mass spectra contained signatures from singly-charged parent molecules ($Z = 1$).

For imaging, we used a threshold of 3σ the noise level to subtract noise and calculate the intensity under selected peaks in the mass spectrum. The depth profiles of Figure III.c.3 were constructed as follows. Selected peak areas of alanine corresponding to $m/z \leq 90$ and of Nile red with $90 < m/z \leq 319$ were summed up for each ablation event. Mean analyte signal amplitude

was obtained by averaging over a matrix of 4×4 ablation events in each layer. Since the ablated volume decreases with every consecutive ablation event following a sub-linear behavior, the mean peak amplitude for each analyte was normalized to the ablated volume and maximum mean analyte signal. The normalized mean amplitude versus depth is plotted in Figure III.c.3. The error bar on each point is the variance of the values of the amplitude.

A similar analysis was used to construct the 2D ion images of Figure III.c.4. In this case four ion peaks from the resist at m/z 74.0, 77.1, 91.1 and 121.1 were selected and their amplitudes were weight-averaged.

IV BIOLOGICAL APPLICATIONS OF THE SYSTEM

In this chapter a brief overview of vast field of lipids research in conjunction with cell membranes is given from the standpoint of available mass spectrometry imaging capabilities. EUV TOF performance in EUV-only ablation and ionization and in VUV post-ablation ionization modes is discussed on the examples of key cell membrane compounds.

IV.a Current state of cell membrane lipids research

Phospholipids play important role in animals organisms. They are a major constituent of the cell membrane, forming a lipid bilayer together with proteins and sterols. Due to their surfactant properties phospholipids are part of pulmonary surfactant providing flexibility to lungs necessary for breathing. Phospholipids can be classified in two groups: glycerophospholipids (phosphatidylcholine or DPPC, phosphatidylethanolamine or DPPE) and phosphosphingolipids (sphingomyelin etc.). All these three components will be covered in the next paragraph.

The molecular structure of phospholipids determines their amphiphilicity – ability to be both hydrophilic due to the presence of polar headgroup and lipophilic because of two fatty acyl chains in the tailgroup. It allows them to undergo interactions in both aqueous/polar and non-polar media. By minimizing surface energy they tend to align such that, for instance, in aqueous solution lipophilic tails are enclosed by hydrophilic heads. These forms are presented as semi-flat bilayers or globular structures like micelles and liposomes as shown on Figure IV.1.

4. A version of this chapter will be published in *Journal of American Society for Mass Spectrometry*: Kuznetsov et al. (2018)

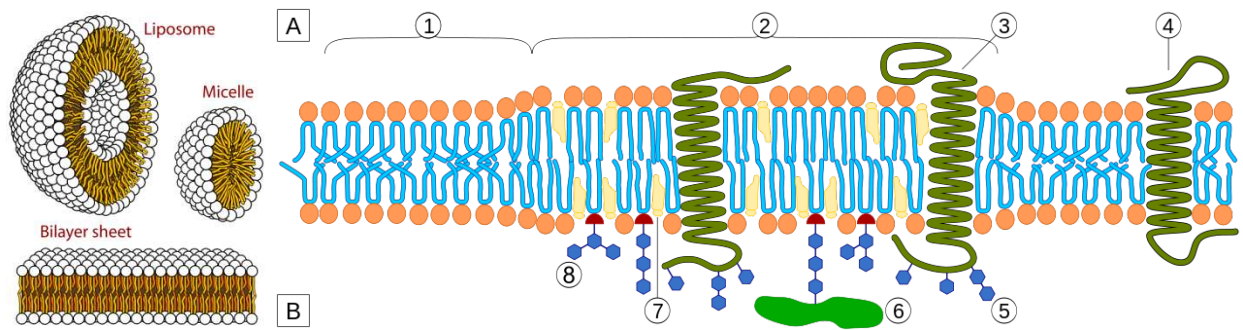


Figure IV.1: Lipid bilayer structures and common representation of the cell membrane with lipid raft (© A.J. Fijalkowski / CC-SA-2.5). Region 1 of the membrane is the standard lipid bilayer, region 2 - so-called lipid raft, 3 – transmembrane protein embedded in raft, 4 – non-embedded into raft protein, 5 – modification of glycolipids or glycoproteins by glycosylation, 6 – GPI-anchored protein, 7 – cholesterol, 8 – glycosylphosphatidylinositol (GPI) anchor.

The cell membrane separates the cell inner compartment from the external environment while providing certain communications and material transfer. Bilayers consisting purely of phospholipids are non-permeable. The real cell membrane has a lot of inclusions in the form of transmembrane proteins and glycosphingolipids. They are believed to group into structural domains called lipid rafts. As Figure IV.1 shows, these domains are also characterized by the elevated presence of cholesterol intercalated into both leaflets compacting and stabilizing this substructure. Lipid rafts essentially float in more fluid standard lipid bilayers.

Lipid rafts are defined as “small (10÷200 nm), heterogeneous, highly dynamic, sterol- and sphingolipid-enriched domains that compartmentalize cellular processes. Small rafts can sometimes be stabilized to form larger platforms through protein-protein and protein-lipid interactions.”⁵⁶ Models show that it is possible to form a stable heterogeneous structure with few tens of phospholipids and few proteins in it with the effective diameter of 5÷20 nm. As for the time scale of lipid raft formation and transitions, estimates vary by orders of magnitude, starting from 100 ns of half-lifetime⁵⁷. Such wide range used for characterization questions viability of the lipid raft theory. Modelling showed that it takes ~10 μs for domain formation⁵⁸. Label-free

imaging of lipid nanodomains reports that 50 nm domains have a lifetime of 220 ± 60 ms⁵⁹. Sceptics also debate about the exact protein/lipid ratio that should be considered as a lipid raft, and about the role these structural domains play in biophysical processes of the cell.

Mass spectrometry is considered to be one of the most accurate tools for membrane study: in principle it does not require external labelling that can alter the local chemistry. The analysis is performed by detecting the mass of molecules, and under certain conditions, can attain nanoscale spatial resolution in the lateral probing of the lipid domains. SIMS study of phospholipid samples is usually performed under static limit conditions, i.e. when primary ion dose density (PIDD) onto sample does not exceed $\sim 1 \times 10^{13}$ ions/cm². At this dose each primary ion hits only a fresh spot of the sample²⁹. Primary ions can be atomic, usually In, Cs, Ga, Au, or polyatomic, usually Bi₃, Au₃ or C₆₀. Lower mass ions can be focused to spots down to 50 nm. Unfortunately, this increases PIDD and limits the attainable resolution after merging (binning) of several small pixels to add up secondary molecular ion counts and reduce signal noise. Polyatomic projectiles distribute their energy among its constituent atoms, reduce chemical damage and increase secondary ion yield up to three orders of magnitude^{12,26}.

SIMS has been widely used for the study of model phospholipids system. For example, the lateral heterogeneity of DPPE-cholesterol and DPPC-cholesterol Langmuir-Blodgett films at various lipid concentrations was investigated by the combination of SIMS TOF and AFM⁶⁰. In this study it was found that unless the DPPE:cholesterol ratio is equal to 1:1, a homogeneous phase does not occupy the whole sample surface. In other cases a homogeneous phase is present only in domains, the size of which depends on the DPPE:cholesterol ratio. A 15 keV Ga⁺ ion beam at $< 1 \times 10^{12}$ ions/cm² dose could reveal DPPE by its entire tail group fragment with a 552 Da peak and cholesterol by M-H and M-OH peaks. An AFM study showed that DPPE:cholesterol

homogeneous phase is 0.85 nm thinner than pure DPPE domain due to its compaction by cholesterol. It was also found that the DPPC:cholesterol phase is thicker than pure DPPC layer. Thickness differences allow cholesterol-enriched membrane to co-localize spatially with DPPC on the outer and DPPE on the inner leaflets.

Despite clear advantages of detecting full or nearly full lipid molecules, tightly focused atomic beams were also successfully utilized in the study of lipid organization. A beam of 15 keV Cs^+ focused to 70 nm diameter with a dose of 5×10^{14} ions/cm² mapped the dorsal surface of fixated fibroblast cells. At high ion dose only small molecular fragments like CH and CN were detected and quantified. Identification of the sphingolipids from glycerolipids in the membrane was achieved by metabolic isotope enrichment with ¹⁵N (labeling mostly sphingolipids) and ¹³C (labeling all fatty acids to verify membrane integrity). After excluding all possible interferences, the study showed: a) sphingolipids domains are definitely present on the cell membrane, b) these domains can be as small as 200 nm and as big as μm -size, c) cholesterol depletion induced minor changes in sphingolipid domains distribution most likely due to cytoskeleton deformation. Overall, this study supports the presence of lipid rafts in nm-scaled domains. Also bigger sphingolipid domains do not require cholesterol and proteins for their formation and thus perform functions that are not traditionally attributed to lipid rafts. High resolution mass spectrometry analysis of membrane chemistry via isotope labeling was instrumental in proving evidence of the existence of larger lipid clustering that was thought before as a fluorophore-induced artifact. Unfortunately, these kinds of experiments require laborious sample preparation technique of isotope labeling.

An alternative method for extracting molecular information is by increasing molecular ion yield by metal coating or MALDI-like matrix application. Coating of the organic sample by a

few nm of gold showed a several times increase of secondary ion yield^{30,61} both in case of SIMS and MALDI. Even though the exact mechanism of this enhancement is unknown, some considerations come into play: a) migration of analyte onto gold nanoislands and corresponding desorption/ionization enhancement, b) metal acting as cationizing agent, c) a metal layer leads to higher energy localization at the surface by increasing the projectile stopping power. The gold-coating approach allowed mapping the distribution of phospholipids and cholesterol in the section of rat brain tissue with Bi_3^{2+} beam. MALDI matrix based on ionic liquid is also capable of aiding in better analyte ionization in SIMS. 300÷400 times improvement of molecular ion yield of DPPC and DPPE, as well as 40÷60 times improvement for cholesterol M-H and M-OH ion⁶².

The study of lipid rafts is highly problematic due to the highly dynamic and transient character of these structures. Experiments can cover long temporal and spatial scales. While molecular modeling, in contrast, covers short—up to μs —times and relatively small molecular assemblies. Bridging this gap will allow better experimental verification of the modeling results. For imaging the lipid rafts *in-vivo* the sample must be at least frozen and thus reveal a time-snap image of itself. Flash freezing of the sample and keeping it in a frozen and hydrated state under vacuum conditions will prevent it from drying out and losing the original internal organization. Other problems include: selective ionization affected by the matrix chemistry (*a priori* knowledge on matrix and analyte is required to decipher the data⁶³) and high internal energy of sputtered species. This causes excessive fragmentation and loss of signature peaks in mass spectra²⁴.

The implementation of post-ionization (PI) with a vacuum ultraviolet (VUV) source can overcome both of these limitations^{23,64}. Most organics exhibit ~10 eV or less ionization energy

(IE) because the more atoms compose the molecule, the lower ionization energy it has. Typical photoionization cross-section is $2\div 20$ Mbarn. The VUV span is $\sim 100\div 200$ nm, or $6\div 12$ eV, provides seamless ionization with little excess energy above IE threshold. PI results in more predictable and simpler fragmentation pattern, but in case of synchrotron at the expense of $1e3$ less sensitivity²⁵.

VUV sources generally have low pulse energy, i.e. 9th harmonic of YAG laser, or hard accessibility as in case of synchrotrons. A newly developed alternative post-ionization approach involves the use of strong field ionization by tunable femtosecond infrared (IR) lasers. SIMS primary ion beam of 20 keV C_{60}^+ combined with 1350 nm 40 fs pulse of $5e13$ W/cm² intensity showed $10\times$ molecular signal yield of β -estradiol molecule as compared to SIMS without such post-ionization⁶⁵. β -estradiol is a precursor for a family of biologically relevant sterols. The authors claim that with more powerful laser up to 2.5% of sample utilization efficiency can be reached.

IV.b Phospholipid detection on EUV TOF

EUV TOF mass spectrometer capabilities in the realm of lipids research were assessed on the example of: a) palmitic acid, sphingomyelin and POPC lipids in EUV-only mode, and b) DPPC and DPPE phospholipids in EUV and VUV PI modes. Palmitic acid (PA) is a common saturated fatty acid in animals. SM is present in the cell plasma membrane and is specifically abundant in myelin – a sheath that insulates signal transmission in neurons via axons. POPC is also part of the eukaryotic cells membrane.

Experimental results shown as averaged mass spectra and signal yield comparison to established techniques demonstrated that all phospholipids reveal some commonly observed

peaks except for parent molecules. Observed peaks lack any signature ones that would allow distinguishing these compounds from one another. Ternary mixture of POPC/SM/cholesterol deposited in the form of a Langmuir-Blodgett film changes the whole landscape of fragment formation except for peak at 184 Da as shown on Figure IV.3. A table with the molecular structure identification of the observed fragments is presented in Appendix VII.I. Typical ion yields shown in Table IV.1 demonstrate that SIMS has a similar yield of both fragments and molecules after $1e2$ yield correction factor is applied as was discussed in section II.c.iii. With optimization of the EUV TOF spectrometer and sample preparation, phospholipid-related study on this instrument can be more beneficial as compared to SIMS TOF.

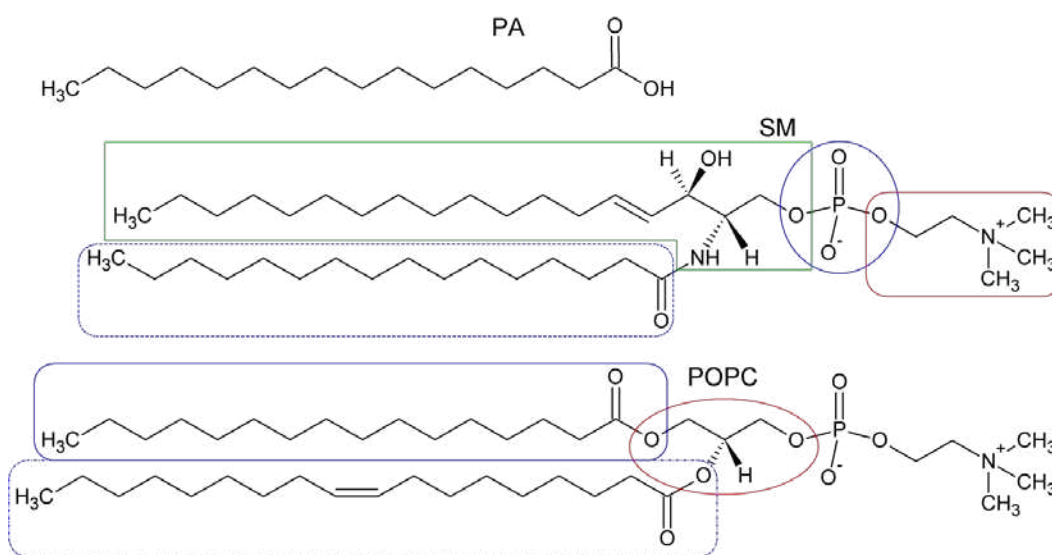


Figure IV.2: Molecular structures of palmitic acid (PA, C₁₆H₃₂O₂, 256.43 Da), egg sphingomyelin (SM, C₃₉H₇₉N₂O₆P, 710.97 Da) and 1-palmitoyl-2-oleoyl-sn-glycero-3-phosphocholine (POPC, C₄₂H₈₂NO₈P, 790.09 Da). Green polygon – sphingosine, blue rectangle – palmitic acid/acyl group, blue ellipse – phosphate, red rectangle – choline, blue dashed rectangle on POPC – oleic acid, red ellipse – glycerol.

Table IV.1: Yields of peak at 184 Da of PA, SM and POPC lipids. SIMS consistently demonstrates 1÷4 orders of magnitude higher secondary ion yield even when utilizing tightly focused low-mass projectiles. However, with 2 orders of magnitude offset from the stated yield it becomes comparable. SIMS secondary ion yields were taken directly from the cited literature without calculation.

Method	Sample preparation	Mass Da	Secondary ion counts	Photon/ion type	Primary photon/ion number	Secondary ion yield	Comments
EUV	Dry-spot. solution	184 PA	111	26.4 eV	9e7	1.2e-6	50-shot average
		184 SM	286		3e7	9.5e-6	25-shot average
		184 POPC	213			7.1e-6	
SIMS	Supported lipid bilayer	184 POPC		3.3 μm Bi_3^+ 40 μm C_{60}^+		1.7e-3	Gunnarson 2010 ²⁷
	LB bi- and monolayer	184 760 POPC		0.25 μm Bi_3^+		1.1e-2 4.4e-5	Prinz 2007 ⁶⁶
	LB film	184 POPC 142 SM		0.3 μm In^+		1e-4 5.5e-5	Piehowski 2009 ⁶⁷

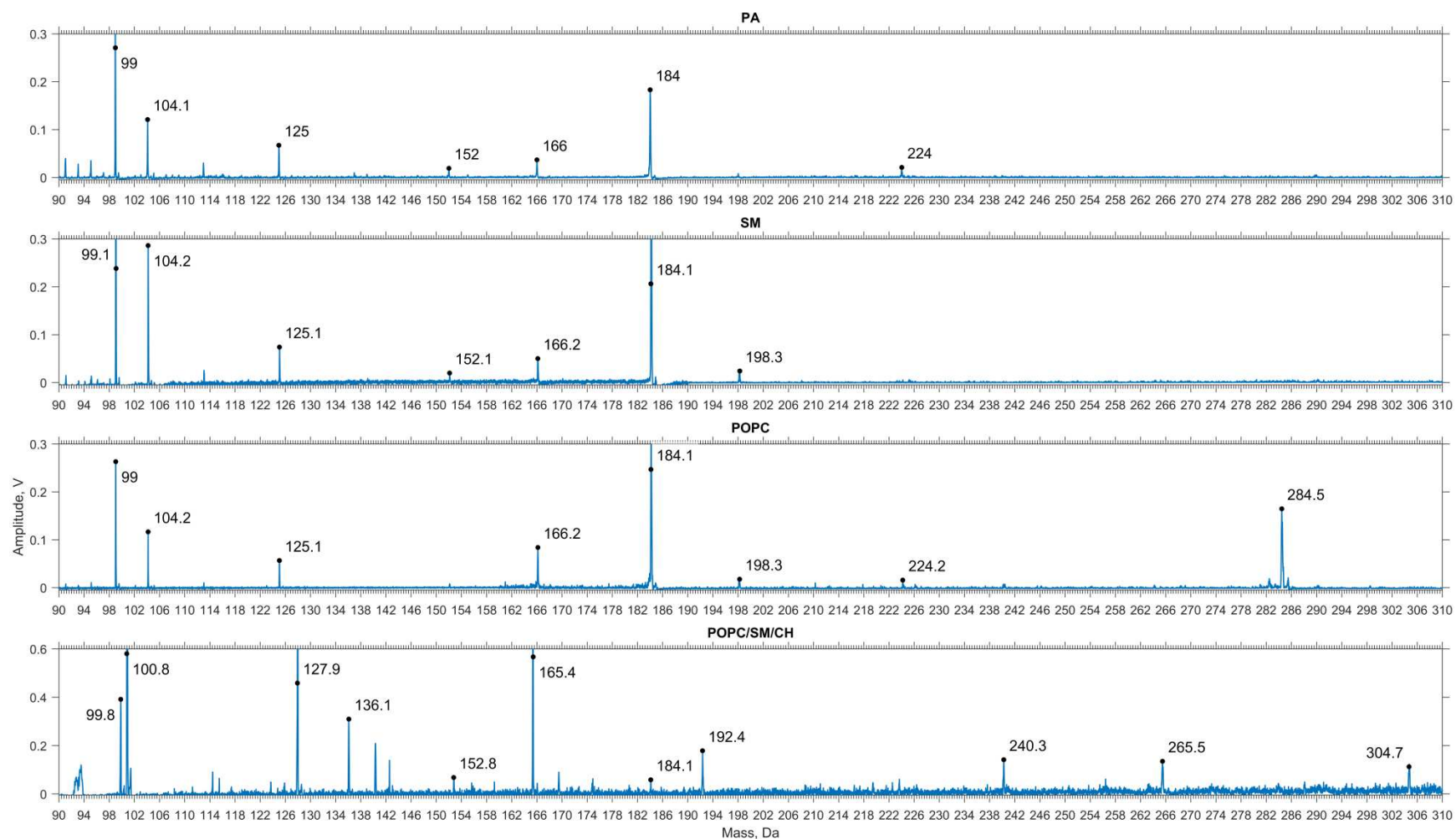


Figure IV.3: EUV TOF Mass spectra of palmitic acid, egg sphingomyelin, POPC and a mixture of these compounds with cholesterol (from top to bottom). All pure components were deposited by dry-spotting of simple solutions, i.e. in ethanol or water, while the mixture was deposited in 16 layers utilizing Langmuir-Blodgett technique. All pure components spectra show very similar peaks making them virtually indistinguishable. The 224 Da peak in POPC spectrum may stand for phosphocholine group and part of glycerol backbone⁶⁷.

DPPC and DPPE phospholipids were studied in their pure forms in EUV-only and VUV PI modes of the EUV TOF instrument. Sample preparation was altered too: spin-coating of 3 mg/mL chloroform solutions of each phospholipid were compared to PVD-deposited powders. No significant differences, except for minute volatility of some peaks that could become signature ones, were discovered. More detailed and longer runs were mostly performed using PVD-deposited samples. DPPC is the major component of pulmonary surfactants, and is the main constituent to form exoplasmic leaflet of the cell membrane. It is a principal phospholipid in animals. DPPE is mainly present in the cytoplasmic leaflet of the lipid bilayer of the membrane; it is also a principal phospholipid in bacteria.

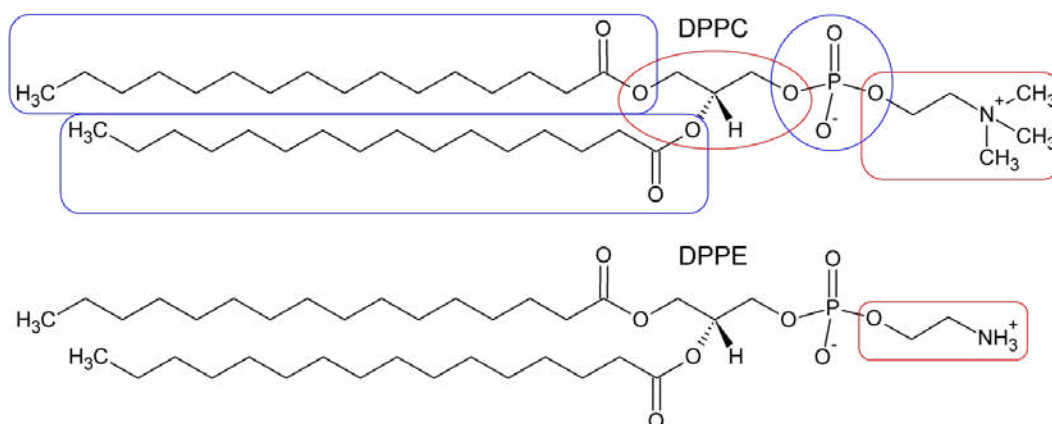


Figure IV.4: Molecular structures of dipalmitoylphosphatidylcholine (DPPC, 1,2-dipalmitoyl-*sn*-glycero-3-phosphocholine, $C_{40}H_{80}NO_8P$, 734.04 Da) and dipalmitoylphosphoethanolamine (DPPE, 1,2-dipalmitoyl-*sn*-glycero-3-phosphoethanolamine, $C_{37}H_{74}NO_8P$, 691.96 Da). Red ellipse – glycerol, blue ellipse – phosphate, red rectangle – choline or ethanolamine correspondingly. Phosphate with choline form polar (hydrophilic) headgroup of the phospholipid. Glycerol backbone with aliphatic chains is a non-polar lipophilic tailgroup.

There was no improvement of ion counts by converting from EUV-only to VUV PI mode as shown on the example of the heaviest fragment with mass 552 Da in Figure IV.6. Traditionally this peak is attributed to the tailgroup of two aliphatic chains with glycerol backbone, but fragmentation analysis done in the ACD/MS fragmenter software

(Appendix VII.1) points out to other interpretations as well. The use of VUV PI did not reveal any new peaks otherwise well presented on the EUV-only mass spectra peaks. Hence the use of VUV PI mode for related DPPC or DPPE detection experiments is currently unnecessary.

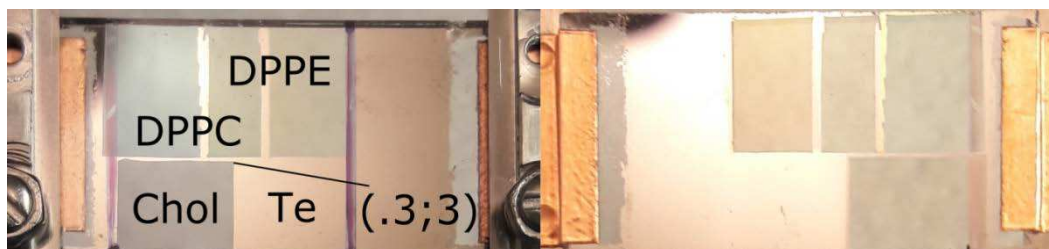


Figure IV.5: Picture of the PVD-deposited film, including Te and cholesterol for mass calibration and verification of the optimal VUV PI parameters. DPPC and DPPE were deposited separately and partially overlapped in the middle section with DPPE on top. All individual organic films have ~100 nm thickness, while Te – 50 nm. Left part of the picture shows the samples as seen from behind in the optical microscope. The right part is the front side of the sample exposed to the EUV laser.

Table IV.2: Comparison of the highest 552 Da mass fragment yield of DPPC and DPPE obtained on the EUV TOF system to parent molecular signal yield obtained on SIMS at high-resolution imaging settings. In addition to the capability of detecting parent molecules, SIMS also demonstrates 2÷5 orders of magnitude higher of sensitivity-corrected yield without using post-ionization.

Method	Sample prep.	Mass Da	Secondary ion counts	Photon/ion type	Primary photon/ion number	Secondary ion yield	Comments
VUV PI	PVD	552 DPPC	12	10.5 eV	6e11	2e-11	100-shot average
		552 DPPE	9			1.5e-11	
EUV		552 DPPC	36	26.4 eV	1.2e9	3e-8	
		552 DPPE	33			2.8e-8	
SIMS	Spin-coating	734 DPPC		0.2 $\mu\text{m Ga}^+$ 50 $\mu\text{m C}_{60}^+$		7.2e-5 5.8e-2	Ostrowski 2005 ²⁶
	LB film	735 DPPC		1 $\mu\text{m Ga}^+$		4e-5	Bourdos 2000 ⁶⁸

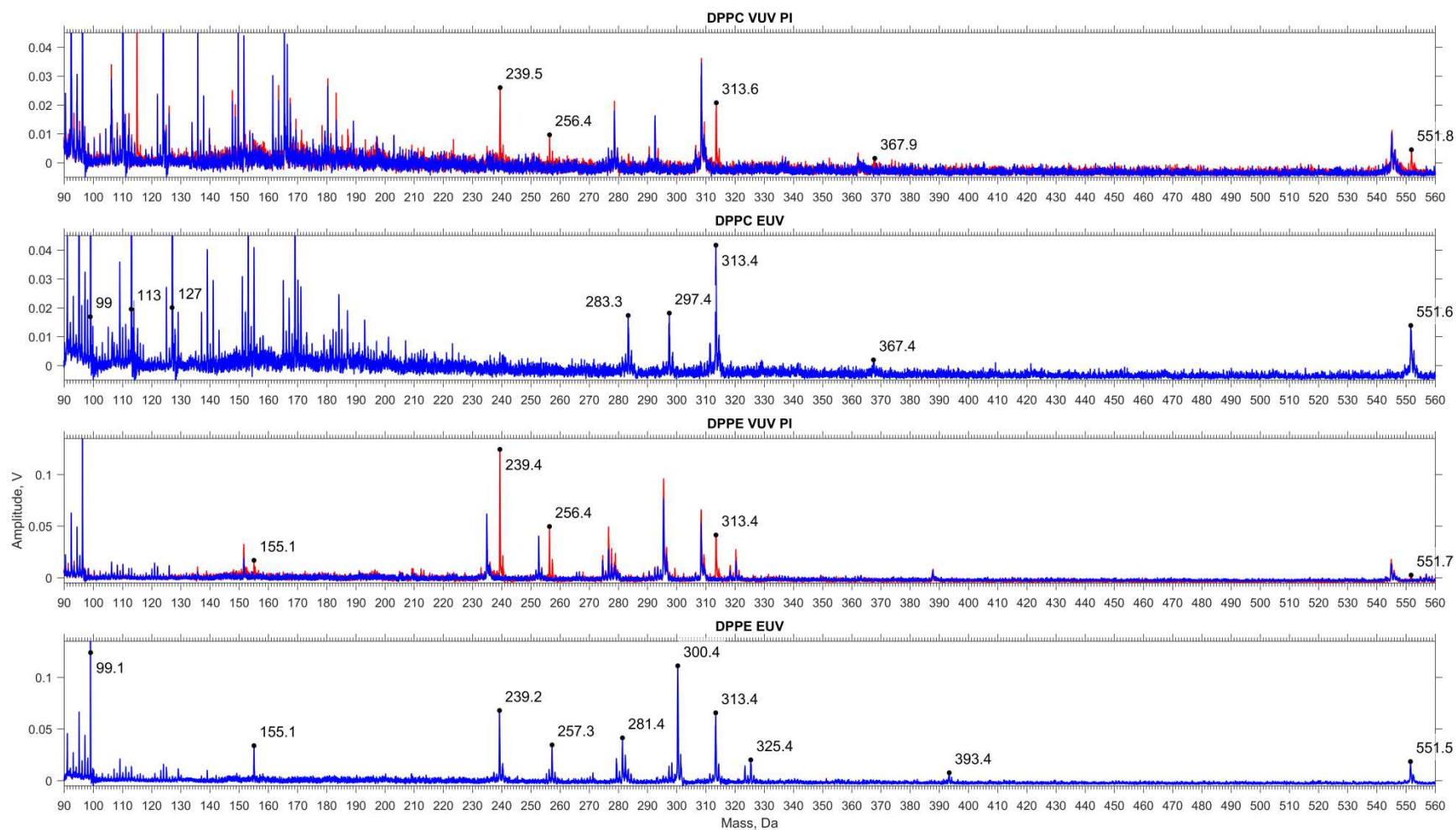


Figure IV.6: Mass spectra of DPPC and DPPE lipids obtained in VUV PI and EUV-only modes. Red spectral lines show VUV PI signal, blue lines in the same plots show the background signal at the same conditions without focused VUV light present. All distinguishable VUV PI peaks are also present in the EUV spectra, meaning that there is no necessity in using VUV PI mode in detecting these fragments.

IV.c Detection of cholesterol by post-ablation ionization

Direct ionization of analyte molecules implies complex mechanisms that are often poorly understood even though the instruments relying on this type of ionization (SIMS or MALDI) are widely accepted in scientific community. Among common problems are: low yield of ions of interest (~ 10 ions from $0.5 \times 0.5 \mu\text{m}^2$)¹², chemical environment interplay (matrix effect), introduction of electronic, fragment- or non-analyte-related noise. In contrast, ionization of neutral species in the ejected plume based on separate ionization source can eliminate or decrease negative effects. There are many more neutrals in low-temperature plasmas than ions. And since neutrals do not undergo initial ionization, their internal energy is lower, which helps to preserve complex molecules. Neutrals desorption yield is also less susceptible to the local chemical environment²⁵. The use of soft post-ionization (PI) sources also decreases signal noise by avoiding ionization of background gases or matrices²³.

Detection of cholesterol in the EUV TOF mass spectrometer in VUV PI mode showed the necessity of a softer means of ionization in identifying fragile molecular compounds. Cholesterol ($\text{C}_{27}\text{H}_{46}\text{O}$, 386.65 Da, ionization energy $\leq 10 \text{ eV}$ ⁶⁹) is a sterol compound. It is the principle sterol synthesized by all animals. Cholesterol serves as precursor for the biosynthesis of steroid hormones (testosterone, progesterone), bile acid and vitamin D. Animal cell membranes contain about 30% of cholesterol, which modulates membrane fluidity and structure. Embedment in the cell membrane is performed by binding of the cholesterol hydroxyl group with polar heads of phospho- and sphingolipids, placing steroid part of the molecule within the bilayer among lipid tailgroups enhancing the membrane packing.

A thin cholesterol sample (Figure IV.5) was generated by means of physical vapor deposition, i.e. sublimation in vacuum through ohmic heating of tungsten boat with cholesterol

powder with ~100 A current for a few minutes. At 386.6÷421.31 K (NIST/TRC Web Thermo Tables) cholesterol sublimates and forms ~100 nm thick uniform film on substrate.

Figure IV.7 shows molecular ion of cholesterol detected at 386.7 Da in VUV PI mode with EUV laser attenuated to 1 μ J per pulse. At higher EUV laser power the signal decays while at lower powers an undetectable amount of analyte is ablated. A 34 mV amplitude M^+ peak is seen on the 100-shot averaged spectrum at the optimal conditions. Integration of the peak results in ~30 counts while average noise amplitude is about 5 mV. The peak at 387.7 Da stands for the cholesterol isotopologue and not for $[M+H]^+$ ion. Firstly because the ratios of the M and M+1 peaks matches the predicted 1:0.3 ratio based on the natural isotope abundance. Secondly, cholesterol fragment peaks F (275.7, 368.8 and 371.8 Da) exhibit the same pairing with F+1 peak. Another reason for stating that M+1 or F+1 peaks stand for isotopologues rather than protonated molecules is that SPI ionization happens at ~0.5 mm distance from the sample surface. The plasma density there is much less than the solid density hindering chemistry-assisted ionization.

Observed fragments perfectly correlate with other experiment that used 6 mJ/pulses of 1064 nm Nd:YAG laser for desorption and tunable synchrotron radiation for post-ionization⁶⁹. It was discovered that the onset of ionization happens around 10 eV and at higher photon energies fragments intensity elevates. The mass of fragment peaks was computationally verified⁶⁹ with molecular structures and are presented in Table IV.3.

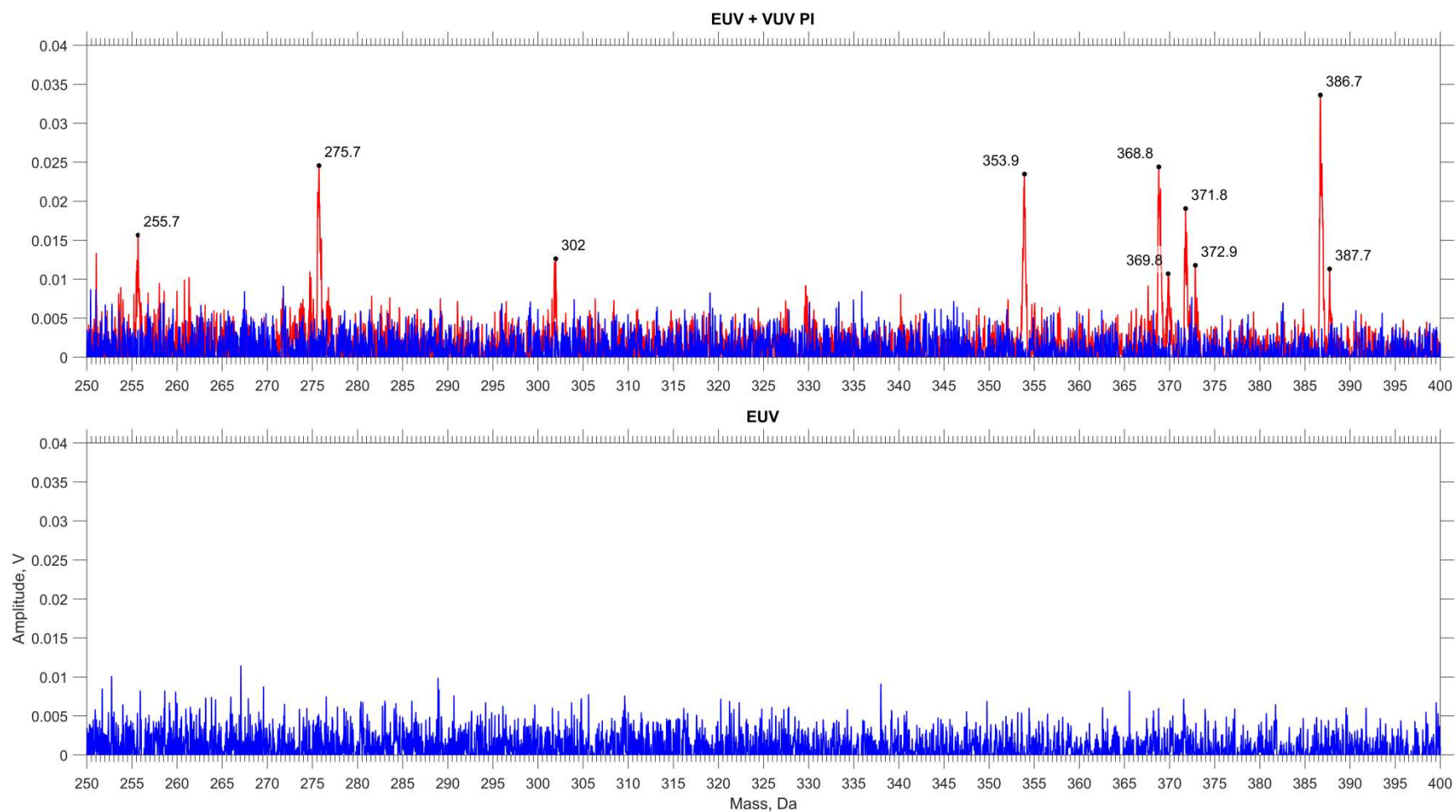
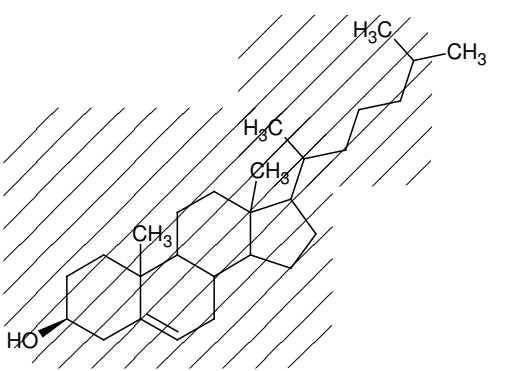
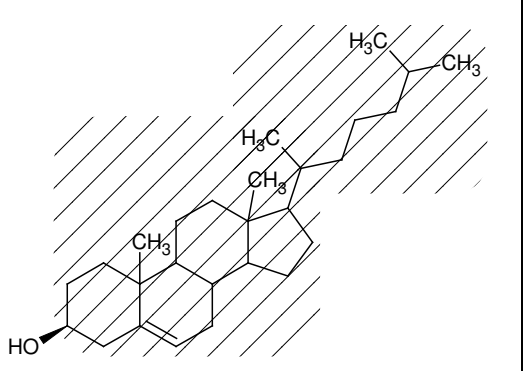
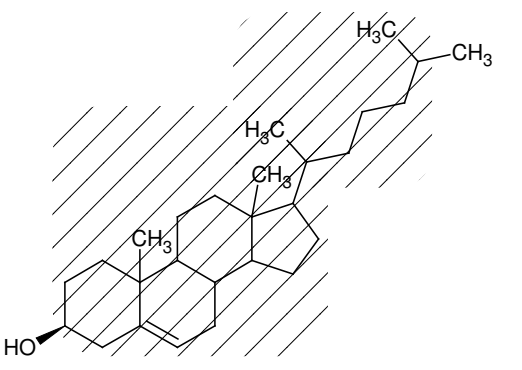
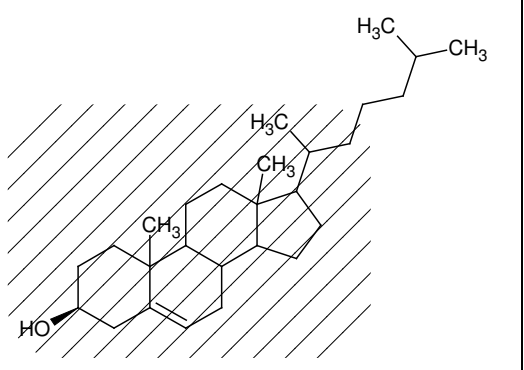
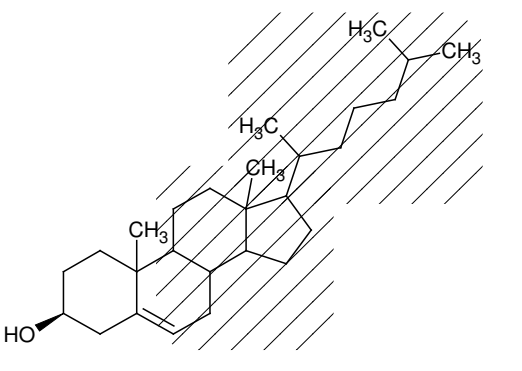
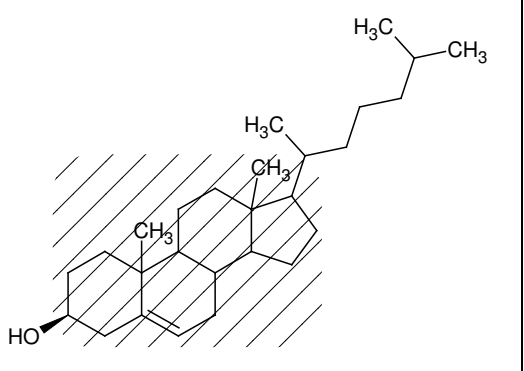


Figure IV.7: Averaged cholesterol spectra in VUV PI (top) and EUV only (bottom) mode. Red spectral lines identify the VUV PI signal; blue line on the same plot shows the background signal that was obtained at the same conditions excluding focused VUV light. Bottom plot is the EUV-only signal showing nothing but noise. This result indicates that cholesterol together with its high mass fragments can be detected only by using VUV light in PI mode.

Table IV.3: Cholesterol fragments obtained by photodissociative 10.5 eV post-ablation ionization taken from the literature⁶⁹. VUV PI results of the EUV TOF system exhibit great correlation with this data.

Da	Fragment	Da	Fragment
371		368	
353		301	
275		255	

For single pixel imaging a signal-to-noise ratio (SNR) has to be⁷⁰ ≥ 5 . A single shot spectra analysis was performed to validate if this requirement would be met. Data was collected in single shot mode resulting in 14 mV of M^+ peak intensity after 100-shot averaging. The single shot spectra on Figure IV.8 shows that the amplitude of the noise reaches almost 200 mV. It is at

the same level as the signal peaks are. SNR for imaging is traditionally determined as the ratio of average signal value μ_{sig} to the standard deviation σ_{noise} of the background:

$$SNR = \frac{\mu_{sig}}{\sigma_{noise}} = \frac{405 \text{ mV}}{166 \text{ mV}} = \frac{22 \text{ counts}}{9 \text{ counts}} = 2.44 \quad (\text{IV.13})$$

To facilitate $SNR \geq 5$ for single shot imaging of pure cholesterol the average signal count should be twice more, above 40 counts. Alternatively, noise should be reduced. As for real-world samples with diluted cholesterol content, SNR should be improved even further. Table IV.4 compares ion yield in EUV TOF and various SIMS systems that are already capable of mapping cholesterol distribution in biological tissues.

Table IV.4: Comparison of cholesterol molecular and quasi-molecular yield in different mass spectrometers. SIMS studies utilize various primary ion types and setup configurations, consistently showing sensitivity-corrected 5÷7 magnitude higher yield of cholesterol-specific signal.

Method	Sample preparation	Mass, Da	Secondary ion counts	Photon/ion type	Primary photon number	Secondary ion yield	Comments
VUV PI	PVD	386	29	10.5 eV	6e11	4.8e-11	100-shot averaged spectrum Figure IV.7
			16			2.7e-11	100-shot averaged spectrum Figure IV.8
SIMS	Corpus callosum of rat brain	385		$\sim \mu\text{m Bi}^+$ $0.1 \mu\text{m Bi}_3^+$		$8.3\text{e-}5$ $7\text{e-}4$	Brunelle 2005 ²⁹
	Spin-coating			$0.2 \mu\text{m Ga}^+$ $50 \mu\text{m C}_{60}^+$		$1.9\text{e-}4$ $9.8\text{e-}3$	Ostrowski 2005 ²⁶
	PVD	369		$5 \mu\text{m C}_{60}^+$		$1\text{e-}4 \div 1\text{e-}5$	Kozole 2008 ⁷¹
		147		$0.3 \mu\text{m In}^+$		$5.5\text{e-}5$	Piehowski 2009 ⁶⁷

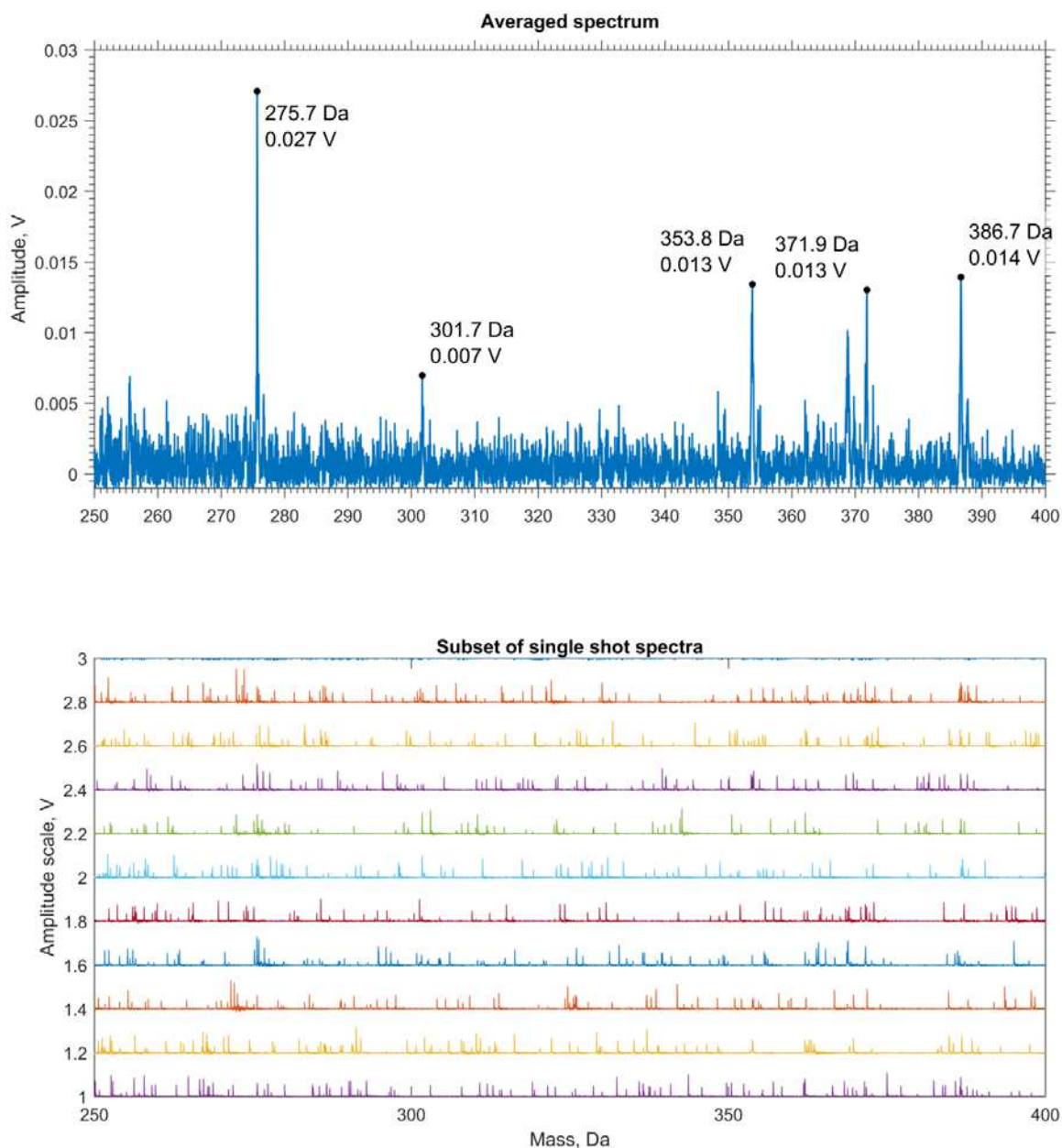


Figure IV.8: Cholesterol mass spectra in VUV PI mode. Top figure shows 100-shot averaged spectrum of the PVD film. Bottom figure is a subset of ten ($100 \div 15$) single shot spectra used for constructing the average. Single shot spectra noise amplitude is $\sim 0.15 \div 0.2$ V making similarly intense peaks indistinguishable. For single shot imaging of diluted cholesterol in biological samples SNR has to be increased several times.

EUV TOF has demonstrated that its sensitivity in fragments detection of POPC, PA and SM with masses up to 300 Da is similar to SIMS TOF. There is a decent probability to see intact

molecules of them in VUV PI mode as in case of cholesterol. 552 Da fragments of DPPC and DPPE phospholipids were detected by EUV ablation and ionization only as well as in VUV PI mode. When the library of detectable compounds is formed, a proper analytical application niche in microbiology can be selected. After increasing SNR through the system upgrade an investigation of spatial organization and chemistry of the cell membranes might be possible at nanoscale resolution. Achieving higher resolution imaging of the cell that is flash frozen and thus representing a time snap of its structure will facilitate verification of accurate computer simulations that usually operate with small material quantities during short time intervals.

V CONCLUSIONS AND OUTLOOK

This dissertation described the development and first demonstration of an extreme ultraviolet (EUV) laser ablation mass spectrometer for composition imaging in 3D with nanoscale resolution. This breakthrough was achieved by the implementation of a unique EUV laser for ablation and ionization. The 46.9 nm wavelength laser beam can be focused to <100 nm spots providing down to 80 nm spatial resolution when the instrument is used in imaging mode. The shallow penetration depth results in 20 nanometers depth resolution as was shown on an example of an organic bilayer. The 26.4 eV energy per photon exceeds the ionization energy of any element in the periodic table or molecule rendering high single photon ionization efficiency. The sensitivity of the EUV TOF instrument was measured to be ~0.02 amol using alanine as the analyte which is 20× better than that of SIMS TOF¹¹.

It was shown that EUV TOF allows for constructing 3D sub-micron images of a single mycobacterium. However, the detection mass range was limited, specifically for biological applications where high mass molecules carry significant information. Towards this goal, a post-ablation ionization (PI) setup was introduced into the system. The secondary light source for PI is YAG laser that can operate in UV (355 nm) or VUV (118 nm). By using high intensity UV laser pulses a sensitivity gain of 2.5× was obtained in the atomic signal of trace elements. Soft ionization by 10.5 eV photons revealed the biology-relevant cholesterol molecular signal at 386.7 and 387.7 Da for the first time. Even though VUV PI mode did not provide additional molecular information on phospholipids, also a component in a cell's membrane, compared to EUV-only mode, the signal yield of EUV TOF in select cases was shown to be comparable to the

published results of SIMS TOF. Altogether these achievements proved the viability of the EUV TOF concept as a high resolution IMS technique for molecular and trace element detection.

In future work, more understanding has to be gained on the most optimal ionization strategy. For example, it was shown recently that VUV ablation and ionization can result in lesser fragmentation of similar organic compounds that were tested with EUV TOF⁷². An alternative way to promote softer ionization is cryocooling of a flash-frozen biological specimen. Continuous supply of water vapor influx to the sample in order to form a thin ice sheet would aid in water-to-analyte proton transfer. Alternatively, signal yield increase and mass range improvements could possibly be implemented using a femtosecond tunable IR laser in PI mode.

There are other considerations that could lead to improvements in sensitivity and mass range of EUV TOF. Currently EUV TOF uses a dual-plate microchannel plate (MCP) detector that has to operate at the highest bias in order to produce a significantly large amplified signal on the digitizer. In such mode, noise grows faster than ion-to-electron gain that reduces the signal-to-noise ratio (SNR). A Z-gap MCP consisting of three plates could increase gain up to two orders of magnitude while being moderately biased and thus less noisy. However, certain precautions must be exercised. First, reflection and scattering of EUV light should be significantly quenched as compared to the present geometry. Otherwise the MCP when biased with a DC voltage will saturate on the laser pulse rendering its inability to detect any mass spectra. Second, saturation by the high intensity low mass peaks should be avoided with the implementation of a pulsed electrode arrangement in front of MCP. This add-on would divert intense ion bunches from the sensitive detector area. An alternative way for atomic trace spectroscopy applications would be the use of a magnetic sector analyzer instead of a TOF.

The imaging resolution, positioning precision and stability of EUV TOF have been optimized to achieve a record 80 nm lateral resolution. Further improvements can be obtained by upgrading long-travel piezo translators. It would be possible to carry out quantitative analysis with EUV TOF. To implement this capability the vacuum chamber will need to be converted to the ultra-high vacuum specifications. Otherwise all surfaces inside the vacuum vessel, including the sample surface, are covered by a monolayer of H and carbonaceous compounds in a matter of seconds. The signal from these low mass carbonaceous compounds and of water produce interferences on every spectrum at a few Hz acquisition rate.

With further development the EUV TOF IMS could find applications in microbiology to help understand lipid rafts variations in composition, dimensions and functions. Detection of unfragmented cholesterol with EUV TOF PI and the ability to differentiate it from phospholipids with high imaging resolution will allow for localization of lipid domain boundaries. This experiment can be performed in three stages. A model of the cell membrane can be analyzed on Langmuir-Blodgett films with varying ratios of cholesterol and phospholipids. The second stage of experiment may include imaging of the deposited extract from the cells containing natural ratios of the components. Lastly, *in situ* imaging of a flash-frozen cell can be attempted at the nanoscale resolution. Such step-by-step verification process of cell membrane structural domains will allow for drawing accurate conclusions on the lipid raft structure and its role in the animal cell membrane processes.

There are many other potential applications that could benefit from EUV TOF nanoscale 3D resolution and attomole sensitivity. In pharmacology and related areas of life sciences, an instrument with nanometer resolution could be used to study, for example, drug or nutrient penetration at the single cell level, and this would advance fundamental knowledge for

understanding drug and nutrient intake. In materials science and chemistry, EUV TOF could be used to investigate nanoscale catalysis on surfaces and on nanostructures and investigate how dimensions influence chemistry, to map isotopic distributions in actinide-containing samples with unsurpassed spatial resolution or identify organic distributions in microdomains in atmospheric aerosols which are important from environmental considerations.

VI REFERENCES

- 1 Griesche, A. *et al.* Three-dimensional imaging of hydrogen blister in iron with neutron tomography. *Acta Materialia* **78**, 14-22, doi:10.1016/j.actamat.2014.06.034 (2014).
- 2 Tian, H., Six, D. A., Krucker, T., Leeds, J. A. & Winograd, N. Subcellular chemical imaging of antibiotics in single bacteria using C60-secondary ion mass spectrometry. *Analytical Chemistry* **89**, 5050-5057 (2017).
- 3 Green, T. *et al.* Characterization of extreme ultraviolet laser ablation mass spectrometry for actinide trace analysis and nanoscale isotopic imaging. *Journal of Analytical Atomic Spectrometry* **32**, 1092-1100, doi:10.1039/c7ja00088j (2017).
- 4 Eberlin, L. S. *et al.* Cholesterol Sulfate Imaging in Human Prostate Cancer Tissue by Desorption Electrospray Ionization Mass Spectrometry. *Analytical Chemistry* **82**, 3430-3434, doi:10.1021/ac9029482 (2010).
- 5 Attwood, D. *Soft x-rays and extreme ultraviolet radiation: principles and applications.* (Cambridge University Press, 2000).
- 6 Vaschenko, G. *et al.* Nanometer-scale ablation with a table-top soft x-ray laser. *Opt. Lett.* **31**, 3615-3617, doi:10.1364/ol.31.003615 (2006).
- 7 Berrill, M. *et al.* Warm photoionized plasmas created by soft-x-ray laser irradiation of solid targets. *JOSA B* **25**, B32-B38 (2008).
- 8 Kuznetsov, I. *et al.* in *SPIE Optical Engineering+ Applications.* 958905-958905-958909 (International Society for Optics and Photonics).
- 9 Pikuz, T. *et al.* Optical features of a LiF crystal soft x-ray imaging detector irradiated by free electron laser pulses. *Optics express* **20**, 3424-3433 (2012).
- 10 Kuznetsov, I. *et al.* Nanoscale 3D molecular imaging by extreme ultraviolet laser ablation mass spectrometry: a new analytical tool for the organic and inorganic solid state. *Abstracts of Papers of the American Chemical Society* **249** (2015).
- 11 Kuznetsov, I. *et al.* Three-dimensional nanoscale molecular imaging by extreme ultraviolet laser ablation mass spectrometry. *Nature Communications* **6**, 1-6, doi:10.1038/ncomms7944 (2015).
- 12 Vickerman, J. C. Molecular imaging and depth profiling by mass spectrometry—SIMS, MALDI or DESI? *Analyst* **136**, 2199-2217 (2011).
- 13 Heinbuch, S., Grisham, M., Martz, D. & Rocca, J. J. Demonstration of a desk-top size high repetition rate soft x-ray laser. *Optics Express* **13**, 4050-4055 (2005).
- 14 Anderson, E. H. Fabrication technology and applications of zone plates. *X-Ray/EUV Optics for Astronomy and Microscopy* **1160**, 2-11 (1989).
- 15 Dong, F. *et al.* Formation and distribution of neutral vanadium, niobium, and tantalum oxide clusters: Single photon ionization at 26.5eV. *The Journal of Chemical Physics* **125**, 164318, doi:10.1063/1.2358980 (2006).
- 16 Rocca, J. J. *et al.* Demonstration of a discharge pumped table-top soft-x-ray laser. *Physical Review Letters* **73**, 2192-2195, doi:10.1103/PhysRevLett.73.2192 (1994).
- 17 Ganeev, R. A., Kulagin, I. A., Usmanov, T. & Khudaiberganov, S. T. A study into the stimulated-emission of the coherent radiation at $\lambda=118.2$ nm from inert-gases. *Kvantovaya Elektronika* **9**, 2508-2514 (1982).

- 18 Brizuela, F. *et al.* Reflection mode imaging with nanoscale resolution using a compact extreme ultraviolet laser. *Optics Express* **13**, 3983-3988, doi:10.1364/OPEX.13.003983 (2005).
- 19 Burian, T., Kuznetsov, I., Juha, L., Rocca, J. & Menoni, C. Vol. 5-6 259-263 (Institute of Physics of the ASCR, v. v. i., 2015).
- 20 Kuznetsov, I. *et al.* Composition depth profiling by soft x-ray laser-ablation mass spectrometry. *SPIE Optical Engineering + Applications* **8849**, 1-6 (2013).
- 21 Anderson, E. H. *et al.* Nanofabrication and diffractive optics for high-resolution x-ray applications. *Journal of Vacuum Science & Technology B: Microelectronics and Nanometer Structures Processing, Measurement, and Phenomena* **18**, 2970-2975, doi:10.1116/1.1321282 (2000).
- 22 Takahashi, L. K., Zhou, J., Wilson, K. R., Leone, S. R. & Ahmed, M. Imaging with mass spectrometry: a secondary ion and VUV-photoionization study of ion-sputtered atoms and clusters from GaAs and Au. *The Journal of Physical Chemistry A* **113**, 4035-4044 (2009).
- 23 Hanley, L. & Zimmermann, R. Light and Molecular Ions: The Emergence of Vacuum UV Single-Photon Ionization in MS. *Analytical Chemistry* **81**, 4174-4182, doi:10.1021/ac8013675 (2009).
- 24 Zhou, J., Takahashi, L. K., Wilson, K. R., Leone, S. R. & Ahmed, M. Internal Energies of Ion-Sputtered Neutral Tryptophan and Thymine Molecules Determined by Vacuum Ultraviolet Photoionization. *Analytical Chemistry* **82**, 3905-3913, doi:10.1021/ac1004629 (2010).
- 25 Takahashi, L. K. *et al.* Vacuum-Ultraviolet Photoionization and Mass Spectrometric Characterization of Lignin Monomers Coniferyl and Sinapyl Alcohols. *Journal of Physical Chemistry A* **115**, 3279-3290, doi:10.1021/jp111437e (2011).
- 26 Ostrowski, S. G. *et al.* Secondary ion MS imaging of lipids in picoliter vials with a buckminsterfullerene ion source. *Analytical Chemistry* **77**, 6190-6196, doi:10.1021/ac0508189 (2005).
- 27 Gunnarsson, A., Kollmer, F., Sohn, S., Hook, F. & Sjovall, P. Spatial-Resolution Limits in Mass Spectrometry Imaging of Supported Lipid Bilayers and Individual Lipid Vesicles. *Anal. Chem.* **82**, 2426-2433, doi:10.1021/ac902744u (2010).
- 28 Saleem, M. & Galla, H. J. Surface view of the lateral organization of lipids and proteins in lung surfactant model systems-A ToF-SIMS approach. *Biochimica Et Biophysica Acta-Biomembranes* **1798**, 730-740, doi:10.1016/j.bbamem.2009.10.011 (2010).
- 29 Brunelle, A., Touboul, D. & Laprevote, O. Biological tissue imaging with time-of-flight secondary ion mass spectrometry and cluster ion sources. *Journal of Mass Spectrometry* **40**, 985-999, doi:10.1002/jms.902 (2005).
- 30 McDonnell, L. A., Heeren, R. M. A., de Lange, R. P. J. & Fletcher, I. W. Higher sensitivity secondary ion mass spectrometry of biological molecules for high resolution, chemically specific imaging. *Journal of the American Society for Mass Spectrometry* **17**, 1195-1202, doi:10.1016/j.jasms.2006.05.003 (2006).
- 31 Kuznetsov, I. *et al.* in *X-ray Lasers and Coherent X-ray Sources: Development and Applications*. 102430G (International Society for Optics and Photonics).
- 32 Swanson, D. E. *et al.* Single vacuum chamber with multiple close space sublimation sources to fabricate CdTe solar cells. *Journal of Vacuum Science & Technology A: Vacuum, Surfaces, and Films* **34**, 021202, doi:10.1116/1.4941071 (2016).

- 33 Yeh, J. & Lindau, I. Atomic subshell photoionization cross sections and asymmetry parameters: $1 \leq Z \leq 103$. *Atomic data and nuclear data tables* **32**, 1-155 (1985).
- 34 Munshi, A. *et al.* (Journal of Electronic Materials, 2018).
- 35 Tatsumi, K., Muto, S. & Yoshida, T. Detection of hydrogen at localized regions by unoccupied electronic states in iron carbides: Towards high spatial resolution mapping of hydrogen distributions. *Journal of applied physics* **101**, 023523 (2007).
- 36 Hanna, T., Hiramatsu, H., Sakaguchi, I. & Hosono, H. Highly hydrogen-sensitive thermal desorption spectroscopy system for quantitative analysis of low hydrogen concentration ($\sim 1 \times 10^{16}$ atoms/cm³) in thin-film samples. *Review of Scientific Instruments* **88**, 053103 (2017).
- 37 Qin, Z. Y., Caruso, J. A., Lai, B., Matusch, A. & Becker, J. S. Trace metal imaging with high spatial resolution: Applications in biomedicine. *Metallomics* **3**, 28-37, doi:10.1039/c0mt00048e (2011).
- 38 Becker, J. S. Bioimaging of metals in brain tissue from micrometre to nanometre scale by laser ablation inductively coupled plasma mass spectrometry: State of the art and perspectives. *International Journal of Mass Spectrometry* **289**, 65-75, doi:10.1016/j.ijms.2009.10.011 (2010).
- 39 Kraft, M. L., Weber, P. K., Longo, M. L., Hutcheon, I. D. & Boxer, S. G. Phase separation of lipid membranes analyzed with high-resolution secondary ion mass spectrometry. *Science* **313**, 1948-1951, doi:10.1126/science.1130279 (2006).
- 40 Vickerman, J. C. Molecular imaging and depth profiling by mass spectrometry-SIMS, MALDI or DESI? *Analyst* **136**, 2199-2217, doi:10.1039/c1an00008j (2011).
- 41 Watrous, J. D. *et al.* Microbial metabolic exchange in 3D. *Isme J.* **7**, 770-780, doi:10.1038/ismej.2012.155 (2013).
- 42 Cornett, D. S., Frappier, S. L. & Caprioli, R. M. MALDI-FTICR imaging mass spectrometry of drugs and metabolites in tissue. *Anal. Chem.* **80**, 5648-5653, doi:10.1021/ac800617s (2008).
- 43 Karas, M., Bahr, U. & Giessmann, U. Matrix-assisted laser desorption ionization mass-spectrometry. *Mass Spectrom. Rev.* **10**, 335-357, doi:10.1002/mas.1280100503 (1991).
- 44 Karas, M., Ingendoh, A., Bahr, U. & Hillenkamp, F. Ultraviolet-laser desorption ionization mass-spectrometry of femtomolar amounts of large proteins. *Biomedical and Environmental Mass Spectrometry* **18**, 841-843, doi:10.1002/bms.1200180931 (1989).
- 45 Seeley, E. H. & Caprioli, R. M. 3D Imaging by Mass Spectrometry: A New Frontier. *Anal. Chem.* **84**, 2105-2110, doi:10.1021/ac2032707 (2012).
- 46 Zavalin, A. *et al.* Direct imaging of single cells and tissue at sub-cellular spatial resolution using transmission geometry MALDI MS. *J. Mass Spectrom.* **47**, 1473-1481, doi:10.1002/jms.3108 (2012).
- 47 Seeley, E. H. & Caprioli, R. M. Molecular imaging of proteins in tissues by mass spectrometry. *Proc. Natl. Acad. Sci. U. S. A.* **105**, 18126-18131, doi:10.1073/pnas.0801374105 (2008).
- 48 Spengler, B. & Hubert, M. Scanning microprobe matrix-assisted laser desorption ionization (SMALDI) mass spectrometry: Instrumentation for sub-micrometer resolved LDI and MALDI surface analysis. *J. Am. Soc. Mass Spectrom.* **13**, 735-748, doi:10.1016/s1044-0305(02)00376-8 (2002).
- 49 Wucher, A. & Winograd, N. Molecular sputter depth profiling using carbon cluster beams. *Anal. Bioanal. Chem.* **396**, 105-114, doi:10.1007/s00216-009-2971-x (2010).

- 50 Svava, F. N., Kiss, A., Jaskolla, T. W., Karas, M. & Heeren, R. M. A. High-Reactivity Matrices Increase the Sensitivity of Matrix Enhanced Secondary Ion Mass Spectrometry. *Anal. Chem.* **83**, 8308-8313, doi:10.1021/ac202222h (2011).
- 51 Anderson, E. H. Specialized electron beam nanolithography for EUV and X-ray diffractive optics. *IEEE J. Quantum Electron.* **42**, 27-35, doi:10.1109/jqe.2005.858451 (2006).
- 52 Juha, L. *et al.* Ablation of organic polymers by 46.9-nm-laser radiation. *Appl. Phys. Lett.* **86**, doi:10.1063/1.1854741 (2005).
- 53 Henke, B. L., Gullikson, E. M. & Davis, J. C. X-ray interactions: photoabsorption, scattering, transmission, and reflection at E=50-30000 eV, Z=1-92,. *Atomic Data and Nuclear Data Tables* **54**, 181-342 (1993).
- 54 Berrill, M. *et al.* Warm photoionized plasmas created by soft-x-ray laser irradiation of solid targets. *J. Opt. Soc. Am. B-Opt. Phys.* **25**, B32-B38, doi:10.1364/josab.25.000b32 (2008).
- 55 Fletcher, J. S., Rabbani, S., Henderson, A., Lockyer, N. P. & Vickerman, J. C. Three-dimensional mass spectral imaging of HeLa-M cells - sample preparation, data interpretation and visualisation. *Rapid Commun. Mass Spectrom.* **25**, 925-932, doi:10.1002/rcm.4944 (2011).
- 56 Pike, L. J. Rafts defined: a report on the Keystone Symposium on Lipid Rafts and Cell Function. *Journal of Lipid Research* **47**, 1597-1598, doi:10.1194/jlr.E600002-JLR200 (2006).
- 57 Shaw, A. S. Lipid rafts: now you see them, now you don't. *Nature Immunology* **7**, 1139-1142, doi:10.1038/ni1405 (2006).
- 58 Levental, K. R. *et al.* Polyunsaturated Lipids Regulate Membrane Domain Stability by Tuning Membrane Order. *Biophysical Journal* **110**, 1800-1810, doi:10.1016/j.bpj.2016.03.012 (2016).
- 59 de Wit, G., Danial, J. S. H., Kukura, P. & Wallace, M. I. Dynamic label-free imaging of lipid nanodomains. *Proceedings of the National Academy of Sciences of the United States of America* **112**, 12299-12303, doi:10.1073/pnas.1508483112 (2015).
- 60 McQuaw, C. M., Sostarecz, A. G., Zheng, L. L., Ewing, A. G. & Winograd, N. Lateral heterogeneity of dipalmitoylphosphatidylethanolamine-cholesterol Langmuir-Blodgett films investigated with imaging time-of-flight secondary ion mass spectrometry and atomic force microscopy. *Langmuir* **21**, 807-813, doi:10.1021/la0479455 (2005).
- 61 Altelaar, A. F. M. *et al.* Gold-enhanced biomolecular surface imaging of cells and tissue by SIMS and MALDI mass spectrometry. *Analytical Chemistry* **78**, 734-742, doi:10.1021/ac0513111 (2006).
- 62 Fitzgerald, J. J. D., Kunnath, P. & Walker, A. V. Matrix-Enhanced Secondary Ion Mass Spectrometry (ME SIMS) Using Room Temperature Ionic Liquid Matrices. *Analytical Chemistry* **82**, 4413-4419, doi:10.1021/ac100133c (2010).
- 63 Sostarecz, A. G. *et al.* Influence of molecular environment on the analysis of phospholipids by time-of-flight secondary ion mass spectrometry. *Langmuir* **20**, 4926-4932, doi:10.1021/la0496892 (2004).
- 64 Akhmetov, A., Moore, J. F., Gasper, G. L., Koin, P. J. & Hanley, L. Laser desorption postionization for imaging MS of biological material. *Journal of Mass Spectrometry* **45**, 137-145, doi:10.1002/jms.1716 (2010).

- 65 Kucher, A., Wucher, A. & Winograd, N. Strong field ionization of β -estradiol in the IR: strategies to optimize molecular postionization in secondary neutral mass spectrometry. *The Journal of Physical Chemistry C* **118**, 25534-25544 (2014).
- 66 Prinz, C., Hook, F., Malm, J. & Sjoval, P. Structural effects in the analysis of supported lipid bilayers by time-of-flight secondary ion mass spectrometry. *Langmuir* **23**, 8035-8041, doi:10.1021/la7004634 (2007).
- 67 Piehowski, P. D. *et al.* Time-of-Flight Secondary Ion Mass Spectrometry Imaging of Subcellular Lipid Heterogeneity: Poisson Counting and Spatial Resolution. *Analytical Chemistry* **81**, 5593-5602, doi:10.1021/ac901065s (2009).
- 68 Bourdos, N. *et al.* Analysis of lung surfactant model systems with time-of-flight secondary ion mass spectrometry. *Biophysical Journal* **79**, 357-369, doi:10.1016/s0006-3495(00)76297-7 (2000).
- 69 Pan, Y., Zhang, L.-d., Guo, H.-j., Yin, H. & Qi, F. Photoionization and dissociative photoionization study of cholesterol by IR laser desorption/tunable synchrotron VUV photoionization mass spectrometry. *Chinese Journal of Chemical Physics* **22**, 129 (2009).
- 70 Bushberg, J. T. *The essential physics of medical imaging*. (Lippincott Williams & Wilkins, 2002).
- 71 Kozole, J., Wucher, A. & Winograd, N. Energy deposition during molecular depth profiling experiments with cluster ion beams. *Analytical Chemistry* **80**, 5293-5301, doi:10.1021/ac8002962 (2008).
- 72 Wang, J. *et al.* A new instrument of VUV laser desorption/ionization mass spectrometry imaging with micrometer spatial resolution and low level of molecular fragmentation. *Review of Scientific Instruments* **88**, 114102, doi:10.1063/1.4994173 (2017).
- 73 Le Dourneuf, M., Lan, V. K., Taylor, K. & Burke, P. The photoionization of neutral aluminium. *Journal of Physics B: Atomic and Molecular Physics* **8**, 2640 (1975).
- 74 <http://www.eag.com/>. *Evans Analytical Group*, 2014).
- 75 Postawa, Z. *et al.* Microscopic insights into the sputtering of Ag{111} induced by C-60 and Ga bombardment. *J. Phys. Chem. B* **108**, 7831-7838, doi:10.1021/jp049936a (2004).
- 76 Russo, M. F. & Garrison, B. J. Mesoscale energy deposition footprint model for kiloelectronvolt cluster bombardment of solids. *Anal. Chem.* **78**, 7206-7210, doi:10.1021/ac061180j (2006).
- 77 Rading, D., Moellers, R., Cramer, H. G. & Niehuis, E. Dual beam depth profiling of polymer materials: comparison of C-60 and Ar cluster ion beams for sputtering. *Surf. Interface Anal.* **45**, 171-174, doi:10.1002/sia.5122 (2013).
- 78 Caroline, M. L., Sankar, R., Indirani, R. M. & Vasudevan, S. Growth, optical, thermal and dielectric studies of an amino acid organic nonlinear optical material: L-Alanine. *Materials Chemistry and Physics* **114**, 490-494, doi:10.1016/j.matchemphys.2008.09.070 (2009).

VII APPENDIX

In this Appendix standard operation procedures (SOP) for EUV TOF are presented. Details of design and principle of work of sub-systems are described.

VII.a Various procedures for system operation

VII.a.i SOP

The list below represents all major steps required for conventional system operation. Step-by-step actions are grouped in respected paragraphs afterwards.

1. Laser alignment
2. Zone plate alignment
3. Loading of the sample
4. Overnight pumping of sample and TOF chambers
5. System start up:
 - a. Oil circulation
 - b. Laser and switchyard chambers vacuum
 - c. Power supplies warming
 - d. Refreshing of spark gaps air
 - e. Establishing argon flow in the capillary
6. Laser warming
7. Laser power measurement
8. System parameters recording in the Experimental form

9. Attenuation cell calibration
10. Zone plate focusing
11. PI laser tuning
12. TOF setting optimization
13. Mass calibration
14. Data acquisition
15. Data interpretation → go to #7 until experimental goals are reached
16. Laser power verification, system parameters recording
17. System shutdown in reverse order from #5.

VII.a.ii TOF setting optimization

1. Select peak in mid-mass range
2. Vary by 10÷50 V steps the Retarding grid voltage and observe change of the peak shape
3. Select optimal rounded-up voltage that makes selected peak Gaussian-like
4. If ZP has bigger than 50 µm diameter central opening, or system is used in other mode, try enhancing the signal by engaging Einsel lens
5. Optimize overall signal yield by varying the Deflector plate voltages.

VII.a.iii Zone plate fine-focusing

1. If previously used TOF voltages are known, enable them
2. If not, set them all to 0 V and gradually increase to the values that are expected to work well for current experiment

3. For transparent sample re-measure sample-ZP distance with microscope objective
4. For non-transparent sample primarily, move ZP 100 μm or closer to the sample than it is expected by known thickness and distances
5. Turn on GaGe scope software and recall saved settings
6. Fire the laser once or few times at each spot while observing ablation craters appearance (for transparent sample) or change in signal
7. Correct microscope objective position to center the square mark on the ablation crater
8. Move ZP forward by 5-10 μm and past the focus until the optimal position is known:
 - a. Ablation crater is the smallest
 - b. Signal shows the most amount of element-associated peaks
 - c. Multilayer stack is ablated through with least amount of shots
9. Move sample by 3-5 μm so that laser hits fresh spot at every new ZP position
10. Verify optimal ZP distance and move sample to an area where data should be collected

VII.a.iv Data acquisition

1. Select acquisition parameters for each experimental task and verify them while being in GaGe software GUI:
 - a. Vertical range in Volts
 - b. Signal attenuation (hooked up externally)
 - c. Time delay for MCP
 - d. Laser energy by gas cell
 - e. Number of shots per spot and number of spots/pixels
2. Switch off GaGe software and turn on or switch back to LabView

3. Enter or re-enter above defined parameters in LV
4. Set delay generator for selected timing
5. Put proper signal attenuator in and/or signal amplifier/filter
6. After moving sample to intended position disable motor controlling LV
7. Write down all data acquisition parameters in the spreadsheet
8. Acquire data and watch over the process

VII.a.v PI laser tuning and use

1. For 3rd harmonics use, pump the tripling cell
2. Warm up the laser for 10÷20 min at 1.4 kV
3. Verify that beam goes through spatial filter unperturbed by using yellow paper reference
4. Maximize power at 1.5÷1.6 kV by optimizing crystals orientation – turn vertical knob on the second crystal. Be cautious about sounds laser is making – if light reflects back into the YAG rod, you will hear loud bangs that may compromise laser. Find dangerous range of knob position while being at low voltage and try to avoid them at higher power.
5. Check if 20 mJ can be reached within 1.7÷1.8 kV and go to #3 if not
6. For 9th harmonic put 250 Torr of Xe:Ar into the tripling cell
7. Check timing at delay generator and connect YAG for external triggering
8. Put quartz lens in the corresponding to the selected harmonic position
9. Move OAP in x and z while firing the lasers:
 - a. If spectrum is very noisy, YAG hits or is close to one of the plates – move away
 - b. Scan OAP z position to locate focal spot close to the sample
 - c. Scan x position to optimize signal yield

10. Check laser power
11. Do experiment with periodic power verification
12. Repeat from #8 for other harmonic if intended

VII.b EUV laser operation principles

Laser operation starts with charging a capacitor bank C with 60 kV from the General Atomics DC power supply as shown on Figure VII.1. It is done during 80 ms after receiving the fire command from primary delay generator. While charging, this voltage is also delivered through resist R_6 to the capillary creating low ionized plasma. 100 μ s prior to the end of the 80 ms pulse a secondary delay generator sends a TTL pulse to Maxwell HV pulser. Closing of the spark gap switch SG_1 forms RLC circuit between elements C, L and R_8 that causes 60 kV to oscillate up to 80÷90 kV. This elevated voltage pulse-charges the ring capacitor bank C_3 that surrounds the capillary. It also sits directly on top of the main spark gap switch SG_2 that holds the hot electrode of the capillary in its center. At the same time other circuit involving C_2 , R_1 and R_7 sends a prepulse directly into capillary on top of the DC preionization. Towards full charging of the ring capacitors the main spark gap spontaneously closes delivering ~22 kA current into preionized plasma column inside the capillary resulting in 46.9 nm lasing.

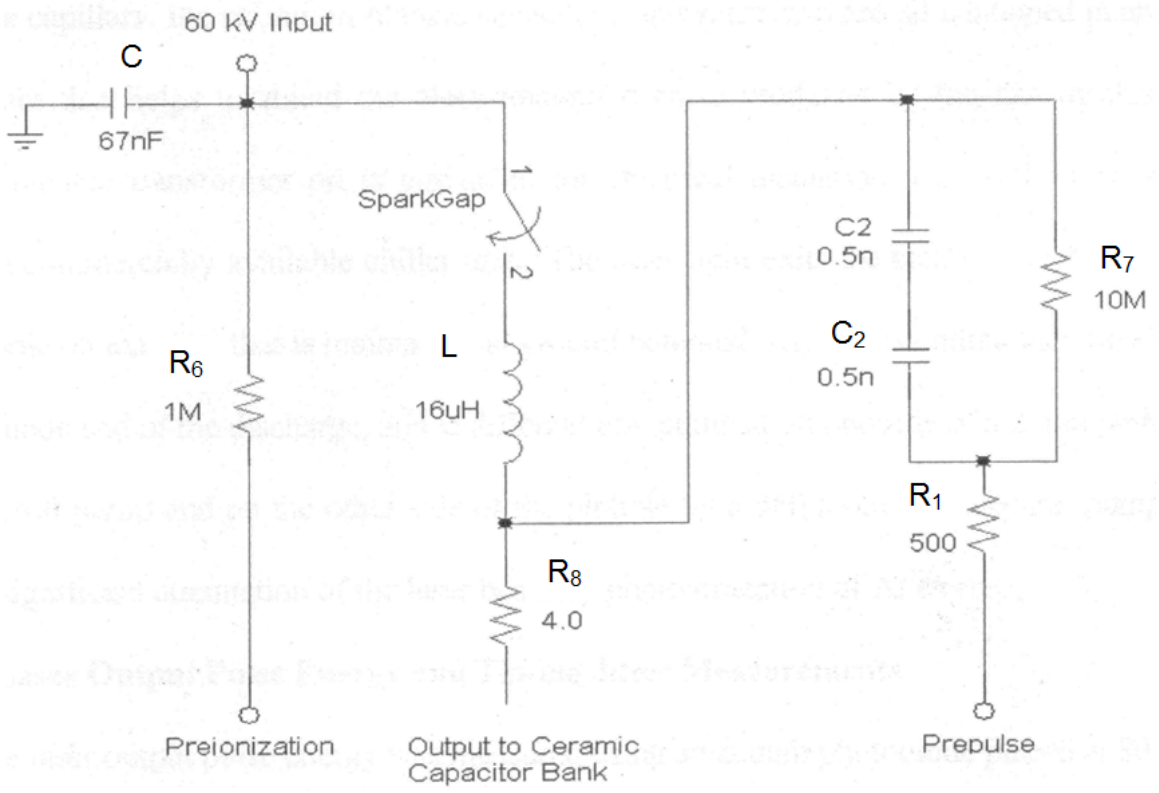
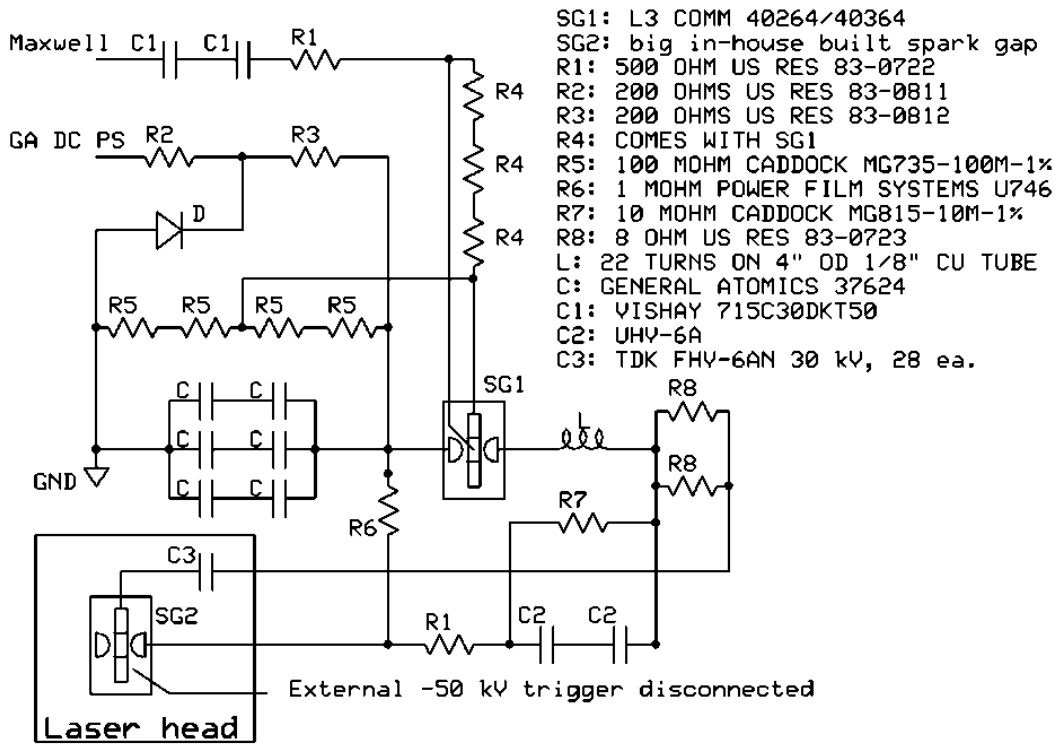


Figure VII.1: Overall scheme describing DC preionization, prepulse and main pulse delivery into the capillary discharge for 46.9 nm lasing in 300 mTorr Ar.

Pulser box top view



Diode bridge "D"

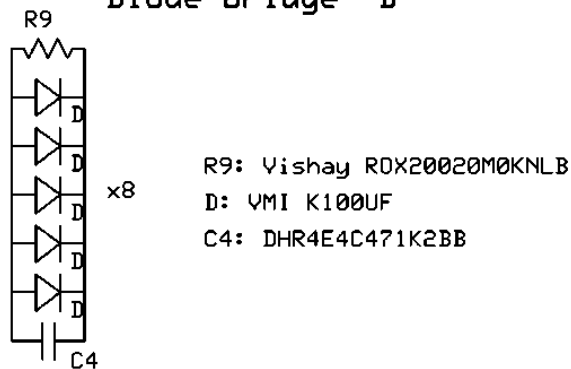


Figure VII.2: Electrical schematic of the laser showing exact components of the Figure VII.1.

The laser requires a number of gases to be supplied with as shown on Figure VII.3. Three spark gap switches in Maxwell trigger, pulser and laser head are fed with zero grade Air from a single tank. The remaining two tanks of argon are fed in a capillary and in the attenuation cell right next to the laser exit aperture. This supply is continuously pumped, while air in the spark

gaps requires periodical refreshment only. Although with built-in flow meters the operation might be even more stable.

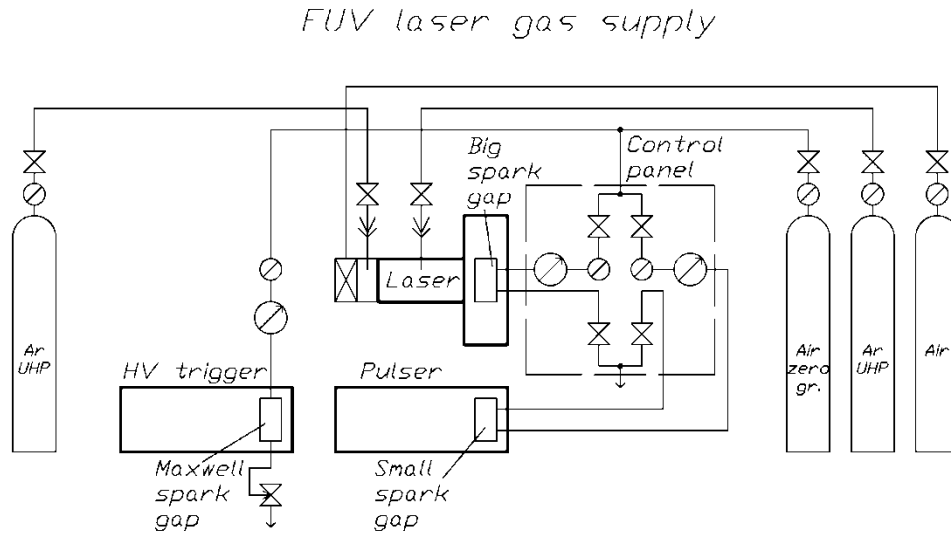


Figure VII.3: EUV laser gas supply scheme.

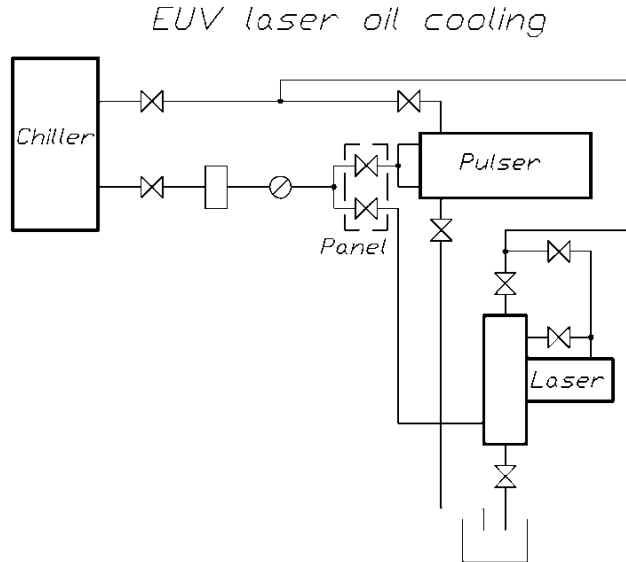


Figure VII.4: EUV laser oil cooling scheme. Opticool-A Fluid or DSI ECO-FR from DSI® can be used.

The laser has to rely on transformer oil circulation to insure: a) electrical insulation of pulsed and DC high voltages from the grounded shell of the system, and b) cooling of the HV

components including capillary promoting their extended lifetime. Conventional industrial chiller for this purpose is used, and the schematic of oil flow is shown on Figure VII.4.

VII.c EUV optical properties for various media

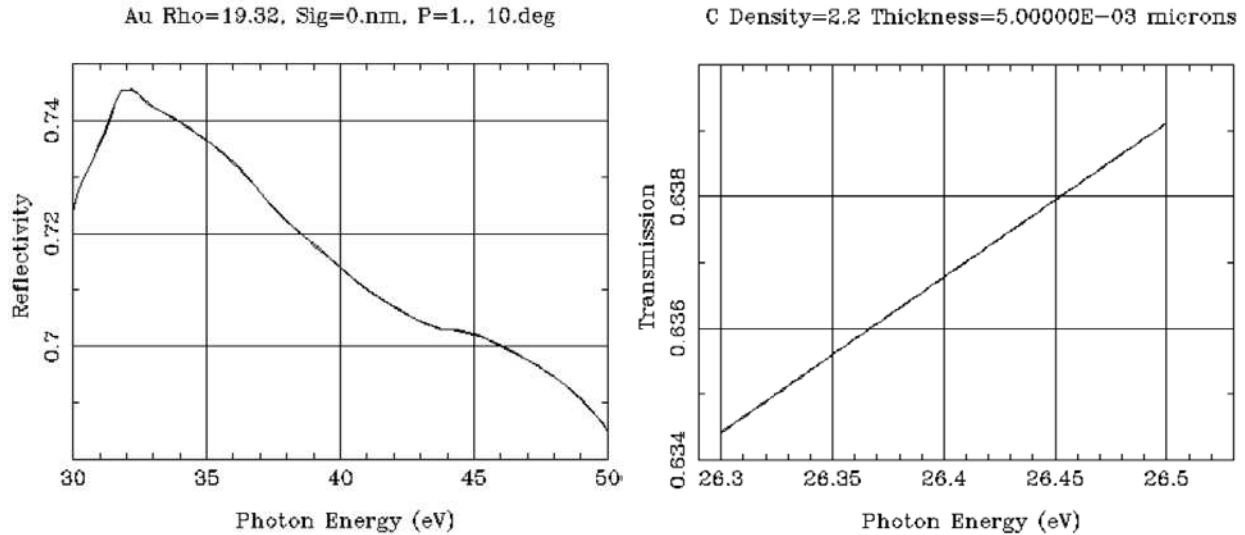


Figure VII.5: Reflectivity of a 100 nm Au coating (left) used in toroidal 10° incidence mirrors for 26.4 eV (46.9 nm) photons. 5 nm carbon film single-pass transmission (right). Data calculated at CXRO website.

The rate of carbon deposition on toroidal mirrors depends on many factors, but generally they should be annually cleaned in the oxygen plasma asher for 10÷20 min at standard conditions. Pure gold coating has reflectivity of ~70% as Figure VII.5 shows. After extended time of use a carbonaceous layer is formed on top of the mirror replicating the oval imprint of the circular beam. When such imprint becomes visible to naked eye (should be checked after each capillary change), reflectivity began steep-curve dropping. Just 5 nm of carbon layer reduces reflectivity by 60% (two passes).

VII.d Ion optics

Potential diagrams shown on Figure VII.6 and Figure VII.7 display a set of voltages tailored for the use in different detection modes: positive and negative polarity, gas phase and post-ablation ionization. The aim of altering the voltages in the sample region is to promote equal 6 keV acceleration of the majority of ions created, so that the rest of the system operate at similar parameters for better data comparison between the modes. As can be noted in the Figure VII.6, negative ion detection mode requires different field structure in the MCP since now both measured ions and electrons bear negative charge. Ions acceleration in the MCP prior to impact on the plate is still kept at 2 keV, as well as subsequent electrons acceleration within the chevrons.

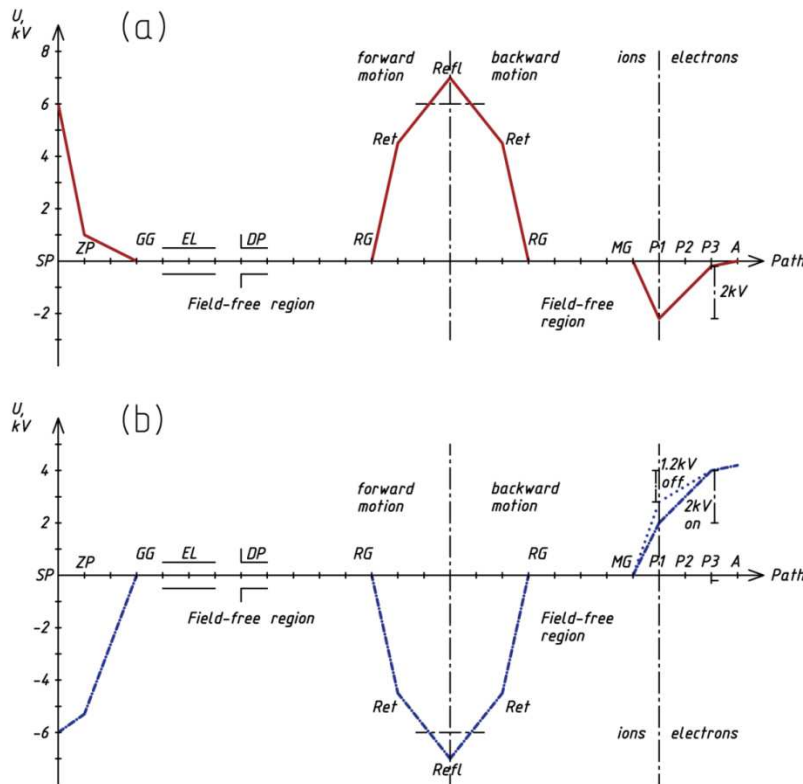


Figure VII.6: Potential diagram for positive (a) and negative (b) ion extraction modes.

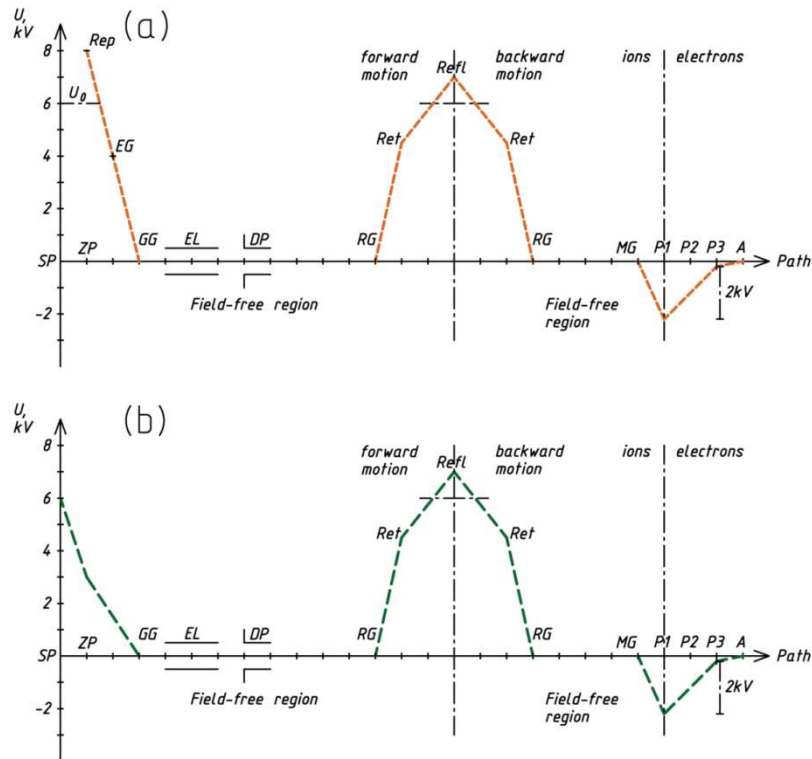


Figure VII.7: Potential diagrams for gas phase (a) and UV or VUV post-ionization (b) modes of operation.

VII.e Optics alignment

The amount of optics used in the system and precision requirements necessitated the development of an elaborate alignment procedure that can be group in three major steps:

1. EUV laser alignment with HeNe
2. Zone plate alignment and sample loading
3. Nd:YAG harmonics alignment near ZP and sample

EUV laser alignment is probably the most challenging because:

- 46.9 nm is not visible without the aid of EUV-sensitive scintillator or camera;
- it requires high vacuum for propagation;

- pulse energy is low - every photon counts;
- beam cross-section is doughnut-shaped rendering more complex and often uneven intensity distribution compared to regular Gaussian-shaped beams;
- zone plate active area is just $\varnothing 0.5$ mm, hence $\varnothing 3$ mm collimated beam of a source that is ~ 3 m away from the sample has to be pointed very well in order to properly illuminate the zone plate and collect enough laser intensity for ablation.

VUV laser alignment is as tricky as the EUV one for exactly same reasons. Although it can be essentially pre-aligned using visible 355 nm (white-blueish 3rd harmonic) since both of them propagate in the same direction upon frequency up-conversion in the tripling cell. Final alignment stage usually requires a fraction of a millimeter correction. As in the EUV and zone plate case, it is done in high vacuum and explained in great detail further below.

For practical ease we chose to proceed with EUV alignment using EUV-sensitive photoresist polymethyl methacrylate (PMMA) as means of imprinting the beam and thus gain information on: a) location – two references are needed to reconstruct the beam path, and b) beam shape and intensity distribution within for assessing quality of the newly installed capillary. 2÷4% solution of PMMA in anisole or chlorobenzene (PMMA A2 or C4 from MicroChem) is spin-coated in the clean room environment onto our standard ITO-coated 25×25×1 mm glass slide for 1 min at ~ 3000 rpm. Soft baking for 0.5 h at $\sim 100^\circ$ C forms 100÷300 nm smoothly distributed polymer film. These slides are then placed into specially designed flanges facing laser illumination with PMMA for subsequent exposure. The alignment flanges are designed to have a V-shaped holder for the slides so that when they are removed and placed back they fall into the same location. This is needed when a) slides are removed for development and b) slides are removed during HeNe alignment for letting the beam to propagate

further. PMMA photoresist development is best done in the paddle style, i.e. when developer solution is administered on top of the slide in the form of a paddle. MIBK:IPA 1:1 should sit for ~10 s or until the imprinted doughnut from the EUV beam shows up. If everything is fine and re-exposure is not required, a specially designed cross-hair printed on the black background is concentrically attached on the back side of the ITO slide with sticky tape. The use of such arrangement allows for visual inspection of HeNe beam centering on the imprint from the back of the slide. An example of properly assembled alignment flanges is shown on Figure VII.8 and their location as the references - on Figure VII.9.



Figure VII.8: Beam-facing (top), and other views of the alignment flanges serving as EUV beam references.

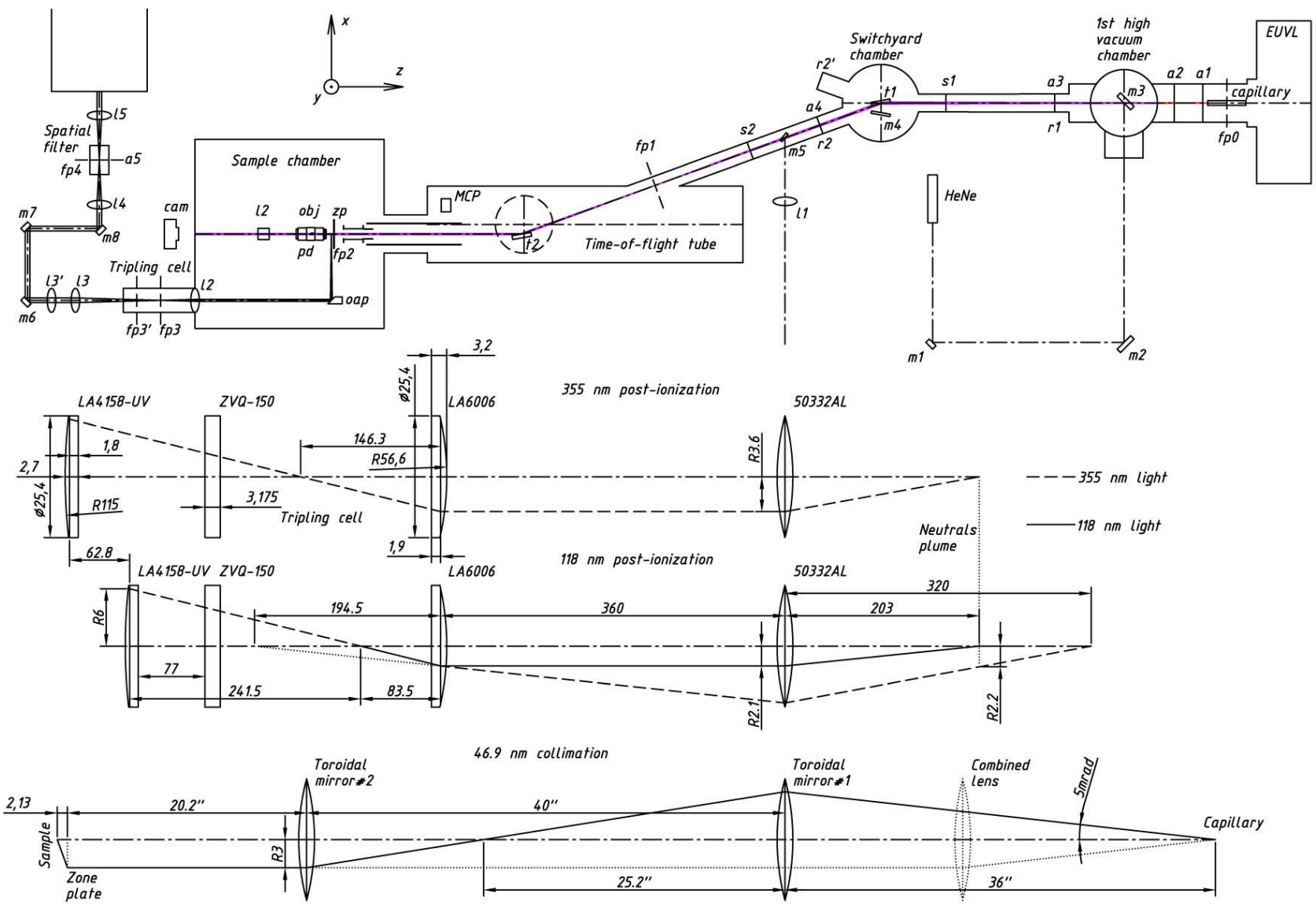


Figure VII.9: Alignment diagram for EUV, UV and VUV beams.

Due to small size of the ZP active area and its distant placement from the light source, a special alignment technique with respect to the EUVL beam was developed. ZP is just big enough to capture the most intense profile of the collimated 3 mm beam at the sample, so the accuracy is of the fraction of a millimeter.

Due to the presence of central hole, 50% transmission of the zones, and 100% opacity of the surrounding membrane, ZP can essentially act as an aperture, allowing only light within its 0.5 mm outer diameter to pass through. By placing photodetector behind the ZP and moving the ZP transversely in x and y axes, an intensity profile of the doughnut-shaped EUVL beam can be successfully constructed (Figure VII.10). For that the light intensity on the photodetector has to be averaged and recorded for each position, typically separated by 0.5 mm. Given the EUVL beam size and the 0.5 mm “pixel” size, up to 100 data points have to be recorded. This process is facilitated by employing an in-house written LabView software, the graphic user interface (GUI) of which is shown on Figure VII.10.

Gridded plot on the left of the figure displays the field of view, which is wide enough considering that EUV beam was pre-aligned before to be somewhat centered on the Sample chamber axis with HeNe. Red dot on the plot shows the current ZP position; green dots indicate coordinates at which zero intensity was recorded, while gray-shaded squares represent the local beam intensity. The hue to this shading ranges from 0 to 1, where 1 corresponds to the highest intensity recorded – its value is stated in the vertical bar to the right of the grid and in the “Voltage value” window below. The rest of the parameters represent number of shots to average in each position, settings of the digitizer to capture the photodetector signal (shown as a single peak in the spectrum to the right of the window), motors settings etc.

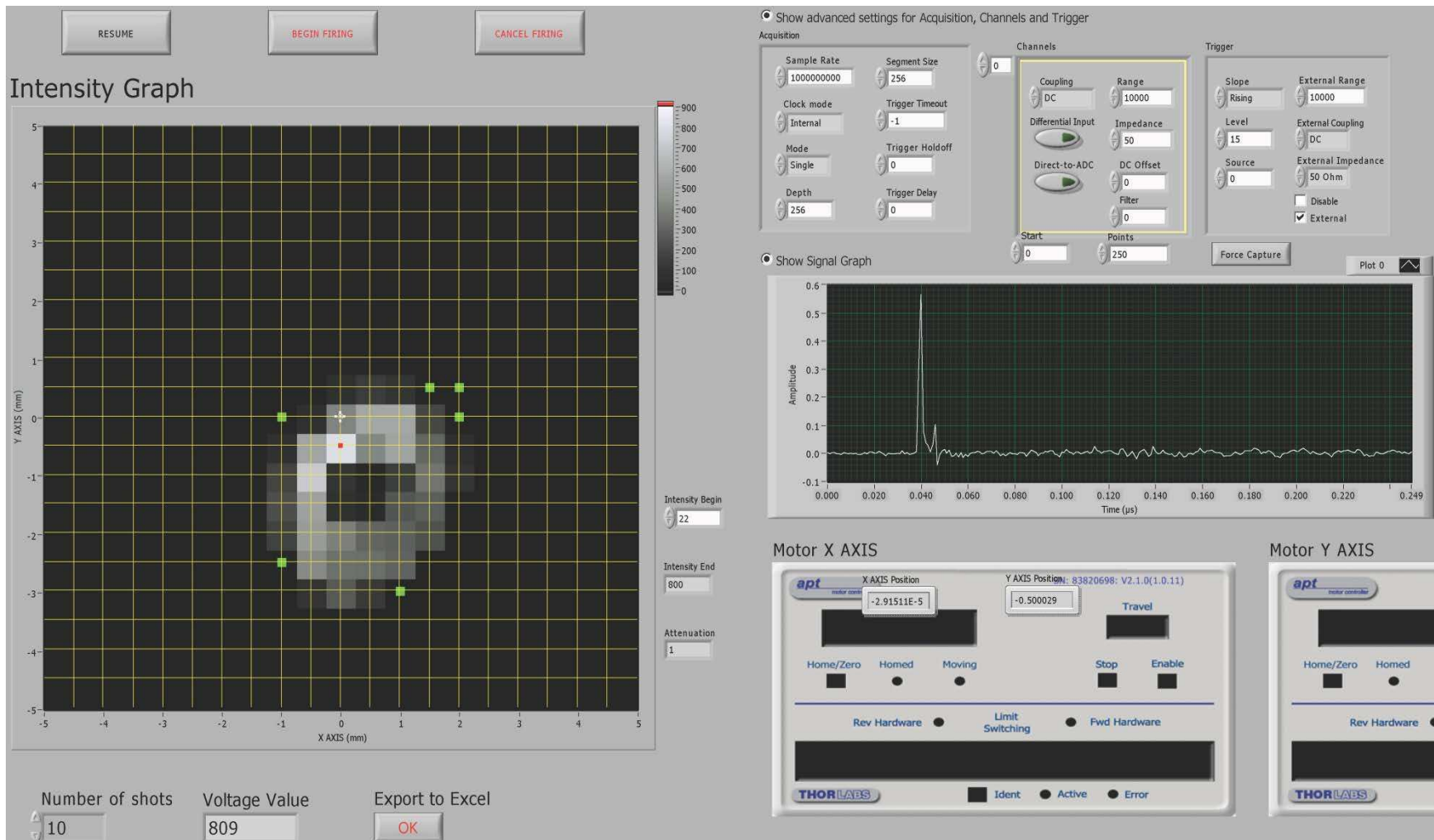


Figure VII.10: User interface of the semi-automatic LabView program for the ZP alignment with respect to the EUVL beam.

VII.e.i EUV laser alignment procedure with HeNe

Refer to Figure VII.9 for identification of optical elements mentioned below.

1. Install 2nd reference in the r2 (past toroidal mirror) or r2' (past flat mirror) position
2. Pump down the chamber
3. Start up the laser and bring it to full power with aluminum PD in position s1
4. Retract PD and expose 2nd reference with 200÷300 shots
5. Vent the system, develop 2nd reference and repeat from step #1 if it looks bad
6. Remove section s1÷a3 and install 1st reference at the r1 position
7. Pump down and expose 1st reference with 100÷200 shots
8. Vent, develop 1st reference; if looks good, proceed
9. Turn on HeNe for warming up and stabilizing
10. Put the center mark behind each reference with Sharpie
11. Attach cross hairs to the back of the slides while centering them with the mark
12. Remove high vacuum gauge and venting valve from the laser chamber
13. Install mirrors m1, m2, m3, and reference r1 in place
14. Center HeNe on mirrors as much as possible
15. Using mirror m1 center HeNe beam on r1
16. Remove r1 and using mirror m2 center HeNe beam on r2
17. Put back r1 and repeat from step #15 until HeNe beam is centered on both references without additional corrections by mirrors m1 and m2
18. If necessary, vent TOF chamber, remove section s2÷a4, turn on Thorlabs controllers
19. Install mirror m5 and orient it such that HeNe beam goes through the center of lens l1 at various positions

20. Put a screen (list of paper) on the wall where HeNe hits
21. Translate toroidal t1 so the beam hits it in the center
22. Adjust tilt of the toroidal t1 until HeNe preserves circular shape during l1 translation through the focus of the beam
23. Remove mirror m5; remove ZP, sample, objective and camera from the sample chamber
24. Put screen on the wall where beam hits
25. By translating toroidal t2 and observing the screen find horizontal center of the toroidal t2
26. By tilting toroidal t1 in y direction find vertical center of the toroidal t2
27. Adjust x and y tilt of toroidal t2 to provide with best circular shape of the reflected beam, as well as centering and parallelism with the sample chamber axis
28. If necessary, go back to any step before, check beam centering with references
29. Put back ZP and verify that the beam is close to its center; put back camera
30. Remove reference r2
31. Center aperture a4 with the beam and put back section s2-a4
32. Remove reference r1
33. Center aperture a3 with the beam and put back section s1-a3
34. Remove mirror m3 and put back missing flange assembly
35. Turn off HeNe and store references for future comparison of beam imprints

VII.e.ii Zone plate alignment and sample loading

1. If performed after alignment with HeNe, go to step #4
2. Vent the sample chamber
3. Remove current sample if present

4. Place aluminum PD behind the ZP and connect it to the electrical feedthrough
5. Pump and start the system – vacuum of $\sim 1e-5$ Torr is sufficient
6. Connect Rogowski coil to the trigger input of the GaGe scope
7. Connect PD signal cable to the channel input of the GaGe scope
8. Bias PD with +1.5 kV
9. Turn on Thorlabs controllers and connect them with the PC cable
10. Turn on LV program for ZP alignment, follow displayed instructions
11. Obtain EUVL beam profile with ZP in the LabView interface
12. Leave ZP in the most intense yet symmetrical spot
13. Export beam profile in PDF and XLS formats, turn off LV
14. Unpower PD, unplug cables from GaGe
15. Vent and remove PD
16. Adjust ZP z-coordinate based on thickness difference of the new sample with Oriel motor
17. Reset ZP stopper to be $0.5 \div 1$ mm away toward sample for 1st order ablation
18. Turn on Thorlabs software and move Objective to the same position as ZP
19. Put sample in
20. Turn on microscope software and PI sample stages – calibrate by positive limit
21. Focus microscope on the front sample (if transparent) surface, zero objective coordinate here, otherwise on the back side of the sample
22. If sample is transparent or there is a window, locate ZP with objective, center on it, and bring ZP to 2.1 mm distance away from the sample's front surface
23. By moving sample around, measure coordinates of the target areas or their boundaries
24. Leave all software running, close the chamber and pump

VII.e.iii Nd:YAG harmonics alignment near ZP and sample

1. Warm up flash lamps and then laser in Q-switch mode for 10÷20 min at 1.4 kV
2. Verify that beam goes through spatial filter a5 unperturbed
3. Center beam on mirror m7 by adjusting m8
4. Similarly center on mirror m6
5. Put lens to l3' position (3rd harmonic operation)
6. Center on tripling cell window with mirror m6
7. Center on lens l2 by moving mirror m6
8. Re-center on tripling cell window with mirror m7
9. Repeat from step #7 until centered
10. Translate OAP such that focal spot is 1 mm away from the ZP plate
11. Adjust OAP so that focal spot center is equally distant from top and bottom of ZP plate
12. Merge ZP center and focal spot center by moving OAP in x-direction
13. Zero these OAP coordinates
14. Move lens l3 forward (9th harmonic position)
15. Verify that the beam is still centered on lens l2 and adjust if necessary from step#7
16. Center focal spot similarly near the ZP and record these OAP coordinates
17. Put the sample in and verify that the beam is not clipped by any harmonic - should be done in conjunction with step #16 of the Zone plate alignment and sample loading routine

VII.f EUV photodetectors

Since the introduction of the EUV laser an aluminum-anode detector employing photoelectric effect was used with prior calibration of electron yield at the synchrotron¹⁶.

This type of very simple and reliable PD is still utilized in the system, but there are concerns about the measurement reliability. First, aluminum oxidizes in air, so even though the electron/photon yield was measured on the oxidized surface, it may not be considered as an ultimate solution in the long term. Second, it turned out that laser pulse intensity creates too many electrons that form volumetric charge. It prevents their efficient extraction in the electric field. Hence the number of measured electrons is no longer proportional to the number of photons that have hit the photocathode surface. The quickest way to deal with it is putting a set of meshes in front of the PD assuming that their combined transparency is the multiplication of the transparency of each. However, detailed calculations of smoothing out of the beam by diffraction upon interaction with metal mesh (woven wires) were not performed at the time. Local hot and cold spots of intensity based on particular overlay of the wires and the incident angle of the beam becomes prevalent. Third, due to the opaqueness of the photodetector, it can measure only when the beam is blocked by it from the application. And since the laser intensity variation is quite significant¹³, it causes uncertainty of exact delivered energy per shot. This may be critical for high spatial resolution single shot composition imaging that the system is designed for. Lastly, mirrors degradation over time caused by hydrocarbon deposition results in a discrepancy between the powers measured before the mirrors and the expected one to be delivered to the sample.

The principle of work of the inline detector involves photoionization of residual argon gas coming off the capillary and attenuation cell. The device consists of two concentric tubes

electrically insulated by the nylon caps at the ends. Outer tube is grounded, while inner one is biased with positive potential attracting electrons emerging upon gas ionization. This tube is connected to both a HV power supply and oscilloscope with a coupling box separating them. The response of this detector depends mostly on ambient pressure and ratio of electrons to photons emerging from the capillary. At set vacuum level the response is fairly linear, but when laser power degrades through the capillary lifetime and attenuation cell is used, this dependence becomes hard to formalize and calibrate. Thus, inline PD is capable of providing linear response at a given Ar pressure, with calibration prior to experiment. The biggest advantage of this PD though is that it doesn't perturb the beam allowing its unrestricted use in the application.

For absolute power measurement a PD with gold-coated photocathode is the most reliable, simply because gold is not a reactive material. As Figure VII.11 shows, the PD consists of uniformly coated with 100 nm of gold copper cathode that is electrically insulated from the aluminum body and connected, as the inline detector, via coupling box to the power supply of negative polarity and oscilloscope. Negative polarity is needed in order to repel emerging photoelectrons toward grounded mesh in front. This mesh is devised out of thin Mylar sheet with randomly placed holes. We took a microscope picture of it and processed it in Matlab in order to calculate average transmissivity. The mesh was also coated with ~100 nm gold on both sides for good electrical contact and full opacity to the EUV beam outside holes. Random and close placement of the holes in the mesh provides high accuracy of beam energy measurement. In case if measured 4% transmissivity of the mesh is not sufficient in the future, a second mesh can be placed no closer than 4 cm apart. Only in this case diffraction will overcome particular holes arrangement of two meshes and smooth out the attenuated beam intensity distribution.

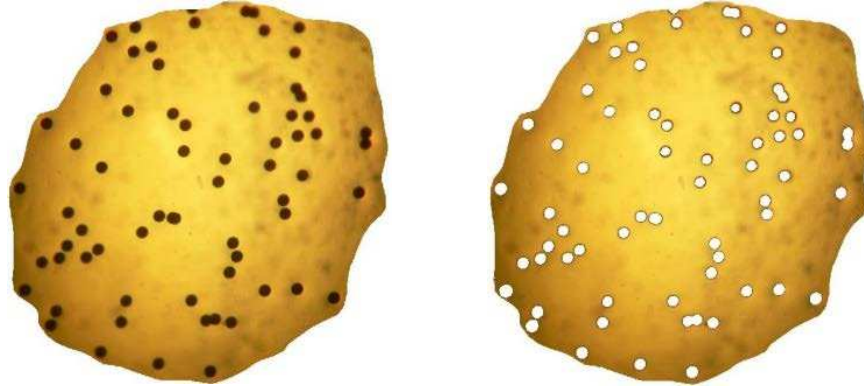


Figure VII.11: Microscope picture of the gold-coated mesh used as a ground electrode for gold EUV detector.

Laser beam energy measured by the gold PD is calculated using the following formula:

$$E = \frac{\int V dt * E_{ph} * A}{T * q_e * R} = \frac{4.5e - 9 [V \cdot s] * 26.4 [eV] * 10}{0.04 * 0.054 \left[\frac{e}{ph} \right] * 50 [\Omega]} = 11 \mu J \quad (VI.14)$$

Where $\int V dt$ - integrated signal peak from the detector, E_{ph} - energy per photon, A - signal attenuator used for measurement, T - measured mesh transparency, q_e - quantum efficiency for 46.9 nm light, and R - impedance. Calculated 11 μJ beam energy based on average integrated signal peak from tables at 1.7 kV bias below is well within the reported $\sim 10 \mu J$ specification.

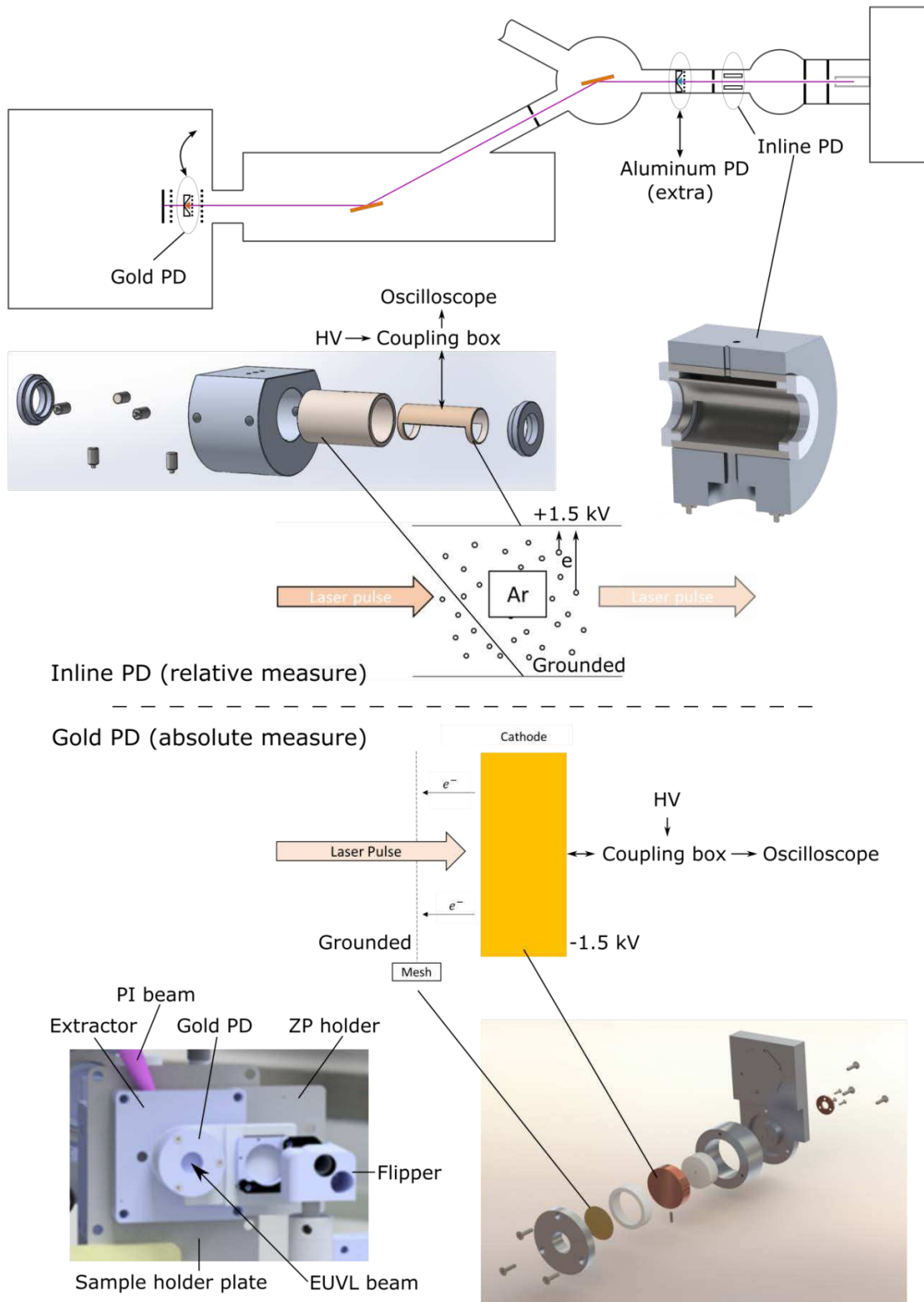


Figure VII.12: Photodetectors placement in the system (top) and description of their principle of work.

Inline and gold detector have to be used together. Currently, since this technology is not yet fully integrated in the system (LabView or Matlab code needs to be written and oscilloscope with two automatically recording channels has to be acquired), old aluminum detector temporarily replaces the gold one. However, typical usage of the pair of inline and gold PDs may be summarized in the following list:

1. Ensure that the laser is warmed up
2. Select attenuation degree by stabilizing the desired Ar pressure in the cell
3. Gather a set of signals with single laser shot
4. Retract the gold detector and collect data/image recording with each shot both mass spectra and inline detector signal
5. Repeat step 3
6. Feed data into the algorithm for inline detector calibration and mass spectra intensity correction based on corresponding laser pulse energy

This procedure will ensure a normalized to laser pulse energy variation of mass spectral output from the collected data points. We have manually collected and analyzed gold and inline detector signals in order to verify that they correlate between each other depending on the pulse energy. We collected spectra from each detector at three bias voltages three times. Bias was varied for gold PD. For simplicity, Figure VII.13 shows averaged spectra at each bias voltage, together with corresponding cumulative integrals, while Table VII.1 shows integrated signal for every single shot at every condition.

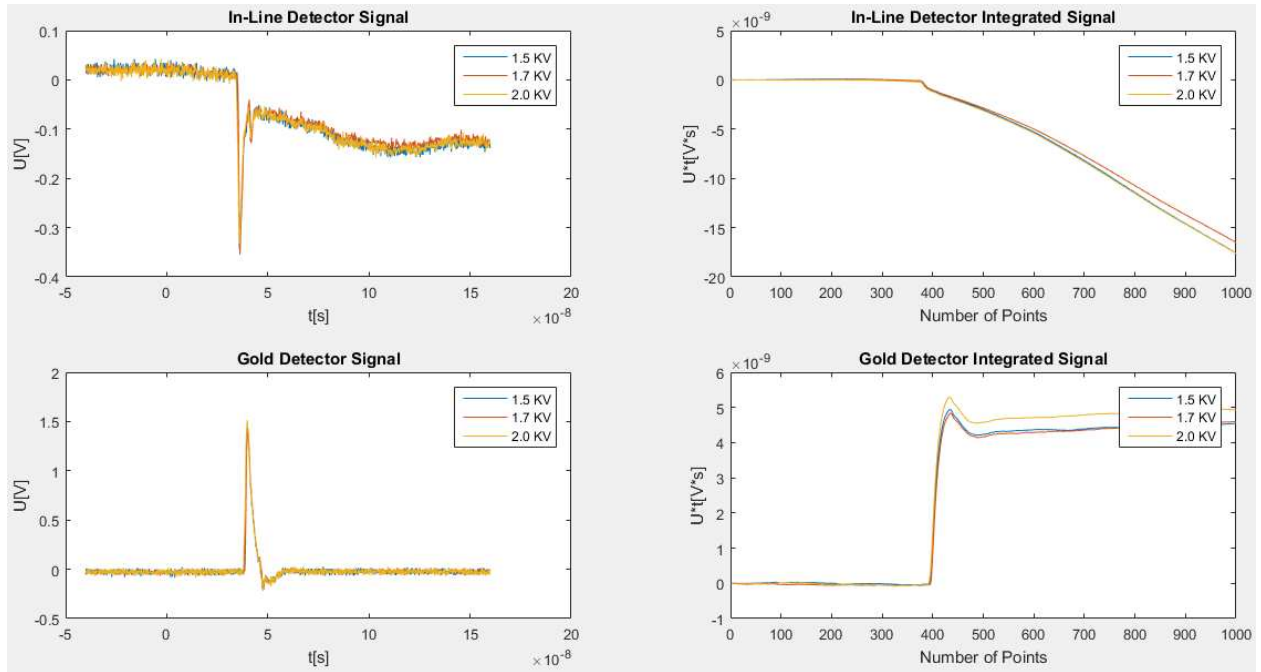


Figure VII.13: Averaged spectra of detectors (left) and respective cumulative integrals (right) for different bias voltages.

Table VII.1: Integration of single shot signals from each detector at various bias voltages.

Integrated signal at 1.5 kV, V·s	Inline	Gold	Gold/Inline	
Shot 1	1,72E-08	4,27E-09	2,48E-01	
Shot 2	1,91E-08	4,89E-09	2,56E-01	
Shot 3	1,65E-08	4,20E-09	2,55E-01	
Average Gold/Inline	0,25			
Integrated signal at 1.7 kV, V·s	Inline	Gold	Gold/Inline	
Shot 1	1,74E-08	4,68E-09	2,68E-01	
Shot 2	1,54E-08	4,14E-09	2,70E-01	
Shot 3	1,67E-08	4,53E-09	2,71E-01	
Average Gold/Inline	0,27			
Integrated signal at 2 kV, V·s	Inline	Gold	Gold/Inline	
Shot 1	1,64E-08	4,71E-09	2,88E-01	
Shot 2	1,85E-08	5,03E-09	2,72E-01	
Shot 3	1,79E-08	4,80E-09	2,68E-01	
Average Gold/Inline	0,28			

Table VII.1 shows that gold/inline integrals ratio grows by 8% when gold detector bias is increased from 1.5 kV to 1.7 kV indicating that 1.5 kV is not sufficient to pull and hence measure all photoelectrons out of the photocathode. But increase of bias from 1.7 kV to 2 kV demonstrates almost no impact on data – a mere growth by 3.7 %. The conclusion is that 1.7 kV is sufficiently high voltage for gold detector to be biased with. If signal doesn't grow at higher bias, it means that all electrons are detected, and thus we call it “photodetector saturation”. Although this saturation is a good term meaning that the true pulse energy is being measured.

In addition to the saturation test it is important to verify the linearity between two detectors, i.e. when both signals proportionally increase or decrease based on higher or lower pulse energy received. Figure VII.14 shows that linearity is remarkably good when we provide detectors with 1.5 and 1.7 kV potentials. Deviation starts at 2 kV probably due to formation of hot spots or some other imperfections. In conclusion to the linearity and saturation test, it was defined that the gold detector needs to be operated at -1.7 kV. Inline PD was previously and separately tested showing that +1.5 kV is an optimal bias for it.

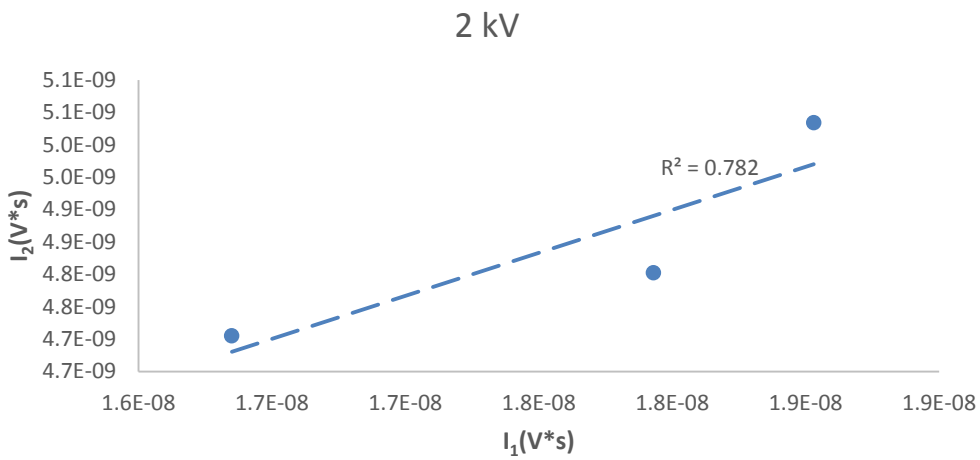
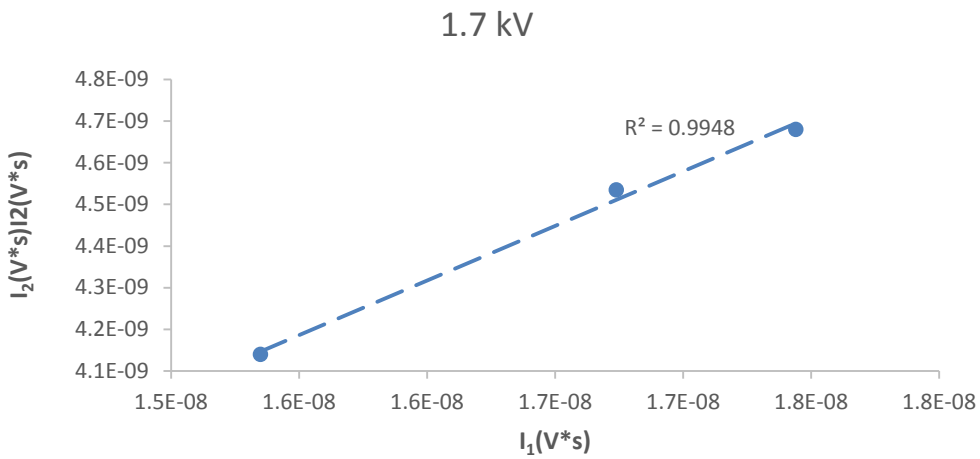
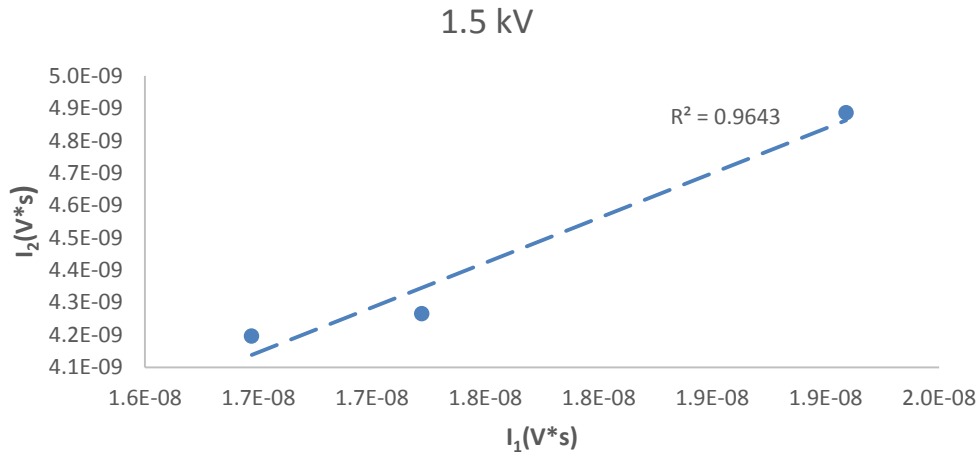


Figure VII.14: Linearity test between detectors at three bias voltages.

VII.g MCP sensitivity

A sample with low and uniform concentration of embedded elements was ablated at various laser fluences - NIST calibration standard with $\sim 500 \mu\text{g/g}$ of U and Th. Left plots of Figure VII.16 show 1200 averaged spectra at each fluence indicating that U, Th and their oxides diminish accordingly. The plots on the right show histogram analysis of the individual spectra out of each array - all four peaks were integrated with resulting voltage plotted. Two distinct distributions indicate the average signal corresponding to zero and one counts, verified by the shift between the distributions intensity as a function of laser fluence. Average histogram was fitted with three-term Gaussian function (Figure VII.15) and the distance between the maxima shows that single ion count corresponds to 18.5 mV. With that an MCP electron gain G is:

$$U = IR = \frac{q}{t}R = \frac{Gq_0}{t}R \Rightarrow G = \frac{Ut}{q_0R} = \frac{1.85e-2 [V] * 1e-9 [s]}{1.6e-19 [C] * 50 [\Omega]} \quad (\text{VI.15})$$

$$= 2.31e6 [e/\text{count}]$$

Where U – voltage corresponding to single ion count, t – digitizer time resolution, q_0 – elemental charge, R – impedance of the coaxial cables, G – MCP gain.

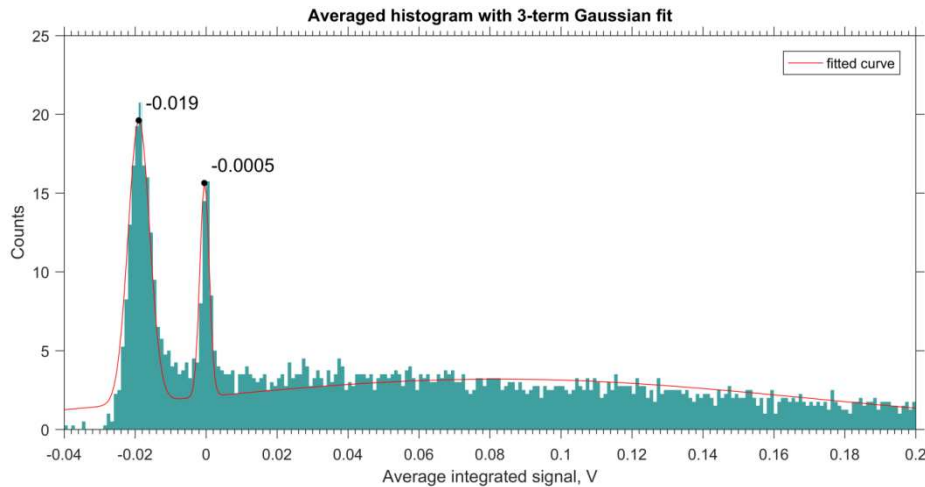


Figure VII.15: Averaged histogram in single ion counting experiment.

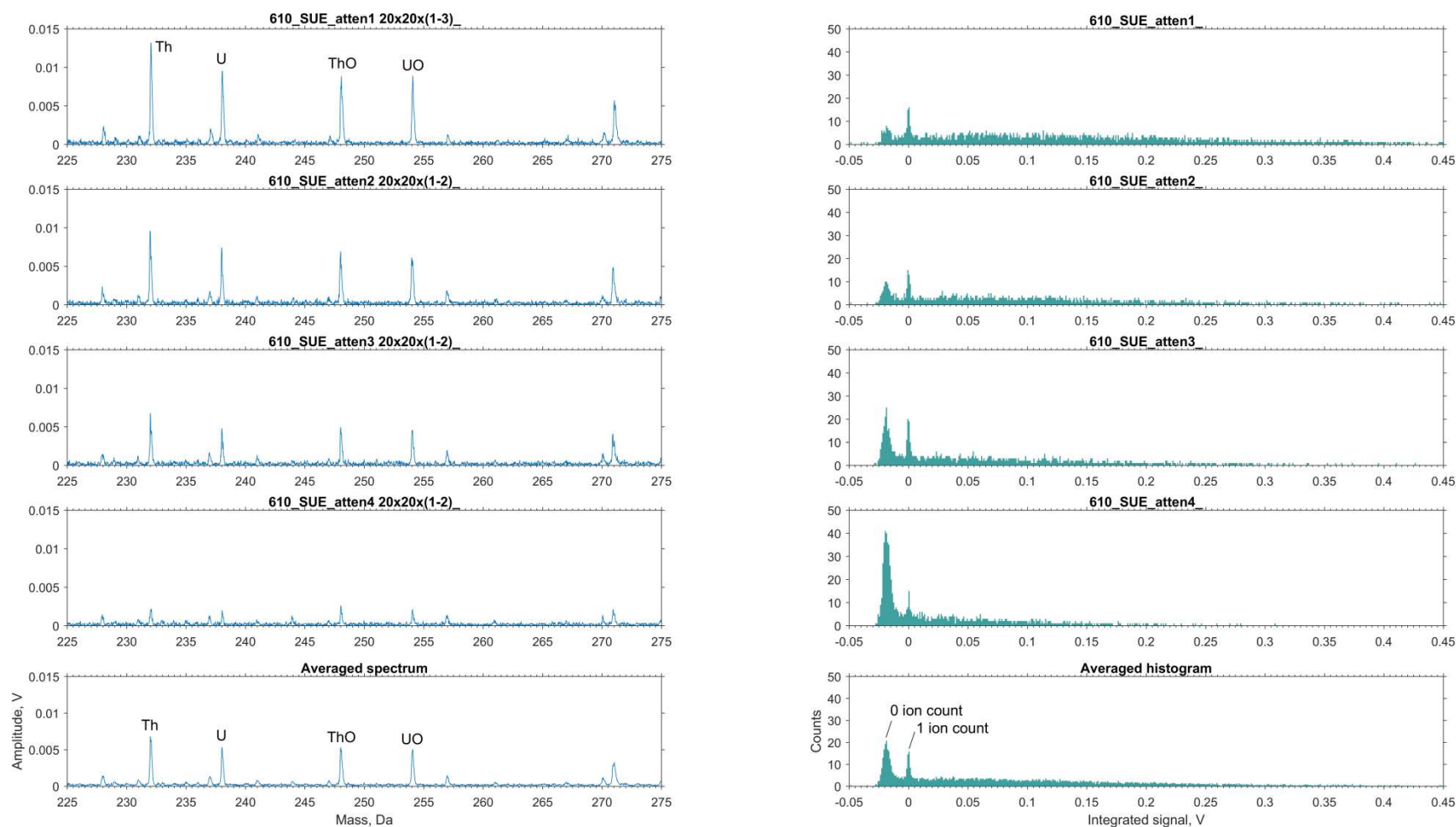


Figure VII.16: Averaged spectra (left) and corresponding Th, U, ThO and UO sum-integration histograms (right) for single ion counting. Histograms demonstrate gradual amplitude shift of two distinct distributions, indicating lower detection probability of signal corresponding to single count at lower laser fluence.

VII.h PI efficiency calculation

PI efficiency calculation is based on estimation of ionization probability of single Aluminum atom ($I_e = 5.98$ eV) flying through the ionization region at thermal velocity. This probability defines number of ionized species of the plume, based on ablation crater volume and on number of evacuated atoms from there. Calculations were initially done for the CW source from Energetiq Technology Inc., EQ-99X, and then applied to other sources. Average photoionization cross-section of neutral aluminum atom in 170÷210 nm region, including the vicinity of 120 nm ($1 \text{ Mb} = 1e-18 \text{ cm}^2$), can be assumed⁷³ to be $3e-17 \text{ cm}^2$. Plasma expansion velocity is determined by:

$$C_s = \sqrt{\frac{\gamma kT}{m}} = \sqrt{\frac{5 * 0.1 [eV] * 1.6e - 19 [J]}{3 * 27 [Da] * 1.66e - 27 [kg]}} = 7.7e - 4 [cm/s] \quad (\text{VI.16})$$

Where γ – adiabatic constant, kT – neutral's initial energy, and m – mass of Al atom. The time that Al atoms fly through the 1 mm region is $t = 0.1 [\text{cm}] / 7.7e4 [\text{cm/s}] = 1.3 [\mu\text{s}]$, and energy of the CW lamp, received during this time is $E = P \times t = 3.3e-3 [\text{W}] \times 1.3 [\mu\text{s}] = 4.2e-9 [\text{J}]$. Energy per the central wavelength 190 nm photon is $E_{\text{ph}} = 1240 / 190 \times 1.6e-19 [\text{J}] = 1e-18 [\text{J}]$, and number of photons is $N_{\text{ph}} = 4.2e-9 [\text{J}] / 1e-18 [\text{J}] = 4.2e9 [\text{ph}]$. Corresponding photon flux of the EQ-99X lamp: $F = N_{\text{ph}} / (\pi(0.1 \text{ cm})^2/4) / t = 4.2e9 [\text{ph}] / 8e-3 [\text{cm}^2] / 1.3e-6 [\text{s}] = 4e17 [\text{ph/cm}^2/\text{s}]$. With a single shot an average crater as big as 100 aL (500 nm FWHM diameter and 500 nm depth) can be ablated. Considering bulk aluminum, this corresponds to $1e-19 \text{ m}^3$, or $2.7e-16 \text{ kg}$, or $6e9$ Al atoms. With these assumptions a number of post-ionized neutrals can be estimated:

$$\begin{aligned}
N_{PI} &= N_{abl} \eta \alpha \sigma F t \\
&= 6e9 * 1 * 0.1 * 3e - 17 [cm^2] * 4e17 \left[\frac{ph}{cm^2s} \right] * 1.3e \\
&\quad - 6 [s] = 9.4e3
\end{aligned} \tag{VI.17}$$

Where constants N_{abl} - number of ablated atoms per shot, η - neutrals extraction efficiency based on geometrical overlapping of the beams, α - detection efficiency of the system, σ - photoionization cross section of aluminum atoms, F - photon flux into the ionization region from the VUV source, t - duration of the VUV ionization process.

VII.i Vacuum

High vacuum conditions are required for EUV laser and secondary ion propagation. Mean free path of the ions in typical vacuum of the TOF tube:

$$l = \frac{kT}{\sqrt{2}\pi d^2 p} = \frac{1.38e - 23 \left[\frac{J}{K} \right] * 300 [K]}{\sqrt{2} * \pi * (500 [pm])^2 * 7e - 6 [Pa]} \cong 500 m \tag{VI.18}$$

Where k - Boltzmann constant, T - gas temperature, d - average kinetic diameter of the interacting molecules, p - gas pressure converted from $5e-8$ Torr. The mean free path in the TOF tube is greater than the approximate 1m length of it, and the mean free path at one order of magnitude worse vacuum found in the sample chamber still provides sufficient $l \sim 50$ m.

EUV transmission of the evacuated medium at various pressure shows that vacuum should be better than $1e-4$ Torr as Figure VII.17 shows.

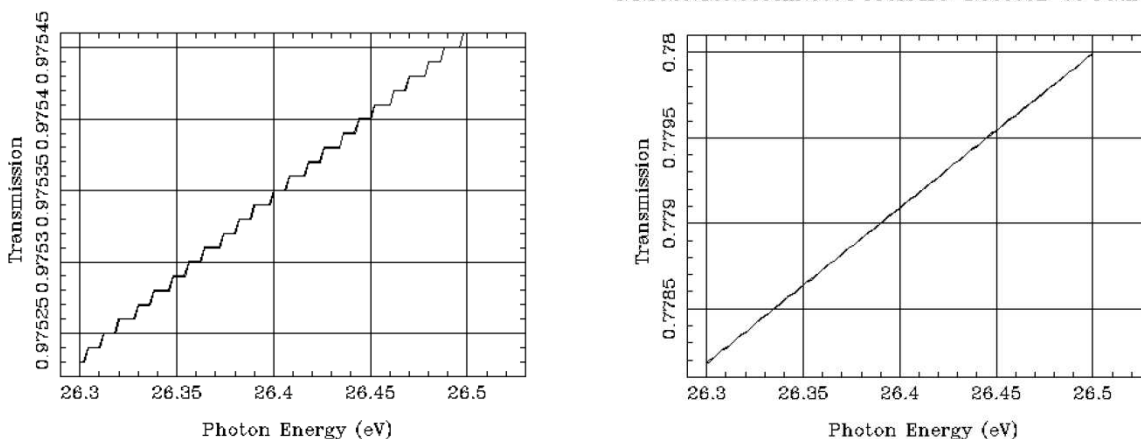


Figure VII.17: Transmission of air column of 3 m length at 1e-4 Torr (left) and 1e-3 Torr (right) pressure to 46.9 nm radiation. Data taken from the CXRO website.

There are few more aspects to the necessity of using higher vacuum than is solely required by ions loss through collision with residual gas molecules or EUV beam propagation. Dual MCP detector is a sensitive element that can be compromised by accidental discharge between its plates due to accumulation of water during exposure to the atmosphere. Thus MCP specification limits its operating pressure to the minimum of 1e-6 Torr and advises pumping for about 24 hours after venting. Unfortunately, without load-lock chamber for sample replacement, the system has to be fully vented from time to time. In order to reduce waiting to ~12 hours (overnight pumping) it was decided to lower the base pressure to 1e-7 Torr and below by installation of more powerful TOF pumping stage. After prolonged pumping it is still possible to operate at 1e-6 Torr as was done in the gas phase experiment.

The last aspect of operating at the upper limit of high vacuum range is reduction of average time of monolayer film of adsorbed residual gas molecules deposition onto sample surface. It can be estimated using formula:

$$t \sim \frac{1e19}{F} = \frac{\sqrt{2\pi mkT} * 1e19}{p} \quad (\text{VI.19})$$

$$= \frac{\sqrt{2\pi * 1.66e-27 [kg] * 1.3e-23 \left[\frac{J}{K}\right] * 300 [K] * 1e19}}{7e-5 [Pa]} = 1 \text{ s}$$

Where F – incident flux of residual gas molecules, m – molecular mass (calculated for hydrogen), k – Boltzmann constant, T – gas temperature, p – gas pressure in the sample chamber converted from $5e-7$ Torr. It takes about a second to form a homogeneous monolayer of hydrogen on the sample surface loaded into the sample chamber. This result explains why H is so prevalent on each single shot spectra obtained at 1 Hz EUV laser frequency - see CdTe film depth profiling in the Imaging section. For carbon it would take same time multiplied by $\sqrt{12}$, i.e. ~ 3 seconds, for water - $\sqrt{18} \sim 4$ s. It explains why the surface shot is always rich with H, C, O and their derivatives not necessarily attributed to the analyte, and why subsequent shots at the same spot exhibit much lesser surface-related contamination. With vacuum better than $1e-9$ Torr, i.e. ultrahigh vacuum (UHV, $1e-9 \div 1e-12$ Torr), entire surface coverage happens on the hour scale. In case if sample-native H or other low-mass elements content monitoring will be required, vacuum conditions will have to be drastically improved.

Overview of maintaining vacuum in the system:

1. Pumping down the sample and TOF chambers (requires several hours to overnight)
2. Pumping down the tripling cell (several hours for 9th harmonic use)
3. Pumping down the switchyard and laser chambers (half an hour prior to experiment)
4. Establishing required gas flows and pressures and conducting the experiment
5. Complete shutting down and venting of the system (or laser side for data analysis)
6. Partial venting and re-pumping for quick sample replacement

VII.i.i Pumping down the sample and TOF chambers

Refer to Figure VII.18 for identification of the vacuum system element.

1. Check that all valves and lids are closed
2. Turn on sp3 pump
3. Slowly open av4 valve
4. Open av3 valve
5. When vg4 shows below $1e-1$ Torr start tp3 and tp4 pumps
6. Watch that both pumps accelerate to normal operation
7. Turn on cooling water
8. When vg4 shows below $1e-4$, open gv2
9. Verify that pressure keeps going down and pumps don't vibrate or heat

VII.i.ii Pumping down the tripling cell

1. Check that all valves are closed
2. Start sp4 pump
3. Open for few turns av5 valve
4. Open av6 and gv3 valves
5. When vg7 shows below $1e-1$ Torr, start tp5 pump and its cooling fan
6. If pumping of the gas supply lines are needed, then:
 - a. Close gv3 and av6, open av7 (limit such position to 20 min) if lines are pressurized, then reverse for finishing pumping with tp5
 - b. For Xe:Ar open sc15 valve and slowly open mv3; close after pressure stabilizes

- c. For He:C₃H₆ slowly open sc13, then sc11 and sc12; close afterwards

VII.i.iii Pumping down the switchyard and laser chambers

1. Check that all valves are closed
2. Verify that auto turn on and off pressures of vg1 are set to 0.5 Torr and that it is supplied with 80 PSI of air
3. Start sp1 and sp2 pumps
4. Slowly open av0, av1 and av2
5. When vg2 shows below 1e-1 Torr start tp1 and tp2
6. After few minutes turn on vg3 and enable vg1 auto shut-off function
7. Make sure that vacuum goes down to ~5e-6 Torr
8. Turn on cooling water and verify the absence of turbo vibrations or heating
9. For the use of gas cell open sc1 and slowly open mv1 until vented; loosely close mv1

VII.i.iv Establishing required gas flows and pressures

1. For capillary open sc2 and adjust mv2 after 10 min to 300 mTorr displayed on vg1, monitor this pressure during the run and properly adjust within ±20 mTorr
2. For gas cell enable Ar-1 flow and adjust mv1 to required pressure with vg2
3. Open gv1 valve to conduct experiment
4. For tripling cell and 9th harmonic:
 - a. Close gv3 valve
 - b. Open sc15 and slowly open mv3 to get to 250 Torr or more by vg5 gauge; close

- c. If less pressure is needed, open mv4 (0.1 mm orifice) and wait until pumping slows down, then open mv5 (0.3 mm) until 0 on vg5 is reached, then open gv3
 - d. If vacuum has to be provided quickly, close gv3 and av6, open av7, then reverse
5. For gas phase MS open sc16 and mv6, loosely close mv6, open sc14 and regulate the flow with mv6 by vg4 gauge – limit max pressure to $1e-6$ Torr as per MCP specs

VII.i.v Complete shutting down and venting of the system

1. Close all valves
2. Shut down all pumps
3. After 30 min or when turbos stop open sc8 and sc5 at low N₂ pressure and sc3
4. After $4e2$ Torr is reached on vg4 gauge open the lid on sample chamber and close sc5
5. Turn off cooling water

VII.i.vi Partial venting and re-pumping for quick sample replacement

1. Turn off tp4 pump
2. Close gv2 and av4 valves
3. After 10 min open sc8 and sc5 at low N₂ pressure
4. After $4e2$ Torr is reached on vg4 gauge open the lid on sample chamber and close sc5
5. Replace the sample and close the lid
6. Close av3 valve (limit to ~20 min) and open av4 valve
7. When vg4 shows less than $1e-1$ Torr start tp4 pump
8. When vg4 reaches $1e-4$ open av3 valve, then gv2

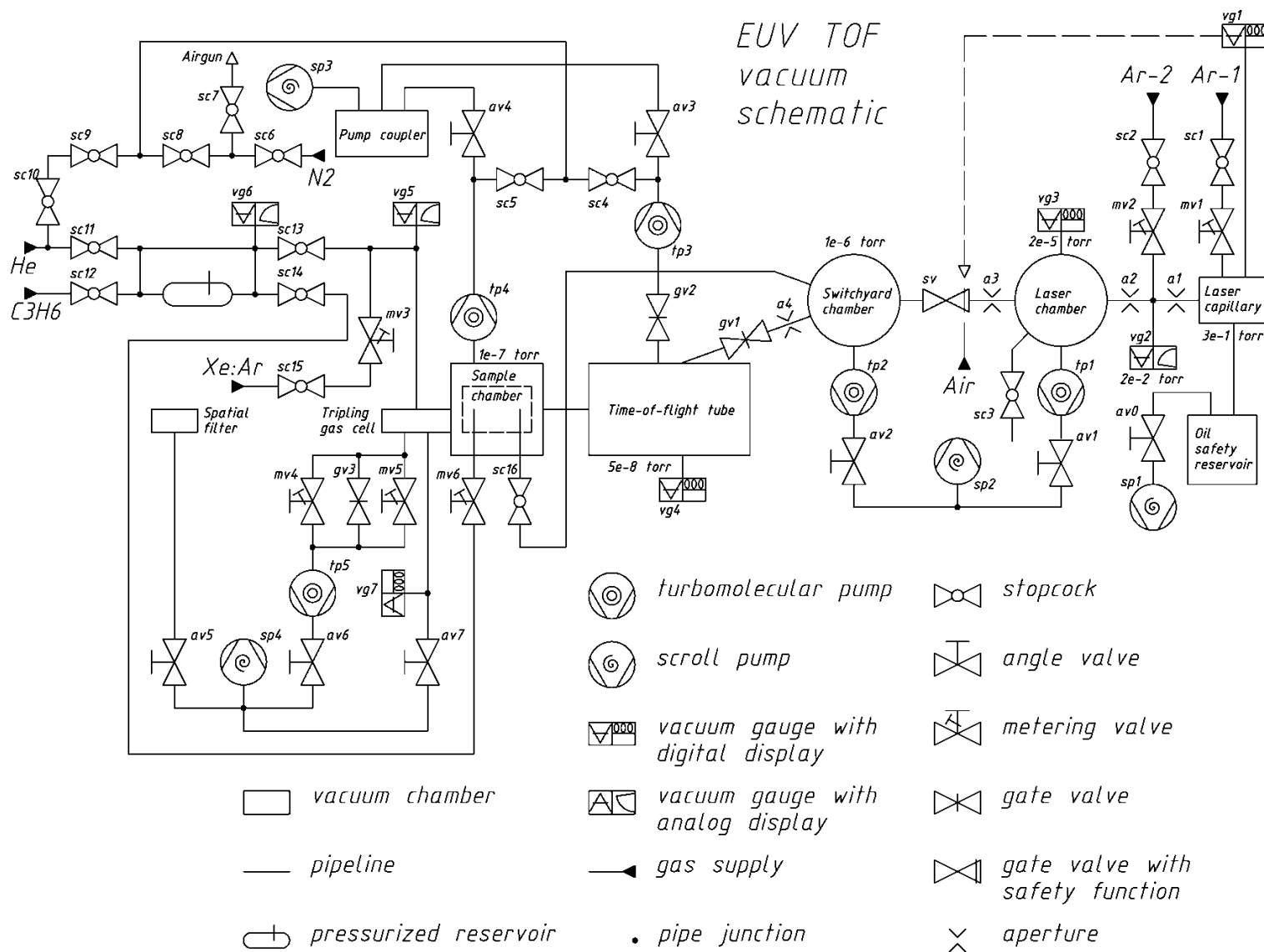


Figure VII.18: Vacuum scheme of the EUV TOF system with description of elements and pressures in the differentially pumped sections.

VII.j Timing

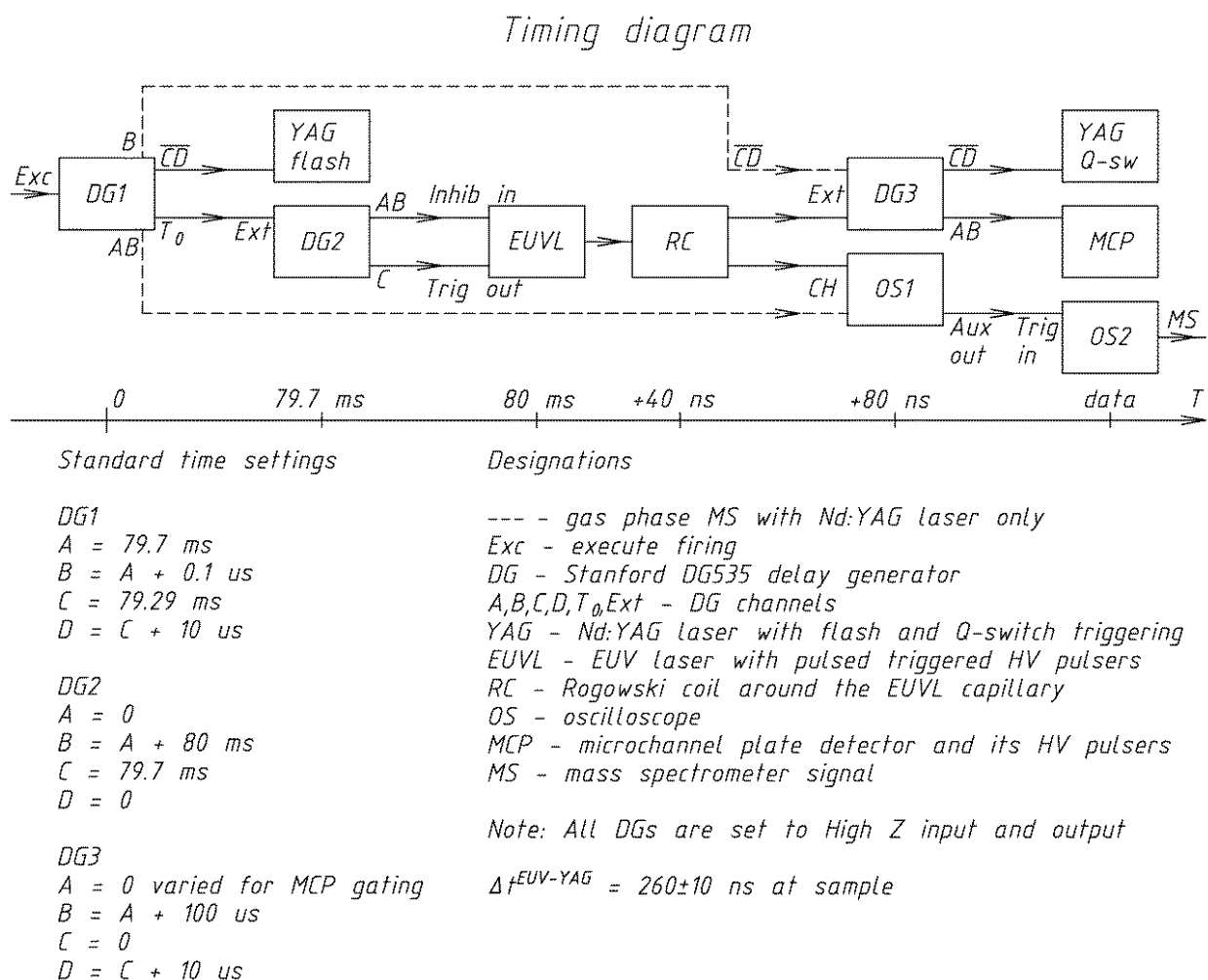


Figure VII.19: Timing diagram with acronyms of the block names explained and typical setting for delay generators DG1÷3.

VII.k Baseline adjustment

Very often quantitative analysis of spectra requires peaks integration and for that the baseline adjustment shown on Figure VII.20 allows bringing the integration base to zero across the whole range. This is done automatically in the BioInformatics toolbox in Matlab® after

selection of proper parameters. The algorithm first fits parametric line to the bottom of the existing baseline point-by-point and then brings it to zero. An extra offset is then additionally applied in order to bring the mean of the baseline to zero and thus realize near-zero integration of any interval between mass peaks. The original amplitude of mass peaks is preserved throughout the baseline adjustment procedure.

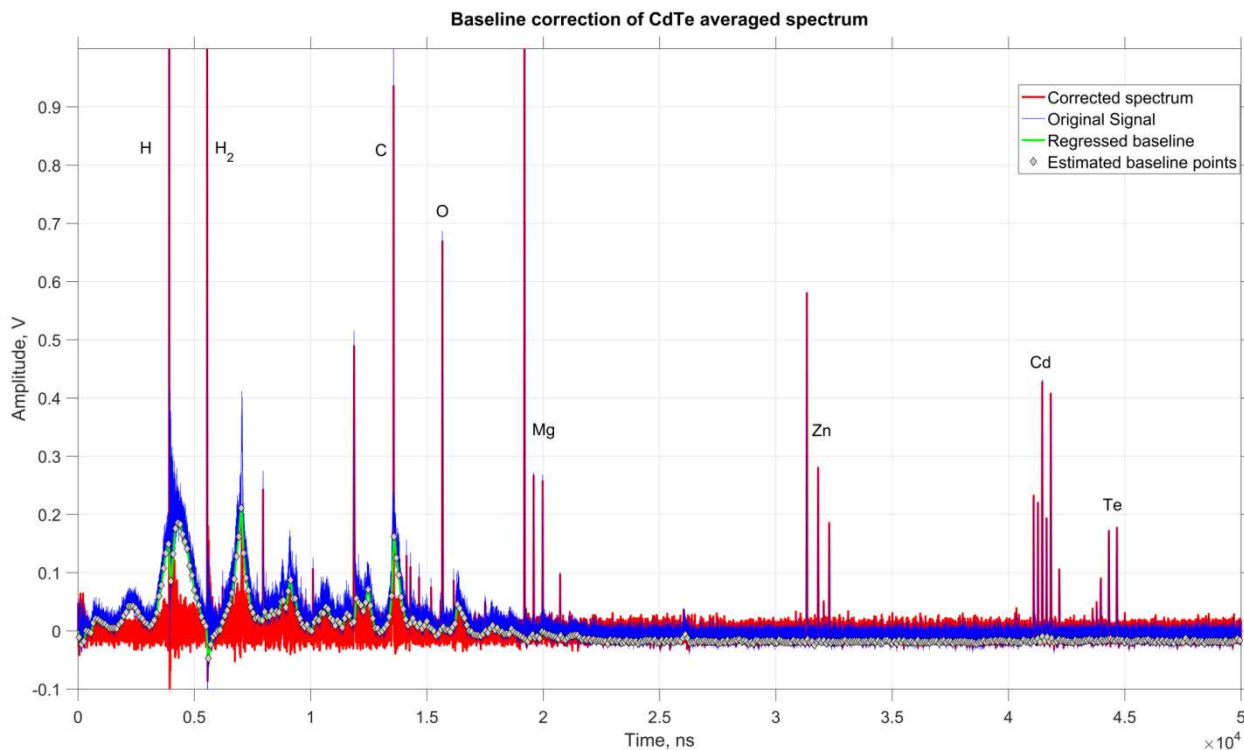


Figure VII.20: Illustration of the baseline adjustment on the example of CdTe averaged spectrum.

VII.1 Fragmentation

Fragmentation modeling was performed in ACD/MS Fragmenter software which predicts fragment ions based on established fragmentation rules from the literature.

Table VII.2: Conditions selected for standard fragmentation prediction by means of protonation on the example of Nile red molecule for the analysis of 319, 303 and 275 Da positive ions formation.

Reactions	Polarity	Positive
	Ionization Type	Other (CI, FAB,...)
	Distonic Ions Formation	Hydrogen Shift
	Common Reactions	Resonance Reactions
		Rings Formation
		Hydride Shift
	Bonds Cleavage	All Bonds
	Fragmentation Activation	CID/CAD
	Maximum Number of Fragments on Each Step	1000
	Number of Fragmentation Steps	5
	Minimum Mass Value	1
	Specific Fragmentation	Heterolytic Cleavage
β - Distonic with Radical Site Shift		
Even-Electron Ions		
Homolytic Cleavage		Negative Ions with Hydrogen Shift
		Odd-Electron Ions
		δ - Distonic with Radical Site Shift
		Distonic Ions with Radical and Neutral Losses
		Even-Electron Ions
		Negative Ions with Radical Loss
Hydrogen Rearrangements		Protonated Ions with Hydrogen Shift
		Include H Loss
		1,3-Shift
		1,5-Shift
		McLafferty Rearrangement
Neutral Losses		NL Before Ionization
		NL After Ionization
		1,3-Shift
		1,4-Shift
		1,5-Shift
Skeletal Rearrangements		Ejection from Cyclic Structures
		1,2-Shift
	1,3-Shift	
	1,4-Shift	
	1,5-Shift	
	Nitro Group	
	Sulfinyl Group	
Specific Oxygen Loss	Sulfonyl Group	
	Migration to Cation Center in Esters	
	N-Containing Compounds	
	P-Containing Compounds	
Target Ions	Target Ions	S-Containing Compounds
		319
		303
		275

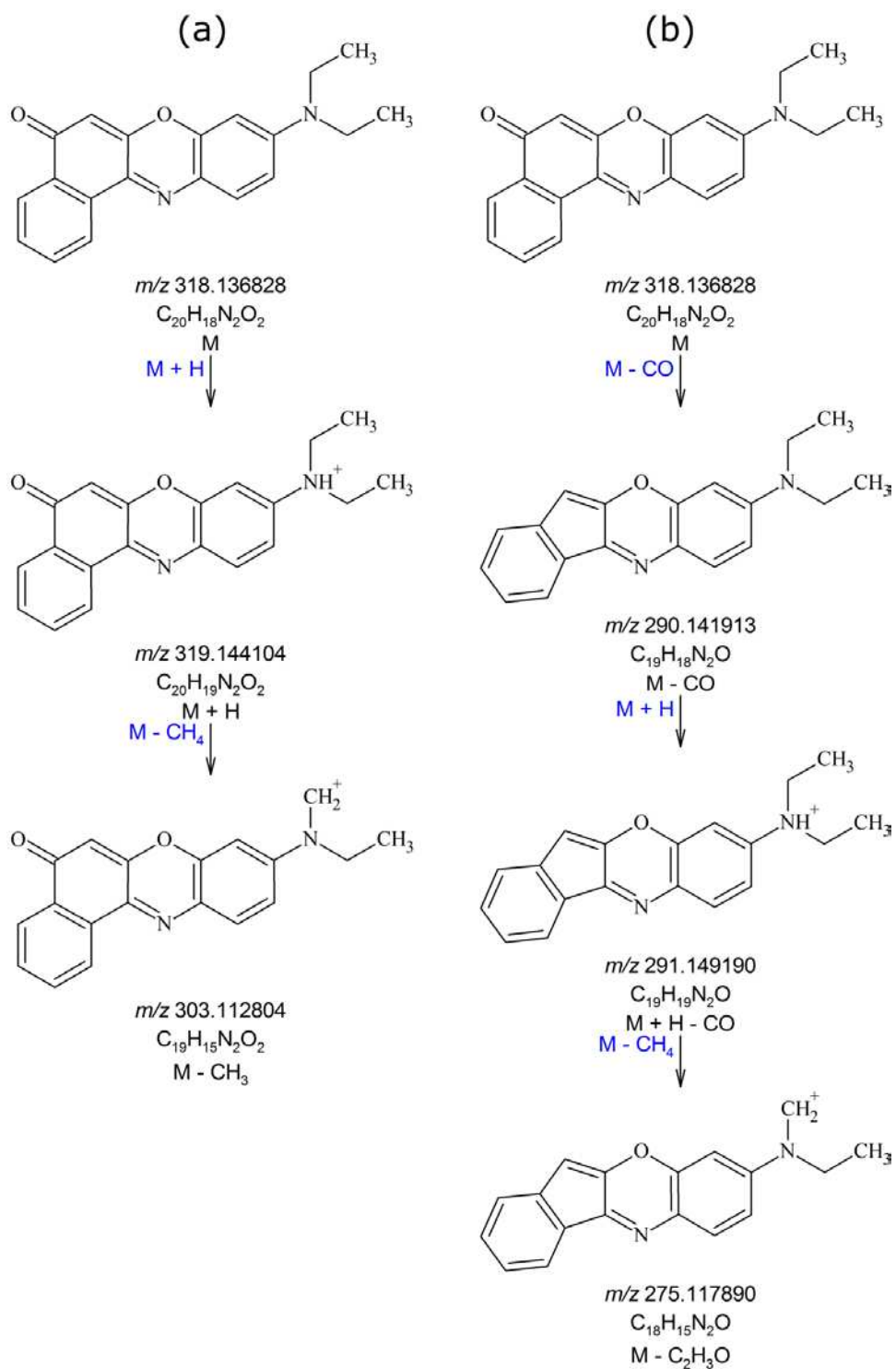


Figure VII.21: Fragmentation pathways of Nile red 318 Da molecule. (a) Formation of 303 Da ion via initial protonation to 319 Da and subsequent cleavage of methyl group. (b) Formation of 275 Da ion initiated by carbonyl group detachment followed by rearrangement of the aromatic ring, protonation of the 290 Da neutral, and cleavage of same methyl group as in 303 Da formation.

Table VII.3: Simplified representation of positive and negative ion fragments of trimethoprim and Nile red at detected masses modeled by protonation mechanism in the ACD/MS Fragmenter.

Mass	Trimethoprim	Mass	Trimethoprim
+275		-243	
+261		-227	
+245		-215	
	Nile red		Nile red
+303		-289	
+247		-274	
+218		-261	

Table VII.4: Possible fragment ions of PA, SM and POPC obtained by analysis in ACD/MS Fragmenter using ionization by protonation approach. SM and POPC fragments appear to be the same, while they differ from PA.

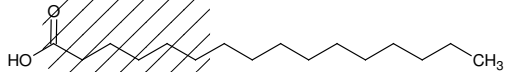
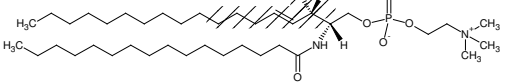
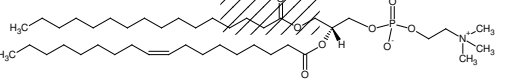
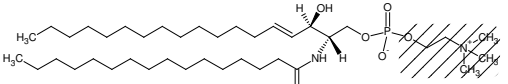
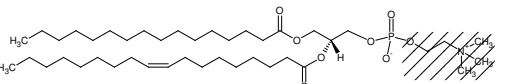
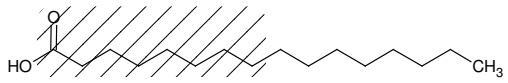
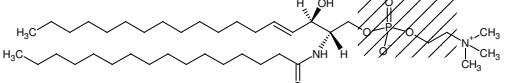
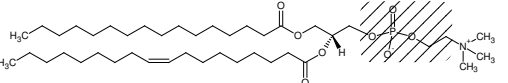
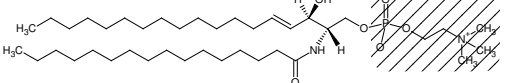
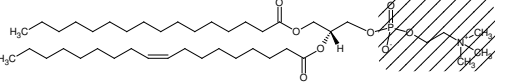
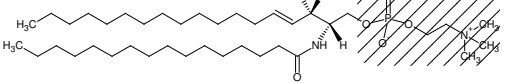
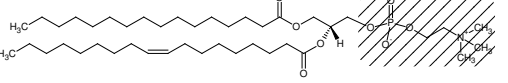
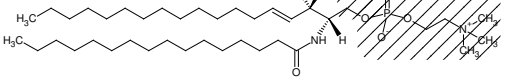
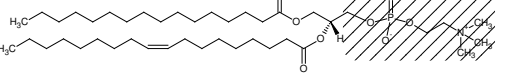
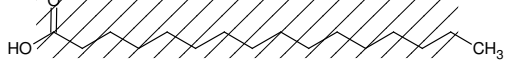
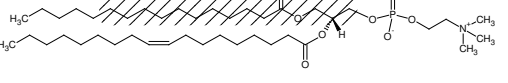
Mass	PA	SM	POPC
99			
104	?		
125			
166			
184			
198			
224		-	
284	-	-	

Table VII.5: Analysis of DPPC and DPPE fragment ions via protonation ionization mechanism. Mostly all fragments significantly differ in composition despite their similarity in mass.

Mass	Fragment	DPPE	DPPC
99	Fraction of aliphatic chain		
155	Half of aliphatic chain		
239	Almost full aliphatic chain		
256	Full aliphatic chain or head group with glycerol		
281-325	Aliphatic chain with glycerol		
393, 367	Aliphatic chain with part of head group		
551	Full tail group or head with part of tail group		

VII.m Nature Communications paper supplementary material

VII.m.i Comparison of EUV TOF and other mass spectrometry methods

EUV TOF brings new opportunities to MSI by making possible to assess molecular composition in 3D at nanoscale dimensions with high sensitivity. To contrast EUV TOF with leading molecular mass spectrometry methods—ultraviolet laser desorption ionization time of flight mass spectrometry (UV LDI TOF) and static secondary ion mass spectrometry (SIMS TOF)—we conducted experiments in which the same alanine sample was analyzed by the three methods. The SIMS TOF results were obtained by Evans Analytical Group (EAG) using a ION TOF instrument⁷⁴ TOF.SIMS 5. For the UV LDI TOF experiments we used a Bruker Ultraflex 2 mass spectrometer without applying a matrix for ionization enhancement to simulate the conditions of EUV TOF.

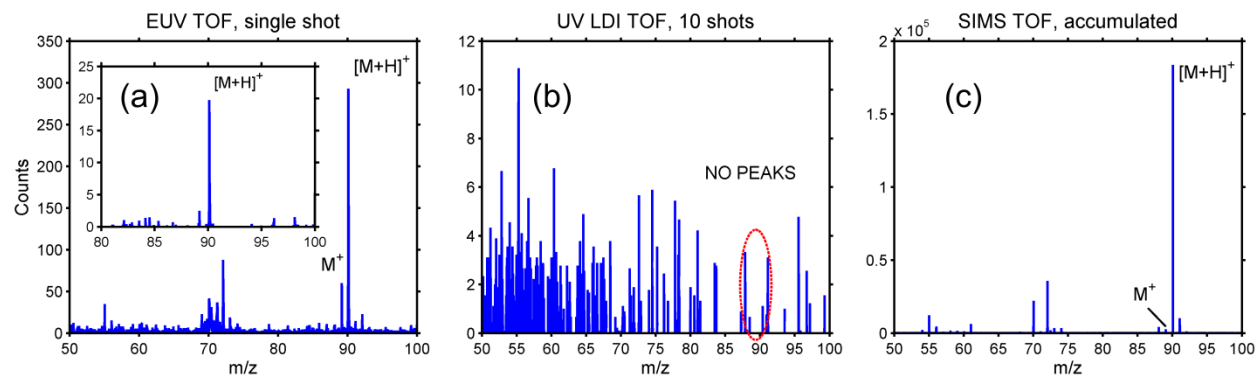


Figure III.h.1: Mass spectra of a ~120 nm thick layer of alanine obtained with (a) EUV TOF, (b) UV LDI TOF and (c) SIMS TOF. The M^+ and $[M+H]^+$ ion peaks are identified. The spectrum in (a) was obtained from an ablated analyte volume of 12.8 aL, and the one in the inset from a 50 zL volume.

The alanine mass spectra obtained from each method are shown in Figure III.h.1. Comparison between EUV TOF and SIMS TOF reveals the presence of the parent analyte ions, $[M+H]^+$, the radical M^+ and similar fragments' distribution. The main difference is that the

aforementioned peaks in the EUV TOF spectrum are well resolved even when the information is extracted from the single shot ablation of a crater with a volume of 50 zL (Figure III.h.1a inset). Instead the SIMS TOF spectrum was obtained by scanning 20 times an area of $150 \times 150 \mu\text{m}^2$ with a $5 \mu\text{m}$ diameter Bi_3^+ primary ion beam. The atomic force microscope image of the 50 zL crater ablated in PMMA as the same conditions of alanine is shown in Figure III.h.2a.

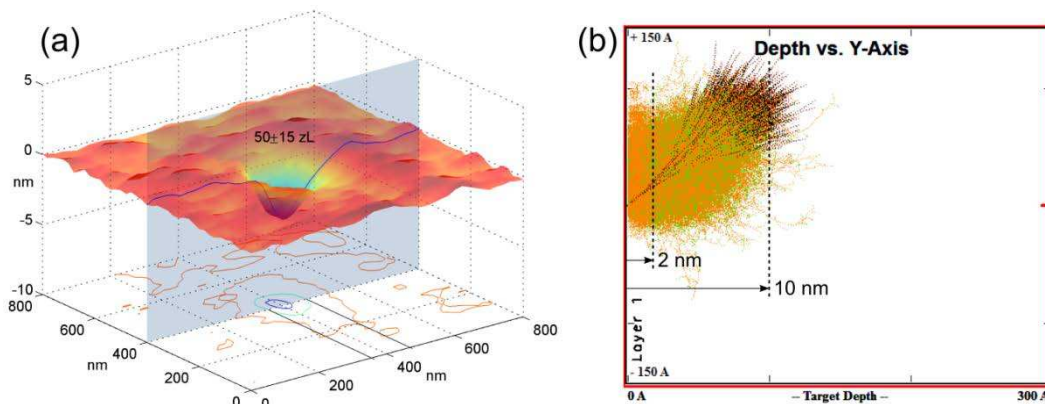


Figure III.h.2: (a) Atomic force microscope image of a 50 zL crater ablated in polymethyl methacrylate. The blue and orange contour lines show the profiles at 10 and 90% of the crater's depth. At the same irradiation conditions, a crater ablated in alanine produced the mass spectrum shown in the inset of Figure III.h.1a. (b) TRIM program simulation of a collision cascade as a result of 10 keV Bi^+ ion (1000 ions total) interacting with a solid carbon target. The primary ions are incident at 45° . Cascading happens within ~ 10 nm. The black lines show the primary ion trajectories with red dots at the end, the orange lines represent the displaced atoms (more densely distributed within 2 nm of probe depth) and the green dots show the end of the trajectories for the displaced atoms.

The sensitivity of a mass spectrometry method is calculated as the ratio of the ablated/sputtered analyte mass in moles to the counts within the area of the dominant parent ion, i.e. $[\text{M}+\text{H}]^+$. Using the alanine spectrum in the inset that shows $[\text{M}+\text{H}]^+$ peak is well above the noise level we calculate the sensitivity of EUV TOF to be 0.01 amol.

A similar calculation was performed for SIMS TOF. Since the depth of the analyte region probed by SIMS TOF was not provided by EAG, we made use of commercial software (TRIM – Transport of Ions in Matter, based on the Monte-Carlo simulation method, <http://www.srim.org/>)

to estimate the ion/analyte interaction region and the depth from which secondary ions are generated. Because the primary ions used for sputtering were relatively small clusters of Bismuth— Bi_3^+ at energies of 30 keV—we modeled this interaction as that of a single Bi projectile of 10 keV energy. Z. Postawa et al showed that multi-atomic inorganic projectiles dissociate upon impact, hence the energy is divided equally among its species⁷⁵. We also simplified the target to be pure carbon. A plot of the primary ion trajectories and the displaced atoms as a result from the collision cascade process in SIMS TOF is shown in Supplementary Figure III.h.2b. It has been shown secondary ions originate from the top few monolayers of the analyte's surface⁷⁶, i.e. 2 nm. This assumption correlates well with our modelling. The displaced target atoms, indicated by the orange traces in Supplementary Figure III.h.2b, are most dense within the top 2 nm of the carbon sample. However, the collision cascade contributing to surface ejection of sputtered species, occupies deeper layers, 10 nm, as also shown in Figure III.h.2b⁷⁷. We used a conservative probe depth of ~2 nm for SIMS TOF to calculate the alanine mass from which ions originate in the spectrum of Figure III.h.1c. This value is a lower estimate for the penetration depth because alanine has lower density than carbon. A depth of 2 nm corresponds to 4 monolayers of alanine. The sensitivity of SIMS TOF is calculated to be 0.4 amol, which is 40× lower than that of EUV TOF. Supplementary Table I summarizes the results of the sensitivity analysis.

Table III.6: Parameters used in the calculation of sensitivity and level of fragmentation for EUV TOF and SIMS TOF

Alanine	EUV TOF	SIMS TOF
# of primary particles (dose)	$3.9 \cdot 10^6$	$4.1 \cdot 10^8$
# of secondary ions at 90 m/z	80	$1.76 \cdot 10^6$
Area probed (μm^2)	$4.5 \cdot 10^{-2}$	$2.25 \cdot 10^4$
Depth probed (μm)	$3.5 \cdot 10^{-3}$	$2 \cdot 10^{-3}$
Volume probed (aL)	0.05	$4.5 \cdot 10^4$
Sensitivity (amol)	0.01	0.4
Ion yield normalized to probed volume (L^{-1})	$4 \cdot 10^{14}$	$8.5 \cdot 10^{10}$
Level of fragmentation	1.1	1

The model simulation also shows that for the conditions of the SIMS TOF experiment, the depth resolution in MSI cannot be better than ~ 10 nm, the extend of the collision cascade process where the analyte is damaged. The work by D. Rading et al⁷⁷ showed that the type of clusters and their energy can be selected to reduce the depth of the ‘damaged’ region in SIMS TOF. Notice that in contrast to SIMS TOF, there is no damage to the sample outside the ablated crater in EUV TOF.

The differences between EUV TOF and UV LDI TOF can be accounted for by analyte absorption at the different wavelengths. Alanine has minimum absorption at $\lambda = 333 \text{ nm}$ ⁷⁸, thus the mass spectrum mainly contains spurious peaks even after 10 laser shots were accumulated. Instead in EUV TOF organic solids are strong absorbers at $\lambda = 46.9 \text{ nm}$, making it possible to controllably ablate and efficiently ionize the analyte.

The level of fragmentation was also calculated from the EUV TOF and SIMS TOF spectra of Figure III.h.1 as the ratio of total counts within $[\text{M}+\text{H}]^+$ to the total number of counts in the spectrum within the m/z range 50÷90, namely the peaks at m/z 55, 70, 72 and 89. For EUV TOF we used the mass spectrum obtained from the ablated 12.8 aL crater. The level of

fragmentation of EUV TOF is found similar to SIMS TOF. Supplementary table I summarizes the results of this comparison.

In summary, based on the results of the analysis of the same alanine sample it is shown that EUV TOF has higher sensitivity and similar level of fragmentation. EUV TOF also has significantly smaller 3D localization. In comparison with UV LDI TOF, the results show EUV light is naturally suited for mass spectrometry of organic analytes due to the high absorption of these materials at $\lambda = 46.9$ nm.